DISSERTATION

A Quantitative Analysis of Critical Factors in Pitting Corrosion

Presented to:
The Faculty of the School of Engineering and Applied Science
at the University of Virginia

In partial fulfillment of the requirements for the degree of
Doctor of Philosophy in Materials Science and Engineering

Prepared by:

Armando Shehi

May, 2025

Doctoral committee

Name	Role	Department
Prof. James T. Burns	Committee chair	Materials Science and Engineering
Prof. John. R. Scully	Committee member	Materials Science and Engineering
Prof. Elizabeth. J. Opila	Committee member	Materials Science and Engineering
Prof. Gary. M. Koenig	Committee member	Chemical Engineering
Ph.D. Nicholas Laycock	Committee member	Qatar Shell Research and Technology Centre
Prof. Robert. G. Kelly	Dissertation advisor	Materials Science and Engineering

Abstract

The exposure of many alloys to aqueous electrolytes often leads to the formation of surface films that are more stable than the alloy itself. These films are typically considered protective (passive) due to their ability to significantly reduce the alloy's dissolution rate even in highly aggressive environments. However, localized breakdown of these films can result in pitting corrosion-one of the most aggressive and challenging forms of corrosion to manage due to its highly dynamic and complex nature. Fundamentally an electrochemical process, understanding pitting corrosion requires a detailed analysis of the interactions between current/ potential inside the pit with the surrounding chemical and electrochemical reactions coupled with inside and outside pit mass transport processes. The intricate nature of high current densities/potentials, and the highly concentrated, evolving solution inside the pit (anode) adjacent to a passivated alloy surface (cathode), has posed a challenge for decades.

This dissertation aims to provide a quantitative analysis of critical factors influencing pitting corrosion through a combined experimental and computational approach, focusing on pit propagation and the conditions leading to repassivation. Specifically, the study investigates pitting corrosion in stainless steels (SS) 316L and 304 in chloride-containing environments. A newly developed framework integrating experimental and modeling approaches is introduced to correlate key factors in pit repassivation, including repassivation potential, repassivation current density, critical pit stability product, fraction of highly aggressive solution saturation, in-pit pH, and the ratio of local cathodic to anodic current densities. This framework is then applied to characterize variations in these critical parameters in mixtures of chloride and sulfate-containing environments, which are known for their corrosion-inhibiting properties for the SS316/L and SS304/L alloys.

In order to apply the findings to more applicable engineering scenarios, the dissertation extends, through modeling approach, the typically one-dimensionally (1D) acquired critical pitting factors into three-dimensional (3D) ones. Then, the conservativism of existing 3D pit size predictive models, such as the Chen and Kelly's analytical model and numerical Finite Element Analysis (FEA) methods, in estimating maximum pit size for a given alloy-electrolyte system is also assessed. The dissertation concludes with an evaluation of electrochemical processes near the electrode-electrolyte interface in localized corrosion while also exploring the efficacy of the Laplace with variable conductivity (Lvk) reduced-order model (ROM) in reducing computational costs. Two additional novel ROM techniques for localized corrosion through FEA, introduced and demonstrated for the first time in this dissertation work, are shown to significantly enhance computational efficiency while maintaining very high accuracy in the obtained results.

Acknowledgments

To those who believed when I didn't…

It would be impossible for me to stand here and claim that I could have done this without the person who believed in me from day one and cheered me on every step of the way-my advisor, Professor Robert G. Kelly. I can still remember our first meeting, discussing my application to UVA, and how that moment shaped the path that led me here. Your unwavering support, kindness, and trust in me have been invaluable. You not only allowed me to carve my own path as a researcher, but you also had faith in me when I often didn't have it in myself. The lessons you've shared go far beyond the realms of a Ph.D., electrochemistry, or corrosion. In this world and field, we love, few are lucky enough to say that. This one is for you…

To my committee members: Professor James T. Burns, Professor John R. Scully, Professor Elizabeth J. Opila, Professor Gary M. Koenig, and Dr. Nicholas Laycock-thank you for being integral to this journey, for reading the work of the last four years of my life, and providing your valuable expertise in improving it and my understanding of the field I am so passionate about.

To the professors at UVA who sparked my passion for Materials Science and Engineering and helped me grow as a critical thinker: most heartedly, thank you! And to the professors at Cal Poly Pomona who first ignited my interest in corrosion-Professors Lupanar Ravi and Juan Carlos Nava-thank you for introducing me to a field that has since captured my heart.

A special thank you to my colleagues in the *Kelly Group* over the years, who made the discussions on localized corrosion and modeling so enriching: Emma Laubengayer, Alice Pandaleon, Duane Macatangay, Carolina Moraes, Utibe-Eno Charles-Granville, Rebecca Marshalls, Ryan Katona, Victor Kontopanos, Timothy Montoya, and Savannah Horowitz. The lab and office wouldn't have been the same without you. And of course, I must give a huge shoutout to my colleague, mentor, postdoc, and now professor—Sanjay Choudhary! Your expertise, patience, and willingness to entertain my most outlandish ideas have been invaluable. *"Did we solve pitting yet?"*

To my dear friend Lauren thank you for sticking by me through it all. Your emotional support was my lifeline when things got tough, and I couldn't have come this far without it. To *Claire*, I will always treasure your positivity, understanding, and the kindness you brought into my life-and most importantly, for turning my *Blue Banisters* green! To *Jose*, thank you for believing in me when I couldn't, for seeing my potential, and for always being my unwavering supporter.

And most importantly, *to my dads*: Alex, Pedro, and Oscar. Your unconditional love and sacrifices have been the foundation on which I stand. You saw in me what I couldn't see in myself, and your constant support and patience over the past four years made this possible. I dedicate this dissertation to you-*¡los quiero mucho!*

…I once had dreams of becoming [someone], but upon an unfortunate series of events saw those dreams dashed and divided like a million stars in the night sky that I wished on over and over again, sparkling and broken. But I didn't really mind because I knew that it takes getting everything you ever wanted and then losing it to know what true freedom is…

Who are you? Are you in touch with all of your dreams? Have you created a life for yourself where you can experience them?

I have,

I [might sound] crazy

But I am free…

LDR

Bibliography

Publications as a product of the dissertation are listed below (all of them in the process of publication/review):

A. Shehi, R. G. Kelly. (2025). The Shape Factor for Pits and Its Impact on Pit Stability. *Journal of The Electrochemical Society.*

A. Shehi, S. Choudhary. R. G. Kelly. (2025). Repassivation of stainless steels: A unifying quantitative framework. *Corrosion Science.*

A. Shehi, A. Pandaleon. R. G. Kelly. (2025). Pitting and repassivation in the presence of sulfates: a controlled 1D pit approach. *Journal of The Electrochemical Society.*

A. Shehi, C. V. Moraes. R. G. Kelly. (2025). A comparison of FEM results from the use of different governing equations in a galvanic cell part III: Localized corrosion case-impact of high current density, supporting electrolyte concentration, and diffusion coefficient of electrochemically active species. *Electrochimica Acta.*

A. Shehi, R. G. Kelly. (2025). Investigation of a new subroutine in FEM developed to circumvent simultaneously solve NPE governing equation: An application to various studies. *Electrochimica Acta.*

A. Shehi, R. G. Kelly. (2025). From 1D to 3D: Maximum pit size predictions with different levels of complexity. *Journal of The Electrochemical Society.*

R. Skelton Marshall, **A. Shehi,** R. M. Katona, M. A. Melia, R. G. Kelly. (2025). Perspective – An Alternative Calculation of the Repassivation Potential, to Represent Less Conservative and More Realistic Values. *Journal of The Electrochemical Society,*

Table of Contents

List of in-text figures

List of figures in Appendices

List of figures in *Appendix i*

List of in-text tables

List of tables in Appendices

List of tables in *Appendix i*

Chapter 1. Introduction

1.1 Overview

The interim storage of spent nuclear fuel (SNF) waste in the United States relies on large-scale concrete containment structures housing stainless steel canisters containing the SNF made from alloys such as type 304L/304 or 316L/316.[1] Originally intended as a temporary solution, these storage systems were implemented over four decades ago with the expectation that SNF would eventually be transferred to permanent repositories. However, the development of these long-term disposal facilities remains an ongoing challenge.

These canisters are licensed for a limited operational lifespan of 20 to 40 years, necessitating periodic inspections and safety assessments to identify potential failures and implement necessary precautions.[2–4] Given that many of these storage sites are located in coastal environments, the canisters are particularly vulnerable to environmental degradation. This degradation is primarily driven by the formation of an aggressive electrolyte on their surfaces, which can initiate corrosion- a process in which the metal undergoes electrochemical reactions with its surrounding environment.[2,3,5]

Among various forms of corrosion, localized corrosion, specifically pitting corrosion, is of particular concern. Pitting can create stress concentration sites that significantly increase the risk of stress corrosion cracking (SCC).[6,7] The progression from pitting corrosion to SCC could compromise the structural integrity of the canisters, posing a containment risk. Recognizing this threat, regulatory bodies such as the Nuclear Regulatory Commission (NRC) and the Nuclear Waste Technical Review Board (NWTRB) have emphasized the importance of continued research and monitoring to mitigate these risks.[7]

1.2. Background

1.2.1 SNF canisters

In near-marine environments, aerosols generated by wave action and evaporation processes can deposit onto the surface of SNF storage canisters.[8–10] Initially, these aerosol particles are typically small, measuring only a few microns in diameter. However, their size and volume can change in response to environmental factors such as relative humidity (RH) and surface temperature.[10]

When first deployed, canister surface temperatures can exceed 150°C, causing any aqueous solutions, including aerosol droplets, to rapidly evaporate, leaving behind dry salt deposits.[2] Over time, as heat dissipates through ventilation cooling from the bottom of the canister, its surface temperature decreases, creating conditions more favorable for the formation and retention of an aqueous electrolyte.

An aqueous electrolyte forms when the environmental RH exceeds the deliquescence relative humidity (DRH) of the salts present on the canister's surface. This transition occurs as moisture from the surrounding atmosphere is absorbed, resulting in a thin liquid electrolyte layer. The gradual decrease in surface temperature, combined with increasing RH, enhances the formation and persistence of this electrolyte layer.[2] This phenomenon is significant because it facilitates pit initiation and growth, which can ultimately lead to SCC and compromise the structural integrity of the canisters.

For corrosion to occur, four essential components must be present: an anode, a cathode, a path for electron flow, and an ionic path (electrolyte) connecting the anode and cathode. While the canister itself provides the electron pathway, both the cathode and anode surfaces must be covered by an electrolyte. In the case of pitting corrosion, the cathode surface area required to sustain pit growth is much larger than that of the anode (the pit itself). Existing literature suggests that an electrolyte is expected to be present on dry storage canisters (DSCs) at surface temperatures at or below around 60°C.[11] At these temperatures, the RH remains low for any level of absolute humidity found on Earth, leading to high concentrations of aggressive species such as chloride ions. However, at high temperatures, the initial electrolyte volume is expected to be low due to evaporation, which limits the wetted cathode area and, in turn, restricts deep pit formation.

As the canister temperature decreases, surface RH increases, leading to a larger wetted area. Under these intermediate conditions, environmental factors become more favorable for pit initiation and propagation. A sufficiently large portion of the canister surface remains wet to sustain pit growth, while the high concentration of aggressive species in the electrolyte, combined with elevated temperature, promotes rapid pit propagation. However, as temperature continues to drop and RH further increases, the electrolyte-covered area expands, while the concentration of aggressive species decreases. In such conditions, while a sufficient electrolyte layer remains to sustain pitting, the reduced aggressiveness of the environment slows deep pit growth kinetics.

This dynamic gives rise to the concept of an "Inverse Goldilocks" scenario-a specific range of temperature and RH in which both are sufficiently high to provide a large cathode surface area and an aggressive environment that supports rapid pit growth kinetics. However, the precise environmental conditions on a given canister's surface can vary significantly depending on site-specific factors such as ambient temperature, absolute humidity, initial heat load, canister geometry, and local climate conditions.[12] Thus, when assessing the extent of pitting corrosion damage, it is essential to account for location-specific variations in environmental factors and their impact on pitting corrosion.

1.2.2 Pitting corrosion

The primary characteristic of pit initiation is the localized breakdown of the passive film on an alloy, followed by rapid dissolution of the exposed metal. This breakdown can occur through various mechanisms, including mechanical wear, weakly protected or unprotected surfaces containing inclusion sites such as manganese sulfide (MnS), defects within the oxide film, or chemical dissolution of the passive layer in the presence of aggressive species such as chloride ions.[13–16] A schematic of the issue is presented in Figure 1a.

Once the passive film is compromised, a high rate of alloy dissolution ensues due to the formation of a localized low-pH environment, driven by cation hydrolysis:

$$M^{n+} + H_2O \leftrightarrow M(OH)^{(n-1)+} + H^+ \tag{1.1}$$

This hydrolysis reaction leads to the generation of hydroxy metal cations and acidification of the surrounding environment. The resulting acidic conditions attract additional anions, such as chloride ions, to maintain electroneutrality. Consequently, the oxygen-depleted interior of the pit exhibits a more aggressive chemical environment-characterized by low pH and high chloride concentration compared to the solution on the bulk alloy surface.

Once initiated, pit growth becomes self-sustaining, or autocatalytic, as the corrosion process continues to accelerate within the confined pit environment, Figure 1b. The continuous supply of metal cations, their hydrolysis, and the subsequent acidification of the pit microenvironment contribute to the progressive deepening and expansion of the pit. Thus, pit growth involves three key stages: localized passive film breakdown, rapid metal dissolution, and the establishment of an oxygen-depleted, acidified microenvironment within the pit.

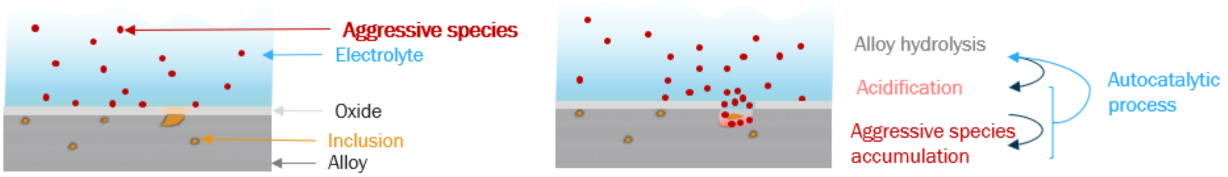

(a) **(b)**

Figure 1.1. (a) Schematic of an alloy (grey) containing an oxide layer (white), inclusion sites (yellow) exposed to an electrolyte containing aggressive species (red) and **(b)** representation of pit initiation and the autocatalytic process.

Studies on pit growth under atmospheric conditions suggest that many material-environment combinations follow a time-dependent power law relationship:[17]

$$d = At^{b} \tag{1.2}$$

where d represents pit depth, t represents time, A corresponds to the pit size at year one, and b is an exponent typically less than 0.6. However, applying this empirical model to SNF canisters presents several challenges.

First, experimental studies conducted under atmospheric conditions require prolonged exposure periods, often exceeding the expected service life of these canisters. This limitation makes direct extrapolation of such data unreliable for predicting pit growth in nuclear waste storage. Second, power law expressions for pitting can be misleading, particularly when environmental conditions change over time. As the storage environment evolves, predictive errors associated with power law models increase, reducing their reliability. Lastly, power laws inherently suggest that pit growth is unbounded, implying indefinite propagation. However, this assumption lacks a fundamental electrochemical basis and fails to account for mechanisms that may slow or halt pit growth, such as repassivation or changes in environmental conditions.

Given these limitations, alternative approaches that incorporate electrochemical principles and site-specific environmental factors are necessary for accurately predicting pit growth and assessing the long-term integrity of SNF storage canisters.

1.2.3 Modeling of pitting corrosion/localized corrosion

As previously discussed, conducting long-term atmospheric exposure experiments to study pitting corrosion is impractical for engineering applications such as those addressed in this work. To overcome this limitation, accelerated electrochemical techniques have been developed to study corrosion, including localized corrosion, within a shorter time frame. These methods provide key parameters, such as the pitting potential (E_{pit}) and repassivation potential (E_{rp}), which are critical for characterizing the corrosion behavior of various alloys (Figure 2).

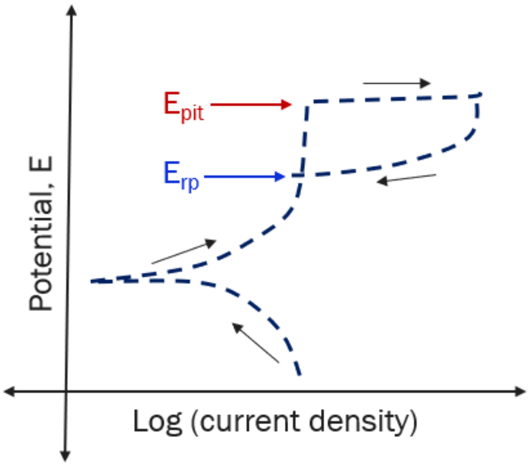

Figure 1.2. Schematic of a typical cyclic potentiodynamic polarization scan with ordinate being potential and abscissa being the current density. The typical values of E_{pit} and E_{rp} are demonstrated in red and blue, respectively.

Traditionally, these parameters are interpreted as follows: E_{pit} represents the potential at which pit initiation occurs on the alloy surface, while E_{rp} defines the threshold potential above which existing pits continue to grow and below which no new pits initiate.[18–23] The value of E_{rp} not only provides insight into the electrochemical stability of the corroding surface but also serves as a lower boundary condition for pit susceptibility, informing alloy design and implementation in corrosion engineering. Research by Sridhar and colleagues has demonstrated that pits can initiate at potentials below E_{pit}; however, no pit propagation has been observed below E_{rp} even at very long times (e.g., 3-4 yrs).[24–26]

Typically, E_{rp} values for different alloys in various electrolytes are determined using cyclic potentiodynamic polarization (CPP) experiments as depicted in Figure 2. In a CPP experiment, the sample is positively polarized from its open circuit potential (E_{OCP}/OCP) at a controlled scan rate until a sharp increase in current density (i) is observed, indicating pit initiation at E_{pit}. A predefined current density limit is imposed, and once this limit is reached, the scan is reversed toward lower potentials at the same scan rate. If the reverse scan intersects the forward scan, pit passivation is considered to have occurred, marking the E_{rp}.[27]

Experimental studies have shown that factors such as scan rate, maximum current density, and the extent of prior pit growth can influence the measured E_{rp} values.[28–30] However, research by Sridhar et al. has demonstrated that by passing a sufficient total charge density during long term immersion experiments, therefore increasing the pit depth on the surface of such alloys, the E_{rp} value eventually reaches a plateau.[24,26] This plateau represents a conservative engineering safety boundary for pit propagation.

While quantifying E_{rp} for a given alloy in a specific environment provides a useful means of assessing the lower boundary for pit propagation, it does not inherently describe pit growth kinetics. Building on the foundational work of Vetter and Pickering,[31,32] Galvele developed a more comprehensive electrochemical transport-based model for one-dimensional pit growth in the 1970s.[33] According to this model, for a pit of depth *x* to sustain a critical local chemistry at its base, a corresponding metal dissolution current density (i_{rp}) must be maintained, Figure 1.3.

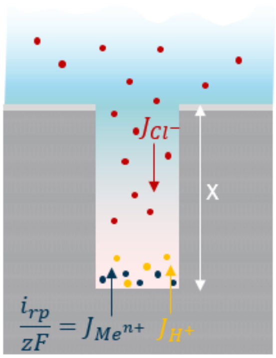

Figure 1.3. Generalized schematic of a typical 1D pit dissolution.

This relationship, known as the pit stability product (i·x), is derived from electrochemical and transport-based equations that account for factors such as metal dissolution rate, equilibrium reactions, species concentrations, and diffusivities within the pit environment. By incorporating electrochemical and mass transport phenomena, Galvele's model provides a more mechanistic understanding of pit growth and the critical factors influencing its propagation.

1.2.4 Modeling pit growth

Galvele's work on pit growth kinetics provides a fundamental understanding of pitting corrosion by emphasizing the need for sufficient anodic dissolution to maintain an aggressive electrolyte environment, preventing oxide formation and passivation that would occur if the pit solution is sufficiently depleted by diffusion.[33–35] However, pit growth, like any corrosion process, is governed by the simultaneous coupling of oxidation and reduction reactions. Specifically, anodic dissolution within the pit releases electrons, which are consumed by cathodic reduction reactions on the passivated surface surrounding the pit. This galvanic coupling adheres to the principles of Mixed Potential Theory (MPT) and ensures charge conservation, Figure 1.4.

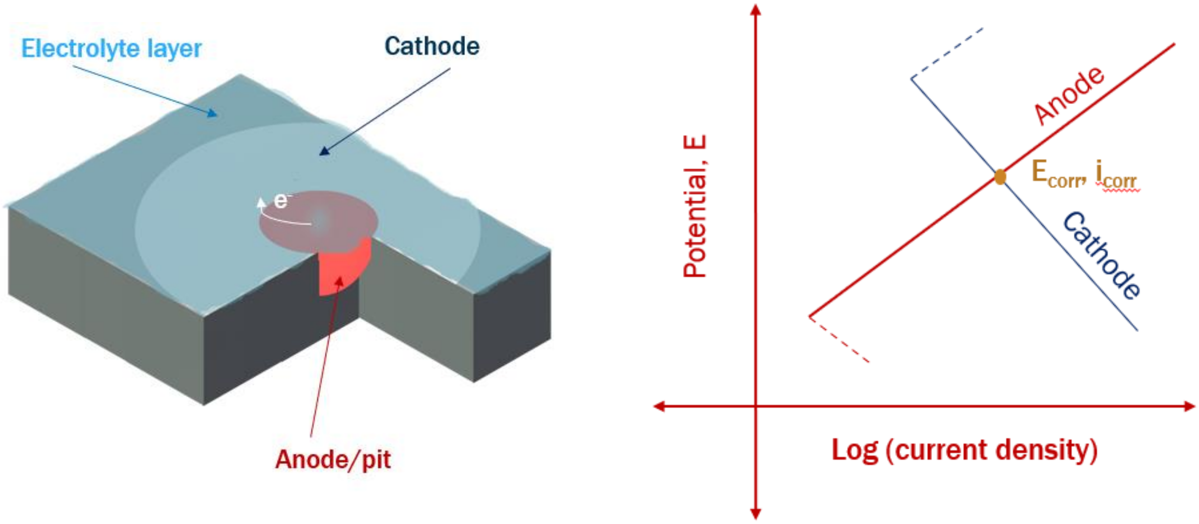

(a) (b)

Figure 1.4. **(a)** Schematic of a typical galvanic coupling between an anode (pit) and cathode (surrounding alloy) covered in electrolyte layer and **(b)** Schematic of potential versus logarithm of current density demonstrating the electrochemistry behind the MPT.

Over the past several decades, various models have been developed to predict pit growth, including empirical power-law models,[17] analytical models,[36–38] finite volume models,[39] finite element models (FEM),[40,41] and deterministic approaches.[42–44] A more comprehensive modeling approach integrates Galvele's electrochemical transport-based model with repassivation considerations, as seen in Chen and Kelly's Maximum Pit Size Model.

1.2.5 Chen and Kelly's maximum pit size

To understand this model, the fundamentals of pitting corrosion can be revisited. As discussed earlier, a natural galvanic coupling exists between the anode inside the pit (where anodic dissolution occurs) and the wet passivated alloy surface outside the pit (acting as the cathode). During pit growth, the anodic current demand-determined by the electrons released from metal dissolution-must be balanced by cathodic reduction reactions, such as the oxygen reduction reaction (ORR) or the hydrogen evolution reaction (HER).

Chen and Kelly's model builds upon Galvele's work by incorporating the critical pit stability product $(i \cdot x)_{crit}$, which defines the minimum anodic dissolution rate necessary to sustain a pit. For a three-dimensional (3D) hemispherical pit, the total anodic current demand is determined by multiplying the 1D pit stability product by three. This relationship is expressed as follows:[37,38]

$$I_{LC} = 3n \cdot (i \cdot x)_{crit} \cdot r_a = \left(\frac{I_{pit}}{r_{pit}}\right)_{crit} \cdot r_a \tag{1.3}$$

Where I_{LC} described the total anodic current demand, n is the shape factor, r_a is the size of the anode r_{pit} is the size of the pit, I_{pit} is the minimum current to maintain anodic dissolution sufficient to maintain aggressive environments and keep the pit active (Figure 1.5).

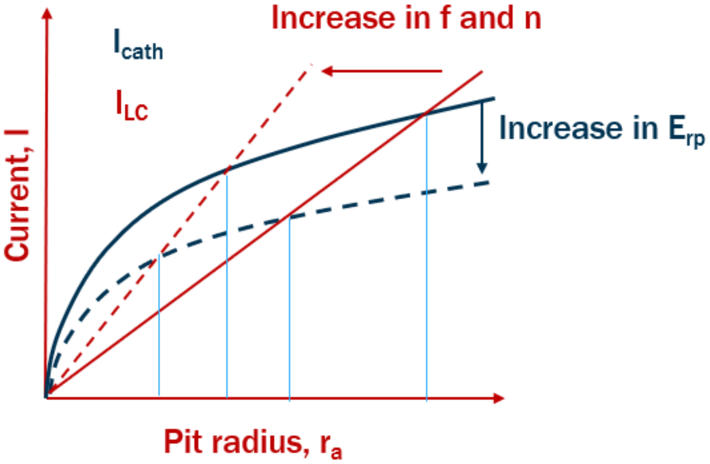

Figure 1.5. Schematic of typical total anodic current (I_{LC}- red lines) and total cathodic current (I_{cath}-dark blue lines) as a function of the pit radius from Chen and Kelly's maximum pit size model and the effect of changing some of the model's input parameters.

While the anode drives metal dissolution, the cathode must sustain this current demand. The potential at the pit mouth is assumed to be E_{rp}, representing the lowest potential within the cathode region. However, electrolyte resistance within the thin electrolyte layer covering the cathode surface introduces an ohmic voltage drop. Moving away from the pit mouth, the potential increases due to these losses until reaching the OCP, beyond which the cathode can no longer sustain anodic current density beyond that of the local passive current density. At this point, passive dissolution dominates rather than active cathodic reduction.

To quantify the total cathodic current, Chen and Kelly's model uses the following Equation 1.4:[36–38]

$$\ln(I_{cath}) = \frac{4\pi kW\Delta E}{I_{cath}} + \ln\left[\frac{\pi e r_a^2 \int_{E_{OCP}}^{Erp}(i_c - i_p)dE}{\Delta E}\right] \tag{1.4}$$

Where I_{cath} is total cathode current, W is the water layer thickness, k is the solution conductivity, e is the Euler's number, i_c is the cathode current density and i_p is the passivated current density, both as a function of potential E.

For pit growth to continue, I_{cath} must match or exceed the anodic current demand I_{LC}, as demonstrated in Figure 1.5. The maximum pit size r_{max} is achieved when the cathode fully supports the anode's current, meaning $r_a = r_{max}$. If $r_a < r_{max}$, the pit continues to grow because the cathode can sustain the required current. However, if $r_a > r_{max}$, the cathode's current supply becomes insufficient, leading to a loss of the aggressive, low-pH environment within the pit. Consequently, the pit passivates, halting further growth.

1.2.6 Assessment of critical parameters in pitting corrosion

The value of (i·x) is typically obtained using a 1D pencil electrode experiment, where a fine metal wire (a few micrometers in diameter) is embedded in an epoxy coating.[45–47] When dissolved at a high current density, this wire forms a salt film composed of metal cations and anions (*e.g.,* chlorides) on the pit surface. Under these conditions, metal dissolution is governed by the diffusion of metal-chloride species out of the pit. This process can be described by Fick's first law of diffusion at steady state:

$$i_L = \frac{zFD_{M^+}\,\Delta C}{x} \tag{1.5}$$

Here, i_L represents the limiting current under diffusion control, z is the number of electrons associated with the stoichiometric dissolution of the alloy, F is Faraday's constant (96,485 C/mol), D_{M^+} is the diffusion coefficient of the metal cation species, ΔC is the concentration difference of the metal cation species between the bottom of the pit (C_{sat}) and the bulk solution ($C_{bulk} \approx 0$), and x is the pit depth. Rearranging Equation 1.5 yields:

$$i_L \cdot x = zFD_{M^+}\,\Delta C = (i \cdot x)_{sf} \tag{1.6}$$

Although salt films indicate highly aggressive conditions, they are not essential for sustaining pit activity. In fact, such extreme conditions are considered unrealistic for in-service pit propagation.[21,45,48,49] Notably, Galvele's original theory on the pit stability product did not include the presence of a salt film. Instead, only a fraction (f) of the is believed to be necessary to maintain pit activity.[18,50–52] This leads to the definition of the critical pit stability product:

$$(i \cdot x)_{crit} = f * (i \cdot x)_{sf} \tag{1.7}$$

Determining the precise value of $(i\cdot x)_{crit}$ remains challenging. However, experimentally obtaining $(i\cdot x)_{sf}$ under diffusion-controlled conditions is feasible. Reported values for f range from 0.43 to 0.75, but this remains a topic of ongoing debate.[18,48,49] Therefore, refining the value of f is crucial for accurately predicting maximum pit size using Chen and Kelly's models.

As discussed earlier, the determination of E_{rp} has also been a subject of debate. Traditional methods for measuring E_{rp}, such as those applied to SS316L in 0.6M NaCl, often yield conservative estimates. The experimental determination of E_{rp} in 1D tests depends on various factors, including potentiodynamic scan rates and the chosen i_{rp} utilized to extract the potential values. [53]

Both E_{rp} and $(i\cdot x)_{crit}$ serve as lower bounds for pit growth, and their calculated values should ideally be consistent. However, research by Marshall et al. has demonstrated significant differences in the maximum pit sizes predicted using E_{rp} in FEM modeling versus those obtained using $(i\cdot x)_{crit}$ for SS316L in 0.6M NaCl.[52] To reconcile these discrepancies, a higher E_{rp}, a higher f, or a combination of both is required. These findings highlight the need for refining the methods used to determine E_{rp} and $(i\cdot x)_{crit}$ to establish less conservative and more accurate models for pit growth prediction.

Another key parameter in Equation 1.3 is the shape factor, n. This parameter is frequently used in steady-state heat transfer to convert flux from a 1D to a 3D system, as described by Fourier's law.[54,55] In the context of pitting corrosion, n serves a similar function, enabling the translation of 1D experimental measurements into realistic 3D scenarios by accounting for mass transfer and the Ohm's law relationship. From Equation 1.3, it is evident that variations in n significantly affect both the $(I/r)_{crit}$ value and the maximum pit size predictions, as n influences the slope of the anodic line. Given its impact, it is crucial to explore different pit growth scenarios based on experimental results and in-field observations. Establishing a systematic approach to translate 1D pit growth experiments into more realistic 3D cases will improve the predictive accuracy of pitting models and enhance their applicability to real-world corrosion challenges.

1.7 Other issues on pit modeling and computational approaches

Pitting corrosion presents a significant scientific challenge due to the complex electrochemical interactions that arise in the highly aggressive, concentrated solution chemistries formed during its initiation and propagation. Quantifying the impact of these extreme environments on both anodic and cathodic dissolution-inside and outside the pit-remains a persistent challenge in localized corrosion research. Several factors contribute to these difficulties, including:

- The absence of a comprehensive thermodynamic database for highly concentrated and evolving pit chemistry.
- The time-dependent nature of hydrolysis reactions (Equation 1.1) and their influence on local pH and metal ion speciation.
- The influence of microstructural effects, such as grain boundaries and inclusions, on localized corrosion behavior.
- Knowledge gaps in electrolyte mass transfer mechanisms within pits, particularly in the presence of highly concentrated solutions.
  - The complex interdependencies between potential and current distribution with mass transfer, which complicate accurate electrochemical modeling.
- The significant computational demands required to simulate such intricate chemistries.

1.3. Research goals

This research aims to establish a fundamental, quantitative, and qualitative framework for assessing the electrochemical kinetics and thermodynamics of localized corrosion, particularly pitting phenomena. By investigating the key parameters that govern pit propagation and repassivation, this work seeks to clarify their interrelationships and enhance their application in scientific and engineering predictions. Ultimately, this study underscores the critical role of variability in experimentally measured, computationally applied electrochemical parameters, advancing accuracy, reliability, and enhancing computational expenses related to localized corrosion prediction strategies.

1.4. Scope of this work

This dissertation comprises seven chapters, including **Chapter 1-Introduction** and **Chapter 7-Summary and Future Work**. Additionally, an overall Appendix supplements the findings and overarching objectives of this work. Each chapter includes its own Appendix and references to ensure a logical flow, allowing readers to easily access supplementary data relevant to each section.

The dissertation follows a structured progression:

- **Chapter 2** presents a methodology to unify concepts and parameters governing pit growth and repassivation in SS316L and SS304 exposed to 0.6M NaCl. This approach integrates thermodynamic simulations with experimental investigations.
- **Chapter 3** extends the methodology of Chapter 2 by exploring pit propagation in NaCl and $MgCl_2$ solutions containing varying SO_4^{2-}/Cl^- molar ratios. The objective is to quantify the role of sulfate ions as inhibitors of pit growth and kinetics.
- **Chapter 4** employs FEM modeling to analyze the influence of the shape factor (*n*) on pit growth. This chapter aims to improve the conversion of 1D experimental data into 3D pit

geometries, ultimately refining predictions of maximum pit size under critical growth conditions.

- **Chapter 5** builds upon Chen and Kelly's model by incorporating FEM modeling with Secondary current distribution (potential and current dependence effects) and Tertiary current distribution (reactions and species concentration effects on potential and current distribution). This analysis quantifies the model's conservatism, explains its origins, and identifies key factors influencing its predictive accuracy for maximum pit size.
- **Chapter 6** explores reduced ordered models (ROMs) such as Laplace with variable conductivity Lvk in localized corrosion applications. It evaluates the strengths and limitations of this model, comparing their discrepancies with the Nernst-Planck Equation with Electroneutrality (NPE).

In Appendix i of this dissertation we introduce a novel computational approach-**Full Secondary + Transport (FST)-** designed by me to enhance accuracy relative to NPE while significantly reducing computational time and cost.

1.5. References

1. Rigby, D. B. Review Board Evaluation of the Technical Basis for Extended Dry Storage and Transportation of Used Nuclear Fuel December 2010. *United States Nucl. Waste Tech. Rev. Board* 1–10 (2010).
2. Bryan, C. R. *et al.* Physical and chemical properties of sea salt deliquescent brines as a function of temperature and relative humidity. *Sci. Total Environ.* **824**, (2022).
3. Katona, R. M., Knight, A. W., Maguire, M., Bryan, C. R. & Schaller, R. F. Considerations for realistic atmospheric environments: An application to corrosion testing. *Sci. Total Environ.* **885**, (2023).
4. Bryan, C. R. & Enos, D. G. Analysis of Dust Samples Collected from Spent Nuclear Fuel Interim Storage Containers at Hope Creek , Delaware , and Diablo Canyon , California. (2014).
5. Bryan, C. *et al.* Surface Sampling Techniques for the Field Demonstration. (2021).
6. Katona, R. M., Knight, A., Bryan, C., Schaller, R. F. & Kelly, R. *Determination of Key Marine Environment Effects on Bounding Pit Size Predictions*. *ECS Meeting Abstracts* vols MA2020-02 (2020).
7. U.S. Nuclear Waste Technical Review Board. Chloride-Induced Stress Corrosion Cracking Potential in Dry-Storage Canisters for Spent Nuclear Fuel. 1–5 (2017).
8. Fitzgerald, J. W. Marine aerosols: A review. *Atmos. Environ. Part A, Gen. Top.* **25**, 533–545 (1991).
9. Saha, A. & Moorthy, K. K. Impact of precipitation on aerosol spectral optical depth and retrieved size distributions: A case study. *J. Appl. Meteorol.* **43**, 902–914 (2004).
10. Xia, L. & Gao, Y. Chemical composition and size distributions of coastal aerosols observed on the US East Coast. *Mar. Chem.* **119**, 77–90 (2010).
11. Chu, S. *Literature Review of Environmental Conditions and Chloride-Induced Degradation Relevant to Stainless Steel Canisters in Dry Cask Storage Systems*. (2014).
12. Knight, A., Nation, B., Maguire, M., Schaller, R. & Bryan, C. FY22 Status : Corrosion-Resistant Coatings on Spent Nuclear Fuel Canisters to Mitigate and Repair Potential Stress Corrosion Cracking. (2022).
13. Sato, N. A theory for breakdown of anodic oxide films on metals. *Electrochim. Acta* **16**, 1683–1692 (1971).
14. Szklarska-Smialowska, Z. Mechanism of pit nucleation by electrical breakdown of the passive film. *Corros. Sci.* **44**, 1143–1149 (2002).
15. Hoar, T. P. The production and breakdown of the passivity of metals. *Corros. Sci.* **7**, 341–355 (1967).

16. Lin, L. F., Chao, C. Y. & Macdonald, D. D. A Point Defect Model for Anodic Passive Films: II . Chemical Breakdown and Pit Initiation. *J. Electrochem. Soc.* **128**, 1194–1198 (1981).

17. Michio Nakata, Naoto Ono, Y. U. State of Stainless Steels Roofing in Okinawa and Characteristics of CorrosionResistance in Atmosphere of Various Stainless Steels. *Zairyo-to-Kankyo* **564**, 559–564 (1997).

18. Srinivasan, J. & Kelly, R. G. On a recent quantitative framework examining the critical factors for localized corrosion and its impact on the galvele pit stability criterion. *Corrosion* **73**, 613–633 (2017).

19. Leckie, H. P. & Uhlig, H. H. Environmental Factors Affecting the Critical Potential for Pitting in 18–8 Stainless Steel. *J. Electrochem. Soc.* **113**, 1262 (1966).

20. Szklarska-Smialowska, Z. & Janik-Czachor, M. The analysis of electrochemical methods for the determination of characteristic potentials of pitting corrosion. *Corros. Sci.* **11**, 901–914 (1971).

21. Ernst, P. & Newman, R. C. Pit growth studies in stainless steel foils. I. Introduction and pit growth kinetics. *Corros. Sci.* **44**, 927–941 (2002).

22. Sridhar, N. Local corrosion chemistry - A review. *Corrosion* **73**, 18–30 (2017).

23. Newman, R. C. Protection potentials for pitting of stainless steel in neutral chloride solutions. *Corros. Sci.* **23**, 1045–1046 (1983).

24. Dunn, D. S., Sridhar, N. & Cragnolino, G. A. Long-Term Prediction of Localized Corrosion of Alloy 825 in High-Level Nuclear Waste Repository Environments. *Corros.* **52**, 115–124 (1996).

25. Sridhar, N. & Cragnolino, G. A. Applicability of repassivation potential for long-term prediction of localized corrosion of alloy 825 and type 316L stainless steel. *Corrosion* **49**, 885–894 (1993).

26. Dunn, D. S., Cragnolino, G. A. & Sridhar, N. An electrochemical approach to predicting longterm localized corrosion of corrosion-resistant high-level waste container materials. *Corrosion* **56**, 90–104 (2000).

27. ASTM Standard G61-86. 'Standard Test Method for Conducting Cyclic Potentiodynamic Polarization Measurements for Localized Corrosion Susceptibility of Iron, Nickel or Cobalt Based Aalloys'. *Annu. B. ASTM Stand.* **86**, 1–5 (2010).

28. Frankel, G. S. Pitting Corrosion of Metals: A Review of the Critical Factors. *J. Electrochem. Soc.* **145**, 2186–2198 (1998).

29. Wilde, B. E. & Williams, E. The use of current/voltage curves for the study of localized corrosion and passivity breakdown on stainless steels in chloride media. *Electrochim. Acta* **16**, 1971–1985 (1971).

30. Wilde, B. E. A Critical Appraisal of Some Popular Laboratory Electrochemical Tests for

Predicting the Localized Corrosion Resistance of Stainless Alloys in Sea Water. *Corros. Sci.* **28**, (1972).

31. Frankenthal, R. P. & Pickering, H. W. On the Mechanism of Localized Corrosion of Iron and Stainless Steel. *J. Electrochem. Soc.* **119**, 1304 (1972).
32. Vetter, K. J. Electrochemical Kinetics, Theoretical and Experimental Aspects. (1967).
33. Galvele, J. R. Transport Processes and the Mechanism of Pitting of Metals. *J. Electrochem. Soc.* **123**, 464–474 (1976).
34. Galvele, J. R. Transport processes in passivity breakdown-II. Full hydrolysis of the metal ions. *Corros. Sci.* **21**, 551–579 (1981).
35. Gravano, S. M. & Galvele, J. R. Transport processes in passivity breakdown—III. Full hydrolysis plus ion migration plus buffers. *Corrosion* **24**, 517–534 (1984).
36. Chen, Z., Cui, F. & Kelly, R. G. An Analytical Modeling Method for Calculating the Current Delivery Capacity of a Thin-Film Cathode and the Stability of Localized Corrosion under Atmospheric Environments. *ECS Trans.* **3**, 443–457 (2007).
37. Chen, Z. Y., Cui, F. & Kelly, R. G. Calculations of the Cathodic Current Delivery Capacity and Stability of Crevice Corrosion under Atmospheric Environments. *J. Electrochem. Soc.* **155**, C360 (2008).
38. Chen, Z. Y. & Kelly, R. G. Computational Modeling of Bounding Conditions for Pit Size on Stainless Steel in Atmospheric Environments. *J. Electrochem. Soc.* **157**, C69 (2010).
39. Scheiner, S. & Hellmich, C. Finite Volume model for diffusion- and activation-controlled pitting corrosion of stainless steel. *Comput. Methods Appl. Mech. Eng.* **198**, 2898–2910 (2009).
40. Liu, C. & Kelly, R. G. A review of the application of finite element method (FEM) to localized corrosion modeling. *Corrosion* **75**, 1285–1299 (2019).
41. Nguyen, V. A., Newman, R. C. & Laycock, N. J. 2-Dimensional Simulations of Pit Propagation and Multi-Pit Interactions. *J. Electrochem. Soc.* **169**, 081503 (2022).
42. Krouse, D., Laycock, N. & Padovani, C. Modelling pitting corrosion of stainless steel in atmospheric exposures to chloride containing environments. *Corros. Eng. Sci. Technol.* **49**, 521–528 (2014).
43. Laycock, N. J., Krouse, D. P., Hendy, S. C. & Williams, D. E. Computer simulation of pitting corrosion of stainless steels. *Electrochem. Soc. Interface* **23**, 65–71 (2014).
44. Laycock, N. J. & White, S. P. Computer Simulation of Single Pit Propagation in Stainless Steel under Potentiostatic Control. *J. Electrochem. Soc.* **148**, B264 (2001).
45. Srinivasan, J. & Kelly, R. G. One-Dimensional Pit Experiments and Modeling to Determine Critical Factors for Pit Stability and Repassivation. *J. Electrochem. Soc.* **163**, C759–C767 (2016).

46. Srinivasan, J., McGrath, M. J. & Kelly, R. G. A High-Throughput Artificial Pit Technique to Measure Kinetic Parameters for Pitting Stability. *J. Electrochem. Soc.* **162**, C725–C731 (2015).

47. Srinivasan, J., Liu, C. & Kelly, R. G. Geometric Evolution of Flux from a Corroding One-Dimensional Pit and Its Implications on the Evaluation of Kinetic Parameters for Pit Stability. *J. Electrochem. Soc.* **163**, C694–C703 (2016).

48. Gaudet, G. T. *et al.* Mass transfer and electrochemical kinetic interactions in localized pitting corrosion. *AIChE J.* **32**, 949–958 (1986).

49. Pistorius, P. C. & Burstein, G. T. Growth of corrosion pits on stainless steel in chloride solution containing dilute sulphate. *Corros. Sci.* **33**, 1885–1897 (1992).

50. Moayed, M. H. & Newman, R. C. The Relationship Between Pit Chemistry and Pit Geometry Near the Critical Pitting Temperature. *J. Electrochem. Soc.* **153**, B330 (2006).

51. Ghahari, M. *et al.* Synchrotron X-ray radiography studies of pitting corrosion of stainless steel: Extraction of pit propagation parameters. *Corros. Sci.* **100**, 23–35 (2015).

52. Marshall, R. S., Katona, R. M., Melia, M. A. & Kelly, R. G. Pit Stability Predictions of Additively Manufactured SS316 Surfaces Using Finite Element Analysis. *J. Electrochem. Soc.* **169**, 021506 (2022).

53. Srinivasan, J. & Kelly, R. G. Evaluating the Critical Chemistry for Repassivation at the Corroding Surface Using Mass Transport Model-Based Artificial Pit Experiments. *J. Electrochem. Soc.* **163**, C768–C777 (2016).

54. Warren, R. M., James, H. P. & I.Young, C. *Handbook of Heat Transfer*. *Computer Vision* (McGraw-Hill, 1998). doi:10.1007/978-3-030-63416-2_844.

55. Yovanovich, M. A general expression for predicting conduction shape factors. in *11th Aerospace Sciences Meeting* (American Institute of Aeronautics and Astronautics, 1973). doi:doi:10.2514/6.1973-121.

Chapter 2. Repassivation of stainless steels: A unifying quantitative framework

A. Shehi, S. Choudhary, R. G. Kelly
*Center for Electrochemical Science and Engineering, Department of Materials Science and Engineering, University of Virginia, Charlottesville, VA 22904

Contributions: A. Shehi - Conceptualization, Data curation, Formal analysis, Investigation, Methodology, Visualization, Writing – original draft, Writing – review and editing, **S. Choudhary** - Conceptualization, Formal analysis, Investigation, Visualization, Writing – review and editing, **R. G. Kelly** - Conceptualization, Funding acquisition, Data curation, Formal analysis, Project administration, Resources, Project administration, Investigation, Methodology, Visualization, Writing – original draft, Writing – review and editing

2.1 Summary

This study presents a unifying quantitative framework for understanding the repassivation process, connecting the values of E_{rp} to key parameters such as pH, $(i{\cdot}x)_{crit}$, anodic and cathodic kinetics, i_c/i_a, f, and electrode-electrolyte interfacial chemistry. The framework integrates potentiostatic, fast potentiodynamic, and galvanodynamic experiments with thermodynamic modeling using a mixed solvent thermodynamic database. Using SS316L and SS304 in 0.6M NaCl as exemplars, the study demonstrates that repassivation potential decreases with pit depth until it plateaus, with SS316L showing a potential of -0.15 to -0.165 V vs. SCE and SS304 at -0.18 to -0.2 V vs. SCE. The differences in repassivation potential between the alloys are attributed to two roles the Mo in SS316L plays, namely suppressing anodic kinetics and accelerating cathodic kinetics. The relative rate of local cathodic kinetics within the pit are crucial for repassivation via CrOOH precipitation, with experimental i_c/i_a values of 2-4.5% for SS316L and ≤ 1% for SS304 and up to 9.5-10.5% required theoretically at high fractions of saturation. The $(i{\cdot}x)_{crit}$ was found to be similar for both alloys, approximately 0.32 A/m², with f ranging between 0.35 and 0.4. Anodic and cathodic kinetics were found to be independent of the pit depth at critical repassivation conditions.

Keywords: Repassivation potential, Pitting, SS316L, SS304, fraction of saturation, $(i{\cdot}x)_{crit}$

2.2. Introduction

Repassivation, the process by which a metal or alloy regains its passive state after being activated in the form of rapid dissolution, has been a subject of scientific debate for over a century. The systematic study of passivity began in 1738 when Lomonosov examined iron (Fe) in nitric acid (HNO_3). [1] However, the concept of an oxide layer as the foundation of passivity did not emerge until Faraday's 1836 assertion, attributing Schönbein's observations of Fe in dilute and concentrated HNO_3 to the formation of such a layer. [2–5] Over the next century, numerous experiments and theories contributed to understanding passivity and repassivation, culminating in Evans' 1927 visual confirmation of the oxide layer by "peeling" the oxide of passive Fe in potassium iodide (KI) solutions and observing it in optical microscope. [6] Notably, Lille's 1918 paper was the first to introduce the term "repassivation," describing the activation and subsequent repassivation of Fe in HNO_3.[7]

The connection between repassivation and pitting corrosion was first explored by Pourbaix in 1962, who introduced the concept of the repassivation potential, E_{rp} (also known as the protection potential, E_p). [8] He defined E_{rp} as the potential at which the reverse scan current density matches that of the forward scan in a cyclic potentiodynamic (CPP) experiment and represented the potential below which localized corrosion would cease. [8] This advancement, alongside pioneering theoretical contributions from Vetter, [9–11] Frankenthal and Pickering, [12], Isaacs and Tester,[13,14] and Galvele, [15–17] laid the groundwork for an expanding body of research on pitting corrosion and repassivation.

A significant breakthrough occurred in 1975 when Tester and Isaacs developed an experimental method that validated the theoretical one-dimensional (1D) approach, creating unidirectional dissolution by embedding an ~0.9-cm diameter wire in epoxy and then dissolving it back. [13] Many subsequent theories sought to identify the critical conditions under which a pit ceases to propagate. [14–43] In 1976, Galvele was the first to relate the critical current density (i_{crit}) required to sustain a 1D pit of depth (x) to the local pH at the pit's bottom. [15] A much later publication by Newman further correlated this ($i \cdot x$) parameter with an alloy's E_{rp}, reinforcing its significance. [20]

Other researchers have investigated the role of metal cation concentrations near the surface in maintaining pit activity. Reported critical concentrations of metal cations range from 40% to full saturation, depending on the alloy, environment, as well as the experimental and theoretical approach. [13,26,27,30,38,44–54] The interplay between critical concentration, C_{crit} and i_{crit} has been a focal point in understanding pit stability.

Another critical factor in repassivation is the influence of local cathodic kinetics within pitting. Srinivasan and Kelly demonstrated that for a pit to repassivate in SS316L in 0.6M NaCl, the local cathodic-to-anodic current density ratio (i_c/i_a) must be approximately 0.03%.[30] Their work integrated thermodynamic considerations of chromium oxyhydroxide (CrOOH) precipitation based on Okada and Anderko's work, as well as semi-quantitative analyses of the critical conditions required for repassivation.[18,23–25]

Most recently, a series of studies by Li et al. have developed a framework (LSF Framework) involving multiple parameters, including the critical pitting temperature (CPT), $i_{diss,max}$ (which describes the capacity of the pit dissolution rate for given condition and its relation with i_{crit} (also known as $i_{diss,crit}$ in the LSF) and E_{rp}, by integrating theoretical and experimental 1D data. [33–38] The LSF framework provides valuable insights, although it may not fully account for the effects of specific dissolved chemical species on local chemistry, electrochemistry at the electrode-electrolyte interface, and overall electrolyte thermodynamics. Additionally, the identification of critical currents and potentials in 1D potentiodynamic experiments-and their significance-could be subject to interpretation based on the analysis of the 1D potentiodynamic curves.

Methods for determining E_{rp} has varied across publications, employing cyclic potentiodynamic polarization (CPP) [55–58] with different scan rates and reverse current densities, 1D pit polarization curves, and i_{crit} values ranging from near the mass transport-to-activation controlled region to near the open circuit potential (OCP) of the scan. [35,37,40,52] One of the most pivotal experimental studies on E_{rp} determination was conducted by Dunn, Cragnolino, and Sridhar in 2000. [59] Their long-term potentiostatic exposure experiments unequivocally confirmed the existence of E_{rp} as a potential below which any active localized corrosion sites will repassivated, and no new ones will form. Their realistic experimental conditions provided strong evidence that E_{rp} can be an industrially applicable parameter, under which no pit can grow to a size of engineering concern.

In this chapter, we aim to establish a unifying quantitative framework that integrates the kinetics of controlled 1D pitting experiments with state-of-the-art, non-dilute electrolyte thermodynamics. This approach seeks to connect the key factors influencing repassivation, including E_{rp}, $i_{crit}/(i\cdot x)_{crit}$, f, aqueous ionic speciation and oxide formation, pH, and local cathodic kinetics. By doing so, we seek to provide an understanding of how these parameters can be determined and related to one another while exploring the difference in repassivation between two major stainless steel alloys, SS316L and SS304.

2.3. Methodology

This study investigates the repassivation behavior of SS316L and SS304 stainless steels using a combination of computational and experimental techniques. By integrating thermodynamic data with kinetic electrochemical parameters, the research aims to identify the conditions under which an active pit achieves the necessary state for repassivation to begin. The study approaches this objective from three perspectives: (1) computational thermodynamic modeling, (2) potential control through combined potentiostatic and fast potentiodynamic experiments, and (3) current control via galvanodynamic experiments.

2.3.1. Computational approach

Thermodynamic simulations in this study were conducted using OLI Studio version 12.0 with the Mixed Solvent Electrolyte (MSE) database. It is commonly assumed that the aggressive environment within a localized corrosion site, such as a pit, consists of metal cation-chloride salts at varying saturation levels. To investigate the stable aqueous and solid compounds across different metal-chloride saturation levels, stoichiometric compositions of stainless steel (SS)-chloride salt mixtures were used. Table 2.1 provides the stoichiometric compositions of SS316L and SS304 utilized to carry on the calculations.

Table 2.1. Weight percent of each element composing SS316 and SS304 utilized in OLI Studio thermodynamic calculations.

	Ni	Cr	Mo	Fe
SS316	12.00	17.00	2.00	69.00
SS304	9.25	19.00	-	71.75

The corresponding chloride salts of each one of these elements utilized as input parameters are those of $FeCl_2$, $NiCl_2$, $CrCl_3$, and $MoCl_3$. Additionally, during the simulations, redox reactions involving Fe^{2+}, Ni^{2+}, Cr^{3+}, Mo^{3+}, Mo^{4+}, and Mo^{6+} were kept active. The simulations were conducted at a constant temperature of 298.15 K and a pressure of 1 atm. To adjust the total salt composition, the concentration of H_2O was varied as needed.

2.3.2. Experimental approach

All electrochemical experiments were conducted using artificial one-dimensional (1D) pits with a wire diameter of 50.8µm. The certified compositions of SS316L and SS304 wires used in this study are presented in Table 2.2.

Table 2.2. Composition in weight percentage of SS316L and SS304 alloys utilized in this study.

	C	Mn	P	S	Si	Cr	Ni	N	Cu	Mo	Co	Al	Ti	Fe

SS316L	0.02	1.46	0.032	0.002	0.24	16.65	10.02	0.043	0.444	2.36	0.22	0.003	0.005	Bal.
SS304	0.05	1.44	0.030	0.001	0.22	18.23	8.03	0.045	-	-	-	-	-	Bal.

To ensure controlled exposure, the wires were embedded in epoxy, leaving only the cross-sectional area (2.0268×10^{-5} cm^2) exposed. Prior to experimentation, the samples were metallographically prepared to a 320-grit surface finish, followed by cleaning in deionized (DI) water and air-drying. All experiments were performed in 100mL solution of 0.6 M NaCl at 25°C utilizing a saturated calomel electrode as a reference. A schematic representation of the artificial pit experimental setup is provided in Figure 2.1.

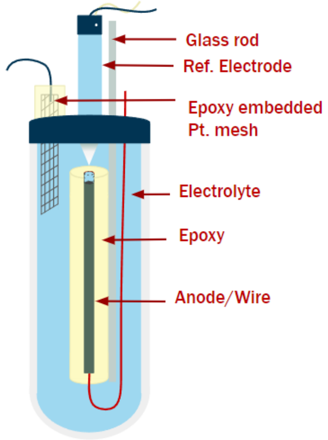

Figure 2.1. Schematic configuration of the artificial pit experiments.

2.3.2.1. Potentiostatic electrochemical parameters

Using the cell configuration presented in Figure 2.1, a series of electrochemical techniques were applied cyclically to the artificial pit: (1) a 30s open circuit potential (OCP), (2) potentiostatic polarization to -1V versus saturated calomel electrode (SCE) for 2min to disrupt any residual protective layer and facilitate an easy and homogenous pit initiation, (3) potentiostatic polarization to +0.75 V vs. SCE for 1-5 minutes to initiate the pit, (4) potentiostatic polarization to +0.55V vs. SCE for 5min-1h to propagate the pit to the desired depth, (5) a linear sweep voltammetry (LSV) at a scan rate of 5mV/s from +0.55V vs. SCE to a desired applied potential, E_{app}, (6) a potentiostatic hold at E_{app} for 1h, (7) a LSV at 5mV/s scan rate from E_{app} to +0.75V vs. SCE. Step 3 was then repeated as needed. A schematic of a cycle containing all the steps above is shown in Figure 2.2a. For both alloys, the potentials applied during the potentiostatic step (step 6) were 0 V, -0.05 V, -0.075 V, -0.1 V, -0.125 V, and -0.15 V, all referenced to SCE.

2.3.2.2. Fast potentiodynamic electrochemical parameters.

The fast potentiodynamic experiments were conducted to determine the anodic and cathodic kinetics at E_{app}, replicating the conditions expected during potentiostatic experiments. The fast scan rate was used to minimize the amount of dilution of the solution within the pit. These experiments followed the same procedure as steps 1 through 5 of the potentiostatic method.

However, in step 6, instead of maintaining a constant potential, a rapid voltage sweep was applied at a scan rate of 400 mV/s from E_{app} to -0.95 V vs. SCE. This approach ensured the absence of crevice formation and maintained the intended chemical environment once E_{app} was reached. Consequently, a complete fast potentiodynamic experiment consisted of six steps. As with the potentiostatic experiments, step 3 was repeated as needed. A schematic of the experimental sequence is provided in Figure 2.2b.

Fast potentiodynamic experiments were also utilized to identify the potential at the pit base, E_{base}, expected during the potentiostatic experiments. Using these data, pit resistance can be determined as a function of pit depth, which can be applied to a correction for potential drop (IR correction) to the tested potentials during potentiostatic experiments. For each pit depth, the resistance (R) was determined from the LSV experiment. At high overpotentials, within the activation-controlled region of the LSV, the relationship between E_{app} and the current (I) is dominated by ohmic resistance, resulting in an expected linear correlation between these parameters. The resistance was calculated as the slope of the E_{app} versus I plot in linear scale at high overpotentials, typically near the activation-to-mass transfer-controlled transition region of the LSV of the 1D experiments. The total potential drop (IR) from the reference electrode to the bottom of the pit was obtained by multiplying R and I. Consequently, to calculate the E_{base}, the IR term was subtracted from E_{app}, as expressed in Equation 2.1:

$$E_{base} = E_{app} - IR \tag{2.1}$$

This IR correction enables the accurate identification of the potential at the bottom of the pit. In this chapter, we define the E_{base} to be the repassivation potential, E_{rp}. Given that a single predominant electrochemical reaction occurs on the pit surface, a typical Tafel relationship is expected between the potential and the logarithm of the current on an IR-corrected LSV scan, provided that the overpotential changes within a sufficiently high range from the OCP. Lastly, note that the same value of R is applied to the anodic and cathodic region of the LSV.

2.3.2.3. Galvanodynamic electrochemical parameters

Current-controlled experiments followed a similar procedure to the previously described electrochemical techniques, with several modifications. During the galvanodynamic experiments, steps 1 through 4 of the potentiostatic method were performed. In step 5, an LSV was conducted at a scan rate of 5 mV/s, sweeping from +0.55 V vs. SCE to the transition potential, defined as the potential at which the salt film dissolves.

In step 6, a galvanodynamic test was initiated, starting from 0nA versus the measured current (I_{meas}) and increasing to 10nA at various scan rates (10nA/s, 25nA/s, 50nA/s, and 100nA/s). Step 3 was repeated as needed until a pit depth of approximately 600μm was reached. Once this depth was achieved, step 6 was modified to a galvanodynamic test starting from 0nA versus I_{meas} to 10nA at a scan rate of 1nA/s, followed by the repetition of step 3. The schematic of a typical cycle is shown in Figure 2.2c.

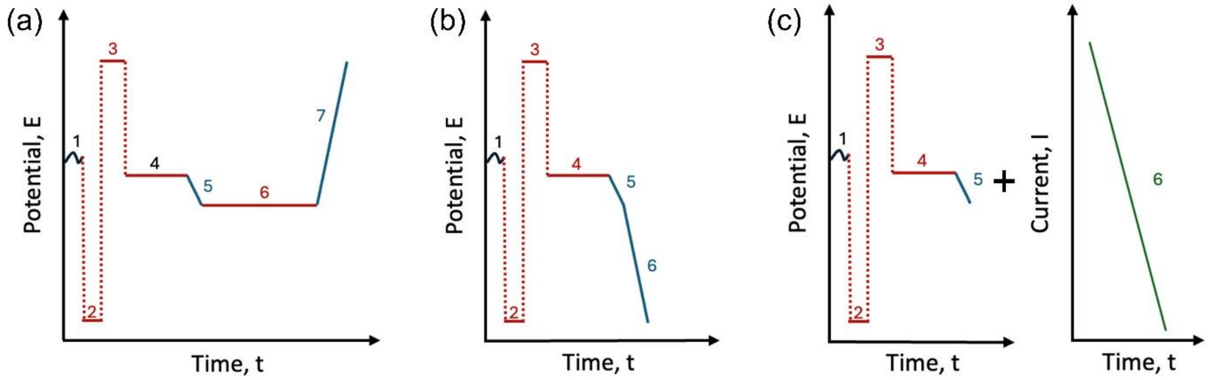

Figure 2.2. Schematic of the steps taken during electrochemical experiments for **a)** potentiostatic, **b)** fast potentiodynamic, and **c)** galvanodynamic experiments for both SS316L and SS304 in 0.6M NaCl. Numbers on top of each line correspond to the number from the text provided in its corresponding experimental section.

2.4. Results

The results section presents experimental data for SS316 and SS304 alloys. The electrochemical kinetic data from combined potentiostatic and fast potentiodynamic experiments will be described. The aim of this section will be to determine the repassivation potential of both alloys in 0.6M NaCl and to identify the critical conditions under which repassivation initiates. Maintaining the same alloys and environment as in the above case, the second part of the results presents the repassivation potential measured using galvanodynamic experiments. The thermodynamic modeling conducted through OLI Studio will be utilized in the discussion section of this chapter with supplementary parts being added to the Appendix, as needed.

2.4.1. Potentiodynamic and potentiostatic experiments

Figures 2.3a and 2.33b present the results for SS316L in 0.6M NaCl, illustrating both a 1h potentiostatic test at -0.1V vs. SCE at various pit depths (Figure 2.3a) and an IR-corrected potentiodynamic scan at 400mV/s for a 1395µm-deep pit (Figure 2.3b). Figure 2.3a shows the evolution of current density with time for pits of different depths. The results indicate that at an applied potential of -0.1V vs. SCE, shallower pits (~700µm) passivate relatively quickly, within less than 5 minutes (see black and blue lines). In contrast, deeper pits require more time to passivate under the same conditions (red and pink lines). Notably, very deep pits remain active even after 1 hour (orange and green lines). This trend is consistent across other applied potentials tested (0 to -0.15 V vs. SCE) and is also observed in SS304.

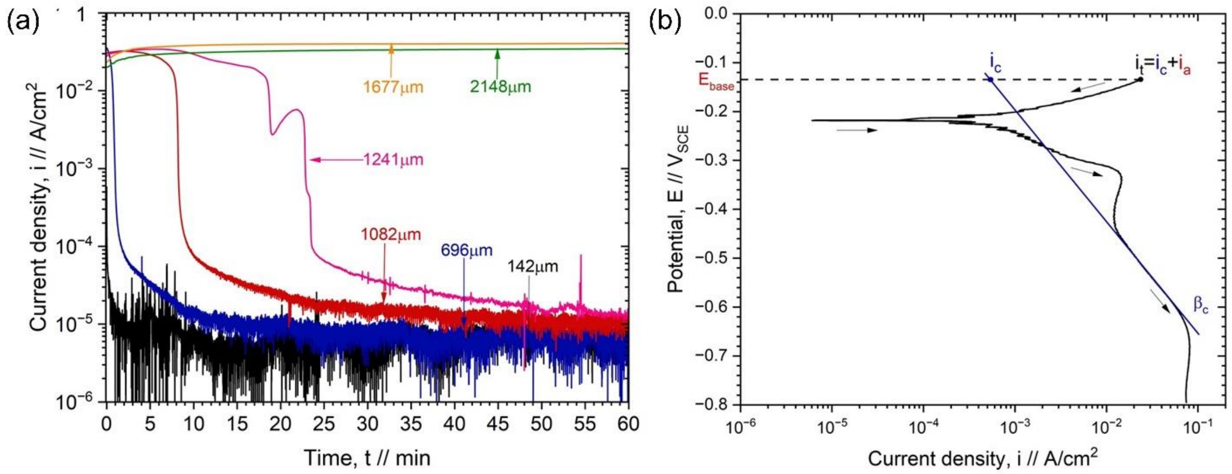

Figure 2.3. a) Current density versus time for a 1h -0.1V vs. SCE potentiostatic experiment for SS316L in 0.6M NaCl for various pit depths, **b)** IR-corrected potentiodynamic scan at 400mV/s of SS316L in 0.6M NaCl at 1395μm pit depth. Note that for **b)** the LSV scan does not initiate at -0.1V vs. SCE but rather at a lower potentiation due to IR correction.

Figure 2.3b presents the IR-corrected potentiodynamic scan for a 1395μm-deep pit in SS316L at a scan rate of 400mV/s. The arrows indicate the direction of the scan. This specific pit depth was selected as it represents the shallowest depth at which pits remained active throughout the 1h potentiostatic experiments. After IR correction, the potential at the initial point of the potentiodynamic scan is labeled as the E_{base}, while the corresponding current density is identified as the total current (i_t), which is the algebraic sum of anodic (i_a) and cathodic (i_c) current densities. Note that in this chapter, we define the E_{base}, as the repassivation potential, E_{rp}. The i_c is extracted from the data using the cathodic Tafel slope (β_c) and assuming Tafel kinetics, allowing for the extraction of the i_c/i_a ratio for a given pit depth.

Figure 2.4 presents two-panel graphs displaying the absolute values of cathode (top) and anode (bottom) current densities as a function of pit depth for SS316L and SS304. To cover the range of the potentials interest to this chapter under which the repassivation of both the alloys fall, the two chosen extreme potentials at which the current densities were extracted are -0.05V vs. SCE and -0.175V vs. SCE, both denoted in Figure 2.4 accordingly. Error bars in both horizontal and vertical directions represent the standard deviation of pit depth and current density across the three repeated experiments.

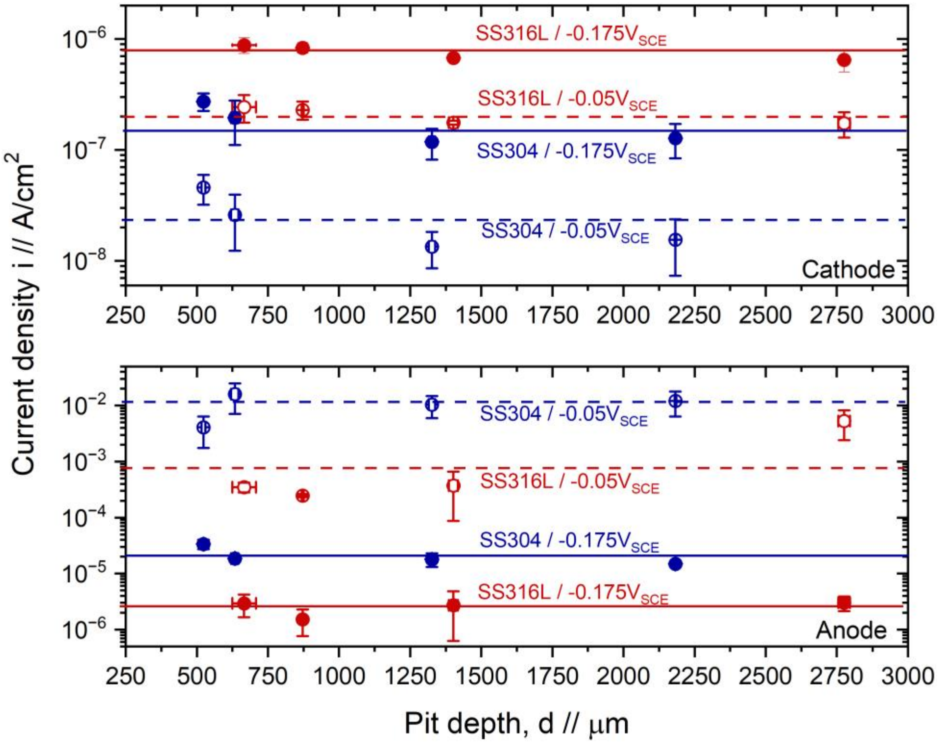

Figure 2.4. Current density as a function of pit depth for cathode (top) and anode (bottom) take at E_{rp} for SS316L (red) and SS304 (blue) taken at -0.05V vs. SCE (empty symbols) and -0.175V vs. SCE (full symbols).

The results in Figure 2.4 indicate that the absolute values of cathodic and anodic current densities at the two extreme potentials remain on average relatively constant across different pit depths under all experimental conditions. As depicted on the top graph, at all tested pit depths the cathodic current density is consistently higher for SS316L than for SS304 at both chosen potentials. Conversely, the bottom graph in Figure 2.4 shows that, on average, the anodic current density is higher for SS304 than for SS316L across all pit depths for both -0.05V vs. SCE and -0.175V vs. SCE.

Figure 2.5a illustrates the absolute values of the anodic (β_a) and cathodic (β_c) Tafel slopes as a function of pit depth for SS316L and SS304. Similar to the current densities at a reference potential shown in Figure 2.4, β_a and β_c exhibit minimal variation with pit depth. A few key trends emerge across all pit depths: (1) the absolute values of β_c are significantly higher-by a factor of 3 to 5-than β_a for both alloys, (2) β_c for SS316L is consistently higher than for SS304, and (3) on average, β_a of SS316L is higher than that of SS304, with the exception of β_a for SS304 at a pit depth of approximately 500μm, which deviates from this trend.

Figure 2.5b presents a schematic Evans diagram for SS316L and SS304 at an arbitrarily chosen pit depth of approximately 650μm. The shaded regions in each curve represent the uncertainty in potential as a function of current density, derived from variations in Tafel slopes and current densities obtained from triplicate experiments at this pit depth.

To construct the anodic shaded region, the anodic Tafel slope from each experiment and the current density recorded at the E_{rp}, as defined above in Figure 2.3b, for the corresponding pit depth were used. The cathodic shaded region was determined using the cathodic Tafel slope and the current density at an arbitrarily chosen potential of -0.475V vs. SCE. This potential was selected for both alloys to fall within the Tafel region of the cathodic portion of the fast potentiodynamic scans. The solid lines in Figure 2.5b represent the average values of the corresponding Tafel slopes and current densities extracted from the triplicate experiments at approximately 650μm pit depth. Additionally, a dashed horizontal line at -0.05V vs. SCE is included to facilitate the comparison of current densities between the two alloys at a constant potential. Notably, this potential falls within the activation-controlled region of the experimental curves for both alloys at the 650μm pit depth.

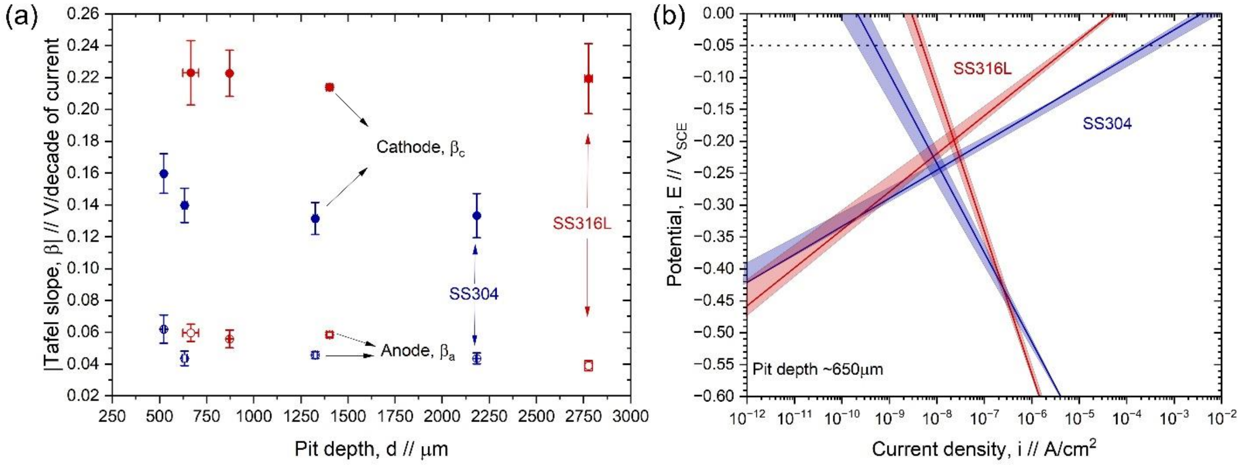

Figure 2.5. a) Absolute value of anodic and cathodic Tafel slope (β) for SS316L (red) and SS304 (blue) in 0.6M NaCl, and **b)** Evans diagram for SS316L (red) and SS304 (blue) in 0.6M NaCl at an approximate pit depth of approximately 650μm. The highlighted region in red and blue corresponds to the boundaries associated with the standard deviation.

In Figure 2.5b, the intersection of the dashed black line with the red and blue lines or regions provides the reader with a clear comparison of the pit kinetics for both the alloys at a constant potential. For example, at -0.05V vs. SCE, the current density of SS316L is approximately one order of magnitude higher than that of SS304. Note that the uncertainty region in both cathodic lines increases with increase in potential. Additionally, Figure 2.5b suggests that the anodic current density of SS316L is about two orders of magnitude lower than that of SS304 at -0.05V vs. SCE. Overall, within the activation-controlled region-where anodic reactions primarily drive pitting corrosion-SS316L exhibits a higher cathodic current density than SS304, while SS304 displays a higher anodic current density than SS316L.

Figures 2.6a and 2.6b illustrate the relationship between potential and pit depth during the transition from passive to active for SS316L and SS304, respectively, in 0.6M NaCl. These results were obtained through potentiostatic experiments. In both graphs, solid dots represent the critical applied potential at which a 1D pit transitions from passive to active for a given depth. A pit was classified as passive if no activation-controlled region was observed during a forward scan at 5mV/s from 0V vs. E_{app} to 0.75V vs. SCE, following the completion of the potentiostatic experiment. An example of the LSV scan highlighting the criteria for this classification is shown in Figure A2.1 in the Appendix of this chapter. The arrows at the final data points in both figures indicate that no pits remained active at lower applied potentials, even for depths up to 3.5mm.

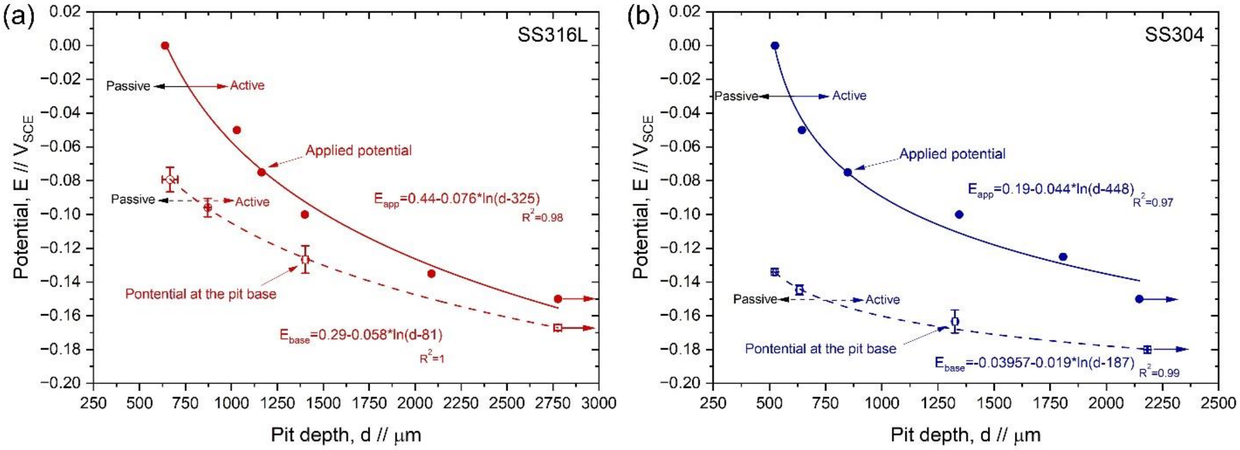

Figure 2.6. Critical applied potential (filled dots), and potential at the pit base (empty) for **a)** SS316L and **b)** SS304 in 0.6M NaCl solution. In each case, a logarithmic relationship fits the experimental data with excellent agreement.

For selected pit depths corresponding to the solid dot data in Figures 2.6a and 2.6b, separate fast potentiodynamic experiments were performed. After applying IR correction to the curves, the relationship between potential and pit depth was plotted using open dot symbols in both figures. The potential at the pit bottom was identified for each depth, with corresponding error bars. The horizontal error bars represent the standard deviation in pit depth based on three experimental replicates, while the vertical error bars indicate the standard deviation in potential.

To better describe the data, a logarithmic correlation was determined to best fit the relationship between applied potential and pit depth, as well as between the potential at the pit bottom and pit depth. The adjusted R^2 values demonstrated an excellent fit to the experimental data. However, the equations shown in Figures 2.6a and 2.6b should be used strictly for interpolation, as the authors do not assign any physical significance to the individual parameters derived from the fitting. Note that a plot of the potential versus the ln (pit depth) for each data set is shown in Figure A2.2 of the Appendix section of this chapter.

Comparing SS316L and SS304, it is evident that for a given pit depth, the transition potential from active to passive is higher for SS316L than for SS304. A similar trend is observed when comparing the potential at the pit bottom for both alloys. Additionally, the IR drop in SS304 is consistently higher than that of SS316L across all examined pit depths.

Figure 2.7a presents the ratio of cathodic to anodic current density (i_c/i_a) expressed as a percentage for SS316L and SS304 as a function of pit depth, derived from the fast potentiodynamic experiments. To obtain these values, the cathodic current density was first extracted from the IR-corrected curve at the potential of the pit bottom, as shown in Figure 2.3b. Using the recorded total current density, the anodic current density and corresponding i_c/i_a were then determined. An example of the i_c/i_a calculations is shown in the Appendix section, specifically Figure A2.3. Similar to previous graphs, the horizontal and vertical error bars in each data point indicate the standard deviation of pit depth and potential from experimental replicas.

The results in Figure 2.7 show that the percentage i_c/i_a increases with pit depth for both SS316L and SS304. At all explored pit depths, SS316L exhibits a higher i_c/i_a than SS304. Specifically, for SS316L, the percentage i_c/i_a remains below an approximate average value of 4% across all tested pit depths, whereas for SS304, this value is significantly lower at approximately 1%. On average, the i_c/i_a for SS316L tends to increase with increasing pit depth. However, due to the variability indicated by the error bars, no definitive conclusions can be drawn from the current dataset. In contrast, the i_c/i_a for SS304 remains relatively constant across all pit depths.

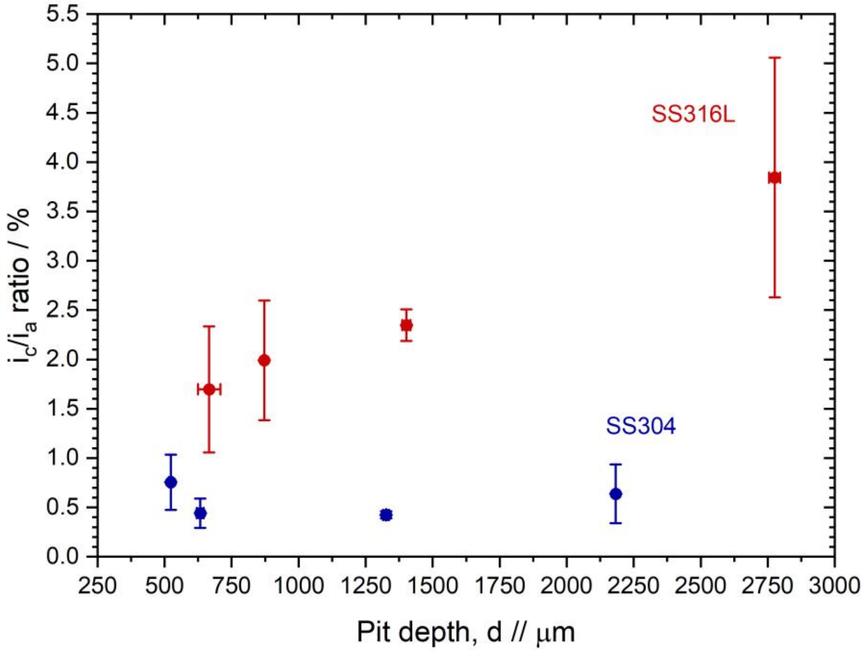

Figure 2.7. Experimental percent cathodic to anodic current density as a function of pit depth for SS316L (red) and SS304 (blue) in 0.6M NaCl.

2.4.2. Galvanodynamic experiments

Figure 2.8 shows representative data from galvanodynamic experiments conducted on SS316L in 0.6M NaCl at various pit depths generated at a 1nA/s scan rate. In all galvanodynamic experiments presented in this chapter, including those shown in Figure 2.8, the current was scanned from high to low values. The potential on the ordinate represents the recorded potential and is not IR-corrected.

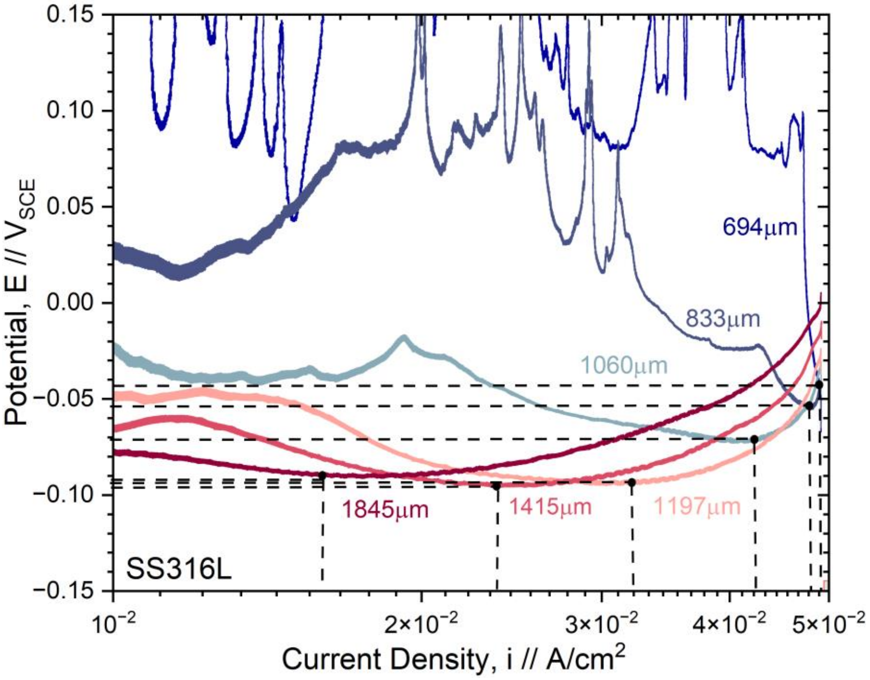

Figure 2.8. Potential versus current density for galvanodynamic experiments at 1nA/s of SS316L in 0.6M NaCl at various pit depths. The direction of current scan was from high to low currents.

Overall, switching to galvanodynamic conditions results initially in a decrease in potential as the applied current decreases. As observed in Figure 2.8, this trend is followed by an inflection point, below which the measured potential begins to rise. These inflection points, marked with orange dots and dashed lines, are recorded as the current and potential corresponding to the onset of surface repassivation. A distinct trend emerges with and increase in pit depth. Initially, as pit depth increases (694μm, 833μm, and 1060μm pits), the recorded potential at the inflection points decreases. Beyond a certain depth (1197μm, 1415μm, and 1845μm pits), the current at which the inflection point occurs continues to decrease, while the recorded potential plateaus.

Figures 2.9a and 2.9b illustrate the linear relationship between the average limiting current density (i_{lim}, half-filled dots) and the repassivation current density (i_{rp}, filled dots) versus the inverse pit depth for SS316L and SS304 in 0.6M NaCl. The limiting current density values were derived from the average pit stability product under a salt film $(i\cdot x)_{sf\text{-}av}$ for each alloy. In 0.6M NaCl, the value of $(i\cdot x)_{sf-av}$ for SS316L was determined to be 0.934 ± 0.017 A/m, which is higher than that of SS304 (0.807 ± 0.045 A/m). Similarly, the critical pit stability product at the repassivation point $(i\cdot x)_{rp}$ was found to be 0.328 ± 0.005 A/m for SS316L and 0.321 ± 0.004 A/m for SS304, indicating that on average, $(i\cdot x)_{rp}$ is slightly higher for SS316L than for SS304.

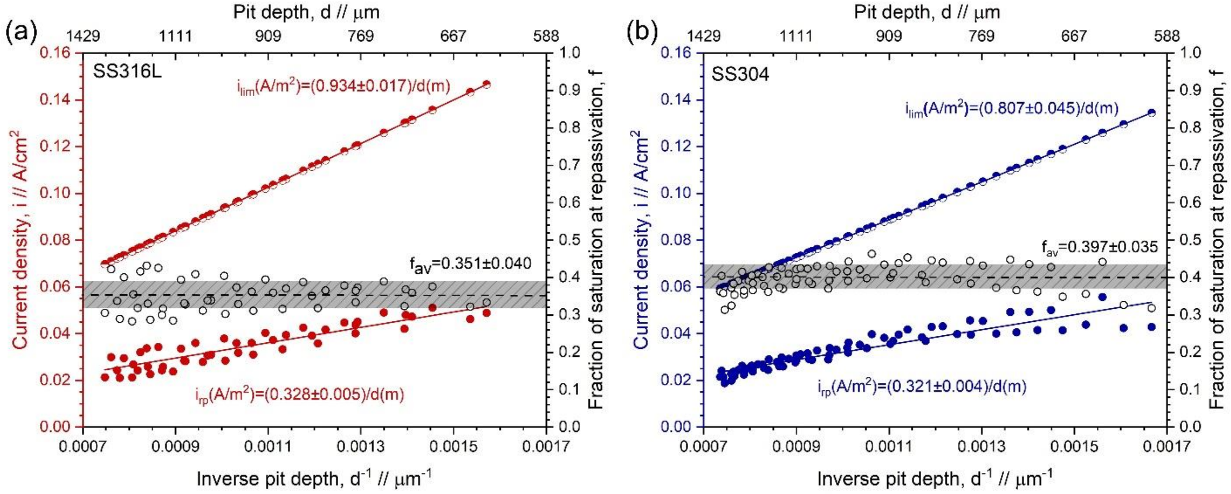

Figure 2.9. Galvanodynamic experiment results for current density (left ordinate) versus inverse pit depth and fraction of saturation (right ordinate) versus inverse pit depth for **a)** SS316L and **b)** SS304 in 0.6M NaCl. Note that the color of the plotted elements corresponds to the color of the ordinate color.

Using the right ordinate and either of the abscissa axes as a reference, Figures 2.9a and 2.9b also depict the relationship between the fraction of saturation and pit depth for SS316L and SS304, respectively, in 0.6M NaCl. Experimental data are represented by empty dots, with the dashed line indicating the average and the highlighted box encompassing the standard deviation. For each data point, the fraction of saturation is calculated as i_{rp}/i_{lim}. The results indicate that the fraction of saturation remains independent of pit depth within the range explored. On average, the fractions of saturation corresponding to the extracted i_{rp} value from the galvanodynamic experiments are found to be 0.351 for SS316L and 0.397 for SS304.

Figures 2.10a and 2.10b illustrate the trends in repassivation potential during galvanodynamic experiments at different scan rates (1 nA/s, 10 nA/s, 25 nA/s, 50 nA/s, and 100 nA/s) for SS316L and SS304, respectively. For both alloys, the plotted potentials have been IR-corrected. In the case of SS316L, the transition from conducting the galvandoynamic experiments at high scan rates (10 nA/s, 25 nA/s, 50 nA/s, and 100 nA/s) to 1 nA/s was done at a pit depth of approximately 700μm across all experiments, as shown in Figure 2.10a. For SS304, this transition depth was done at approximately the same pit depth as in the case of SS316L. In both cases, these transition regions are indicated by arrows in colors corresponding to the initial current scan rate.

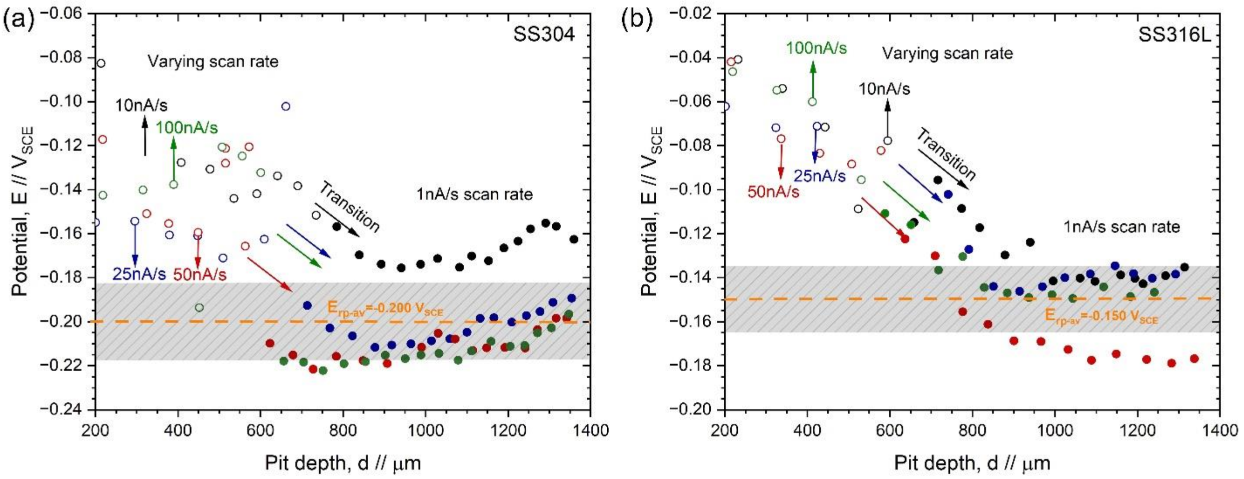

Figure 2.10. Potential versus pit depth for galvanodynamic experiments for **a)** SS316L and **b)** SS304 (right) for different scan rates 1nA/s, 10nA/s, 25nA/s, 50nA/s, and 100nA/s. Note that the potential in these two graphs has been IR-corrected to account for pit and solution resistance.

Consistent with the trends observed in Figure 2.6, an increase in pit depth leads to a decrease in the repassivation potential, regardless of the initial current scan rate. However, for pits larger than approximately 1000µm, the repassivation potential plateaus for both alloys. Using IR-corrected potentials for these large pits, the repassivation potentials in 0.6M NaCl are determined to be -0.15V vs. SCE for SS316L and -0.20V vs. SCE for SS304. The average repassivation potential and its corresponding standard deviation are represented by the orange dashed line and gray box, respectively, in Figures 2.10a and 2.10b.

2.5. Discussion

This chapter aims to provide a unifying quantitative approach to studying the repassivation behavior of SS316L and SS304. To achieve this goal, we integrate kinetics derived from controlled 1D pitting experiments with state-of-the-art thermodynamic simulations. By combining these methods, we leverage thermodynamics to predict the alloy-electrolyte interfacial chemistry through speciation and identification of potential compounds that may form at the bottom of the pit during repassivation while using kinetics to capture the time-dependent nature of these processes.

It is important to recognize that thermodynamics and kinetics do not necessarily align at a single moment in time; thermodynamics describe equilibrium states, whereas kinetics governs the progression of reactions over time. In the context of pitting and repassivation, this distinction is crucial. Although some thermodynamically stable phases, such as $FeCl_2 \cdot 4H_2O$, have been observed, the presence of various other oxides and ionic species-suggested by numerous publications remains a topic of debate and interpretation. [60–62] However, rather than focusing on identifying these species, this study utilizes the most up-to-date thermodynamic insights to better understand and explain the repassivation behavior of SS316L and SS304 as observed through kinetic analysis of parameters that govern it.

Firstly, we consider the thermodynamics of the system of interest. Figure 2.11 presents a thermodynamic stability diagram depicting the equilibrium concentration of various species and compounds (left ordinate) and pH (right ordinate) as a function of the molarity of a stoichiometric SS-chloride mixture for SS316 (solid lines) and SS304 (dashed lines). To facilitate comparison, all concentrations-whether for dissolved or solid species-are expressed in moles per liter of solution. This way, we attempt to build a unifying quantitative approach in which we integrate effects of pH, *f*, icrit, cathodic and anodic kinetics, as well as alloy-electrolyte interfacial chemistry.

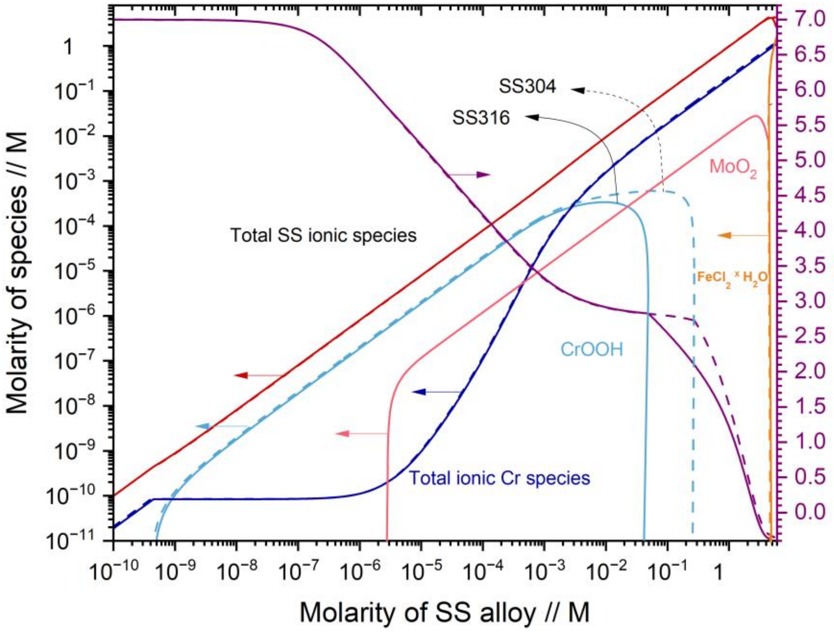

Figure 2.11. Concentration of given species and pH of the solution versus molarity of stoichiometric stainless steel (SS)-chloride mixtures for SS316 (full line) and SS304 (dashed lines) utilizing OLI Studio MSE database. Concentration of solid species is determined as the ratio of moles of solid to volume of solution.

Overall, no significant differences are observed between SS316 and SS304 in terms of total stainless steel ionic species (red line), total ionic chromium species (dark blue line), and $FeCl_2{\cdot}4H_2O$ (orange line). However, three key distinctions emerge between the two alloys: **a)** for SS316L, the CrOOH stability region extends from 5×10^{-10} M to 4×10^{-2} M, whereas for SS304, it spans a wider range, from 5×10^{-10} M to 0.3 M, **b)** for SS-chloride mixture concentrations exceeding 4×10^{-2} M, the solution pH is higher for SS304 than for SS316, and **c)** the presence of

MoO_2 precipitate between 3 × 10^{-6} M and 4 M in the SS316-chloride mixture, a product which is absent in SS304 due to the absence of Mo in the alloy.

Note that passivity and repassivation are two processes that should be approached differently given their nature. From a simple point of view, the passivation process would describe the accumulation of ionic species from electrochemical and chemical reactions, *i.e.,* time would move along the x-axis of Figure 2.11 from left-to-right. For repassivation, the dilution of SS-chlorides through diffusion would be described as time moving along the x-axis from right-to-left. Hence, given that the focus of this chapter is repassivation, an approach that focuses on the dilution of the highly concentrated solution at the pit bottom is followed, hence the speciation graph on Figure 2.11 is read from right-to-left and typical polarization scans are read from top-to-bottom or high-to-low potentials.

2.5.1. Thermodynamic stability of CrOOH

Figure 2.11 suggests that CrOOH precipitates in both SS316L and SS304 during repassivation. It is well established in the corrosion community that the exceptional corrosion resistance of these stainless steels is attributed to a passive layer composed of Cr-based oxides, which exhibit high stability and low solubility. In aqueous environments, this protective layer is generally assumed to consist of hydroxide, oxyhydroxide, and anhydrous oxide forms of chromium, interconnected through varying degrees of dehydration. [63]

Thermodynamic simulations from this study, as well as previous research [30,63] indicate that CrOOH (specifically grimaldiite, γ-CrOOH) is the first Cr-based oxide expected to precipitate as the pit environment transitions from high to low SS-chloride concentrations. The presence of a chromium oxyhydroxide (or hydrated Cr compounds) product on the surface of Cr-containing alloys during the first stages of passive film formation has also been reported experimentally. [64–68] The equilibrium reaction and the corresponding thermodynamic equilibrium constant are:

$$CrOOH_{(s)} + 3H^{+}_{(aq)} \leftrightarrow Cr^{3+}_{(aq)} + 2\,H_2O_{(l)} \qquad K_{eq} = \frac{a_{Cr^{3+}}}{a^{3}_{H^{+}}} = 7.6 \times 10^{4} \qquad (2.2)$$

where K_{eq} is the equilibrium constant and the a_i is the activity of species i. The K_{eq} is calculated utilizing the experimental data from Combs et.al [63] A variation of the same reaction as the one above but with corrected K_{eq} for H_2O can also be found in OLI Studio MSE database. If interested in the details of the reactions associated with such oxides, the reader is directed at the work of Combs, et.al. [63]

It is important to emphasize that this work does not contradict previous studies on the composition of passive Cr-based oxides in chromium containing alloys. [66–70] Rather, it associates the repassivation process with the thermodynamic feasibility of CrOOH formation. The authors acknowledge the ongoing debate surrounding the mechanisms of Cr-induced repassivation and do not propose a specific mechanism in this study. Instead, the assertion that repassivation must be associated with the ability of Cr based oxide (in this study, CrOOH) to first be able to form thermodynamically is a reasonable scientific approach. Whether such phases actually emerge within a given timeframe is a kinetic question - one that could perhaps be addressed through atomistic kinetic-based simulations (e.g., Kinetic Monte Carlo). The authors assert that regardless of whether Cr-based oxide formation occurs through solution-based precipitation [24,25,30,71] or atomistic surface arrangement [70,72,73] the resulting product must be thermodynamically stable to coexist in equilibrium with the electrolyte, given their shared interface. However, the transition from CrOOH to the more commonly observed Cr_2O_3 is beyond the scope of this work. In this chapter we assume that repassivation of SS304 and SS316L initiates rapidly upon CrOOH formation as CrOOH is the first Cr-based oxide to precipitate as the pit environment dilutes.

As the pit environment dilutes, the pH of the solution at the interface is expected to rise, as shown in Figure 2.11 (moving right-to-left along the abscissa). Once the conditions set by the K_{eq} in Equation 2.2 are met, CrOOH begins to precipitate. Notably, CrOOH precipitates in more concentrated pit solutions in SS304 (0.3M) than in SS316L (0.04M). This observation raises an interesting thermodynamic question: why does CrOOH precipitate at a higher SS-chloride concentration mixture for SS304 compared to SS316L? The result is particularly curious given the higher repassivation potential of SS316. [38,57,74–78] It is well known that SS304 contains approximately 2 wt.% more Cr and 2-3 wt.% less Ni than SS316L. However, when the Cr and Ni concentrations were brought to the same value in the alloys (as shown in Figures A2.5a and A2.5b in the Appendix), the results remained unchanged from those in Figure 2.11. This result suggests that the difference arises from the presence of Mo in SS316L.

Mo (present in +3, +4, and +6 oxidation states which are reasonably justifiable in the relevant potential and pH range as originally described by Pourbaix [79]) undergo hydrolysis, causing the pH of the SS-chloride mixture to be slightly lower in SS316L than in SS304 at any given concentration of SS-chloride above 0.04M. Consequently, the precipitation of thermodynamically stable CrOOH is delayed in SS316L compared to SS304. As seen in Figure 2.11, these pH differences, which increase with increase in pit dilution, results in an order of magnitude lower SS-chloride concentration required for CrOOH precipitation in SS316L as compared to SS304.

These findings are crucial as they imply that, under comparable LSV kinetics in the activation-controlled region, the observed E_{rp} for SS304 should be higher than for SS316L. However, experimental results (Figures 2.6a, 2.6b, 2.10a, and 2.10b and [38,57,74–78]) show the opposite trend. Hence, the thermodynamic and kinetic effects arising from the presence of Mo and their influence on these observations will be further explored.

2.5.2. The thermodynamic effects rising from Mo

As previously discussed, the most notable distinction between SS316L and SS304, as illustrated in Figure 2.11, is the precipitation of MoO_2 in SS316L. The diagram in Figure 2.11 indicates that

MoO_2 remains thermodynamically stable in SS316L-chloride mixtures just below full saturation, as evidenced by the presence of $FeCl_2{\cdot}4H_2O$. If MoO_2 functioned as a protective layer, thermodynamic predictions would suggest that SS316L should repassivate at high SS316L-chloride concentrations, corresponding to elevated potentials and current densities. From a thermodynamic perspective, Figure 2.11, along with the Pourbaix diagrams in Figures A2.7, confirms the expected stability of MoO_2 within the potential and pH ranges relevant to this study. The reaction for precipitation of MoO_2 and the resulting equilibrium constant as taken from OLI Studio MSE database is:

$$MoO_{2(s)} + 2H_2O_{(l)} \leftrightarrow Mo^{4+}_{(aq)} + 4\,OH^-_{(aq)} \qquad K_{sp} = a_{Mo^{4+}}a^4_{OH^-} = 6.03 \times 10^{-134} \tag{3}$$

However, research has indicated that Mo alone does not enhance the passivation of stainless steels unless Cr is also present in the alloy. [80] Further studies on Fe-Mo_x alloys have shown that Mo, likely in the +4/+6 oxidation state, is significantly enriched at the pit bottom and within the alloy's oxide layer. [80] Despite this enrichment, Fe-Mo_x alloys do not exhibit improved pitting resistance compared to pure Fe, [80] suggesting that Mo's role in localized corrosion resistance is strongly dependent on the presence of Cr.

The mechanism by which Mo impacts corrosion resistance remains a topic of debate in the literature. [38,64,69,81–84] Two primary mechanisms have been proposed for its influence on repassivation: (1) Mo reduces the active dissolution rate, facilitating repassivation by mitigating acidification [38,81,82], and (2) in acidic environments (such as within the pit), Mo forms Mo (+4/+6) oxides, which precipitate on the pit surface, inhibiting dissolution and promoting the formation of a Cr-based oxide beneath. [64,69,83,84]

Ultimately, two competing effects emerge. On one hand, the presence of Mo in SS316L delays the precipitation of CrOOH to lower SS-chloride concentrations compared to SS304. This delay could create the illusion that, under identical LSV polarization conditions, SS316L may exhibit a lower E_{rp}. On the other hand, Mo in SS316L also contributes to an earlier onset of repassivation at higher potentials, either by facilitating MoO_2 precipitation or by influencing electrochemical kinetics. The following sections explore these seemingly opposing ideas, along with other experimental observations, in greater detail.

2.5.3. E_{rp} plateaus after a pit depth has been reached for SS316L and SS304

The data presented in Figures 2.6a, 2.6b, 2.10a, and 2.10b clearly demonstrate that the E_{rp} reaches a plateau once a critical pit depth is attained. This phenomenon has been previously reported [22,30,40,52,59,85] and is further substantiated in this study through potentiostatic, potentiodynamic, and galvanodynamic experiments. Figures 2.6a and 2.6b specifically illustrate that both the E_{app} and the E_{base} (referred to as E_{rp} here) stabilize once pits exceed a depth of approximately 2.5mm.

Additional potentiostatic experiments conducted at -0.175V vs. SCE on both alloys in 0.6 M NaCl, for pit depths up to ~3.5 mm, indicate that pits beyond this depth do not remain active. A key factor contributing to this behavior is likely the IR drop. Evidence of this IR drop is apparent not only in Figure A2.1 (Appendix) but also in the difference between E_{app} and E_{rp} in Figures 2.6a and 2.6b. Furthermore, IR-corrected solution resistance measurements (Figure A2.6) from multiple LSV curves reveal a linear increase in pit resistance with increasing depth for both alloys. The similarity in slope between the two alloys is expected due to their comparable compositions.

This linear increase in resistance with pit depth aligns with findings from Gaudet et al. [14] who attributed it to the geometric constraints of 1D pit growth. As pit depth increases, solution resistance rises, leading to a corresponding decrease in dissolution current density. Under steady-state diffusion conditions, this decrease is expected to be linear, consistent with Galvele's pit stability product. [15] Consequently, the inverse relationship between resistance and current density necessitates a constant potential drop across the pit depth. Figures 2.6a and 2.6b confirm this, showing a relatively stable potential difference between E_{app} and E_{base}, particularly for deeper pits, as suggested by Gaudet et al. [14]

For shallow pits, the observed variations in IR drop can be attributed to several factors, including deviations from steady-state diffusion, as well as multidimensional (2D or 3D) diffusion effects. The plateau in E_{rp} can thus be linked to this potential drop-approximately 10-15 mV for SS316L and 25-35 mV for SS304-which leads to a substantial reduction in current density at the pit bottom. When the current density falls below the critical threshold necessary to sustain sufficient active dissolution to maintain high SS-chloride concentrations, CrOOH becomes thermodynamically stable and repassivation occurs.

Thus, the observed potential plateau signifies the depth at which the IR drop becomes significant enough to decrease the alloy dissolution and subsequent hydrolysis, ultimately leading to pit repassivation. This analysis primarily considers anodic effects in the repassivation process, the role of cathodic electrochemical reactions will be explored in the following section.

2.5.4. In the activation-controlled region, SS316L has faster cathodic and slower anodic kinetics compared to SS304.

Figure 2.5 clearly illustrates the distinct differences in current densities at -0.05V vs. SCE and -0.175V vs. SCE for SS316L and SS304. Based on these data, we anticipated that the E_{rp} value would fall between these two potentials, making the comparison of these two extrema a logical approach. Regardless of the potential applied or the pit depth explored, our results indicate that SS304 exhibits a higher anodic dissolution rate than SS316L. Additionally, SS316L demonstrates faster cathodic kinetics compared to SS304. Although the enhanced anodic dissolution of SS304 relative to SS316L has been previously established [81,82] this study is the first to our knowledge to report the faster cathodic kinetics of SS316L in solutions relevant to localized corrosion sites.

The Evans diagram in Figure 2.6b, which translates the electrochemical behavior observed in Figures 2.5 and 2.6a, further distinguishes the differences between these two alloys. These findings have important implications on different scales. One can also attempt to adopt a more conservative approach by assuming the same current density and critical conditions are required for passive layer formation. In this scenario, SS316L reaches the necessary potential at a higher value than SS304, contributing to its higher E_{rp}. Furthermore, the larger cathodic current density observed in SS316L suggests that H^+ consumption at the pit bottom occurs at a faster rate compared to SS304 during periods of high dissolution (i.e., at potentials above the OCPs of the alloys). This trend is experimentally supported by Figure 2.7, where the i_c/i_a for SS316L is significantly greater than that of SS304.

Additional thermodynamic analysis further supports these observations and the importance of the local cathodic reaction. Figure 2.11 shows that the percent saturation required for CrOOH precipitation in a diluting pit is approximately 1% for SS316L and 6% for SS304. These saturation levels correspond to extremely low E_{rp} values, approaching E_{corr}, which are not observed experimentally. Therefore, for the pH at the pit bottom to increase while maintaining high dissolution rates, additional reactions must occur to facilitate H^+ consumption. Hydrogen reduction reactions, driven by sufficiently high cathodic kinetics, are necessary to sustain these conditions.

This study expands upon the previous approach by Srinivasan and Kelly by incorporating a more comprehensive thermodynamic framework to better explain the observed electrochemical behavior. Figure 2.12 illustrates the percentage i_c/i_a ratio and the pH as a function of the stoichiometric chloride salt concentration required for repassivation in SS316 and SS304, as obtained from the OLI MSE database. As previously discussed, the condition for repassivation in such thermodynamic simulations is defined as the condition at which CrOOH solid precipitates. The top x-axis of the graph represents the corresponding percent saturation of the molar concentration of SS316L and SS304 chloride salts. Across all tested concentrations, the i_c/i_a for SS316 is slightly higher than that of SS304 by approximately 1%. In addition, as the alloy-chloride concentration increases to ~1.5M (~35% saturation), the i_c/i_a percentage also increases. Beyond this concentration, thermodynamic simulations suggest that the percentage i_c/i_a needed for the precipitation of CrOOH plateaus near a 10.5% value for SS316 and 9.5% for SS304.

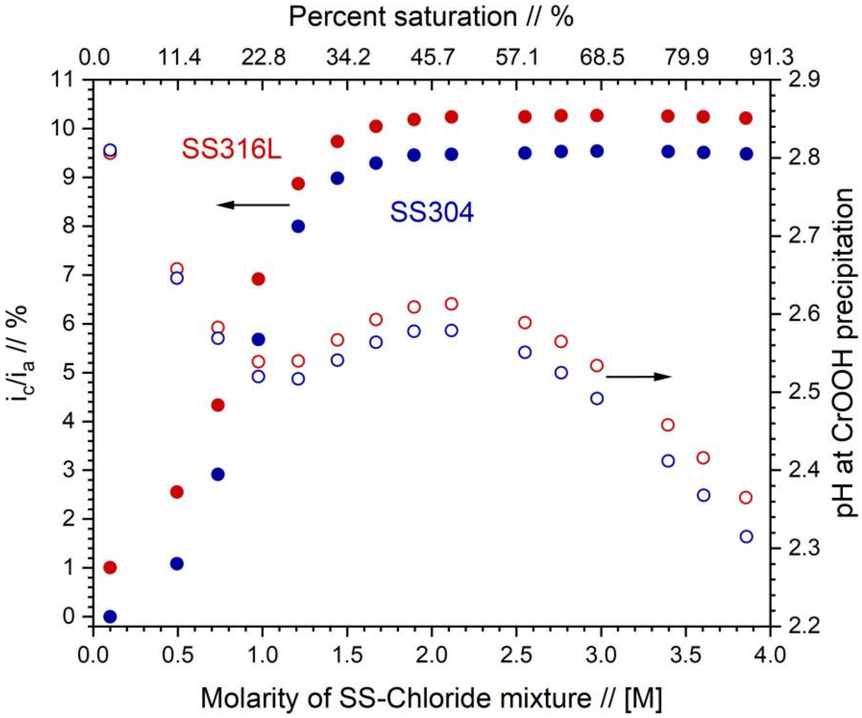

Figure 2.12. Percent cathodic to anodic current density (filled symbols) and pH at the CrOOH precipitation (empty symbols) as a function of pit depth for SS316L (red) and SS304 (blue) in 0.6M NaCl from OLI Studio MSE database. Arrows indicate the y-axis corresponding to the given data.

On the other hand, for both alloys, the pH of the solution at the precipitation point initially decreases from approximately 2.8 to 2.5 as the percent saturation increases to around 25%. As saturation reaches approximately 50%, the pH rises slightly to 2.6 before decreasing again to about 2.3 with further increases in saturation. Notably, the pH at the precipitation point for SS316 remains slightly higher than that of SS304 by approximately 0.6 units.

Figure 2.12 indicates that SS316L requires at least 1% more i_c/i_a than SS304 for CrOOH precipitation across all SS-chloride values. Experimental results from Figure 2.7 demonstrate that this requirement is easily met for SS316L across all tested pit depths, confirming that the necessary kinetic conditions are satisfied. To further expand on this, consider a diluting pit transitioning from high to low concentrations (right to left on the x-axis of Figure 11 or top to bottom in Figure 2.6b). At a fraction of saturation level of 20%, for example, no CrOOH precipitation occurs, as shown in Figure 2.11. However, Figure 2.12 suggests that SS316L requires approximately 4.5% i_c/i_a at this stage, whereas SS304 requires only 3%. Based on Figure 2.7, SS316L achieves the necessary cathodic kinetics to facilitate CrOOH formation, whereas SS304 does not. For SS304 to reach the cathodic kinetics required for CrOOH precipitation, further pit dilution must occur, increasing the cathodic reaction rate at the pit surface and raising the electrolyte pH. This pH increase would create a thermodynamically favorable environment for CrOOH stabilization. However, further dilution inherently reduces the overall current density and potential, leading to a lower repassivation potential for SS304 compared to SS316L By integrating surface chemistry with "pseudo-kinetics" (i_c/i_a in Figure 2.12) derived from thermodynamic modeling and comparing these findings with kinetics obtained from potentiodynamic experiments, this framework quantitatively links the impact of pH and local chemistry to local anodic and cathodic current densities, f, and E_{rp} for our alloys. This comprehensive approach provides a deeper understanding of the differences in repassivation behavior between SS316L and SS304.

As a result, the rigorous analysis presented above strongly supports the hypothesis that the presence of Mo decreases the anodic kinetics in SS316L as compared to SS304. However, our data also provides evidence suggesting that Mo also enhances cathodic kinetics in SS316L at high potentials and dissolution rates. Increased cathodic kinetics due to Mo presence has been documented in other studies related to water electrolysis [86–88] though the precise mechanism remains incompletely understood and is beyond the scope of this study. Indeed, the presence of Mo enhances cathodic kinetics while suppressing anodic dissolution, ultimately resulting in a higher E_{rp} for SS316L compared to SS304.

2.5.6. Galvanodynamic experiments provide a means of obtaining E_{rp} and $(i \cdot x)_{rp}$ for both alloys.

Results from Figures 2.10a and 2.10b demonstrate excellent agreement between galvanodynamic and potentiostatic experiments in determining E_{rp} for both alloys. The data indicate that the E_{rp} value for SS316L in 0.6M NaCl falls within the range of -0.15V to -0.165V vs. SCE, whereas that for SS304 lies between -0.18V and -0.2V vs. SCE. These values are slightly less conservative than those previously reported in the literature [30,40,52,78,85] or that can be obtained directly through OLI Studio simulations.

A key advantage of the galvanodynamic experiments is the ability to determine $(i \cdot x)_{rp}$, also known as the critical pit stability product $(i \cdot x)_{crit}$. The $(i \cdot x)_{rp}$ value obtained in this study represents the minimum current density required for a given pit depth to sustain an active state on the SS surface. This parameter is particularly significant as the methodology ensures that the measured $(i \cdot x)$ represents the threshold below which repassivation occurs. Importantly, $(i \cdot x)_{rp}$ corresponds to the well-established pit stability product derived from Galvele's seminal work [15] as his analysis describes a controlled current density experiment.

The results presented in Figures 2.9a and 2.9b indicate no significant difference in (i·x)rp between SS316L and SS304 in 0.6M NaCl. Although the data scatter might hide a slight difference between the two alloys, the differences in $(i \cdot x)_{rp}$ should not be substantial considering their similarities in composition and electrochemical behavior. Initially, one might assume that the faster anodic kinetics of SS304 compared to SS316L would result in a higher $(i \cdot x)_{rp}$ for the former. However, a closer examination of the LSV data in Figure A2.4 provides insight into why the differences in

$(i{\cdot}x)_{rp}$ between SS316L and SS304 are minimal. Specifically, the current densities extracted at the average E_{rp} values (referred here to as i_{rp}) for both alloys show only minor variation. Figure A2.4 clearly demonstrates that in the activation-controlled region, at any given current density, the difference in polarizability between SS316L and SS304 closely matches their previously reported difference in E_{rp}.

Unlike previous studies that rely on theoretical calculations and assumptions, the galvanodynamic approach used here directly derives $(i{\cdot}x)_{rp}$, a parameter of significant interest since the highly acclaimed work of Galvele. [15] If necessary, however, the value of f can be easily determined as the ratio of $(i{\cdot}x)_{rp}$ to $(i{\cdot}x)_{sf}$. The results in Figures 2.9a and 2.9b indicate that f remains relatively constant with increasing pit depth for both alloys, which aligns with the assumption that the critical chemistry required for repassivation does not vary with depth. However, f is consistently slightly higher for SS304 than for SS316L, a result that corresponds with expectations given that $(i{\cdot}x)_{sf}$ is slightly lower for SS304 than for SS316L. Furthermore, the experimentally obtained values of $(i{\cdot}x)_{sf}$ show strong agreement with existing literature. [14,26,78,85] The calculated values of f, ranging from approximately 0.35 to 0.4 for both alloys, are on the lower end of previously reported values. [14,26,34–36,52,78,85]

Although the similar $(i{\cdot}x)_{rp}$ values suggest comparable pitting corrosion behavior between SS304 and SS316L, this does not necessarily imply that the resulting pits will be identical. While the critical anodic kinetics required for pit propagation are similar for both alloys, Chen and Kelly [29] have demonstrated that cathodic kinetics play a crucial role in determining maximum pit size. Putting further restrictions by assuming comparable cathodic kinetics for both alloys, the difference in E_{rp} suggests that SS304 has a higher total cathodic current capacity than SS316L. According to the model proposed by Chen and Kelly [29] this would lead to larger pit sizes in SS304, a trend that is consistently observed in both laboratory experiments and engineering applications. [29,89–93]

2.5.7. General remarks

The approach outlined above establishes a method for linking the thermodynamics and kinetics of repassivation through electrochemical data. This framework effectively connects the surface concentration of equimolar ionic stainless-steel species to the other previously reported parameters importance to repassivation: pH, i_c/i_a, cathodic and anodic kinetics, f, $(ix)_{rp}$, and E_{rp}. The combined results and discussion presented in this study provide a more complete understanding of the complexities underlying the repassivation mechanism in pitting corrosion of SS316L and SS304. Furthermore, the presented analysis offers a more detailed explanation for the frequently observed phenomenon of SS316L exhibiting a higher E_{rp} than SS304 in the same environment. Undoubtfully, the presence of Mo has been shown to play a critical role in enhancing cathodic kinetics, suppressing anodic dissolution, and slightly decreasing the pH at the electrode-electrolyte interface for SS316L, contributing to its more noble repassivating behavior.

2.5.8. Limitations

In this section, we assess possible key criticisms related to both the experimental and simulation aspects of this study. Some of the limitations discussed here have been considered in previous studies; however, they are briefly reiterated for clarity. One potential experimental concern arises from the use of fast potentiodynamic scans, which serve as the basis for many of the kinetic measurements in this study. The 400 mV/s scan rate may introduce uncertainties related to solution dilution and current contributions from double-layer capacitance.

Regarding dilution, prior work by Srinivasan and Kelly [94] indicates that the dilution occurring within the approximately 1s period required to scan the potential from the anodic to the cathodic region results in less than a 1% overall decrease in surface concentration. Thus, the impact of this expected dilution on the observed kinetics is minimal. Similarly, when considering the influence of double-layer capacitance, a conservative estimate using a surface capacity of 100 $\mu F/cm^2$ and a scan rate of 0.4 V/s yields a current density of approximately 40 $\mu A/cm^2$. This value is negligible compared to the current densities measured in this study, suggesting that capacitive effects do not significantly influence the results.

Another limitation of this study pertains to the availability of thermodynamic (and, in some cases, kinetic) data required for modeling localized corrosion phenomena. A key assumption in our approach is that thermodynamic equilibrium for alloy dissolution is established instantaneously at the electrode-electrolyte interface. However, hydrolysis reactions occurring both at the interface and throughout the solution are time-dependent, as highlighted in the work of Smialowska. [95] This time dependence could influence predicted pH values, although E_{rp} measurements should remain unaffected.

Additionally, the assumptions of uniform dissolution of both alloys and near-instantaneous equilibrium for metal cation hydrolysis introduces further challenges related to equilibrium constants-particularly for CrOOH. Uniform dissolution of a similar alloy has been previously reported by Issacs. [96] Furthermore, upon further examination, the equilibrium constants used for CrOOH precipitation in this study, sourced from the OLI Studio MSE database, are based on data from Combs et al. [63] It must be noted that the experiments used to determine these constants were conducted in high pH solutions and in the absence of chloride ions (Cl^-), which are highly relevant in localized corrosion environments. This example highlights a broader issue in corrosion modeling: the need for more accurate aqueous thermodynamic parameters that reflect the aggressive conditions characteristic of localized corrosion. Future research should prioritize the identification of these parameters in relevant environments to improve the predictive capabilities of corrosion simulations.

2.6. Conclusions

In this chapter, we have presented a unifying quantitative framework for understanding repassivation behavior by connecting key parameters previously identified in the literature: pH, $(i \cdot x)_{rp}$, anodic and cathodic kinetics within the pit, i_c/i_a, *f*, E_{rp}, and electrode-electrolyte interfacial chemistry and oxide precipitation. Our approach enables the extraction of pit kinetics through potentiostatic, fast potentiodynamic, and galvanodynamic 1D pit experiments, while integrating thermodynamic modeling using an advanced thermodynamic MSE database from OLI. This approach was applied to study the repassivation behavior of SS316L and SS304 in 0.6M NaCl. The findings of this study lead to the following conclusions:

1. Potentiostatic, potentiodynamic, and galvanodynamic experiments can be designed in tandem to obtain the repassivation potential, critical pit stability product, i_c/i_a ratio, and *f*.
2. Thermodynamic modeling can be combined with kinetic data to provide valuable insights into critical electrode-electrolyte pH, concentration thresholds, and theoretical estimates for i_c/i_a values.
3. The repassivation potential decreases as pit depth increases for both alloys, plateauing at approximately -0.15 to -0.165 V vs. SCE for SS316L and -0.18 to -0.2 V vs. SCE for SS304 in 0.6M NaCl.
4. The observed differences in repassivation potential are attributed to the role of Mo in SS316L, which suppresses anodic kinetics and accelerates cathodic kinetics at high potentials above the OCP compared to SS304L.
5. Local cathodic kinetics within the pit play a significant role in the repassivation process for both alloys. Experimental results show i_c/i_a values of approximately 2-4.5% for SS316L and ≤ 1% for SS304 in 0.6M NaCl. Thermodynamic analysis also supports the critical role of local cathodic kinetics in repassivation.
6. The $(i \cdot x)_{rp}$ for both alloys in 0.6M NaCl is similar, reported at around 0.32 A/m, with *f* ranging between 0.35 and 0.4.
7. Overall, the anodic and cathodic kinetics under repassivation conditions are independent of pit depth for both SS316L and SS304 in 0.6M NaCl.

2.7. References

1. Tomashov, N. D. & Chernova, G. P. *Passivity and Protection of Metals Against Corrosion. Springer New York, NY* vol. 1 (Springer New York, 2012).
2. Faraday, M. Note from Professor Faraday to Mr. Richard Taylor on the preceding paper. *London, Edinburgh, Dublin Philos. Mag. J. Sci.* **10**, 175–176 (1837).
3. Schœnbein, C. F. XXXVI. Remarks on Faraday's hypothesis with regard to the causes of the neutrality of iron in nitric acid. *London, Edinburgh, Dublin Philos. Mag. J. Sci.* **10**, 172–174 (1837).
4. Schœnbein, C. F. LXXX. Experiments on the peculiar voltaic condition of iron as excited by peroxide of lead; in a letter to Mr. Faraday . *London, Edinburgh, Dublin Philos. Mag. J. Sci.* **10**, 425–428 (1837).
5. Schœnbein, C. F. LIV. Experimental researches on a peculiar action of iron upon solutions of some metallic salts . *London, Edinburgh, Dublin Philos. Mag. J. Sci.* **10**, 267–276 (1837).
6. Evans, U. R. CXL.-The Passivity of Metals. Part I. The Isolation of the Protective film. *J. Chem. Soc* **1**, 1020–1040 (1927).
7. Lillie, R. S. . Transmission of Activation in Passive Metals as a Model of the Protoplasmic or Nervous Type of Transmission. *Sci. New Ser.* **48**, 51–60 (1918).
8. Vanleugenhaghe, C., Klimczak-Mathieu, L., Meunier, J. & Pourbaix, M. Influence de chlorures et d'oxydants sur le comportement d'aciers inoxydables en solution bicarbonique. *Corros. Sci.* **2**, 29–35 (1962).
9. Vetter, K. J. Problems in the Theoretical Treatment of Reactions Occurring at Easily Passivated Metal Anodes. *Angew. Chemie Int. Ed. English* **1**, 583–590 (1962).
10. Vetter, K. J. Electrochemical Kinetics, Theoretical and Experimental Aspects. (1967).
11. Strehblow, H. H., Vetter, K. J. & Willgallis, A. Ermittlung der Zusammensetzung der Oberfläche von Korrosionslöchern auf Eisen während des Lochfraßes mittels der Elektronenmikrosonde. *Berichte der Bunsengesellschaft für Phys. Chemie* **75**, 822–829 (1971).
12. Frankenthal, R. P. & Pickering, H. W. On the Mechanism of Localized Corrosion of Iron and Stainless Steel. *J. Electrochem. Soc.* **119**, 1304 (1972).
13. Tester, J. W. & Isaacs, H. S. Diffusional Effects in Simulated Localized Corrosion. *J. Electrochem. Soc.* **122**, 1438–1445 (1975).
14. Gaudet, G. T. *et al.* Mass transfer and electrochemical kinetic interactions in localized pitting corrosion. *AIChE J.* **32**, 949–958 (1986).
15. Galvele, J. R. Transport Processes and the Mechanism of Pitting of Metals. *J. Electrochem. Soc.* **123**, 464–474 (1976).

16. Galvele, J. R. Transport processes in passivity breakdown-II. Full hydrolysis of the metal ions. *Corros. Sci.* **21**, 551–579 (1981).

17. Gravano, S. M. & Galvele, J. R. Transport processes in passivity breakdown—III. Full hydrolysis plus ion migration plus buffers. *Corrosion* **24**, 517–534 (1984).

18. Okada, T. Considerations of the Stability of Pit Repassivation during Pitting Corrosion of Passive Metals. *J. Electrochem. Soc.* **131**, 1026–1032 (1984).

19. Macha, J. H. & Scully, J. R. Corrosion Properties Of Laser Welded Superaustenitic Stainless Steel Sandwich Structures. *Corros. 2009* **65**, 472–490 (2009).

20. Newman, R. Pitting Corrosion of Metals. *Electrochem. Soc. Interface* **19**, 33–38 (2010).

21. Laycock, N. J. & Newman, R. C. Localised dissolution kinetics, salt films and pitting potentials. *Corros. Sci.* **39**, 1771–1790 (1997).

22. Dunn, D. S., Sridhar, N. & Cragnolino, G. A. Long-Term Prediction of Localized Corrosion of Alloy 825 in High-Level Nuclear Waste Repository Environments. *Corros.* **52**, 115–124 (1996).

23. Tormoen, G., Sridhar, N. & Anderko, A. Localised corrosion of heat treated alloys Part 1 - Repassivation potential of alloy 600 as function of solution chemistry and thermal aging. *Corros. Eng. Sci. Technol.* **45**, 155–162 (2010).

24. Anderko, A., Cao, L., Gui, F., Sridhar, N. & Engelhardt, G. R. Modeling localized corrosion of corrosion-resistant alloys in oil and gas production environments: Part II. Corrosion potential. *Corrosion* **73**, 634–647 (2017).

25. Anderko, A., Sridhar, N. & Dunn, D. S. A general model for the repassivation potential as a function of multiple aqueous solution species. *Corros. Sci.* **46**, 1583–1612 (2004).

26. P.C.Pistorius, G. T. B. Metastable pitting corrosion of stainless steel and the transition to stability. *Philos. Trans. R. Soc. London. Ser. A Phys. Eng. Sci.* **341**, 531–559 (1992).

27. Pistorius, P. C. & Burstein, G. T. Growth of corrosion pits on stainless steel in chloride solution containing dilute sulphate. *Corros. Sci.* **33**, 1885–1897 (1992).

28. Williams, D. E., Stewartt, J. & Balkwill~, P. H. The nucleation, growth and stability of micropits in stainless steel. *Corros. Sci.* **36**, 1213–1235 (1994).

29. Chen, Z. Y. & Kelly, R. G. Computational Modeling of Bounding Conditions for Pit Size on Stainless Steel in Atmospheric Environments. *J. Electrochem. Soc.* **157**, C69 (2010).

30. Srinivasan, J. & Kelly, R. G. Evaluating the Critical Chemistry for Repassivation at the Corroding Surface Using Mass Transport Model-Based Artificial Pit Experiments. *J. Electrochem. Soc.* **163**, C768–C777 (2016).

31. Frankel, G. S., Stockert, L., Hunkeler, F. & Boehni, H. Metastable Pitting of Stainless Steel. *Corrosion* **43**, 429–436 (1987).

32. Frankel, G. S. Pitting Corrosion of Metals: A Review of the Critical Factors. *J. Electrochem. Soc.* **145**, 2186–2198 (1998).

33. Frankel, G. S., Li, T. & Scully, J. R. Perspective—Localized Corrosion: Passive Film Breakdown vs Pit Growth Stability. *J. Electrochem. Soc.* **164**, C180–C181 (2017).

34. Li, T., Scully, J. R. & Frankel, G. S. Localized Corrosion: Passive Film Breakdown vs Pit Growth Stability: Part II. A Model for Critical Pitting Temperature. *J. Electrochem. Soc.* **165**, C484–C491 (2018).

35. Li, T., Scully, J. R. & Frankel, G. S. Localized Corrosion: Passive Film Breakdown vs. Pit Growth Stability: Part III. A Unifying Set of Principal Parameters and Criteria for Pit Stabilization and Salt Film Formation. *J. Electrochem. Soc.* **165**, C762–C770 (2018).

36. Li, T., Scully, J. R. & Frankel, G. S. Localized Corrosion: Passive Film Breakdown vs. Pit Growth Stability: Part IV. The Role of Salt Film in Pit Growth: A Mathematical Framework. *J. Electrochem. Soc.* **166**, C115–C124 (2019).

37. Li, T., Scully, J. R. & Frankel, G. S. Localized Corrosion: Passive Film Breakdown vs Pit Growth Stability: Part V. Validation of a New Framework for Pit Growth Stability Using One-Dimensional Artificial Pit Electrodes. *J. Electrochem. Soc.* **166**, C3341–C3354 (2019).

38. Li, T., Wu, J. & Frankel, G. S. Localized corrosion: Passive film breakdown vs. Pit growth stability, Part VI: Pit dissolution kinetics of different alloys and a model for pitting and repassivation potentials. *Corros. Sci.* **182**, 109277 (2021).

39. Marshall, R. S., Katona, R. M., Melia, M. A. & Kelly, R. G. Pit Stability Predictions of Additively Manufactured SS316 Surfaces Using Finite Element Analysis. *J. Electrochem. Soc.* **169**, 021506 (2022).

40. Katona, R. M., Carpenter, J., Schindelholz, E. J. & Kelly, R. G. Prediction of Maximum Pit Sizes in Elevated Chloride Concentrations and Temperatures. *J. Electrochem. Soc.* **166**, C3364–C3375 (2019).

41. Katona, R. M. *et al.* Quantitative assessment of environmental phenomena on maximum pit size predictions in marine environments. *Electrochim. Acta* **370**, 137696 (2021).

42. Katona, R. M., Knight, A. W., Maguire, M., Bryan, C. R. & Schaller, R. F. Considerations for realistic atmospheric environments: An application to corrosion testing. *Sci. Total Environ.* **885**, (2023).

43. Katona, R. M., Knight, A., Bryan, C., Schaller, R. F. & Kelly, R. *Determination of Key Marine Environment Effects on Bounding Pit Size Predictions*. *ECS Meeting Abstracts* vols MA2020-02 (2020).

44. Alkire, R. C. & Wong, K. P. The corrosion of single pits on stainless steel in acidic chloride solution. *Corros. Sci.* **28**, 411–421 (1988).

45. Bocher, F. & Scully, J. R. Stifling of crevice corrosion and repassivation: Cathode area

versus controlled potential decreases assessed with a coupled multi-electrode array. *Corrosion* **71**, 1049–1063 (2015).

46. Newman, R. C. & Isaacs, H. S. Diffusion-Coupled Active Dissolution in the Localized Corrosion of Stainless Steels. *J. Electrochem. Soc.* **130**, 1621–1624 (1983).
47. Beck, T. R. & Alkire, R. C. Occurrence of Salt Films during Initiation and Growth of Corrosion Pits. *J. Electrochem. Soc.* **126**, 1662–1666 (1979).
48. Woldemedhin, M. T., Srinivasan, J. & Kelly, R. G. Effects of environmental factors on key kinetic parameters relevant to pitting corrosion. *J. Solid State Electrochem.* **19**, 3449–3461 (2015).
49. Laycock, N. *et al.* Localised Dissolution Kinetics From Fast In Situ Radiography of Propagating Pits in Stainless Steel and Implications for Modeling Pitting Corrosion over Long Time-Scales. *ECS Meet. Abstr.* **MA2011-02**, 1685–1685 (2011).
50. Laycock, N. J. & White, S. P. Computer Simulation of Single Pit Propagation in Stainless Steel under Potentiostatic Control. *J. Electrochem. Soc.* **148**, B264 (2001).
51. Moayed, M. H. & Newman, R. C. The Relationship Between Pit Chemistry and Pit Geometry Near the Critical Pitting Temperature. *J. Electrochem. Soc.* **153**, B330 (2006).
52. Srinivasan, J. & Kelly, R. G. One-Dimensional Pit Experiments and Modeling to Determine Critical Factors for Pit Stability and Repassivation. *J. Electrochem. Soc.* **163**, C759–C767 (2016).
53. Srinivasan, J., Liu, C. & Kelly, R. G. Geometric Evolution of Flux from a Corroding One-Dimensional Pit and Its Implications on the Evaluation of Kinetic Parameters for Pit Stability. *J. Electrochem. Soc.* **163**, C694–C703 (2016).
54. Sato, N. The Stability of Pitting Dissolution of Metals in Aqueous Solution. *J. Electrochem. Soc* **129**, 260–264 (1982).
55. Shehi, A. *et al.* Corrosion Behavior of Additively Manufactured and Wrought Ti-6Al-4V Alloys in Phosphate Buffered Saline Solutions. *CORROSION 2021* D121S054R006 (2021).
56. Suleiman, M. I., Ragault, I. & Newman, R. C. The pitting of stainless steel under a rust membrane at very low potentials. *Corros. Sci.* **36**, 479–486 (1994).
57. Montoya, T. *et al.* Influence of Realistic, Cyclic Atmospheric Cycles on the Pitting Corrosion of Austenitic Stainless Steels. *J. Electrochem. Soc.* **170**, 041502 (2023).
58. Ravi, V. A. *et al.* The environmental stability of Boron-containing titanium alloys for Biomedical applications. *JOM J. Miner. Met. Mater. Soc.* **63**, 42–47 (2011).
59. Dunn, D. S., Cragnolino, G. A. & Sridhar, N. An electrochemical approach to predicting longterm localized corrosion of corrosion-resistant high-level waste container materials. *Corrosion* **56**, 90–104 (2000).
60. Li, T. *et al.* Cryo-based structural characterization and growth model of salt film on metal.

Corros. Sci. **174**, (2020).

61. Hammons, J. A. *et al.* Interfacial phenomena during salt layer formation under high rate dissolution conditions. *J. Phys. Chem. B* **117**, 6724–6732 (2013).
62. Sridhar, N. & Dunn, D. S. In Situ Study of Salt Film Stability in Simulated Pits of Nickel by Raman and Electrochemical Impedance Spectroscopies. *J. Electrochem. Soc.* **144**, 4243–4253 (1997).
63. Ziemniak, S. E., Jones, M. E. & Combs, K. E. S. Solubility and phase behavior of Cr(III) oxides in alkaline media at elevated temperatures. *J. Solution Chem.* **22**, 601–623 (1993).
64. Hashimoto, K. Passivation of Amorphous Materials. in *Passivity of Metals and Semiconductors* (ed. Froment, M.) 235–246 (Elsevier, 1983). doi:https://doi.org/10.1016/B978-0-444-42252-1.50041-2.
65. Asami, K., Hashimoto, K. & Shimodaira, S. An XPS study of the passivity of a series of iron-chromium alloys in sulphuric acid. *Corros. Sci.* **18**, 151–160 (1978).
66. Gerard, A. Y. *et al.* The role of chromium content in aqueous passivation of a non-equiatomic Ni38Fe20CrxMn21-0.5xCo21-0.5x multi-principal element alloy (x = 22, 14, 10, 6 at%) in acidic chloride solution. *Acta Mater.* **245**, (2023).
67. Sur, D. *et al.* Factors governing passivation behavior of Fe-Cr-Al-Ti alloys in sulfate containing acidified solutions : Uncovering the many roles of Ti. *Materialia* **39**, 102370 (2025).
68. Sur, D. *et al.* Investigating the long-term synergistic benefits of Al on Cr(III) in the passive films of FeCoNi-Cr-Al CCAs in sulfuric acid. **513**, 1–14 (2025).
69. Choudhary, S., Cruz, V., Pandey, A., Thomas, S. & Birbilis, N. Element-resolved electrochemical analysis of the passivity of additively manufactured stainless steel 316L. *Corros. Sci.* **189**, 109576 (2021).
70. Wang, Z. *et al.* Mechanisms of Cr and Mo Enrichments in the Passive Oxide Film on 316L Austenitic Stainless Steel. *Front. Mater.* **6**, 1–12 (2019).
71. Armstrong, R. D., Harrison, J. A. & Thirsk, H. R. Recent developments in models for theelectrocrystallisation of anodic films. *Corros. Sci.* **10**, 679–686 (1970).
72. Blades, W. H. *et al.* Tuning chemical short-range order for stainless behavior at reduced chromium concentrations in multi-principal element alloys. *Acta Mater.* **277**, (2024).
73. Xie, Y. *et al.* A percolation theory for designing corrosion-resistant alloys. *Nat. Mater.* **20**, 789–793 (2021).
74. Newman, R. C. The dissolution and passivation kinetics of stainless alloys containing molybdenum-II. Dissolution kinetics in artificial pits. *Corros. Sci.* **25**, 341–350 (1985).
75. Palit, G. C., Kain, V. & Gadiyar, H. S. Electrochemical investigations of pitting corrosion in nitrogen-bearing type 316N stainless steel. *Corrosion* **49**, 979–991 (1993).

76. Javidi, M., Karimi Abadeh, H., Yazdanpanah, H. R., Namazi, F. & Shirvani Shiri, N. Synergistic effect of temperature, concentration and solution flow on corrosion and passive film of austenitic SS 304L and 316L in concentrated sulfuric acid. *Corros. Sci.* **237**, 112306 (2024).

77. Mohammadi, M., Choudhary, L., Gadala, I. M. & Alfantazi, A. Electrochemical and Passive Layer Characterizations of 304L, 316L, and Duplex 2205 Stainless Steels in Thiosulfate Gold Leaching Solutions. *J. Electrochem. Soc.* **163**, C883–C894 (2016).

78. Srinivasan, J. A Quantitative Framework Connecting the Critical Factors Determining the Stability of Localized Corrosion. (University of Virginia, Materials Science - School of Engineering and Applied Science, PHD (Doctor of Philosophy), 2016, 2016).

79. Pourbaix, M. T. A.-T. T.-. Atlas of electrochemical equilibria in aqueous solutions. 277 (1966) doi:LK - https://worldcat.org/title/563921897.

80. Schneider, A., Kuron, D., Hofmann, S. & Kirchheim, R. AES analysis of pits and passive films formed on FeCr FeMo and FeCrMo alloys. *Corros. Sci.* **31**, 191–196 (1990).

81. Newman, R. C. The dissolution and passivation kinetics of stainless alloys containing molybdenum-1. Coulometric studies of FeCr and FeCrMo alloys. *Corros. Sci.* **25**, 331–339 (1985).

82. Ilevbare, G. O. & Burstein, G. T. Role of alloyed molybdenum in the inhibition of pitting corrosion in stainless steels. *Corros. Sci.* **43**, 485–513 (2001).

83. Sugimoto, K. & Sawada, Y. The role of alloyed molybdenum in austenitic stainless steels in the inhibition of pitting in neutral halide solutions. *CORROSION* **32**, 347–352 (1976).

84. Pardo, A. *et al.* Pitting corrosion behaviour of austenitic stainless steels - combining effects of Mn and Mo additions. *Corros. Sci.* **50**, 1796–1806 (2008).

85. Srinivasan, J., McGrath, M. J. & Kelly, R. G. A High-Throughput Artificial Pit Technique to Measure Kinetic Parameters for Pitting Stability. *J. Electrochem. Soc.* **162**, C725–C731 (2015).

86. Olivares-Ramírez, J. M., Campos-Cornelio, M. L., Uribe Godínez, J., Borja-Arco, E. & Castellanos, R. H. Studies on the hydrogen evolution reaction on different stainless steels. *Int. J. Hydrogen Energy* **32**, 3170–3173 (2007).

87. Zheng, X. L. *et al.* NimMon (m + n = 5) clusters for hydrogen electric reduction: Synergistic effect of Ni and Mo on the adsorption and OH breaking of H2O. *J. Phys. Chem. C* **123**, 9247–9254 (2019).

88. Bau, J. A. *et al.* Role of Oxidized Mo Species on the Active Surface of Ni-Mo Electrocatalysts for Hydrogen Evolution under Alkaline Conditions. *ACS Catal.* **10**, 12858–12866 (2020).

89. Shibata, T., Kurahashi, H., Kaneko, S., Ohya, T. & Motohashi, K. An Effect of Airborne

Salt Particles on the Atmospheric Corrosion Resistance of Stainless Steels Sheltered with the House Eaves in Marine District. *Zairyo-to-Kankyo* **44**, 281–286 (1995).

90. Johnson, K. E. Airborne contaminants and the pitting of stainless steels in the atmosphere. *Corros. Sci.* **22**, 175–191 (1982).

91. Baker, E. A. & .S, L. T. *Degradation of metals in the atmosphere : a symposium sponsored by ASTM Committee G-1 on Corrosion of Metals*. *ASTM* (1986) doi:10.1520/STP965-EB.

92. Tadokoro, Y. & Takahashi, A. Atmospheric Corrosion Behavior and Estimation Method of Ordinarily Used Stainless Steels. *Zairyo-to-Kankyo* **48**, 34–40 (1999).

93. Michio Nakata, Naoto Ono, Y. U. State of Stainless Steels Roofing in Okinawa and Characteristics of CorrosionResistance in Atmosphere of Various Stainless Steels. *Zairyo-to-Kankyo* **564**, 559–564 (1997).

94. Srinivasan, J. & Kelly, R. G. On a recent quantitative framework examining the critical factors for localized corrosion and its impact on the galvele pit stability criterion. *Corrosion* **73**, 613–633 (2017).

95. Mankowski, J. & Szklarska-Smialowska, Z. Studies on accumulation of chloride ions in pits growing during anodic polarization. *Corros. Sci.* **15**, 493–501 (1975).

96. Isaacs, H. S., Cho, J. -H., Rivers, M. L. & Sutton, S. R. In Situ X-Ray Microprobe Study of Salt Layers during Anodic Dissolution of Stainless Steel in Chloride Solution. *J. Electrochem. Soc.* **142**, 1111–1118 (1995).

A2. Appendix

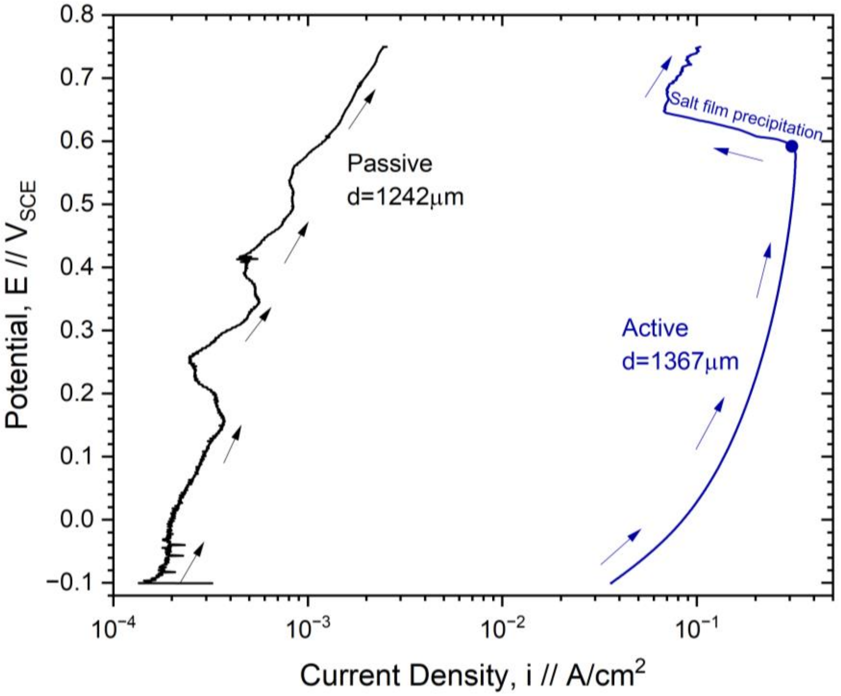

Figure A2.1. Potential versus current density for SS304 in 0.6M NaCl during the LSV scan at 5mV/s after a 1h potentiostatic test at -0.1V vs. SCE. The graph highlights two typical behaviors observed during the upward scan: passive at 1242μm (black curve) active at 1367μm (blue curve). Arrows indicate the direction of the scan rate.

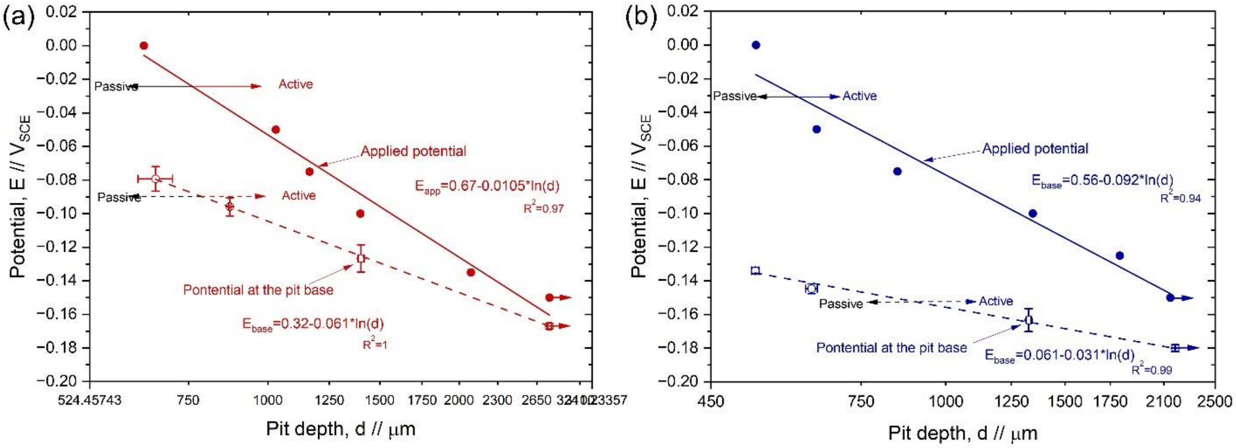

Figure A2.2. Critical applied potential (filled dots), and potential at the pit base (empty) for a) SS316L and b) SS304 in 0.6M NaCl solution. Note the base natural logarithmic (ln) scale of the abscissa axis and the linear fit line for each of the data set.

Example of identifying i_c/i_a using a fast potentiodynamic scan.

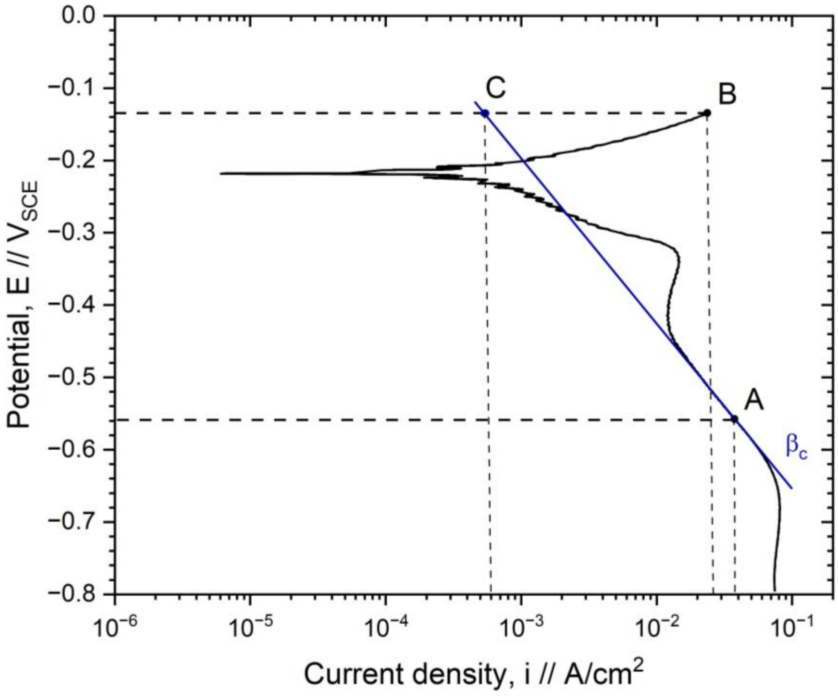

Figure A2.3. IR-corrected potentiodynamic scan at 400mV/s of SS316L in 0.6M NaCl at 1395µm pit depth. Labelled points A, B, and C are utilized in the analysis provided below.

An IR-corrected LSV scan taken at 400mV/s of SS316L in 0.6M NaCl at a 1396µm pit depth is utilized for this demonstration as depicted in Figure A2.3. Experimentally, the LSV for this scan started at -0.1V vs. SCE. The procedure of the IR correction is shown in the methodology section of this chapter. The following steps were taken to calculate the i_c/i_a ratio:

1. β_c of the curve is extracted from the linear region of the cathodic portion of the LSV graph in Figure A2.3. The value of β_c was found to be -0.214V/decade.
2. In the linear region of the cathodic portion of the LSV scan a random point was chosen (point A). The coordinates of this point are: -0.557V vs. SCE, 0.03751 A/cm^2.
3. The first point of the LSV scan was also identified (point B) with the following coordinates: -0.13 V vs. SCE, 0.02367 A/cm^2.
4. A Tafel relationship was assumed and the coordinates of point C in the LSV scan are identified:
    a. $\Delta E = \beta_c \log_{10}\left(\frac{i_c}{i_o}\right) \equiv [-0.136 - (-0.557)]V = -0.214 \log_{10}\left(\frac{i_c}{0.03751\frac{A}{cm^2}}\right) \rightarrow$

       $i_c = 4.04 \cdot 10^{-4} A/cm^2$
5. The i_c/i_a can then be found as follows:
    a. $\frac{i_c}{i_a} \equiv \frac{i_c}{i_t - i_c} = \frac{4.04\cdot10^{-4}\frac{A}{cm^2}}{(0.03751+4.04\cdot10^{-4})\frac{A}{cm^2}} \rightarrow \frac{i_c}{i_a} = 1.07\%$

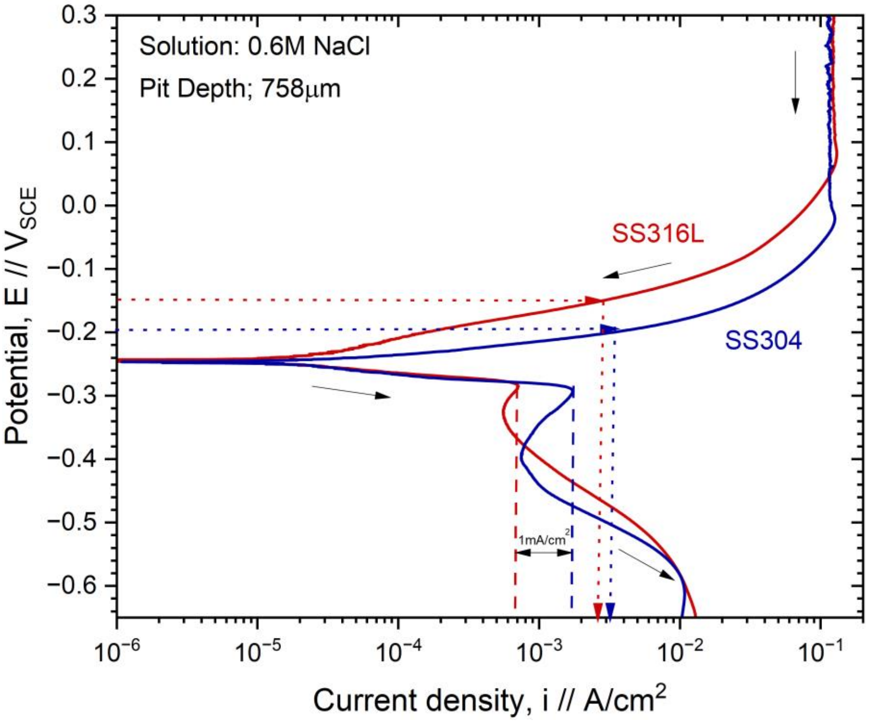

Figure A2.4. Potentiodynamic scan at 5mV/s of SS316L (red) and SS304 (blue) in 0.6M NaCl at 758μm pit depth. Black arrows indicate the direction of the scan while the colored arrows are taken arbitrarily to compare the current density at E_{rp} of both alloys.

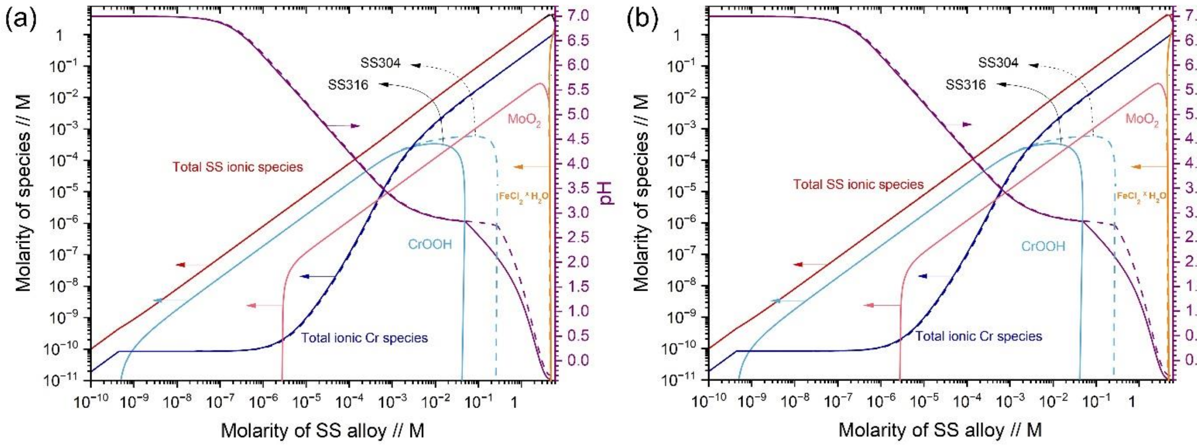

Figure A2.5. Concentration of given species and pH of the solution versus molarity of stoichiometric stainless steel (SS)-chloride mixtures for SS316 (full line) and SS304 (dashed lines) utilizing OLI Studio MSE database in which a) SS304 has the same Cr concentration as SS316 but no Mo and **b)** SS304 has the same Cr and Ni concentration as SS316 but no Mo.

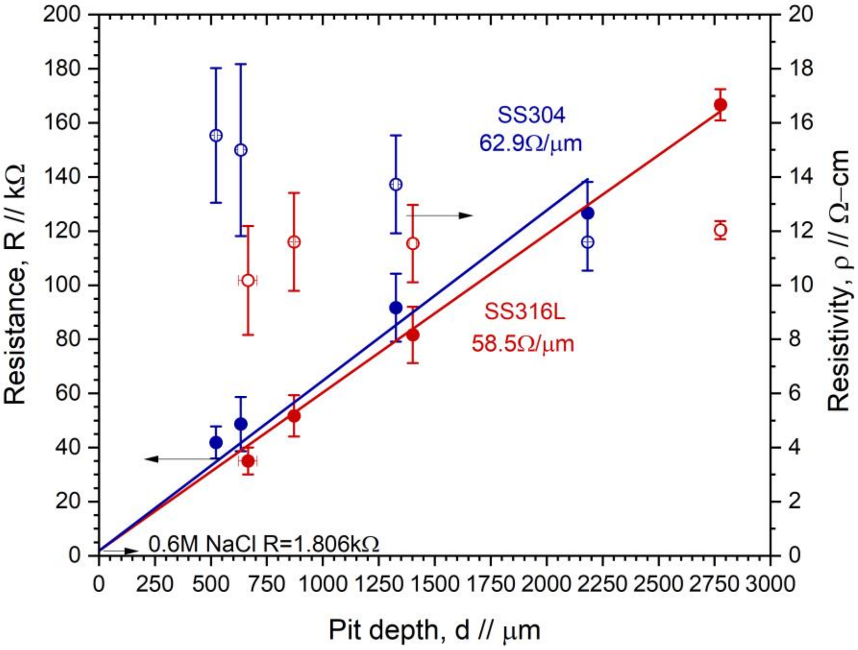

Figure A2.6. Resistance (filled symbols) and resistivity (empty symbols) as a function of pit depth for SS316L (red) and SS304 (blue) in 0.6M NaCl. All the data extracted with bulk solution resistivity of 18.35 Ω-cm 0.6M NaCl, calculated through OLI Studio MSE data

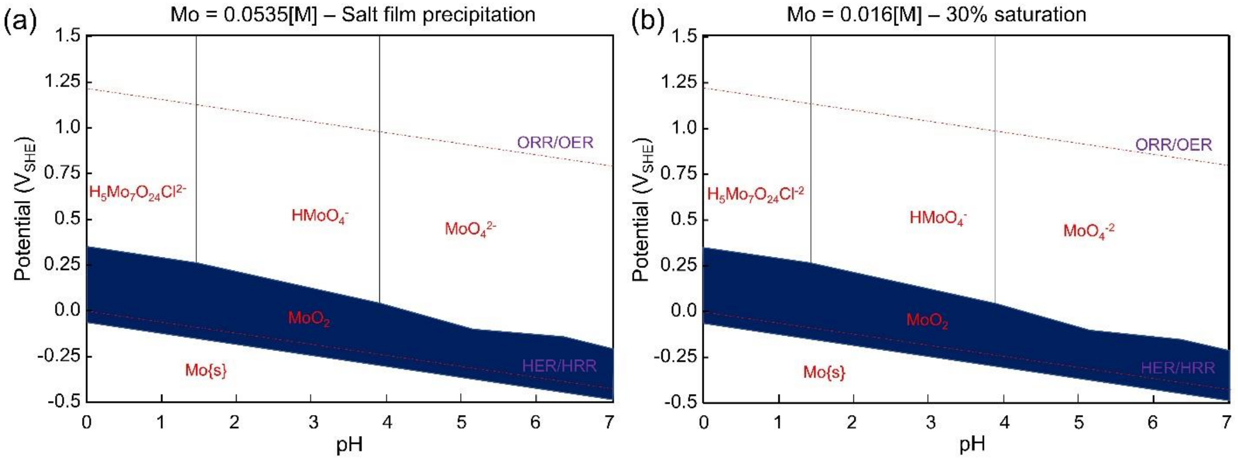

Figure A2.7. Pourbaix diagram of Mo in H_2O obtained through OLI Studio MSE database with Mo species concentration of **a)** 0.0535M, corresponding to the highest amount of Mo species at the bottom of the pit for stoichiometric dissolution of SS316 at the $FeCl_2{\cdot}4H_2O$ salt film precipitation (100% saturation), and **b)** 0.016M, corresponding to the highest amount of Mo species at the bottom of the pit for stoichiometric dissolution of SS316 at 30% saturation.

Chapter 3. Pitting and repassivation in the presence of sulfates: a controlled 1D pit approach

A. Shehi, A. Pandaleon, R. G. Kelly
*Center for Electrochemical Science and Engineering, Department of Materials Science and Engineering, University of Virginia, Charlottesville, VA 22904

Contributions: A. Shehi - Conceptualization, Data curation, Formal analysis, Investigation, Methodology, Visualization, Writing - original draft, Writing-review and editing, **A. Pandaleon** - Investigation, Methodology, Visualization, Writing - original draft, **R. G. Kelly** - Conceptualization, Funding acquisition, Data curation, Formal analysis, Project administration, Resources, Project administration, Investigation, Methodology, Visualization, Writing - original draft, Writing – review and editing

3.1. Summary

Understanding the repassivation behavior of stainless steel in aggressive environments containing inhibitors can be critical for predicting localized corrosion resistance. This study investigates the influence of sulfate-to-chloride (SO_4^{2-}/Cl^-) ratios on the repassivation of SS316L in a 0.6M NaCl solution, utilizing both experimental artificial 1D pits and thermodynamic modeling with the advanced thermodynamic database. Key kinetic and thermodynamic parameters, including E_{rp}, $(i{\cdot}x)_{crit}$, $(i_c/i_a)_{crit,f}$, and pH were analyzed to determine the effects of sulfate ions on pit stability and repassivation mechanisms. Results indicate that sulfate ions increase the pH at the pit bottom, influencing hydrolysis reactions and altering the chemical composition of the localized environment. The presence of sulfates also promotes the precipitation of stable salts, such as $FeSO_4{\cdot}7H_2O$ and $NiCl_2{\cdot}6H_2O$, which are associated with current oscillations observed during experiments under mass-transfer-controlled conditions. In activation-controlled conditions, the presence of SO_4^{2-} decreases β_a, increases the cathodic current density inside the pit, and decreases $(i_c/i_a)_{crit}$ *as compared to SS316L in 0.6M NaCl.* Furthermore, sulfate-containing solutions exhibited a higher repassivation potential and repassivation current density compared to chloride-only environments, despite a lower $(i{\cdot}x)_{sf}$.

Keywords: pitting, sulfates, localized corrosion, stainless steel, critical pit stability product, repassivation potential.

3.2. Introduction

Repassivation is a fundamental phenomenon in corrosion resistance, particularly for surfaces that have already been activated. The stability of pits, a closely related phenomenon, has also been extensively investigated. Research has demonstrated a strong correlation between critical concentrations of metal cations and critical current densities that dictate pit stability.[1–19] In a previous study, we have proposed a unified framework linking repassivation behavior to key parameters, including pH, critical pit stability product $(i{\cdot}x)_{rp}$, anodic and cathodic kinetics within the pit, ratio of cathodic to anodic current density, i_c/i_a, fraction of saturation *f*, repassivation potential E_{rp}, and electrode-electrolyte interfacial chemistry and oxide precipitation.[20] This highlights the complex interplay between thermodynamic and kinetic factors in repassivation.

Local chemistry, particularly the concentration of aggressive anions, plays a critical role in repassivation. While chloride ions have been extensively studied due to their prevalence in corrosive environments, sulfate ions-though less frequently examined are also commonly found in such settings. Sulfate sources include concrete and dust[21–24] with dust being especially relevant in the context of nuclear storage containers.[23] Sulfate ions are generally considered corrosion inhibitors, particularly for steel alloys[25–27] as they compete with chloride ions for surface coverage, thereby mitigating the latter's ability to prevent repassivation. Previous studies have explored the sulfate-to-chloride ratio[28] yet comprehensive analysis of their interaction remains limited. Most literature focuses on a narrow concentration range.[12,29] Notably, Pistorius et al. studied SS304L and found that at a sulfate-to-chloride ratio of 1:10, pitting was partially inhibited, and pit growth occurred at a lower current. [12] Additionally, sulfate ions present in mixtures of sulfate and chloride solutions can lead to a reduction in pit size. While this has been observed in 2D pitting studies, data on 1D pitting remains scarce. [12,29] Given that 1D pitting experiments are critical for isolating kinetic parameters, their inclusion is essential for a deeper understanding of pitting corrosion.

Previous research has largely focused on the role of sulfate ions in pit initiation and growth, leaving a significant gap in knowledge regarding their broader concentration range and impact on repassivation kinetics. A detailed investigation into how sulfate ions influence repassivation parameters could provide valuable insights into the kinetics of pit behavior for alloys exposed to sulfate-containing environment

This study aims to expand our understanding of sulfate's impact on pitting corrosion in stainless steel by integrating thermodynamic and kinetic perspectives. Thermodynamic models will be employed to examine key interfacial chemistry aspects, including surface film stability, ionic species behavior, and the hydrolysis reactions influencing pit propagation and repassivation. These models will be complemented by experimental measurements of pH evolution in pure chloride and mixed chloride-sulfate solutions, shedding light on the kinetic aspects of pitting. Furthermore, artificial 1D pitting experiments utilizing both potentiostatic control and rapid potentiodynamic techniques will be conducted to quantify kinetic parameters governing pit propagation and repassivation. This comprehensive approach aims to provide an in-depth analysis of the effects of sulfate ions on repassivation mechanisms, thereby enhancing our understanding of their role in corrosion processes.

3.3. Methodology

Stainless steel 316L (SS316L) was selected as the primary alloy due to its well-documented repassivation behavior at room temperature in 0.6 M NaCl.[2,11,30,31] Previous research has highlighted the effectiveness of integrating thermodynamic and kinetic parameters to characterize repassivation in specific environments.[20] Building on this foundation, the present work aims to elucidate the kinetics of pit propagation and repassivation in SS316L exposed to chloride-sulfate mixtures, while simultaneously modeling the electrode-electrolyte interface chemistry using state-of-the-art aqueous thermodynamic databases.

To achieve these objectives, we employed two complementary approaches: (1) *electrolyte modeling* to determine the stability of potential surface films, identify key ionic species, and analyze the hydrolysis of species involved in pit propagation and repassivation of SS316L in such environments; and (2) *electrochemical techniques*, including potentiostatic control and rapid potentiodynamic methods, to quantify critical kinetic parameters governing pit propagation and repassivation.

3.3.1. Electrolyte modeling

The electrolyte modeling approach incorporated both computational and experimental perspectives. Thermodynamic simulations were conducted using the OLI Studio version 12.0 with the Mixed Solvent Electrolyte (MSE) database. The aggressive environment within the pit was assumed to result from the stoichiometric dissolution of stainless steel (SS) in chloride and sulfate salts. The stoichiometric composition of SS316L used in this model is presented in Table 2.1 in Chapter 2 of this dissertation. To evaluate the influence of sulfate on pit chemistry, various molar ratios of SO_4^{2-} to Cl^-, ranging from 0 to 2, were investigated across a broad concentration range of dissolved SS ions as the sum of Fe^{2+}, Ni^{2+}, Cr^{3+} and Mo^{3+} ions (10^{-5} M to 10 M).

The corresponding chloride and sulfate salts of each one of these elements utilized as input parameters are those of $FeCl_2$, $FeSO_4$, $NiCl_2$, $NiSO_4$, $CrCl_3$, $Cr_2(SO_4)_3$, and $MoCl_3$. No $Mo_x(SO_4)_y$ salt mixture is available currently in the thermodynamic database; hence, all Mo species were approximated as $MoCl_3$. Note that MoO_2SO_4 is available in the thermodynamic software, however they were not considered in the simulations. Additionally, during the simulations, redox reactions involving Fe^{2+}, Ni^{2+}, Cr^{3+}, Mo^{3+}, Mo^{4+}, Mo^{6+}, S^{2-}, S^{4+}, and S^{6+} were kept active. Simulations were conducted at a constant temperature of 298.15 K and a pressure of 1 atm. To adjust the total salt composition, the concentration of H_2O was varied as needed. The pH of the solution was varied through the addition of LiOH. Any chemical or redox reaction between Li and other ionic species were deactivated prior to the titration process.

Experimentally, electrolytes containing $CrCl_3$ and $CrCl_3$ with additions of $Cr_2(SO_4)_3$ were prepared using commercially available reagent grade $CrCl_3 \cdot 6H_2O$ and $Cr_2(SO_4)_3 \cdot 15H_2O$ salts. The SO_4^{2-} to Cl^- molar ratio was varied from 0 to 1 in increments of 0.2. A calibrated, commercially available pH probe was used to measure the pH of the solutions at various time intervals from the moment of preparation. All pH measurements were performed at 25ºC under ambient air at 1 atm pressure. The presence of O2 dissolved in the electrolyte is not expected to affect the oxidation state of the Cr^{3+} species in the solution, at the given conditions.

3.3.2. Artificial pit experiments

Artificial one-dimensional (1D) pits from a SS316L wire with a diameter of 50.8μm (cross-sectional area $2.0268 \cdot 10^{-5}$ cm^2) were utilized to carry on the experiments. The certified compositions of SS316L utilized in this study is presented in Table 2.2 of Chapter 2 of this dissertation work.

SS316L wires were embedded in epoxy, ensuring that only the cross-section of the wire was exposed to the electrolyte. All SS316L samples were metallographically prepared to a 320-grit surface finish, followed by cleaning in deionized water and air drying. Electrolyte solutions were prepared using NaCl, Na_2SO_4, $MgCl_2$, and $MgSO_4$ with SO_4^{2-} to Cl^- molar ratios ranging from 0 to 1 in increments of 0.2. The concentrations of NaCl and $MgCl_2$ in all solutions were maintained at 0.6 M and 0.3 M, respectively. All experiments were conducted in 100 mL of solution at 25ºC, utilizing a saturated calomel electrode (SCE) as the reference electrode. A schematic of the artificial pit experimental setup is provided elsewhere and in Chapter 2 of this work.[20]

3.3.3. Potentiodynamic electrochemical parameters.

Potentiodynamic experiments were utilized to extract kinetic parameters regarding pit propagation and repassivation in electrolytes containing various mixtures of SO_4^{2-} and Cl^-. As depicted in Figure 3.1a, a series of electrochemical techniques were applied cyclically to the artificial pit in the following order: (1) a 30s open circuit potential (OCP), (2) potentiostatic polarization to -0.75V vs. SCE for 2min to attempt to remove any protective layer therefore ensuring an easy pit initiation, (3) potentiostatic polarization to +0.75 V vs. SCE to initiate the pit, (4) potentiostatic polarization to +0.55V vs. SCE to propagate the pit to the desired depth, (5) a linear sweep voltammetry (LSV) at a scan rate of 5mV/s from +0.55V vs. SCE to a desired applied potential, E_{app}, or to -0.65 V vs. SCE, (6) optional in only some occasions, a rapid voltage sweep was applied at a scan rate of 400 mV/s from E_{app} to -0.95 V vs. SCE. Note that step 6 was only performed in the cases when the cathodic kinetics were extracted. An explanation of how the cathodic kinetics were extracted is given elsewhere.[20] It is worth noting that, in many cases, a potential higher than +0.75 V vs. SCE was required to initiate pitting, particularly in shorter pits, when SO_4^{2-} was present. This indicates that pit initiation was more challenging in sulfate-containing solutions compared to those containing only Cl^-.

As mentioned in Chapter 2 and in our previous publication,[20] a very high scan rate (400mV/s) was employed in fast potentiodynamic experiments to minimize solution dilution within the pit at a given E_{app} and to reduce any effects associated with potential crevice formation in the activation-controlled region. Additionally, the results of these experiments were corrected for potential drop (IR-corrected) following the methodology previously described.[20]

3.3.4. Potentiostatic electrochemical parameters

A schematic of a typical potential-controlled cycle applied to artificial pits during potentiostatic experiments is shown in Figure 3.1b. These experiments followed the same procedure as steps 1 through 5 of the potentiodynamic case described above, with the LSV in step 5 conducted at a scan rate of 5 mV/s until reaching the desired E_{app}. Step 6 consisted of a 1h potentiostatic hold at E_{app} or until the measured current reached less than 5nA. Note that our current and previous results,[20] show that for such experiments, if the current density drops to such significantly low values, pit will remain passive at the E_{app} for the remainder of 1h.

The primary objective of the potentiostatic experiments was to identify a potential within the activation-controlled region at which a pit of a given depth remained active. By correlating these results with those from potentiodynamic experiments, key parameters such as the critical current density (i_{crit}), the repassivation potential (E_{rp}), and the fraction of saturation in the presence of SO_4^{2-} were determined. This approach enables a deeper understanding of the inhibiting effect of SO_4^{2-} on pit propagation kinetics and repassivation in the activation-controlled region, which is particularly relevant to localized corrosion studies. To facilitate comparison with chloride-only solutions, a solution with an arbitrarily selected SO_4^{2-} to Cl^- molar ratio of 0.4 was used for these experiments.

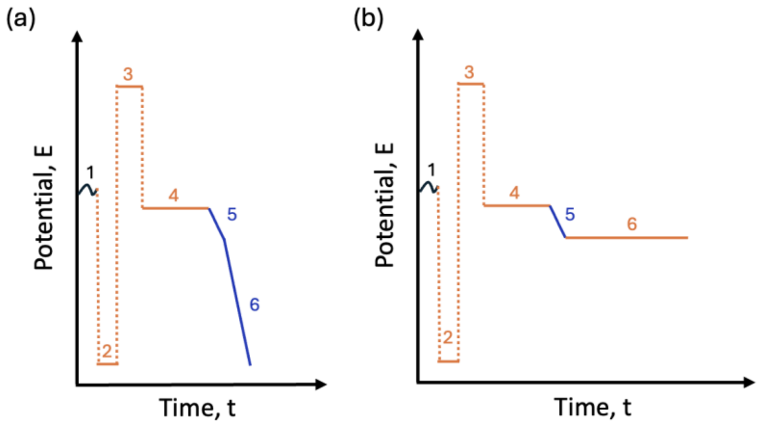

Figure 3.1. Schematic of the steps taken during electrochemical experiments for **a)** potentiodynamic and **b)** potentiostatic for SS316L in electrolytes containing various SO_4^{2-} to Cl^- molar ratio. Numbers on top of each line correspond to the number from the text provided in its corresponding experimental section.

3.4. Results

The results of this study are divided into two sections. The first focuses on solution-based modeling using a state-of-the-art thermodynamic database, while the second presents experimental findings from artificial 1D pitting experiments. These experiments provide the bases for insights into the kinetics of pit propagation and repassivation for SS316L in solutions containing mixtures of chloride and sulfate salts.

By leveraging these two aspects, we gain a detailed understanding of key solution properties and their behavior when sulfate ions are introduced into chloride-based environments. The findings from artificial 1D pit experiments then establish a connection between these solution property changes and their impact on pit propagation kinetics.

3.4.1. Solution modeling and thermodynamics predictions

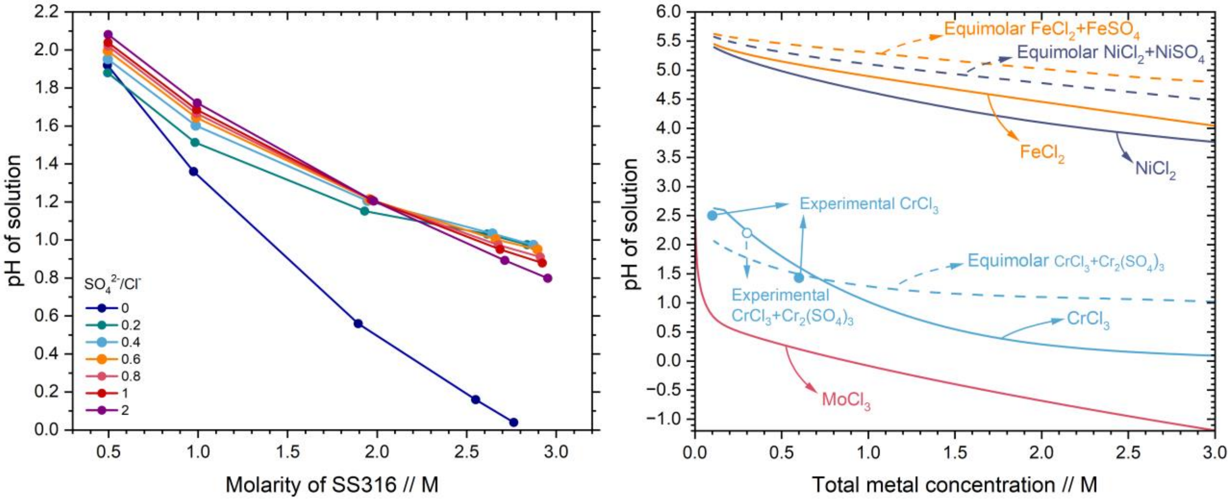

(a) **(b)**

Figure 3.2. a) Solution pH versus total concentration of SS316L in M for various SO_4^{2-}/Cl^- ratios from 0 to 2 obtained through advanced thermodynamic database and **b)** Solution pH versus the total metal concentration in M for $FeCl_2$ (solid orange), equimolar $FeCl_2$ and $FeSO_4$ mixtures (dashed orange), $NiCl_2$ (solid grey), equimolar $NiCl_2$ and $NiSO_4$ (dashed grey), $CrCl_3$ (solid blue), equimolar $CrCl_3$ and $Cr_2(SO_4)_3$ (dashed blue), $MoCl_3$ (solid pink) and experimental results after 8 days (solid filled symbols for solid lines and empty symbols for dashed lines, accordingly).

Figure 3.2a illustrates the changes in solution pH as a function of stoichiometric SS316-chloride and sulfate mixtures, as obtained from the advanced thermodynamic database. The results show that as the concentration of the salt mixture increases, the pH decreases across all SO_4^{2-}/Cl^- ratios. Additionally, for most salt mixtures relevant to pitting corrosion ranging from 30% to 100% saturation (or 1.35M to 4.5M where 4.5M is taken approximately as 100% saturation), solutions without sulfate ions exhibit lower pH values compared to those containing sulfate, with the pH difference becoming more pronounced at higher salt concentrations. The data further indicate that when sulfate is introduced, the pH decreases with lower SO_4^{2-}/Cl^- ratios for salt mixture concentrations ranging from 0.5M to approximately 2.2M. Beyond this concentration, the trend reverses.

Figure 3.2b presents the solution pH as a function of total metal concentration for chloride salts and equimolar mixtures of chloride and sulfate salts of Fe, Ni, and Cr, as obtained from both the advanced thermodynamic database and experimental data. The purpose of these experiments is to understand the effect of sulfate ions in pH arising from each one of the three major species in SS316L. The equimolar ratio between the partaking chloride and sulfate salts was chosen arbitrarily. In all cases, increasing the total metal concentration (whether in the form of chloride salts or a combination of chloride and sulfate salts) results in a decrease in pH. Among the three metals, Mo salts exhibit the lowest pH, followed by Cr, Ni, with Fe salts showing the highest pH. Notably, the pH of Cr and Mo-based salt solutions is significantly lower than that of Fe and Ni solutions, with the difference increasing to over 3-5 pH units at higher concentrations.

The results in Figure 3.2b also suggest that for Fe and Ni, replacing half of the chloride-based salts with sulfate-based salts increases the pH by approximately 0.5 to 1.5 units, with the effect becoming more pronounced at higher metal concentrations. In contrast, for Cr-based salts, a different trend is observed: at total metal concentrations up to 0.5M, a mixture of equimolar $CrCl_3$ and $Cr_2(SO_4)_3$ reduces the pH by up to 0.5 units. However, beyond this concentration, solutions containing only $CrCl_3$ exhibit pH values that are lower by approximately 1 pH unit compared to the equimolar $CrCl_3$ and $Cr_2(SO_4)_3$ mixture. Lastly, the results obtained experimentally after 3 days (empty symbols for $CrCl_3$ and $Cr_2(SO_4)_3$ and filled symbols for $CrCl_3$) are in good agreement with thermodynamically obtained data.

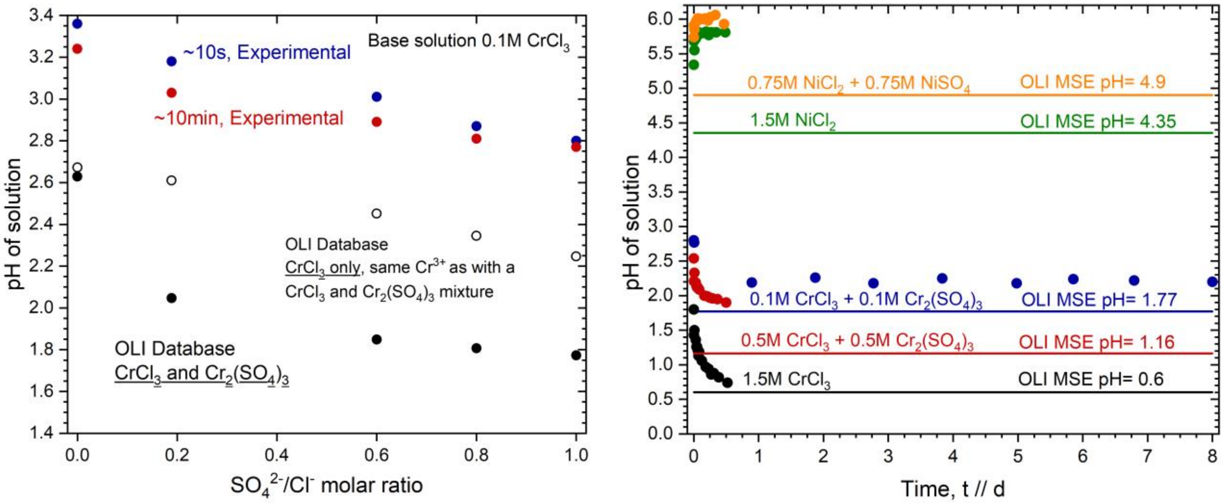

(a) **(b)**

Figure 3.3. **a)** Solution pH versus SO_4^{2-}/Cl^- ratio from for solutions containing 0.1M $CrCl_3$ with various additions of $Cr_2(SO_4)_3$ from experimental after 10s of mixture (blue), 10min after mixture (red), advanced thermodynamic database (solid black), advanced thermodynamic database replacing $Cr_2(SO_4)_3$ with $CrCl_3$ maintaining the same Cr^{3+} content as in $Cr_2(SO_4)_3$ (empty black dots) and **b)** Solution pH versus time for mixture of 1.5M $CrCl_3$ (black), 0.5M $CrCl_3$ and 0.5M $Cr_2(SO_4)$ (red), 0.1M $CrCl_3$ and 0.1M $Cr_2(SO_4)_3$ (blue), 1.5M $NiCl_2$ (green), and 0.75M $NiCl_2$ and 0.75M $NiSO_4$ (orange) obtained through experimental (symbols) and from advanced thermodynamic database (solid line).

The time dependence of solution pH for chloride and sulfate-based Cr salt mixtures is presented in Figures 3.3a and 3.3b. In both cases, the $CrCl_3$ concentration was arbitrarily set at 0.1M. Figure 4a demonstrates that as the SO_4^{2-}/Cl^-ratio increases, the pH decreases for both the experimental data and the computational results obtained from the advanced thermodynamic database. A noticeable drop in pH is observed between the measurements taken at 10 seconds and 10 minutes across different SO_4^{2-}/Cl^- ratios. Additionally, for a given SO_4^{2-}/Cl^- ratio, the pH values predicted by the advanced thermodynamic database (represented by filled black symbols) are approximately 1 pH unit lower than the experimentally measured values.

To further investigate sulfate's role in lowering pH, the total Cr content in $Cr_2(SO_4)_3$ for all SO_4^{2-}/Cl^- ratios was replaced with $CrCl_3$, as shown by the empty black symbols in Figure 3.3a. The results confirm those observed in Figure 3.2b, indicating that at low Cr concentrations, substituting $CrCl_3$ with $Cr_2(SO_4)_3$ leads to a decrease in solution pH.

Figure 3.3b illustrates the time-dependent pH behavior of a mixture containing various concentrations of sulfate and chloride ions mixtures where the cation is Cr^{3+} or Ni^{2+}. For Cr^{3+} species, the pH decreases until it stabilized to a value which is significantly higher than the predicted one from the thermodynamic database for the mixtures of sulfate and chloride salts. A better prediction from the thermodynamic database is given for the case of 1.5M $CrCl_3$. Notice the time dependence of the pH decrease. For example, in the case of experimental data for 0.1M $CrCl_3$ and 0.1M $Cr_2(SO_4)_3$ (blue), initially, the pH decreases slightly within the first 10 minutes of mixing, followed by a more pronounced drop after one day, decreasing by approximately 0.6 pH units from 2.8 to around 2.2. After this point, the pH remains relatively stable. Notably, the experimentally measured pH values are approximately 0.4 pH units higher than those calculated using the advanced thermodynamic database. In the case of Ni^{2+}salts the predictions from the thermodynamic database are significantly off as compared to the ones obtained experimentally by a difference of more than 1 pH value

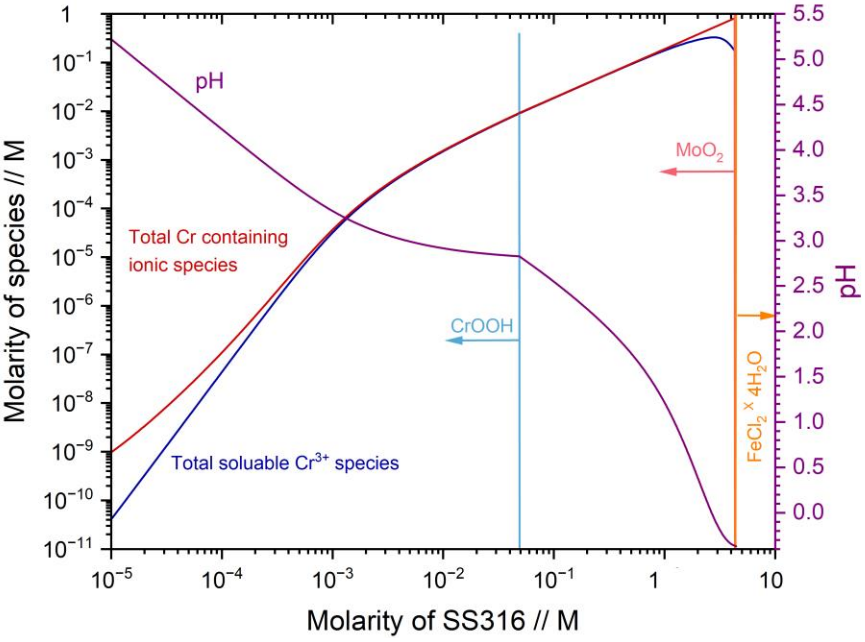

(a)

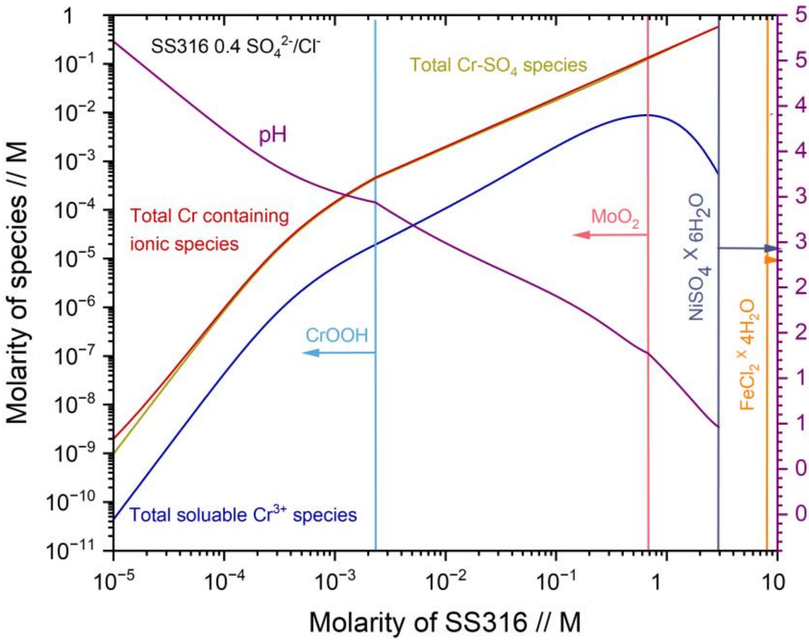

(b)

Figure 3.4. Concentration of given species and pH of the solution versus molarity of **a)** stoichiometric SS316-chloride mixtures and **b)** stoichiometric SS316-chloride and sulfate with $SO_4^{2-}/Cl^-=0.4$ utilizing the advanced thermodynamic database. Vertical lines depict the solid species precipitated at the given SS316 molarity and the arrows accompanying them depict the concentrations of SS316 for which their presence is stable.

Figures 3.4a and 3.4b present speciation diagrams for the stoichiometric dissolution of SS316 in chloride-only mixtures and SS316L in chloride-sulfate mixtures with a SO_4^{2-}/Cl^- ratio of 0.4, respectively. The left ordinate axis represents the concentration of various species, while the right ordinate axis corresponds to the pH (indicated by the violet line). Solid species precipitation is marked by vertical lines with arrows, indicating the SS316 salt mixture concentrations at which the solids remain stable. For instance, in Figure 3.4a, CrOOH is stable at SS316 salt mixture concentrations of 0.0495M and below, whereas $FeCl_2{\cdot}4H_2O$ remains stable at concentrations of 4.5M and above.

A comparison of Figures 3.4a and 3.4b reveals several key differences beyond the pH variations already noted in Figures 3.2 and 3.3: (1) the concentration of soluble ionic Cr^{3+} species (dark blue) is lower in the presence of SO_4^{2-} ions, (2) Figure 3.4b shows that when SO_4^{2-} ions are present, most Cr species exist as Cr^-sulfate complexes (*e.g.,* $CrSO_4OH_{(l)}$ or $CrSO_4^+{}_{(aq)}$), as indicated by the yellow line, (3) the precipitation of MoO_2 and CrOOH occurs at lower SS316 salt mixture concentrations when SO_4^{2-} is present, (4) the precipitation of $FeCl_2{\cdot}4H_2O$ takes place at a higher SS316 salt concentration in the presence of SO_4^{2-}, (5) additional sulfate-based salt precipitates, such as $NiSO_4{\cdot}6H_2O$ and $FeSO_4{\cdot}7H_2O$ (the latter shown in Figures A3.3-A3.6), appear in the chloride-sulfate mixture. Notably, sulfate-based salts precipitate at lower SS316 salt mixture concentrations than $FeCl_2 \cdot 4H_2O$. Additional speciation diagrams for different SO_4^{2-}/Cl^- ratios are provided in Figures A3.2 through A3.6 in the Appendix.

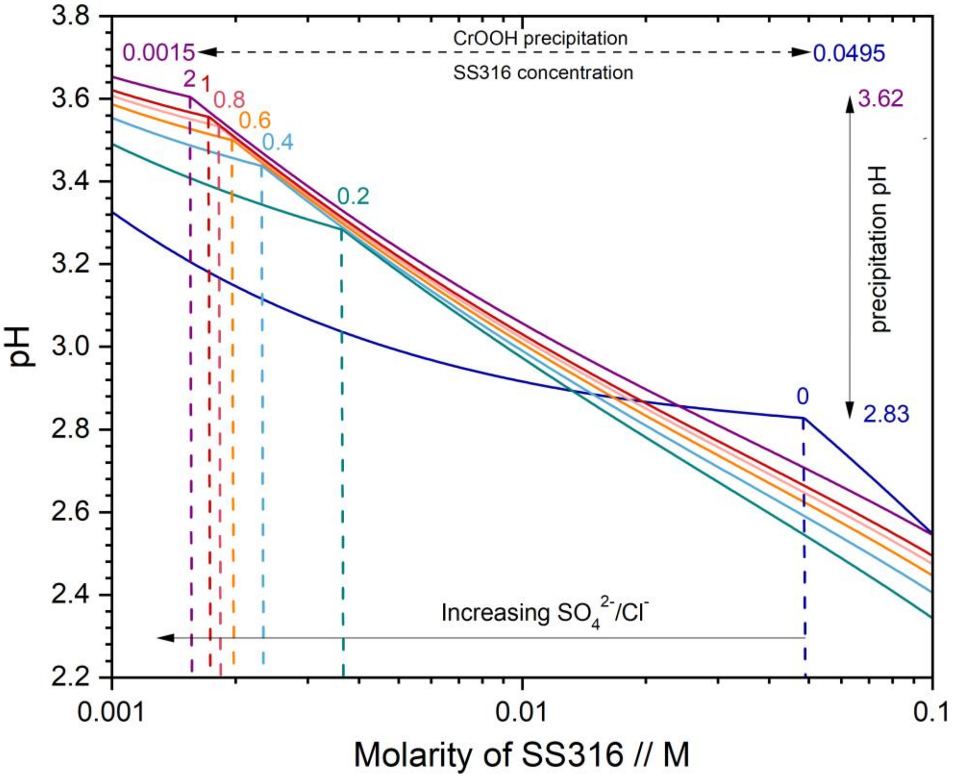

Figure 3.5. Solution pH (solid lines) and CrOOH precipitation (dashed lines) versus molarity of SS316 obtained through the advanced thermodynamic database for different SO_4^{2-}/Cl^- ratios.

Figure 3.5 illustrates the relationship between solution pH and the concentration of the SS316 salt mixture for different SO_4^{2-}/Cl^- ratios (solid lines), with CrOOH precipitation points indicated by dashed vertical lines. A significant shift in the pH vs. molarity curve occurs at the concentration of SS316 salt mixture where CrOOH precipitates for a given SO_4^{2-}/Cl^- ratio.

The results indicate that both the pH and the concentration at which CrOOH precipitates change notably with increasing sulfate content. For pure SS316-chloride salts ($SO_4^{2-}/Cl^- = 0$), CrOOH precipitates at a pH of 2.8 and an SS316 salt mixture concentration of 0.0495M. In contrast, for an SO_4^{2-}/Cl^- ratio of 2, CrOOH precipitates at a pH of 3.62 and a much lower SS316 salt concentration of 0.0015M.

Notably, when increasing the SO_4^{2-}/Cl^- ratio from 0 to 0.2, sulfate has a substantial effect, raising the pH by approximately 0.7 units and reducing the SS316 salt concentration required for CrOOH precipitation by nearly an order of magnitude. However, beyond an SO_4^{2-}/Cl^- ratio of 0.2, while further additions of sulfate continue to increase pH and lower the critical SS316 salt concentration for CrOOH precipitation, the magnitude of this effect diminishes.

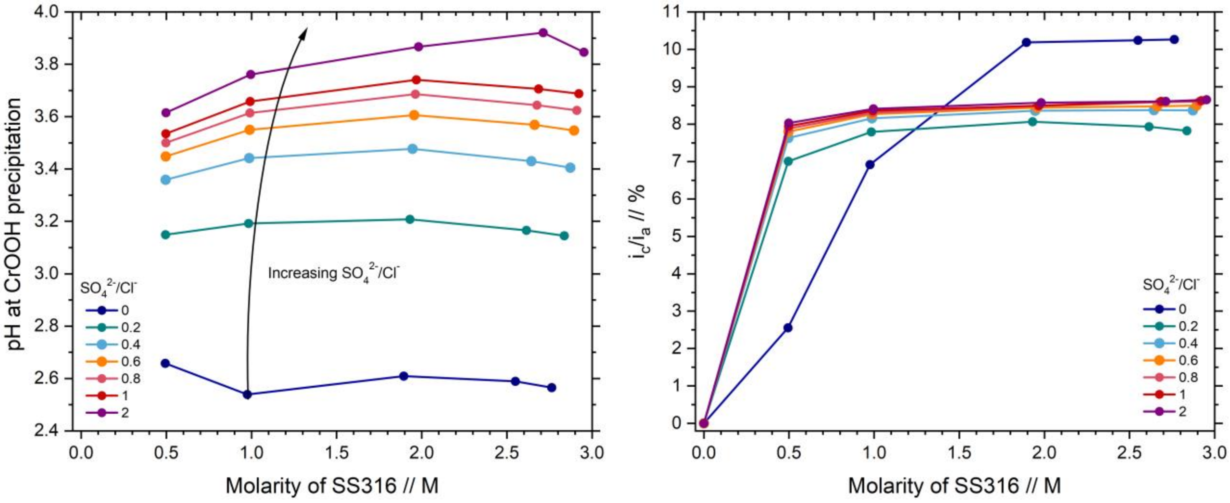

(a) **(b)**

Figure 3.6. a) Solution pH at CrOOH precipitation versus molarity of SS316 for different ratios of SO_4^{2-}/Cl^- and **b)** percent cathodic to anodic current, i_c/i_a, needed to precipitate CrOOH as a function of molarity of SS316 for different SO_4^{2-}/Cl^-. All calculations conducted through advanced thermodynamic database.

Figures 3.6a and 3.6b illustrate the pH and the i_c/i_a ratio at which CrOOH precipitates, $(i_c/i_a)_{crit}$, for different SO_4^{2-}/Cl^- ratios as a function of SS316 salt mixture concentration. These values were obtained through titration with LiOH from the normal solution pH. The purpose of this approach is to estimate the amount of cathodic current - linked to either H^+ consumption or OH^- production required for repassivation via CrOOH formation at different SS316 concentrations. This value of $(i_c/i_a)_{crit}$ in turn, can be correlated to varying degrees of saturation (or current density) at the pit bottom.

Figure 3.6a demonstrates that the pH at which CrOOH precipitates for a given SO_4^{2-}/Cl^- ratio remains independent of the SS316 salt mixture concentration. However, increasing the SO_4^{2-}/Cl^- ratio significantly raises the pH at CrOOH precipitation by approximately 1.5 units when increasing from $SO_4^{2-}/Cl^- = 0$ to 2. The most substantial pH increase (0.6 units) occurs when the SO_4^{2-}/Cl^- ratio rises from 0 to 0.2.

Figure 3.6b presents the changes in $(i_c/i_a)_{crit}$ as a function of SS316 salt mixture concentration for SO_4^{2-}/Cl^- ratios ranging from 0 to 2. The data reveal that $(i_c/i_a)_{crit}$ increases with increasing SS316 salt concentration. For chloride-only salts, this increase plateaus at approximately 2M SS316 salt concentration. In contrast, for SS316 salts containing both sulfates and chlorides, the increase levels off at approximately 0.5M. At high SS316 salt concentrations, the $(i_c/i_a)_{crit}$ ratio is greater for chloride-only SS316 salts (~10.5%) compared to SS316 salts containing both sulfates and chlorides, which range between 7.5% and 8.5%.

3.4.2. Artificial pit experimental results

Figures 3.7a and 3.7b present LSV scans from 0.55V vs. SCE to -0.65V vs. SCE. Figure 3.7a corresponds to $SO_4^{2-}/Cl^-=0.4$, while Figure 3.7b shows results for various SO_4^{2-}/Cl^- ratios ranging from 0 to 1, in increments of 0.2 conducted at a consistent pit depth of approximately 850 μm.

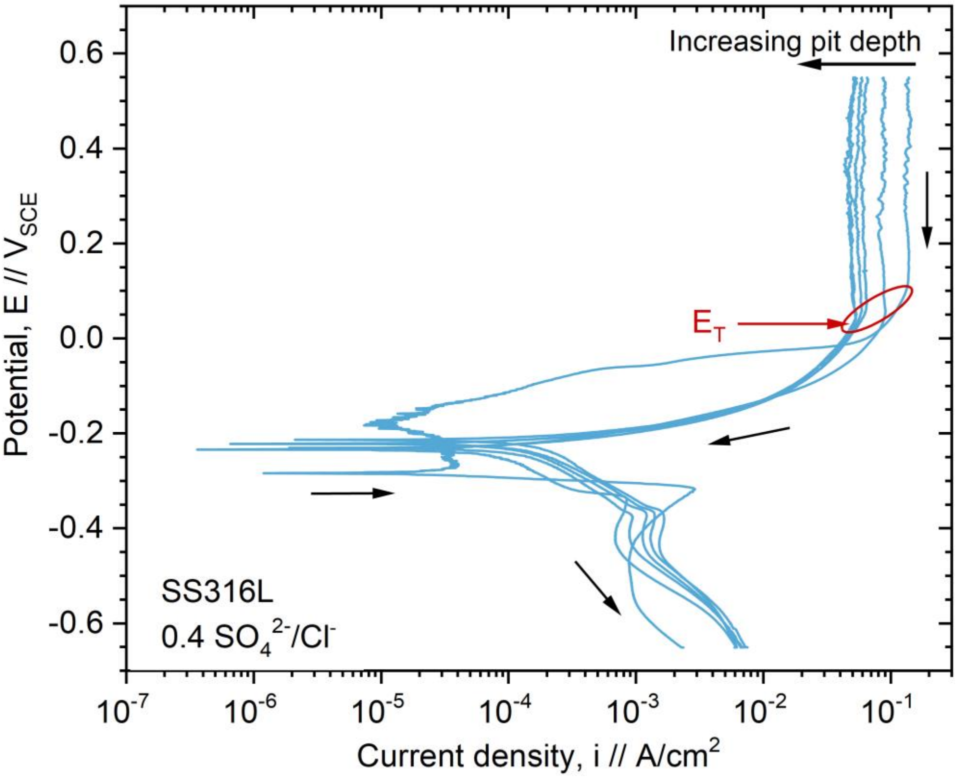

(a)

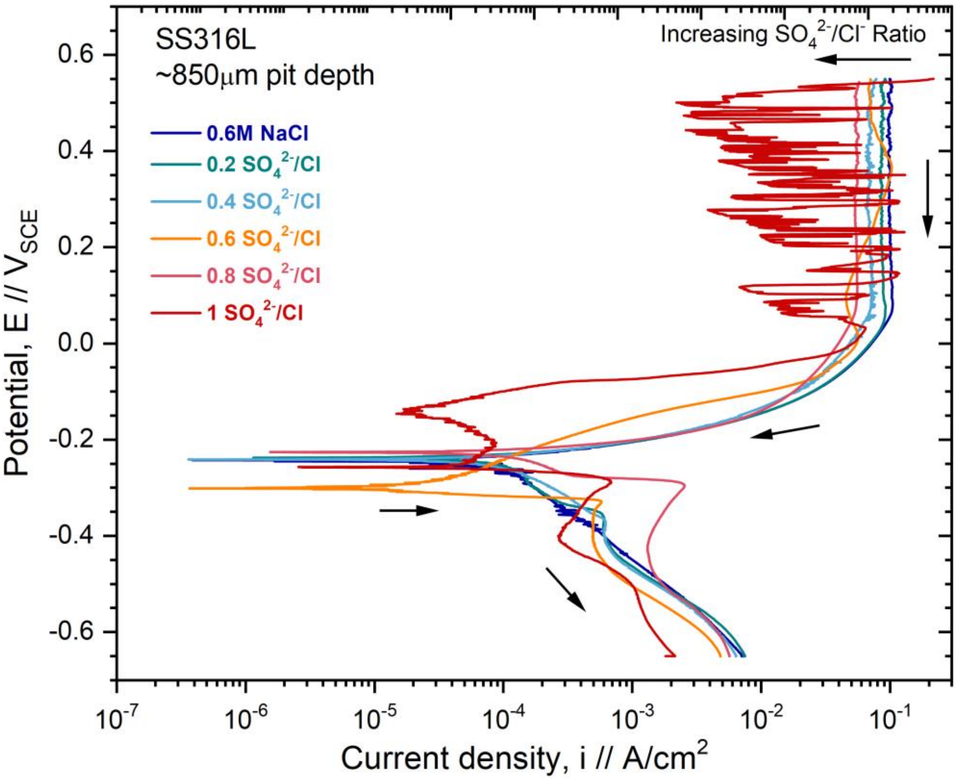

(b)

Figure 3.7. LSV scans from 0.55V vs. SCE to -0.65V vs. SCE at 5mV/s for SS316L in **a)** 0.6M NaCl and 0.24M Na_2SO_4 (SO_4^{2-}/Cl^- =0.4) and **b)** various SO_4^{2-}/Cl^- ratios with base solution being 0.6M NaCl at approximately 850μm pit depth. Arrows indicate the direction of the LSV scan.

In Figure 3.7a, the results indicate that increasing the pit depth leads to a decrease in the limiting current density. The transition potential (E_T) defined as the potential marking the shift from mass transfer-controlled to charge transfer-controlled behavior[9,14] is also shown. A general trend of decreasing E_T with increasing pit depth is observed for SO_4^{2-}/Cl^- =0.4, a trend consistent across other ratios as well.

Figure 3.7b illustrates that as the SO_4^{2-}/Cl^- ratio increases, the limiting current density decreases at a fixed pit depth. However, there is no clear effect of the SO_4^{2-}/Cl^- ratio on E_T. Notably, at very high SO_4^{2-}/Cl^- ratios of 0.8 and 1, significant oscillations in the limiting current density are observed.

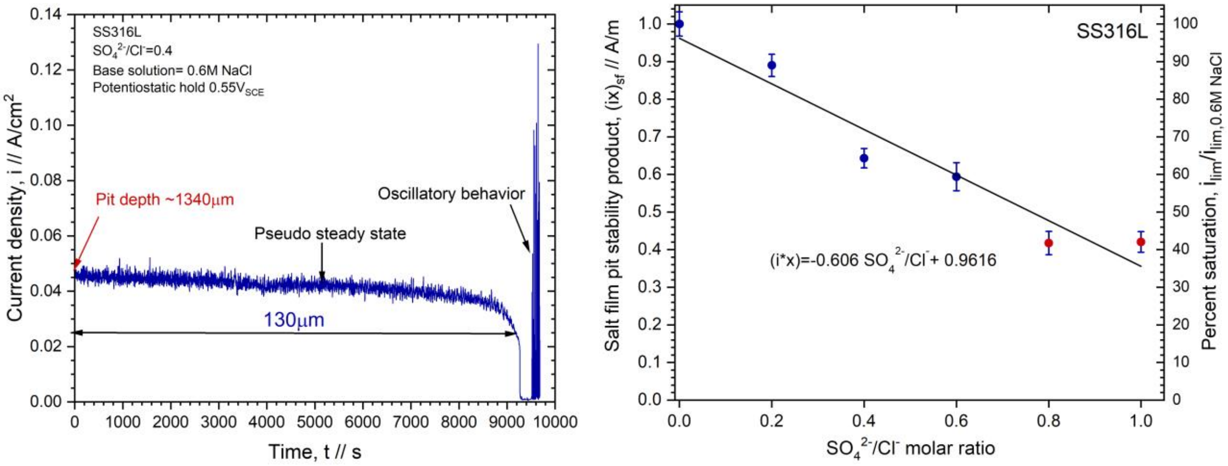

(a) **(b)**

Figure 3.8. a) Current density versus time for a potentiostatic hold of SS316L in solution of 0.6M NaCl and 0.24M Na_2SO_4 at 0.55V vs. SCE (SO_4^{2-}/Cl^- =0.4) and **b)** pit stability product under a salt film $(i\cdot x)_{sf}$ for SS316L in various SO_4^{2-}/Cl^- concentrations with 0.6M NaCl as base solution.

Figure 3.8a presents a typical result of a potentiostatic experiment conducted at 0.55V vs. SCE for an SS316L wire in a solution with SO_4^{2-}/Cl^- =0.4. At time 0s in the figure, the pit had already grown to a depth of 1,340 µm; therefore, the data shown represent only a portion of the complete experiment. The results reveal two key behaviors of SS316L in the presence of sulfate ions: (1) a pseudo-steady-state behavior from 0s to approximately 9000s, and (2) an oscillatory behavior occurring between 9000s and 9800s. It is important to note that pseudo-steady-state behavior is the commonly observed behavior for SS316L in 0.6M NaCl.

Figure 3.8b illustrates the pit stability product for a salt film under different sulfate-to-chloride ratios. The limiting current density was determined as the average current density during the mass transfer-controlled region of the LSV scan, while pit depth was calculated using Faraday's law. For SO_4^{2-}/Cl^- ratios of 0.8 and 1, the limiting current density was instead taken as the last recorded data point of the potentiostatic experiment prior to the LSV scan, as oscillations in current density during the scan were found to influence the limiting current density. To distinguish these data points, they are represented with a different color in Figure 3.8b.

The results in Figure 3.8b indicate that as pit depth increases, the pit stability product decreases. To describe the relationship between $(i\cdot x)_{sf}$ and the SO_4^{2-}/Cl^- ratio, a linear fit was applied, as shown in Equation 3.1 below:

$$(i\cdot x)_{sf}\left(\frac{A}{m}\right) = -0.606\left(\frac{A}{m}\right)\cdot\left(\frac{[SO_4^{2-}]}{[Cl^-]}\right) + 0.9616\left(\frac{A}{m}\right) \tag{3.1}$$

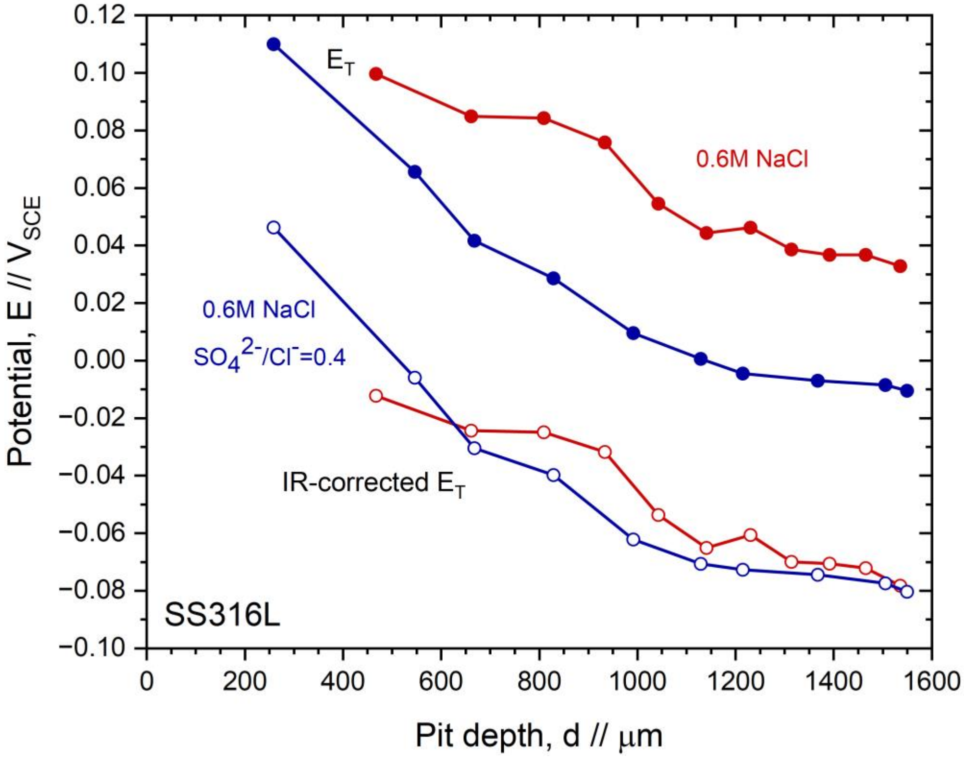

Figure 3.9. Transition potential (solid symbols) and IR-corrected transition potential (empty symbols) versus pit depth for SS316L in 0.6M NaCl (red) and 0.6M NaCl and 0.24M Na_2SO_4 (SO_4^{2-}/Cl^- =0.4) (blue).

Figure 3.9 presents the E_T extracted for SS316L in two different solutions: 0.6M NaCl (red) and a mixture of 0.24M Na_2SO_4 (SO_4^{2-}/Cl^- =0.4), blue. Additionally, an IR-corrected version of the data is shown using empty symbols. The IR correction was applied based on the previously established dependence of resistance on pit depth.[20]

The results indicate that E_T decreases with increasing pit depth. Experimentally, E_T differs by approximately 20-40mV between the two solutions. The IR drop for 0.6M NaCl is approximately 100mV, whereas for the NaCl-Na_2SO_4 mixture, it is approximately 60mV. Notably, after IR correction, the E_T values are similar between the two solutions.

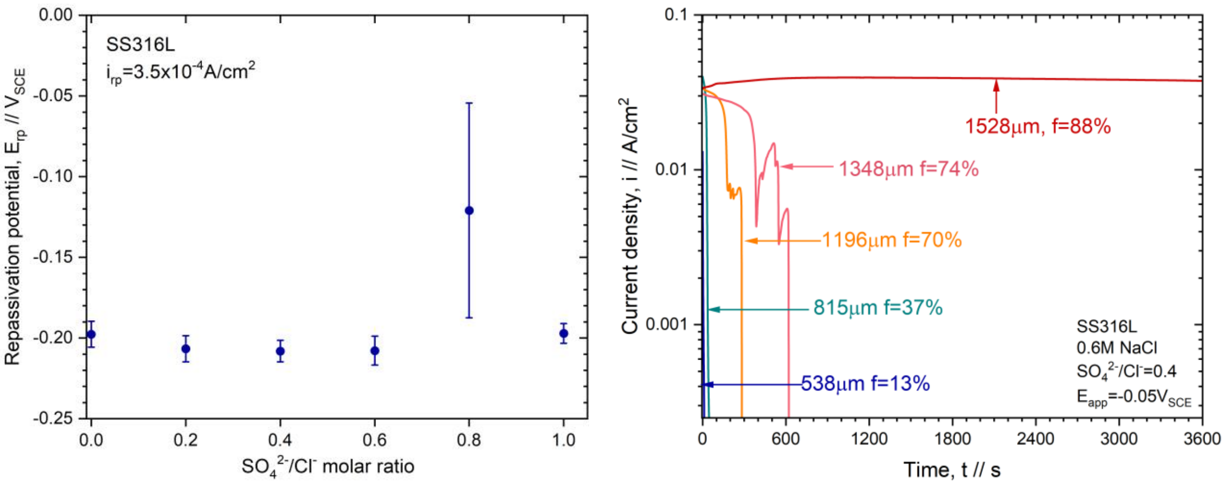

(a) **(b)**

Figure 3.10. **a)** Repassivation potential, E_{rp}, versus SO_4^{2-}/Cl^- ratio for SS316L extracted from LSV scans at a constant current density of $3.5 \cdot 10^{-4}$ A/cm^2 and **b)** current density versus time for potentiostatic experiments at -0.05V vs. SCE for SS316L in 0.6M NaCl and 0.24M Na_2SO_4 (SO_4^{2-}/Cl^- =0.4).

Figure 3.10a presents the E_{rp} extracted from the LSV scans at a repassivation current density i_{rp} of $3.5 \cdot 10^{-4}$ A/cm^2 as a function of the SO_4^{2-}/Cl^- ratio. A similar method utilizing i_{rp} values similar to $3.5 \cdot 10^{-4}$ A/cm^2 have been previously utilized.[13] With the exception of SO_4^{2-}/Cl^- =0.8, the E_{rp} values remain relatively constant at approximately -0.2V vs. SCE, independent of the SO_4^{2-}/Cl^- ratio.

Figure 3.10b illustrates the current density behavior over time for SS316L with SO_4^{2-}/Cl^- =0.4 during a potentiostatic experiment at E_{app}=-0.05V vs. SCE. The results show that for pit depths up to 1348 µm, the current density initially remains high but then drops sharply to very low values after a certain period, signifying pit repassivation. The duration for which a pit remains active increases with pit depth. At a pit depth of 1528 µm, however, the current density remains high throughout the 1h potentiostatic experiment, indicating sustained pit activity.

In this study, for a given pit depth, the applied potential can be associated with E_{rp} after IR correction. By taking the ratio of the current density from the potentiodynamic experiment at this potential and dividing it by the limiting current density corresponding to the given pit depth, the fraction of saturation was determined. At -0.05V vs. SCE, the pit with a depth of 1528 µm remained active with a fraction of saturation of 88%.

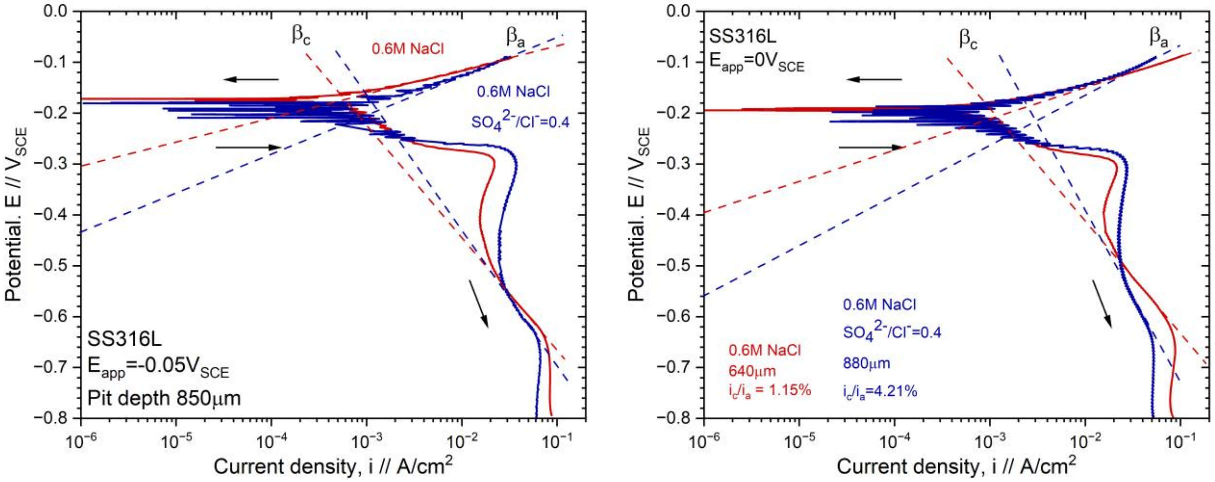

(a) **(b)**

Figure 3.11. IR-corrected LSV scans taken at a scan rate of 400mV/s for SS316L in 0.6M NaCl (red) and 0.6M NaCl and 0.24M Na_2SO_4 (SO_4^{2-}/Cl^- =0.4) at **a)** approximate same pit depth of 850μm and at the same E_{app}=-0.05V vs. SCE and **b)** at two different pit depths corresponding to the pit depth where pit transitioned from passive to active when E_{app}=0Vvs. SCE. Dashed lines represent the extracted cathodic and anodic Tafel line. Arrows indicate the direction of the scan during the LSV.

Figures 3.11a and 3.11b present the IR-corrected fast potentiodynamic scan at 400 mV/s for SS316L in 0.6M NaCl (red) and in 0.6M NaCl with 0.24M Na_2SO_4 (blue). Figure 3.11a corresponds to measurements taken at E_{app} of -0.05V vs. SCE, with a pit depth of approximately 850 μm. Figure 3.11b displays LSV scans initiated at E_{app} = 0V vs. SCE, with pit depths of 640 μm for SS316L in 0.6M NaCl and 880 μm for the sample in 0.6M NaCl with 0.24M Na_2SO_4. In the latter cases, these pit depths represent the first instance at which the pits remained active for one hour after applying a potential of 0V vs. SCE. Each graph also includes the cathodic and anodic Tafel lines (dashed lines). Because the curves are IR-corrected, the starting potential of the scans is lower than the E_{app}.

The results in Figure 3.11a indicate that for the same initial potential and pit depth, the recorded current densities of SS316L are comparable between the two solutions, with slightly lower values in the presence of sulfates. However, the anodic Tafel slope (β_a) is notably higher for SS316L exposed to a solution with SO_4^{2-}/Cl^- =0.4. Conversely, the cathodic current density in the Tafel region is slightly higher in 0.6M NaCl compared to the NaCl-Na_2SO_4 mixture, while the cathodic Tafel slope (β_c) is greater in the latter case. A more pronounced difference in these parameters between the two solutions is also observed in Figure A3.9 (Appendix) for E_{app} =-0.1V vs. SCE and a pit depth of approximately 1400 μm. These trends persist for the case of E_{app} =0V vs. SCE and the critical repassivation pit depth for SS316L in the respective electrolytes.

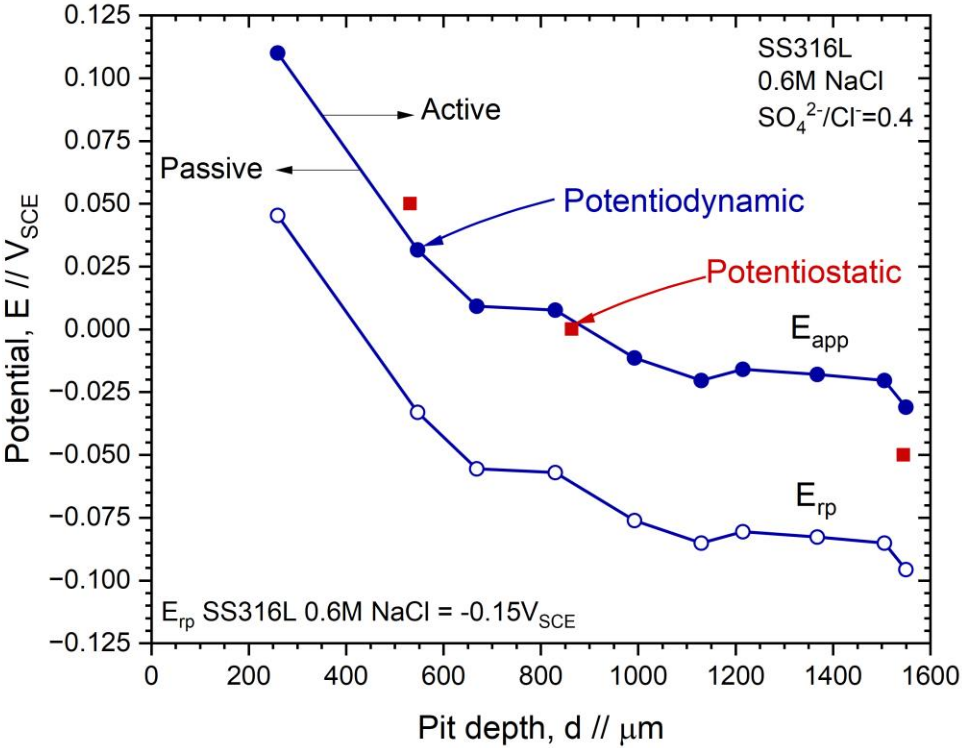

Figure 3.12. E_{app} versus pit depth (solid blue symbols), E_{rp} versus pit depth (empty blue symbols) obtained from potentiodynamic experiments, and E_{app} versus pit depth (red square symbols) obtained from potentiostatic holds.

Figure 3.12 presents the E_{app} and E_{rp} as functions of pit depth, obtained from potentiodynamic (blue) and potentiostatic (red square) experiments. For a given potential, pits remained passive at depths to the left of the curve and active at depths to the right. The E_{app} data were derived from potentiodynamic experiments by applying a *f* of 88%, based on the potentiostatic data in Figure 3.10b. The E_{rp} values were obtained by IR-correcting the corresponding E_{app} values.

Figure 3.12 shows that both E_{app} and E_{rp} decrease as pit depth increases, until reaching a plateau at depths greater than 1000 µm. The plateau values are approximately -0.025V vs. SCE for E_{app} and -0.075V vs. SCE for E_{rp} . The potentiostatic experiment results align well with the data extracted from the potentiodynamic experiments. Overall, the E_{rp} values for SS316L in 0.6M NaCl with 0.24M Na_2SO_4 (E_{rp} =-0.075V vs. SCE) are higher by approximately 0.75 mV compared to those in 0.6M NaCl (E_{rp}=-0.15V vs. SCE).[20]

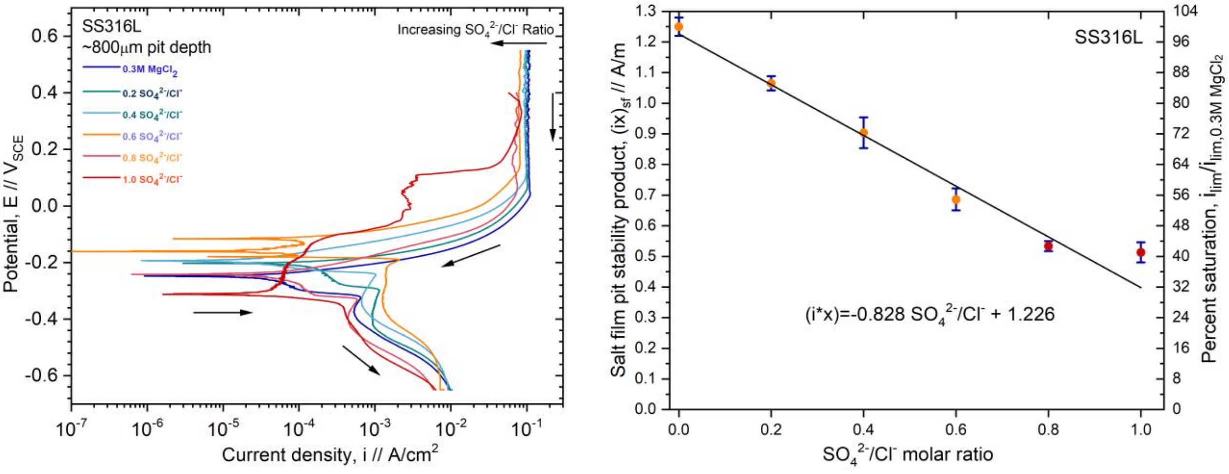

(a) **(b)**

Figure 3.13. a) LSV scans at 5mV/s for SS316L in **a)** 0.3M $MgCl_2$ and various $MgSO_4$ to achieve SO_4^{2-}/Cl^- ratios from 0 to 1 at approximately 800μm pit depth and **b)** pit stability product under a salt film $(i{\cdot}x)_{sf}$ for SS316L in various SO_4^{2-}/Cl^- concentrations with 0.3M $MgCl_2$ as base solution.

Figures 3.13a and 3.13b present the results of LSV scans and the pit stability factor $(i{\cdot}x)_{sf}$ for varying SO_4^{2-}/Cl^- ratios, ranging from 0 to 1 in increments of 0.2, with 0.3M $MgCl_2$ as the base electrolyte salt. These experiments aim to investigate the effect of cation exchange (substituting Na^+ with Mg^{2+}) while maintaining constant Cl^- and SO_4^{2-} concentrations and ratios.

The results in Figure 3.13a indicate that for a fixed pit depth of approximately 800 μm, increasing the SO_4^{2-}/Cl^- ratio leads to a reduction in limiting current density. For SO_4^{2-}/Cl^- ratios of 0.8 and 1, the scan rate was initiated at approximately 0.4V vs. SCE instead of 0.55V vs. SCE due to challenges in maintaining a pseudo-steady-state condition at higher potentials. However, this adjustment does not affect the validity of the results. Notably, the LSV scans for SO_4^{2-}/Cl^- ratios of 0.8 and 1 exhibit oscillations in current density, even as the potential decreases. In the activation-controlled region, an increase in the SO_4^{2-}/Cl^- ratio shifts the curve to the left, resulting in lower recorded current densities. Additionally, a significant reduction in E_T is observed for SO_4^{2-}/Cl^- ratios of 0.8 and 1.

Figure 3.13b illustrates the trend in $(i{\cdot}x)_{sf}$ showing that as the SO_4^{2-}/Cl^- ratio increases, the pit stability product decreases. As previously noted in Figure 3.8b, the final data points for SO_4^{2-}/Cl^- =0.8 and 1 were obtained during potentiostatic experiments at 0.4V vs. SCE due to oscillations in current density within the mass-transfer-controlled region of the LSV scans. To quantify the relationship between $(i{\cdot}x)_{sf}$ and the SO_4^{2-}/Cl^- ratio, a linear fit was applied, as described by Equation 3.2 below:

$$(i \cdot x)_{sf}\left(\frac{A}{m}\right) = -0.828\left(\frac{A}{m}\right)\cdot\left(\frac{[SO_4^{2-}]}{[Cl^-]}\right) + 1.226\left(\frac{A}{m}\right) \tag{3.2}$$

3.5. Discussion

The primary objective of this study was to investigate the role of sulfate ions in the repassivation of SS316L by integrating thermodynamic and kinetic analyses. Thermodynamic modeling, utilizing current thermodynamic databases in conjunction with experimental data, provides insight into the key ionic, liquid, and solid components expected in the electrolyte near the electrolyte-electrode interface, as well as other critical properties such as pH, during the repassivation process. These properties, combined with interfacial corrosion kinetics studied through a controlled 1D artificial pit system, enable a deeper understanding of the repassivation process when both sulfate and chloride ions are present at the pit bottom.

This study aims to address the following key questions:

1. How do the thermodynamic properties of SS316L in chloride$^-$containing solutions compare to those in chloride-sulfate mixtures?
2. In what ways does sulfate influence the kinetics of pit propagation and repassivation?
3. Can a fundamental explanation be provided for the commonly observed inhibitory effect of sulfate on pit propagation and its impact on repassivation?

3.5.1. Electrolyte modeling at the pit bottom in the presence of sulfate ions

Acidification at the bottom of a pit is a key result of metal hydrolysis, which not only enhances anodic kinetics (and thus pit propagation) but also increases the local concentration of electronegatively charged species, including Cl^- and SO_4^{2-}. Although their ratio at the pit bottom may differ from that in the bulk solution, their concentration near the electrode-electrolyte interface is governed by thermodynamic limits, particularly the precipitation of solid corrosion products. Regardless, the presence of these anions significantly influences pit propagation and the so-called “self-sustaining” pits.

One of the primary reactions occurring at the electrode-electrolyte interface is the hydrolysis of the metal cations. The affinity of a given metal cation for chloride or sulfate ions affects the extent of hydrolysis, thereby influencing solution pH. This effect is particularly evident in Figures 3.2a and 3.2b, which highlight the need to determine which metal cation is primarily responsible for the observed increase in pH upon sulfate addition (Figure 3.2a).

3.5.2. Key metal cations affecting pH in the pit environment

Before addressing the role of sulfate, it is necessary to first consider which cations produced from stainless steel dissolution contribute to the decrease in pH by hydrolysis. In solutions with a fraction of saturation between 30% and 100% (where 100% corresponds to approximately 4.5 M SS316 ions), the typical concentration ranges for key metal cations are: Fe^{2+}: 0.918 M -3.059 M, Ni^{2+}: 0.160 M-0.533 M, Cr^{3+}: 0.256 M-0.853 M, Mo^{3+}: 0.016 M-0.054 M

As shown in Figure 3.2b, the thermodynamically predicted solution pH remains between 4 and 5.5 for solutions containing only Fe^{2+} or Ni^{2+} at all concentrations. This result suggests that the significant pH drop observed at the pit bottom (below 2.5) is primarily driven by the hydrolysis of Cr^{3+} and Mo^{3+}. The influence of Cr^{3+}, and consequently Mo, is further demonstrated in Figure A3.1, in which it is shown that increasing the Cr content (while adjusting Ni and Fe content) leads to significant pH reductions. It is evident that Cr^{3+} hydrolysis plays a crucial role in achieving low pH levels.

However, in solutions containing only Fe, Ni, and Mo, the low pH observed (as seen in Figure 3.2b) cannot be attributed to Fe or Ni hydrolysis. Instead, it must be associated with Mo. If the thermodynamic database is accurate, this result underscores the importance of including Mo hydrolysis reactions when predicting electrolyte properties such as pH. Additionally, Mo hydrolysis should be incorporated into finite element method (FEM) simulations where interfacial solution chemistry is considered, depending on the application. However, existing studies on Mo hydrolysis in dilute solutions are limited, and even fewer focus on concentrated, complex solutions such as those found at the pit bottom.[32–34]

3.5.3. Role of Mo and Cr in solution chemistry and repassivation

The role of Mo in influencing solution chemistry is particularly relevant within the potential range studied here, from approximately -0.25 V vs. SCE to 0.75 V vs. SCE (and slightly above -0.25 V vs. SCE for engineering applications). In this range, Mo exists primarily as Mo^{4+} (MoO_2) or Mo^{6+} ionic compounds.[20] The first oxide species to precipitate upon pit dilution is MoO_2, as clearly observed in Figures 3.4a, 3.4b, and A3.2-A3.6.

Despite Mo's influence on solution chemistry, it is not the primary passivating element in SS316L- this role falls to Cr.[20,35] As demonstrated in this study and prior research,[13,20,36,37] CrOOH is the first Cr-based oxide (or oxyhydroxide) to precipitate upon dilution. Consequently, repassivation is thermodynamically associated with CrOOH formation. Unlike pit initiation, for which Figures 3.4a, 3.4b, and A3.2-A3.6 are analyzed from left to right, repassivation is interpreted in the opposite direction (right to left), reflecting the dilution process, increasing pH, and subsequent CrOOH precipitation.

The general reaction for CrOOH precipitation is given as:

$$CrOOH_{(s)} + (3-n)H^{+}_{(aq)} \leftrightarrow Cr(OH)^{(3-n)+}_{n,(aq)} + (2-n)H_2O_{(l)} \tag{3.3}$$

where n can range from 0 to 6. Several pathways for this reaction have been proposed depending on environmental conditions.[32,33,38–40] Among the key factors influencing CrOOH precipitation are pH and the concentration of Cr^{3+}, whether in its fully soluble form or as a hydroxide species.

3.5.4. Impact of sulfate on CrOOH

In the presence of sulfate, CrOOH formation is significantly altered. As shown in Figure 3.4b (where the SO_4^{2-}/Cl^- ratio is 0.4), most Cr species exist as Cr-SO_4 complexes. This is evident from the similarity between the yellow and red lines, indicating that the majority of Cr species are bound to sulfate. Applying this concept to Equation 3.3, the reduced concentration of free Cr^{3+} means that a higher pH is required for CrOOH precipitation.

This finding aligns with experimental observations by Vinokurov[40] whose studies on $Cr_2(SO_4)_3$ dissolution closely match the pH conditions required for CrOOH formation. Although the presence of sulfate increases the overall solution pH (as seen in Figures 3.2a and 3.2b), this effect alone is insufficient for CrOOH precipitation. Additional factors-such as decreasing the total SS316 salt molarity or further increasing pH-are necessary to facilitate repassivation.

3.5.5. Implications for activation-controlled kinetics and E_{rp}

The findings discussed above suggest that for an active pit in SS316L to repassivate, one or more of the following conditions must be met:

- The dissolution rate (current density) of SS316L must decrease, allowing the pH to increase by dilution.
- The cathodic kinetics inside the pit must accelerate sufficiently to raise the pH, even if the SS316L dissolution rate remains high.
- A combination of both mechanisms.

If the first condition were the dominant mechanism, it would imply that the E_{rp} for SS316L in sulfate-chloride mixtures is lower than in pure NaCl solutions, assuming identical Tafel kinetics.

3.5.6. Effect of sulfate on SS316L Tafel kinetics

Our results indicate that sulfate decreases the dissolution rate of SS316L by altering Tafel kinetics. This effect is evident from current density measurements at equivalent pit depths during pit propagation (Figures 3.7b, 3.8b, 3.11b, 3.13a, 3.13b, and A3.9) and from the peak current density measured at pit initiation for $SO_4^{2-}/Cl^- = 0.4$ (see Table A3.1 in the Appendix). These findings strongly support the hypothesis that SS316L dissolution rates are lower in sulfate-chloride mixtures than in pure chloride solutions.

The lowering of the dissolution rate can be attributed to the inhibitory effect of SO_4^{2-} on the pit surface. [12,29] This inhibition could occur through: (1) surface coverage which would lead to Tafel slopes of LSV curves that would remain unchanged but appear shifted relative to each other, and (2) modification of interfacial Tafel kinetics which would manifest as changes in Tafel slopes and/or exchange current densities.

Figures 3.7b, 3.11a, 3.11b, and A3.9 demonstrate that the anodic activation-controlled region of LSV curves varies with SO_4^{2-}/Cl^- ratio. In particular, Figures 3.11a, 3.11b, and A3.9 show pronounced differences during the fast potentiodynamic scan which captures both anodic kinetics at high potentials and cathodic kinetics at lower potentials. Notably, in 0.6 M NaCl with 0.24 M Na_2SO_4, the anodic Tafel slope at a scan rate of 0.4V/s is higher compared to pure 0.6 M NaCl solutions.

3.5.7. Critical conditions for pit stability in the presence of sulfate

Potentiostatic experiments (Figure 3.10b) suggest that the f required for an SS316L pit to remain active is approximately 88% for $SO_4^{2-}/Cl^- = 0.4$. Given an approximate saturation current density $(i{\cdot}x)_{sf}$ of 0.625 A/m, the critical current density $(i{\cdot}x)_{crit}$ is 0.55 A/m, which is significantly higher than the 0.32 A/m measured for SS316L in 0.6 M NaCl. [20]

These findings indicate that the critical conditions for pit stability in the presence of sulfate are 1.7 times higher than those in pure chloride solutions. Because the Tafel kinetics slow in sulfate-chloride mixtures and the critical current density required for pit stability is higher, it follows that E_{rp} must also be higher in the sulfate-containing solution. This expectation is confirmed in Figure 3.12, in which E_{rp} for SS316L in $SO_4^{2-}/Cl^- = 0.4$ is approximately 50 mV higher (-0.10 V vs. SCE) compared to SS316L in 0.6 M NaCl (-0.15 V vs. SCE).[20]

3.5.8. Fraction of saturation and $(i_c/i_a)_{crit}$

At first glance, the critical conditions required for repassivation appear contradictory when comparing thermodynamic predictions and experimental results. On one hand, our findings indicate that an $f<1.0$ is necessary for repassivation in sulfate-containing solutions (or even in pure chloride solutions).[20] On the other hand, thermodynamic modeling suggests that low SS316-chloride-sulfateconcentrations are required for CrOOH precipitation.

This apparent contradiction can be resolved by considering the role of cathodic kinetics: repassivation can occur at high i_{rp} values (high f) as long as the cathodic current for H^+ is sufficiently high. Thus, our results highlight the critical importance of the $(i_c/i_a)_{crit}$. As shown in Figures 3.6a and 3.6b, thermodynamic modeling suggests that the pH required for CrOOH precipitation remains relatively stable across different SS316 concentrations. However, the $(i_c/i_a)_{crit}$ initially increases and then stabilizes between 7.5 and 8.5% for all sulfate-chloride mixtures, slightly lower than in pure chloride solutions. Although a detailed discussion of the thermodynamic database parameters is beyond the scope of this study, it is important to compare the $(i_c/i_a)_{crit}$ obtained from thermodynamic modeling with experimental values for $SO_4^{2-}/Cl^- = 0.4$. The advanced thermodynamic database predicts $(i_c/i_a)_{crit} \approx 7.5\%$ whereas experimental results suggest $(i_c/i_a)_{crit} \approx 4.2\%$. This discrepancy is largely attributed to time-dependent pH evolution in SS316 salt mixtures, a key topic discussed below.

3.5.9. Time dependence

Figures 3.3a and 3.3b underscore the critical role of kinetics versus thermodynamics in determining solution conditions at the dissolving pit surface. In the absence of a salt film, the solution remains transient, meaning individual dissolved metal cations do not persist near the surface for extended periods. Our results indicate that equilibrium pH values predicted by thermodynamic database are often significantly lower than those obtained experimentally and even lower than the initial pH of the electrolyte during salt dissolution. This discrepancy may contribute to the conservative $(i_{c}/i_{a})_{crit}$ values predicted by thermodynamic database.

It is therefore possible that the actual pH at the pit bottom is considerably higher than calculated values, such as those presented in this study. Additionally, the presented experimental findings demonstrate that chloride mixtures containing Cr^{3+} yield significantly lower pH values than those containing both chloride and sulfate. However, both types of solutions appear to reach their equilibrium pH at similar rates, suggesting that the same time-dependent rationale applies to both cases.

3.5.10. Mass transfer-controlled kinetics

It is essential to distinguish between activation-controlled and mass transfer-controlled processes. In the latter, the alloy's dissolution rate (and consequently its current density) depends on both the chemical composition and the transport properties of the salt film on the surface.

As shown in Figure 3.4a, in 0.6M NaCl, $FeCl_2{\cdot}4H_2O$ is the dominant precipitate. This salt film supports high current densities in the mass transfer-controlled regime due to its porous, hydrated nature and relatively high solubility, which maintains a steady dissolution rate and low pH. Thus, pseudo-steady-state conditions are established.

In sulfate-containing environments, additional salt films such as $FeSO_4{\cdot}7H_2O$ and $NiSO_4{\cdot}6H_2O$ form (Figure 3.4b, A3.2-A3.6). These salts exhibit lower solubility than $FeCl_2{\cdot}4H_2O$, with solubility varying based on the SO_4^{2-}/Cl^- ratio. Interestingly, $FeCl_2{\cdot}4H_2O$ solubility increases significantly with higher sulfate concentrations, exceeding 10M in SS316. These solubility trends explain variations in $(i{\cdot}x)_{sf}$ and the current density oscillations observed at high SO_4^{2-}/Cl^- ratios in potentiostatic and LSV measurements.

Figure A3.8 highlights that $FeSO_4{\cdot}7H_2O$ precipitation disrupts pseudo-steady-state behavior. Due to its low solubility, $FeSO_4{\cdot}7H_2O$ forms a surface layer that hinders alloy dissolution, reducing current density at a fixed anodic potential due to an increased IR drop. The ability of the salt film to reestablish its transport properties by equilibrating with the electrolyte is crucial for maintaining dissolution rates. However, $FeSO_4{\cdot}7H_2O$ equilibrates slowly, leading to current density oscillations associated with alternating activation and passivation of the alloy surface. This phenomenon, typical for Fe in H_2SO_4 is also observed in Figure 9a for SO_4^{2-}/Cl^-.

Initially, $FeCl_2·4H_2O$ may dominate the salt film at high potentials during the pit initiation portion of the 1D pit studies, establishing pseudo-steady-state conditions. However, over time, $FeSO_4·7H_2O$ gradually replaces $FeCl_2·4H_2O$, causing a progressive decline in current density. Once the film consists primarily of $FeSO_4·7H_2O$, current density oscillations emerge due to cycles of surface activation and passivation, particularly at high SO_4^{2-}/Cl^- ratios of 0.8 and 1.

These oscillations are critical for alloys like SS316L, which repassivate quickly. If the dissolution current density drops significantly, shallow pits are more likely to repassivate. From an engineering perspective, $FeSO_4·7H_2O$ precipitation could create conditions conducive to CrOOH formation and repassivation, as seen in Figure 9a. $NiSO_4·6H_2O$ may also contribute to this process, though its role remains less understood.

A key question arises: why does $FeCl_2·4H_2O$ precipitate initially if $FeSO_4·7H_2O$ has lower solubility? Salt film formation requires a degree of supersaturation, which likely differs between $FeCl_2·4H_2O$ and $FeSO_4·7H_2O$. During pit initiation at high anodic potentials, dissolution rates can be 5-10 times higher than those in steady-state conditions, allowing both $FeCl_2·4H_2O$ and $FeSO_4·7H_2O$ to precipitate. Further research is needed to clarify these precipitation dynamics.

3.5.11. Effect of the cation

The final part of this study examines the influence of cations on pit growth kinetics, as shown in Figures 3.13a and 3.13b. Striking similarities are observed between cases where the cation is Na^+ or Mg^{2+}. However, at low SO_4^{2-}/Cl^- ratios (up to 0.4), $(i·x)_{sf}$ is higher for Mg-based salts than for Na-based ones. At higher SO_4^{2-}/Cl^- ratios, the differences become negligible. A similar trend (where $MgCl_2$ salts exhibit higher $(i·x)_{sf}$ than NaCl salts at equivalent Cl^- concentrations) has been previously reported.[41] These differences are attributed to cation-dependent changes in solution properties, such as viscosity and diffusion coefficients. However, at high SO_4^{2-}/Cl^-ratios, the current dataset does not allow for a clear distinction due to oscillatory behavior (Figures 3.13a and A3.7).

3.5.12. Limitations

Two key limitations of this study should be considered. The first concerns the pH measurements throughout the experiments. Because the base salts used are chloride-based, the transition from $CrCl_3$ to Cr^{3+} is not necessarily equivalent to the reverse process (Cr^{3+} to $CrCl_3$). This discrepancy implies that the initial pH during $CrCl_3$ dissolution may differ from the pH at the bottom of a pit, where Cr^{3+} dissolves. This complexity is further compounded by potential chlorination of Cr^{3+} species. However, research on Cr^{3+} hydrolysis in the presence of halides, including Cl^-, suggests that Cr^{3+} has a significantly higher affinity for H_2O than for Cl^-.[42] Therefore, $CrCl_3$ salts are often used in experiments to determine the kinetics and equilibrium constants of Cr^{3+} in water, as commonly reported in the literature.

The second limitation pertains to fast potentiodynamic experiments. Previous studies[20] have established that capacitive currents from the high scan rate (0.4 V/s) can be neglected, as the current densities of interest far exceed those associated with double-layer capacitance. For example, for a very conservatively large interfacial capacitance of 100 $\mu F/cm^2$, the capacitive current density would be 40 $\mu A/cm^2$. In Figures 3.7a, 3.7b, 3.8a, 3.11a, 3.11b, and 3.13a the current densities of interest are two or more orders of magnitude higher.

A further concern regarding fast potentiodynamic experiments is the high reduction current density observed during the downward scan, at potentials immediately below the OCP. This phenomenon is often attributed to Cu deposition. However, if Cu deposition were the cause, a previous comparison between SS304 (which lacks detectable Cu) and SS316L from the same manufacturer (California Fine Wire) should have revealed a significant difference. Instead, the observed current density spike was larger for SS304 than for SS316L under identical pit depth and electrochemical conditions.[20]

An alternative argument for Cu deposition relies on the presence of Cu ions near the electrode surface at relevant potentials. However, dilution effects (assumed for the primary SS316L components, such as Fe) should logically extend to minor species like Cu, which constitutes only 0.444 wt.% of the alloy. Consequently, the authors find it challenging to attribute the large reduction current spike solely to Cu deposition.

3.6. Conclusions

In this study, the repassivation behavior of SS316L in various SO_4^{2-}/Cl^- ratios within a 0.6M NaCl base solution was investigated using both kinetic and thermodynamic parameters, including E_{rp}, $(i\cdot x)_{crit}$, f, $(i_c/i_a)_{crit}$, and pH. A combination of artificial 1D experiments and simulations using the advanced thermodynamic database provided insight into the role of SO_4^{2-} ions in pit propagation kinetics and the critical conditions necessary for repassivation. The key findings are as follows:

1. Experimental and thermodynamic simulation results indicate that SO_4^{2-} increases the pH at the pit bottom, with the pH difference becoming more pronounced as f increases.
2. A time-dependent hydrolysis effect from chloride- and sulfate-based salts was observed for major species at the pit bottom. This suggests that the actual solution chemistry inside the pit may differ from thermodynamic predictions, potentially leading to higher localized concentrations than expected.
3. The addition of sulfates to pit-like solutions promotes the precipitation of stable salts, such as $FeCl_2\cdot 7H_2O$ and $NiCl_2\cdot 6H_2O$ (in addition to $FeCl_2\cdot 4H_2O$ predicted in pure chloride electrolytes). These precipitates have been associated with current oscillations during potentiostatic holds in mass-transfer-controlled regions of 1D artificial pit experiments.
4. In activation-controlled regions the inhibiting effects from sulfates can be related to their impact in decreasing anodic kinetics (increasing β_a), increasing the cathodic kinetics in anodic potentials), and decreasing the $(i_c/i_a)_{crit}$.

5. The presence of sulfates at different ratios resulted in a lower $(i \cdot x)_{sf}$ compared to pure chloride solutions. However, in sulfate-containing environments, f was significantly higher (around 88%), and both $(i \cdot x)_{crit}$ and E_{rp} were greater than those observed for SS316L in 0.6M NaCl.

3.7. References

1. Tester, J. W. & Isaacs, H. S. Diffusional Effects in Simulated Localized Corrosion. *J. Electrochem. Soc.* **122**, 1438–1445 (1975).
2. P.C.Pistorius, G. T. B. Metastable pitting corrosion of stainless steel and the transition to stability. *Philos. Trans. R. Soc. London. Ser. A Phys. Eng. Sci.* **341**, 531–559 (1992).
3. Moayed, M. H. & Newman, R. C. The Relationship Between Pit Chemistry and Pit Geometry Near the Critical Pitting Temperature. *J. Electrochem. Soc.* **153**, B330 (2006).
4. Sato, N. The Stability of Pitting Dissolution of Metals in Aqueous Solution. *J. Electrochem. Soc* **129**, 260–264 (1982).
5. Srinivasan, J., Liu, C. & Kelly, R. G. Geometric Evolution of Flux from a Corroding One-Dimensional Pit and Its Implications on the Evaluation of Kinetic Parameters for Pit Stability. *J. Electrochem. Soc.* **163**, C694–C703 (2016).
6. Woldemedhin, M. T., Srinivasan, J. & Kelly, R. G. Effects of environmental factors on key kinetic parameters relevant to pitting corrosion. *J. Solid State Electrochem.* **19**, 3449–3461 (2015).
7. Beck, T. R. & Alkire, R. C. Occurrence of Salt Films during Initiation and Growth of Corrosion Pits. *J. Electrochem. Soc.* **126**, 1662–1666 (1979).
8. Frankel, G. S., Li, T. & Scully, J. R. Perspective—Localized Corrosion: Passive Film Breakdown vs Pit Growth Stability. *J. Electrochem. Soc.* **164**, C180–C181 (2017).
9. Li, T., Scully, J. R. & Frankel, G. S. Localized Corrosion: Passive Film Breakdown vs. Pit Growth Stability: Part III. A Unifying Set of Principal Parameters and Criteria for Pit Stabilization and Salt Film Formation. *J. Electrochem. Soc.* **165**, C762–C770 (2018).
10. Li, T., Scully, J. R. & Frankel, G. S. Localized Corrosion: Passive Film Breakdown vs. Pit Growth Stability: Part IV. The Role of Salt Film in Pit Growth: A Mathematical Framework. *J. Electrochem. Soc.* **166**, C115–C124 (2019).
11. Li, T., Wu, J. & Frankel, G. S. Localized corrosion: Passive film breakdown vs. Pit growth stability, Part VI: Pit dissolution kinetics of different alloys and a model for pitting and repassivation potentials. *Corros. Sci.* **182**, 109277 (2021).
12. Pistorius, P. C. & Burstein, G. T. Growth of corrosion pits on stainless steel in chloride solution containing dilute sulphate. *Corros. Sci.* **33**, 1885–1897 (1992).
13. Srinivasan, J. & Kelly, R. G. Evaluating the Critical Chemistry for Repassivation at the Corroding Surface Using Mass Transport Model-Based Artificial Pit Experiments. *J. Electrochem. Soc.* **163**, C768–C777 (2016).
14. Li, T., Scully, J. R. & Frankel, G. S. Localized Corrosion: Passive Film Breakdown vs Pit Growth Stability: Part II. A Model for Critical Pitting Temperature. *J. Electrochem. Soc.* **165**, C484–C491 (2018).

15. Alkire, R. C. & Wong, K. P. The corrosion of single pits on stainless steel in acidic chloride solution. *Corros. Sci.* **28**, 411–421 (1988).

16. Bocher, F. & Scully, J. R. Stifling of crevice corrosion and repassivation: Cathode area versus controlled potential decreases assessed with a coupled multi-electrode array. *Corrosion* **71**, 1049–1063 (2015).

17. Newman, R. C. & Isaacs, H. S. Diffusion-Coupled Active Dissolution in the Localized Corrosion of Stainless Steels. *J. Electrochem. Soc.* **130**, 1621–1624 (1983).

18. Laycock, N. *et al.* Localised Dissolution Kinetics From Fast In Situ Radiography of Propagating Pits in Stainless Steel and Implications for Modeling Pitting Corrosion over Long Time-Scales. *ECS Meet. Abstr.* **MA2011-02**, 1685–1685 (2011).

19. Laycock, N. J., Krouse, D. P., Hendy, S. C. & Williams, D. E. Computer simulation of pitting corrosion of stainless steels. *Electrochem. Soc. Interface* **23**, 65–71 (2014).

20. Shehi, A., Choudhary, S. & Kelly, R. . Repassivation of stainless steels : A unifying quantitative framework. *Corros. Sci.* (2025).

21. Knight, A., Nation, B., Maguire, M., Schaller, R. & Bryan, C. FY22 Status : Corrosion-Resistant Coatings on Spent Nuclear Fuel Canisters to Mitigate and Repair Potential Stress Corrosion Cracking. (2022).

22. Bryan, C. *et al.* Surface Sampling Techniques for the Field Demonstration. (2021).

23. Yang, L. *et al. Corrosion of Alloy 22 Induced by Dust Deliquescene Brines*. (2001).

24. Sun, C., Chen, J., Zhu, J., Zhang, M. & Ye, J. A new diffusion model of sulfate ions in concrete. *Constr. Build. Mater.* **39**, 39–45 (2013).

25. Cook, A. J. M. C., Padovani, C. & Davenport, A. J. Effect of Nitrate and Sulfate on Atmospheric Corrosion of 304L and 316L Stainless Steels. *J. Electrochem. Soc.* **164**, C148–C163 (2017).

26. Katona, R. M., Knight, A. W., Maguire, M., Bryan, C. R. & Schaller, R. F. Considerations for realistic atmospheric environments: An application to corrosion testing. *Sci. Total Environ.* **885**, (2023).

27. Munis, A., Zheng, M. & Zhao, T. Effect of sulfate and meta-silicate ions on pitting corrosion of stainless steel-316 in chloride containing simulated coal gasifier aqueous effluents. *Mater. Res. Express* **6**, 0–13 (2019).

28. Leckie, H. P. & Uhlig, H. H. Environmental Factors Affecting the Critical Potential for Pitting in 18–8 Stainless Steel. *J. Electrochem. Soc.* **113**, 1262 (1966).

29. Ernst, P. & Newman, R. C. Pit growth studies in stainless steel foils. I. Introduction and pit growth kinetics. *Corros. Sci.* **44**, 927–941 (2002).

30. Srinivasan, J., McGrath, M. J. & Kelly, R. G. A High-Throughput Artificial Pit Technique to Measure Kinetic Parameters for Pitting Stability. *J. Electrochem. Soc.* **162**, C725–C731

(2015).

31. Srinivasan, J. A Quantitative Framework Connecting the Critical Factors Determining the Stability of Localized Corrosion. (University of Virginia, Materials Science - School of Engineering and Applied Science, PHD (Doctor of Philosophy), 2016, 2016).

32. Baes, C. & Mesmer, R. Charles Frederick Baes, Robert Eugene Messmer - The Hydrolysis of Cations-John Wiley & Sons Inc (1976). (1976).

33. Paul, B. L. & Ekberg, C. *Hydrolysis of Metal Ions*. (Wiley-VCH Verlag GmbH & Co. KGaA, 2016). doi:10.1002/9783527656189.

34. Wang, P., Wilson, L. L., Wesolowski, D. J., Rosenqvist, J. & Anderko, A. Solution chemistry of Mo(III) and Mo(IV): Thermodynamic foundation for modeling localized corrosion. *Corros. Sci.* **52**, 1625–1634 (2010).

35. Inman, S. B. *et al.* Passivation and localized corrosion resistance of Al0.3Cr0.5Fe2MoxNi1.5Ti0.3 compositionally complex alloys: Effect of Mo content. *Corros. Sci.* **227**, (2024).

36. Asami, K., Hashimoto, K. & Shimodaira, S. An XPS study of the passivity of a series of iron-chromium alloys in sulphuric acid. *Corros. Sci.* **18**, 151–160 (1978).

37. Hashimoto, K. Passivation of Amorphous Materials. in *Passivity of Metals and Semiconductors* (ed. Froment, M.) 235–246 (Elsevier, 1983). doi:https://doi.org/10.1016/B978-0-444-42252-1.50041-2.

38. Ziemniak, S. E., Jones, M. E. & Combs, K. E. S. Solubility and phase behavior of Cr(III) oxides in alkaline media at elevated temperatures. *J. Solution Chem.* **22**, 601–623 (1993).

39. Vinokurov, E. G. & Bondar', V. V. Prediction of Stability Constants for Cr(III) and Cr(II) Complexes. *Russ. J. Coord. Chem. Khimiya* **29**, 66–72 (2003).

40. Vinokurov, E. G., Kuznetsov, V. V. & Bondar', V. V. Aqueous solutions of Cr(III) sulfate: Modeling of equilibrium composition and physicochemical properties. *Koord. Khimiya* **30**, 530–540 (2004).

41. Katona, R. M., Carpenter, J., Schindelholz, E. J. & Kelly, R. G. Prediction of Maximum Pit Sizes in Elevated Chloride Concentrations and Temperatures. *J. Electrochem. Soc.* **166**, C3364–C3375 (2019).

42. Plane, R. A. & Taube, H. Observations of the kinetics of the exchange of water between Cr(H2O)6+++ and solvent. *J. Phys. Chem.* **56**, 33–38 (1952).

A3. Appendix

Table A3.1 Average pit initiation peak current density and standard deviations for SS316L in 0.6M NaCl and 0.6M NaCl and 0.24M Na_2SO_4 (SO_4^{2-}/Cl^- =0.4)

	0.6M NaCl	**SO_4^{2-}/Cl^- = 0.4**
Current density, A/cm²	4.97±0.29	1.98±0.39

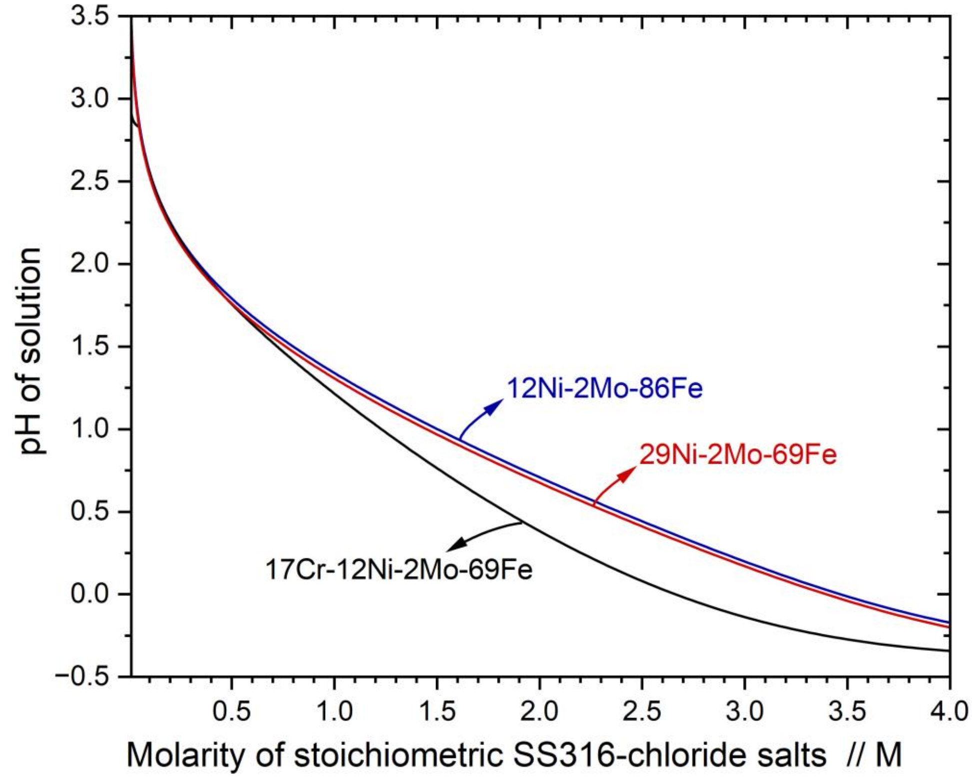

Figure A3.1. Solution pH versus the molarity of SS-chloride solution for 3 cases: typical stoichiometric SS316 composition (black curve), same composition as SS316 with 0 wt.% Cr but Fe being 86 wt.% (blue) and same composition as SS316 with 0 wt.% Cr but Ni being 29 wt.% (red). Note that in the last two cases, the 17 wt.% Cr has been transferred to either Fe or Ni wt.% to see the effect that it has in the solution pH.

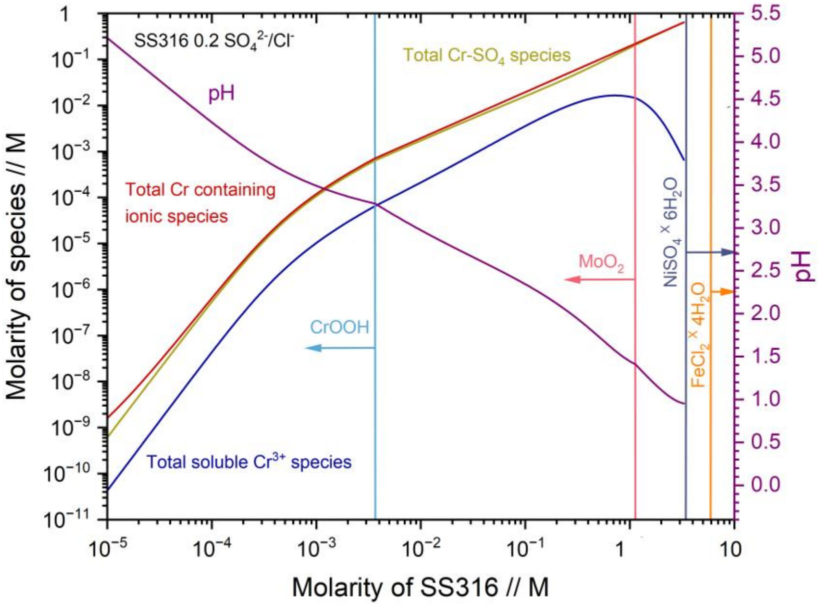

Figure A3.2. Concentration of given species and pH of the solution versus molarity of stoichiometric SS316-chloride and sulfate with SO_4^{2-}/Cl^-=0.2 utilizing the thermodynamic database. Vertical lines depict the solid species precipitated at the given SS316 molarity and the arrows accompanying them depict the concentrations of SS316 for which their presence is stable.

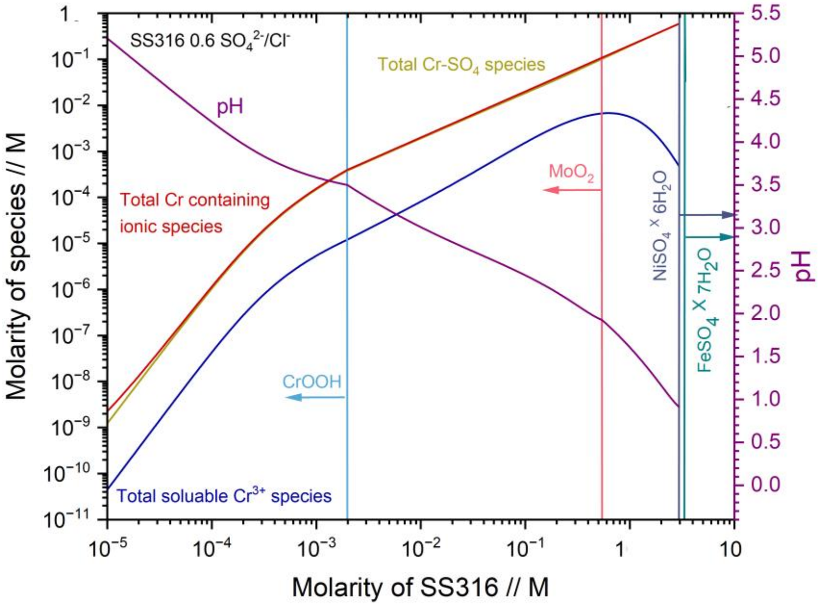

Figure A3.3. Concentration of given species and pH of the solution versus molarity of stoichiometric SS316-chloride and sulfate with SO_4^{2-}/Cl^-=0.6 utilizing the thermodynamic database. Vertical lines depict the solid species precipitated at the given SS316 molarity and the arrows accompanying them depict the concentrations of SS316 for which their presence is stable.

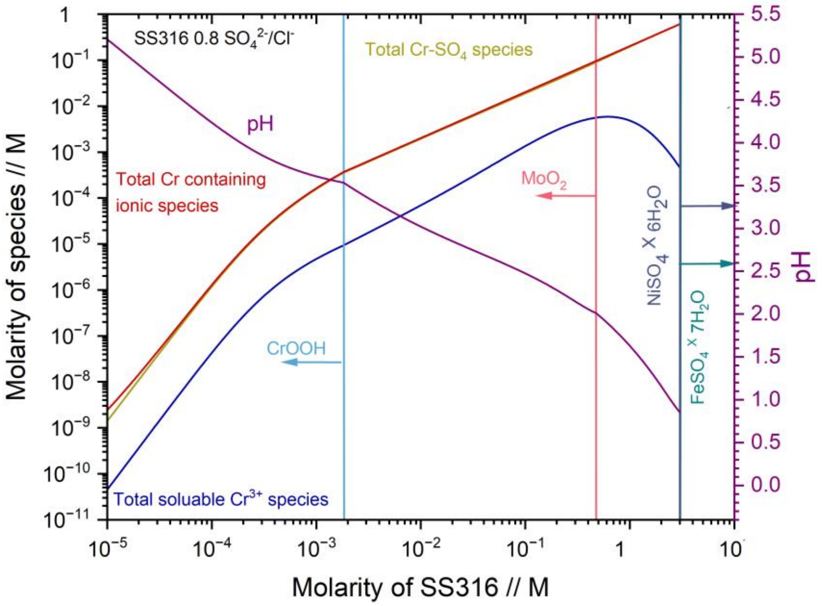

Figure A3.4. Concentration of given species and pH of the solution versus molarity of stoichiometric SS316-chloride and sulfate with $SO_4^{2-}/Cl^-=0.8$ utilizing the thermodynamic database. Vertical lines depict the solid species precipitated at the given SS316 molarity and the arrows accompanying them depict the concentrations of SS316 for which their presence is stable.

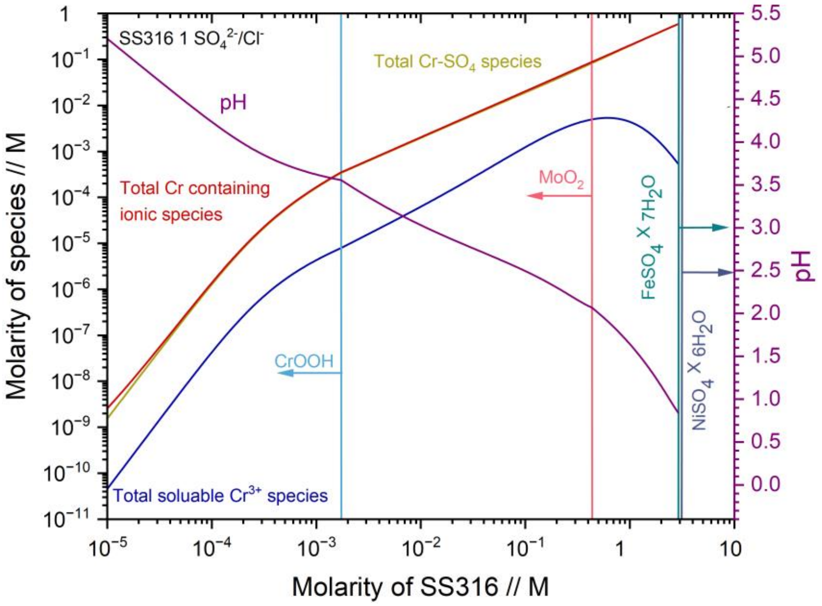

Figure A3.5. Concentration of given species and pH of the solution versus molarity of stoichiometric SS316-chloride and sulfate with $SO_4^{2-}/Cl^-=1$ utilizing the thermodynamic database. Vertical lines depict the solid species precipitated at the given SS316 molarity and the arrows accompanying them depict the concentrations of SS316 for which their presence is stable.

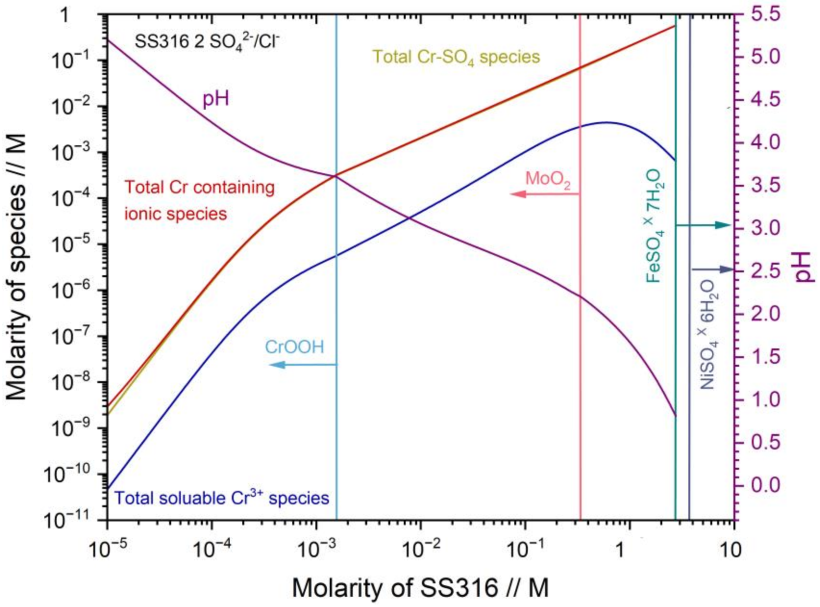

Figure A3.6. Concentration of given species and pH of the solution versus molarity of stoichiometric SS316-chloride and sulfate with $SO_4^{2-}/Cl^-=2$ utilizing the thermodynamic database. Vertical lines depict the solid species precipitated at the given SS316 molarity and the arrows accompanying them depict the concentrations of SS316 for which their presence is stable.

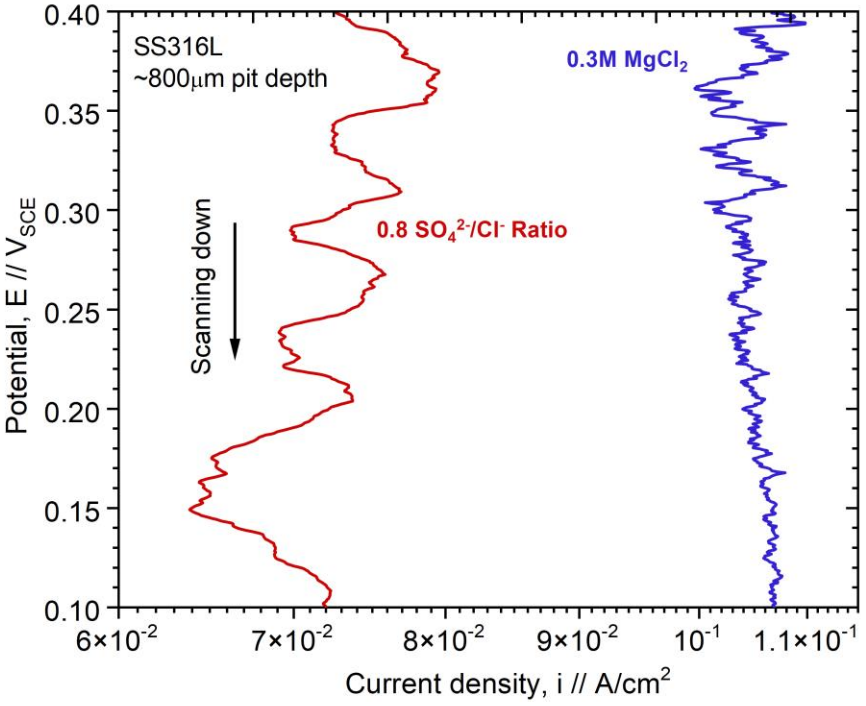

Figure A3.7. LSV scans at 5mV/s for SS316L in 0.3M $MgCl_2$ (blue) and 0.3M $MgCl_2$ with 0.48M $MgSO_4$ to achieve SO_4^{2-}/Cl^- =0.8 (red) at approximately 800μm pit depth.

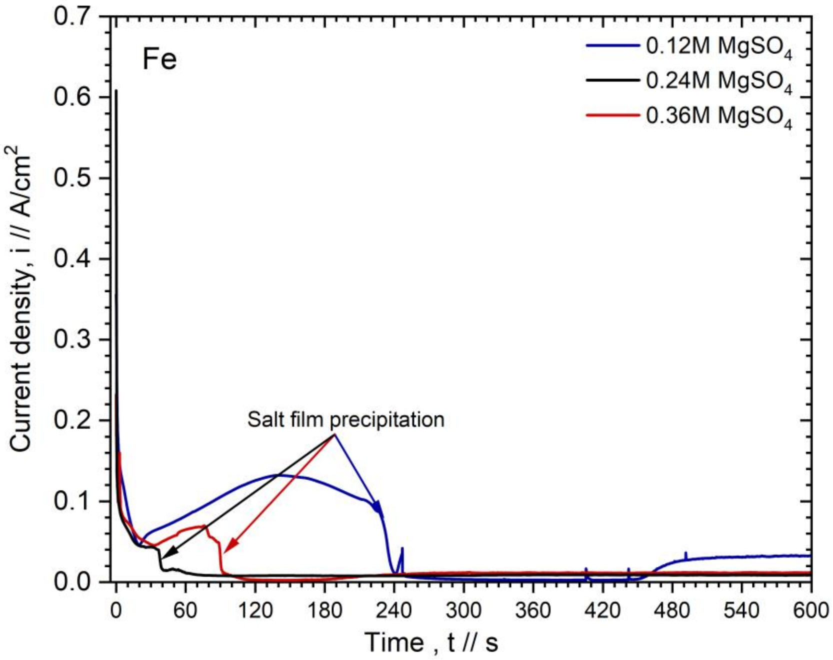

Figure A3.8. Current density versus time for a potentiostatic hold of Fe in solution of 0.12M $MgSO_4$ (blue), 0.24M $MgSO_4$ (black), and 0.36M $MgSO_4$ (red).

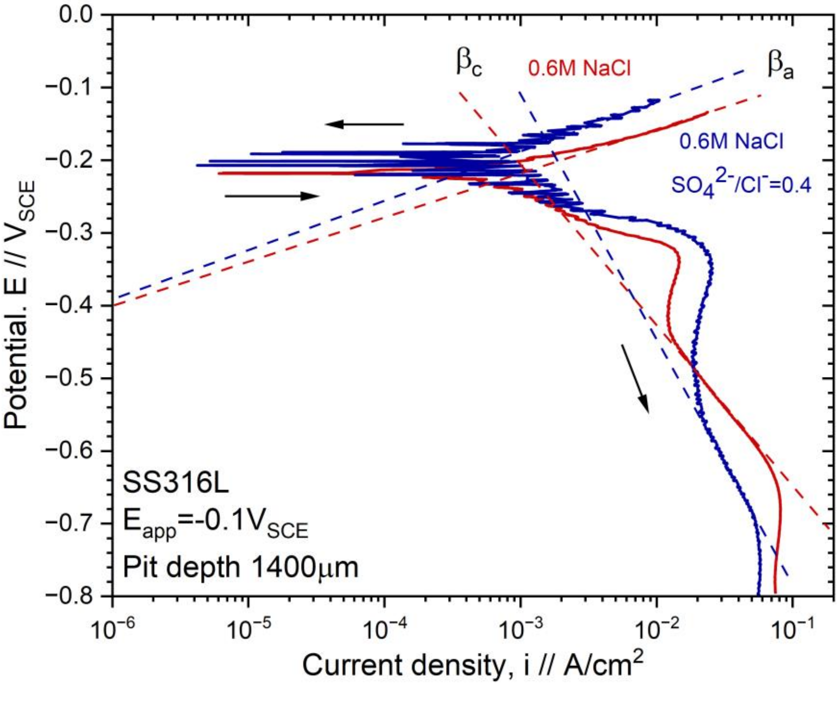

Figure A3.9. IR-corrected LSV scans taken at a scan rate of 400mV/s for SS316L in 0.6M NaCl (red) and 0.6M NaCl and 0.24M Na_2SO_4 (SO_4^{2-}/Cl^- =0.4) at approximate same pit depth of 1400μm and at the same E_{app}=-0.1V vs. SCE. Dashed lines represent the extracted cathodic and anodic Tafel line. Arrows indicate the direction of the scan during the LSV.

Chapter 4. The Shape Factor for Pits and Its Impact on Pit Stability

A. Shehi, R. G. Kelly
Center for Electrochemical Science and Engineering, Department of Materials Science
and Engineering, University of Virginia, Charlottesville, VA 22904

Contributions: A. Shehi - Conceptualization, Data curation, Formal analysis, Investigation, Methodology, Visualization, Writing - original draft, Writing-review and editing, **R. G. Kelly** - Conceptualization, Funding acquisition, Data curation, Formal analysis, Project administration, Resources, Project administration, Investigation, Methodology, Visualization, Writing - original draft, Writing – review and editing

4.1. Summary

This study employs the Finite Element Method (FEM) to predict the impact of pit shape on pit stability via shape factors of various pit geometries relevant to localized corrosion. Lower values of the shape factor indicate an increased ease in maintaining pit stability. Analyzed geometries include undercut pits, bispherical pit-within-pit structures, and covered pits with perforated (lacy) covers. The effect of the water layer thickness, transport properties of the electrolyte inside and outside the pit, and cathode location on the pit shape factor were also explored. Results show that occluded pits exhibit lower shape factors than open ones, with disk-shaped pits decreasing further as *c/r* ratio and occlusion angle increase. The findings also suggest minimal influence from a Secondary pit if the primary remains active. An equation is presented that quantifies the impact of lacy covers, revealing significant shape factor value reduction. Additionally, high salt concentrations inside pits have a limited stabilizing effect compared to geometry, while thin water layers and adjacent cathodic/sinks reduce pit stability.

4.2. Introduction

Over the past five decades, artificial one-dimensional pit experiments have provided a valuable framework for studying the kinetics of pitting corrosion.[1-11] The geometric constraints imposed during 1D pit propagation simplify analytical solutions, leading to a more precise scientific understanding of interfacial processes. The 1D approach is well-established in the scientific community and has been employed for decades to study various heat and mass transfer processes.[12,13] In the field of electrochemistry, Vetter's 1967 publication, *Electrochemical Kinetics*, provides a detailed theoretical approach to various electrochemical processes in 1D, including charge-transfer, diffusion, reaction, and crystallization overvoltage.[14] Then, mass transport relationships in 1D localized corrosion were introduced by Beck and Grens in 1969 in the context of SCC of titanium.[15] However, it was not until 1972 that Pickering and Frankenthal provided a more detailed and expanded qualitative analysis of electrochemical processes occurring inside a pit.[16] In this work, which also adopts a 1D approach, Pickering and Frankenthal introduces the product of current density (i) and pit depth (x), denoted as $i \cdot x$, to describe the concentration of species (c_i), potential (E_s), and pH at the pit surface.

This theory was further developed by Galvele[17–19] in a series of seminal papers, where he introduced the term *pit stability product* to describe the $i \cdot x$ parameter. While x still represents pit depth, Galvele redefines i as the minimum current density required at a given pit depth to sustain an active pit. In Galvele's framework, a pit remains active if the dissolution rate sufficiently replenishes metal cations-maintaining pH through hydrolysis reactions-despite diffusion-driven losses. In subsequent years, Newman imposed additional constraints on this theory to further delineate the conditions necessary for the repassivation of an on-going active pit.[20]

Nevertheless, in all these cases, transport processes are important to maintaining the critical condition(s). Transport is characterized by a flux and is governed by a driving force, along with the ease with which the transported species moves through a medium. The ease with which the transporting species moves through a medium depends on both the characteristics of the medium and the geometry in which it is contained.

Some of the above parameters (c_i, E_s, pH) have been measured or estimated using 1D pits because of the assumed simplicity of the 1D transport, although attainment of 1D conditions requires a pit of sufficient depth (*i.e.*, 8-10x diameter).[21,22] Very few instances of practical importance exist in which the pit or localized corrosion site is truly 1D. Etch tunneling in Al is one,[23–25] but in most alloy/environment combinations, pits with 3D geometrical character are observed. The ability to apply the critical conditions listed above requires a means of translating the 1D pitting results to the range of 3D geometries encountered in pitting.

A more generic approach to the translation of 1D pitting experiments to more general pit shapes can be based on the concept of a shape factor. The concept of *shape factor* is well-established in the study of steady-state heat conduction.[12,26] According to Fourier's law, the dissipation of heat varies based on the geometry of a body.[26] This concept is readily extendable to analogous physical laws, such as Ohm's law for electrical conduction and Fick's first law for diffusion. In the context of Ohm's law, current flow is perpendicular to equipotential surfaces. Because Ohm's law and Fick's first law are mathematically analogous, the flux of a species in Fick's first law must also be perpendicular to isoconcentration surfaces. In such cases, the geometry of a pit or other system constrains the flux of the species, introducing an effective resistance.

Under steady-state conditions, shape factor *S* can be defined as:

$$\mathrm{S} = \frac{1}{\mathrm{uR}} \tag{4.1}$$

where u is a transport property of the medium (u=k for Ohm's law and u=D for Fick's first law), and R is the resistance. S connects the driving force to a flux by accounting for the ability of the medium to allow the flux and the geometry through which the flux moves. Incorporating this into Fick's first law, the steady-state, three-dimensional flux of a species can be expressed as:

$$\frac{\partial \overrightarrow{\mathrm{m_i}}}{\partial \mathrm{t}} = \mathrm{S}\mathrm{D_i}\Delta\overrightarrow{\mathrm{C_i}} \tag{4.2}$$

where m_i is the mass of species i, t is time, S is the shape factor as defined above, D_i is the diffusion coefficient, and ΔC_i is the concentration difference of species i across two locations. Note that shape factor S is a product of a constant and a dimension of the body (such as radius r, length l etc.). Hence, as it will be seen in the future sections of this chapter, the constant of the shape factor will be compared for various geometries. Given that the resistance R can change with a given geometry, the shape factor constant is also expected to change.

In the special case of one-dimensional diffusion, the shape factor simplifies to: $\mathrm{S} = \frac{\mathrm{A_x}}{\mathrm{l}}$ where A_x is the cross-sectional area perpendicular to the flux, and l is the distance between two isoconcentration surfaces. Substituting this into Equation 4.2 yields:

$$\frac{\partial \mathrm{m_i}}{\mathrm{A_x}\,\partial \mathrm{t}} = \mathrm{J} = \frac{\mathrm{D_i}\Delta \mathrm{C_i}}{\mathrm{l}} \tag{4.3}$$

where J is the flux of species i. Equation 4.3 is the widely recognized one-dimensional form of Fick's first law found in standard textbooks.[13]

4.2.1. Application to corrosion studies

The significance of Equation 4.2 was discussed by Pistorius and Burstein.[27] in the context of pitting corrosion. In any electrochemical system, the flux of species can be related to the total current using:

$$\frac{\partial \mathrm{m}}{\partial \mathrm{t}} = \frac{\mathrm{I}}{\mathrm{zF}} \tag{4.4}$$

where I is the total current, z is the number of electrons involved per reaction, and F is Faraday's constant 96,485 C/mol. Combining Equations 4.2 and 4.4 gives, for diffusion-controlled dissolution:

$$\mathrm{I} = \mathrm{SzFD\Delta C} \tag{4.5}$$

Equation 4.5 is fundamental for studying and analyzing the kinetics of pitting. The term $zFD\Delta C$ can be experimentally determined from one-dimensional pit studies and is equivalent to $i \cdot x$. Knowing the shape factor S, Equation 4.6 allows for extrapolating results from controlled one-dimensional experiments to more realistic three-dimensional pits.

$$\mathrm{I_{crit}} = \mathrm{S(i \cdot x)_{crit}} \tag{4.6}$$

where $(i \cdot x)_{crit}$ is the critical pit stability product.

4.2.2. The link between S, pit stability, and data from 1D pit experiments

The main attraction of 1D pit experiments is the fact that all the current can be ascribed to the dissolution of a single, known surface area, unlike most pitting experiments in which numerous pits form, grow, and die on a single surface. The presence of multiple pits prevents connecting the measured current to electrochemical conditions at or within a pit. Because of the simplicity of the transport described above in 1D pits, it is possible to connect measurements of current and potential to the critical parameters listed above[16,17] in the context of pit stability.

In the case of pitting, the shape factor describes the relative ease with which mass or charge moves in a volume (*e.g.,* the solution in and near a pit). Knowing the shape factors of two different geometries allows a quantitative relation of the fluxes, which can be used to establish the stability of a pit because a certain flux is required to maintain the assumed conditions (*i.e.*, pH, c_i, E_s).

Although the focus of most mechanistic pitting studies is the dissolving surface, under open circuit conditions, pits must match their dissolution currents to the available cathodic currents that occur primarily on the outside surfaces due to the law of charge conservation.[28] Thus, the combination of the shape factor and data from 1D pits is necessary, but not sufficient to establish pit stability in service conditions in which open circuit conditions are by far the most common scenario. In all such cases, there is a physical limit to the amount of surrounding area that can provide that current due to ohmic drop. In full immersion geometries, that limit can be high, but under atmospheric conditions, that area can be quite small (~ mm). Given cathodic kinetics of the outside surface and knowledge of the electrolyte composition and geometry, a maximum available cathodic current for a given area can be calculated.[3,29,30] That maximum cathodic current can be combined with the shape factor and data from 1D pits to develop the set of necessary and sufficient conditions for pit stability assessment.[29]

Therefore, this work seeks to expand the shape factor solution space beyond those available analytically by utilizing the Finite Element Method (FEM), especially for geometries for which an analytical solution is complicated, difficult to obtain, or not possible analytically. Those results are then combined with maximum cathodic current calculations to investigate the impact of pit shape on pit stability in practice.

4.3. Methodology

This study employs both analytical and computational approaches to calculate the shape factor with the focus remaining on the computational aspect. The analytical approach, which follows in the method described by Pistorius and Burstein, integrates transferable principles from the fields of heat transfer and electrochemistry and has been described thoroughly in Appendix A. On the other hand, the computational approach leverages FEM simulations. The subsequent sections provide a detailed overview of each approach.

4.3.1. Shape factor-numerical approach

In the general case, geometries are not amenable to analytical solutions, and numerical methods such as FEM must be used. COMSOL Multiphysics® version 6.2, utilizing the Transport of Diluted Species module, was employed for all FEM calculations presented herein. Note that the Primary Current Distribution module (Ohm's law), or the Heat Transfer module (Fourier's law) could have also been utilized. As explained previously, the solutions to the shape factor hold true for Ohm's law, Fourier's law, and Fick's first law, and as such the choice in using a given module is left to the user.

Figure 4.1a and 4.1b show the 3D COMSOL Multiphysics model and the schematic of the 2D cross section of the geometry of interest, respectively. In the schematic presented in Figure 4.1b, two designated surfaces are set at constant species concentrations, c_1 and c_2, assigned arbitrary values. A diffusion coefficient of 1 m^2/s was selected for species i. The total flux of the species i, J_i, is found by integrating the flux normal to the interest surface of the given geometry (*e.g.*, hemisphere, oblate spheroids). Then, the shape factor is calculated utilizing Equation 4.2. Note that in all the following schematics only the two-dimensional cross section of the geometry of interest is shown; however, all calculations were conducted utilizing a three-dimensional geometry.

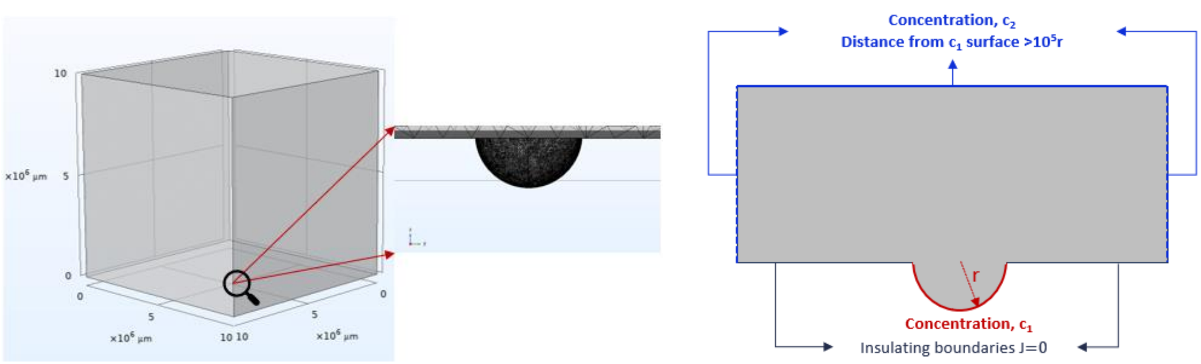

a) **b)**

Figure 4.1. Model utilized to numerically calculate the shape factor **a)** three-dimensional COMSOL Multiphysics model with a zoomed section on the meshed geometry of interest and **b)** a schematic of two-dimensional cross section of the model.

The accuracy of FEM results is influenced by mesh size; therefore, to minimize mesh dependency, the geometry's mesh was refined until the numerically calculated shape factors closely matched those geometrical components for which analytical solutions are available (*e.g.*, a sphere, disk, or hemisphere in an infinite medium).[31] This exercise ensured that FEM results align with theoretical expectations for standard cases and provides a mesh-independent model for the other complex geometries. The mesh of the geometry could further be refined; however, computational benefits would not outweigh the computational expenses.

Table 4.1. Shape factor for a sphere in an infinite medium, thin disk in an infinite medium, and hemisphere in a semi-infinite medium, derived from analytical and FEM methods, with associated percent errors. The gray areas are assumed electrolyte geometries.

Geometry/Cross-section		**Analytical[31]**	**FEM**	**% Error**
Sphere in infinite medium	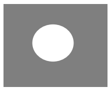	12.57	12.77	1.6
Hemisphere in insulated surface		6.28	6.38	1.6
Thin disk in infinite medium		8.00	8.16	2.0

Table 4.1 summarizes the shape factors for a sphere, thin disk, and cylinder (all depicted in white color) immersed in an infinite medium (depicted in gray color), comparing values obtained through analytical methods[31] and Transport of Diluted Species module of COMSOL Multiphysics® version 6.2, along with the corresponding percent errors. In this depiction, the surfaces of the sphere,

hemisphere, and thin disk are set a constant concentration, c_1, and the surfaces of the medium located at a large distance, ∞, are set at another constant concentration, c_2. Overall, it can be observed that the two methods of calculations are in very good agreement with one another with the error being less than 2% in all cases studied as shown below.

4.4. Results

This section mainly focuses on the results obtained using numerical methods. The results begin with the analytical equation for a spherical pit with different degrees of undercutting followed by results from the FEM approach. The computational approach which was previously described and confirmed against analytical solution is applied to calculations for spherically shaped pits, dish-shaped pits, pits within pits, and lacy-covered pits. Additionally, the effects of different transport media between the inside and outside of the pit, as well as the effects of water layer thickness and cathode size on the shape factor for pitting under atmospheric exposures are also presented. To provide a description of the impact of the findings of the variation of the pit shape factor on the stability of pits, the framework of the maximum pit size model will be utilized for some of the given cases.

4.4.1. Shape factor-analytical approach

As previously mentioned, details of the analytical approach (including schematics of the explored geometries) and the corresponding results are provided in Appendix of this study. To provide a comparison between the analytical and the computational approach in the subsequent section, the shape factor for a spherical geometry with various degrees of undercutting is provided below:

$$S = \frac{2\pi sin(\theta)(1-cos(\theta))}{\pi(1-cos(\theta))-sin(\theta)} r \tag{4.7}$$

where θ is the degree of the geometry which can also be interpreted as the level of undercutting in a pit. For a clearer depiction of geometrical parameters, the reader is referred to Table A4.1 in the Appendix of this chapter. Note that Equation 4.7 here is the same as Equation A4.3 in the Appendix section.

4.4.2. Shape factor-numerical approach

The following subsections present the shape factor calculations for various geometrical configurations obtained using the FEM approach. For each case, a two-dimensional schematic of the geometry along with the corresponding boundary conditions is provided. Each configuration is analyzed individually, with the behavior of the shape factor examined as a function of a specific parameter defined in the given subsection.

4.4.2.1. Spherical geometries

The first case examines the shape factor for concave spherical pits as shown in Figure 4.2. Pits carrying these shapes are based on spheres which intersect the surface at different chords leading to dish-shaped and undercutting pits defined by r and θ (Figure 4.2). The derivation expresses the shape factor as a function of the angle θ, independent of the radius r. For example, when $\theta = 30°$ the geometry represents a shallow spherical cap, *i.e.*, dish-shaped (Figure 4.2a); $\theta = 90°$ corresponds to a hemisphere (Figure 4.2b); and $\theta = 150°$ represents a sphere missing a $30°$ cap, *i.e.*, inkwell-shaped (Figure 4.2c). The latter one could be utilized to simulate a spherical pit with undercutting. Here, the shape factor is determined by calculating the flux from the inner surface (blue) of a spherical cap with radius r and angle θ, to a surface at infinity.

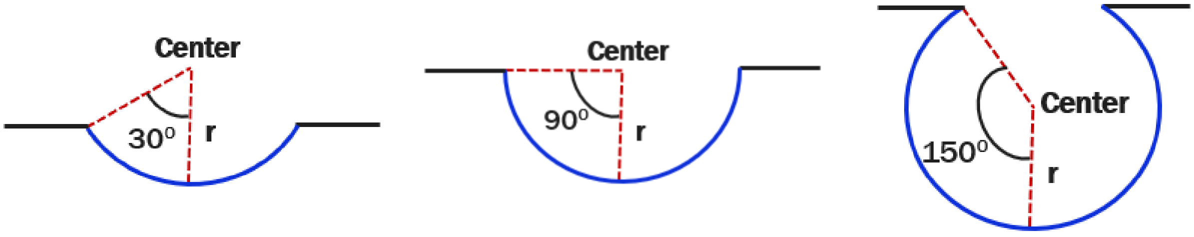

a) **b)** **c)**

Figure 4.2. Spherical cap geometries of interest with different θ angles **a)** 30º **b)** 90º, and **c)** 150º.

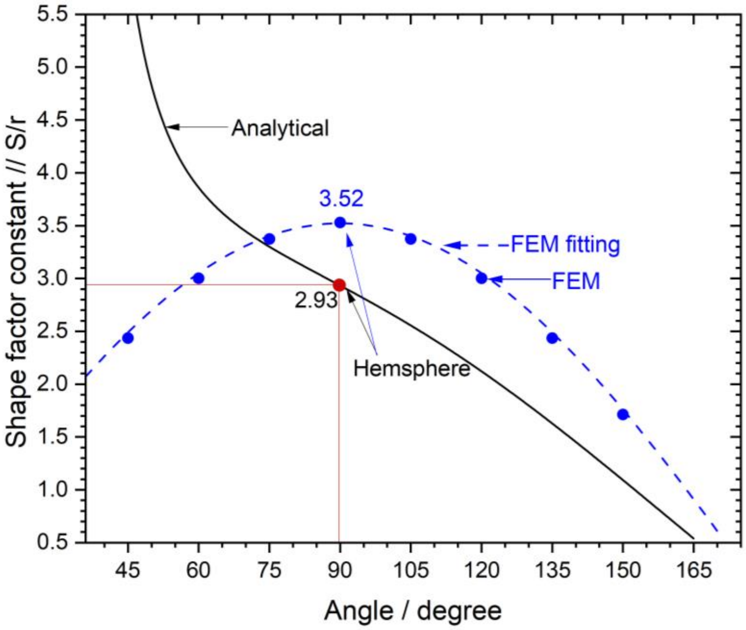

Figure 4.3. Calculations of shape factor constant obtained via analytical method from Equation 4.7 (black), FEM modeling (blue dots), and fitting of the FEM data from Equation 4.9 (blue dotted line).

Figure 4.3. compares the constants of shape factor obtained through FEM to those obtained from analytical approaches (Equation 4.7), and the fitting of the FEM results for spherical geometries across all angles. The results indicate that for $\theta \geq 75°$, the FEM-derived shape factor constants are higher than those from the analytical method. Conversely, for $\theta < 75°$, the analytical approach yields substantially higher shape factor constant values than the FEM model.

The FEM results indicate that the shape factor constant varies with the angle θ, following a trend that closely approximates a sinusoidal function, *sin(θ)*. Because *sin(θ)* relates the radius of a spherical body to the radius of its opening at the mouth via Equation 4.8:

$$r_{mouth} = r_{90°} * sin(\theta) \tag{4.8}$$

The shape factor constant for any spherical geometry can be scaled from that of a hemispherical body by applying Equation 4.9, yielding in Equation 4.9:

$$S_{\theta} = S_{90°} \cdot sin(\theta) \tag{4.9}$$

An equation is fitted to the obtained FEM data to predict the variations of the shape factor with the angle θ. The results are presented in Figure 4.3. The graph demonstrates very good agreement between the fit Equation 4.9 and computational results from FEM. For spherical geometries with $\theta > 90°$, there is a notable separation in flux contributions between the top and bottom regions of the sphere. The definition of the “top region” is that part of the surface above the diameter of the pit with the “bottom region’ being that below the diameter, as shown in Figure 4.4a (note the break in the ordinate scale). Figure 4.4a illustrates the percentage of flux - and consequently the contribution to the shape factor - originating from these regions of the spherical body. The data show that for $\theta > 90°$, most of the flux arises from the top part of the sphere, with this percentage increasing from 78% at $\theta = 105°$ to 98% at $\theta = 165°$.

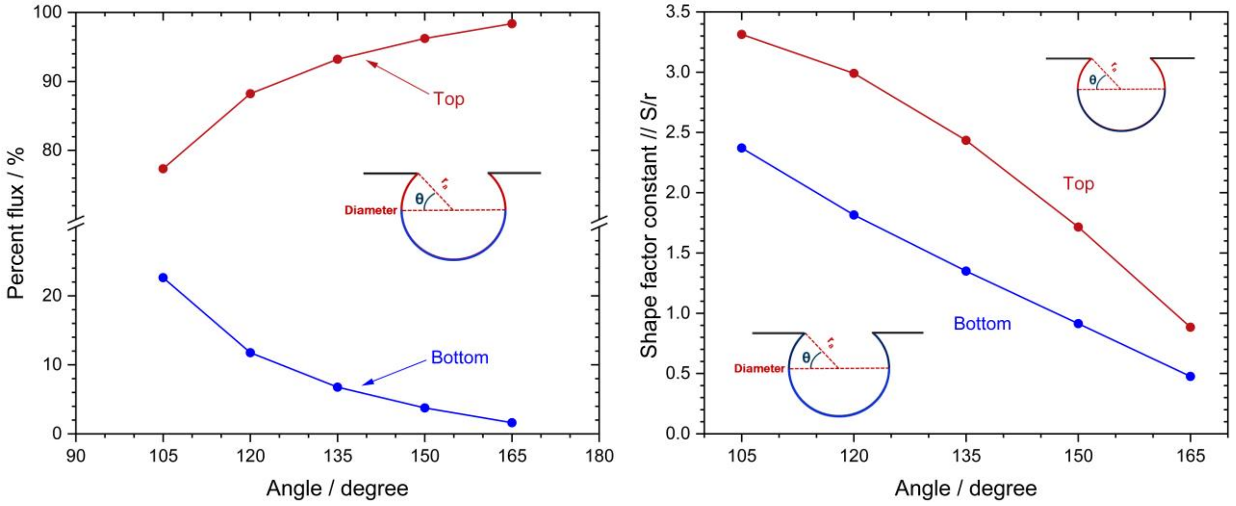

a) **b)**

Figure 4.4. a) Percent of flux arising from the top and the bottom of the spherical cap as a function of θ and **b)** shape factor constant as a function of θ for the cases where only the bottom or the top part of the spherical cap is "active".

This distinct flux distribution prompted separate calculations of the shape factor constant for the top and bottom regions of the spherical body, as shown in Figure 4.4b. For these calculations, only the top or bottom half of the spherical geometry was set at a constant concentration (c_i), while the remaining portion was treated as an insulating boundary. The results reveal that the shape factor constant is consistently higher when the top part of the spherical body is active compared to when only the bottom part is active, across all tested angles. Additionally, for both cases, the shape factor decreases as the angle θ increases from $90°$ to $165°$, as in the previous cases above.

4.4.2. Oblate spheroid geometries

The second geometry considered is that of oblate spheroidal pit, characterized by the condition $a = b \neq c$ where *a, b,* and *c* are the dimensions of the pit from the center point (for a sphere $a = b = c$). In this case, the dimensions *a* and *b* are defined as radius, *r*, and the ratio of the "radius" *r* to the depth *c*, expressed as *c/r*, is used as a measure of the flatness of the geometric structure. Note that for the case of oblate spheroid geometries, *c/r* < 1 represents dish-shaped pits, and for *c/r* =1 the geometry converts into a sphere. Additionally, the angle parameter θ is treated as a variable in the analysis.

Figure 4.5a presents the shape factor constant values for *c/r* ratios of 0.3, 0.6, and 1 as a function of the angle θ. The results reveal that as the *c/r* ratio decreases (*i.e.*, geometry becomes increasingly flat), the shape factor constant also decreases for all tested angles and *c/r* ratios of 0.3, 0.6, and 1 except at $\theta = 90°$, where the shape factor constant remains relatively the same. Notably, for *c/r* ratios of 0.3, 0.6, and 1 at $\theta = 90°$ the shape factor constant is approximately ≈3.52. Similar to spherical geometries, the shape factor for a hemispheroidal body ($\theta = 90°$) can be scaled with respect to θ and the *c/r* ratio using Equation 4.10:

$$S_\theta = \frac{S_{90°}}{\sqrt{1+\left(\frac{cot(\theta)}{\frac{c}{r}}\right)^2}} \tag{4.10}$$

Equation 4.10 inherently accounts for the variations in the radius of the oblate spheroid as a function of angle θ. It is also evident that substituting *c/r*=1, corresponding to a spherical body, reduces Equation 4.10 to Equation 4.9. The predictions from Equation 4.10 are superimposed onto the solutions presented in Figure 4.5a, demonstrating consistency with the FEM data.

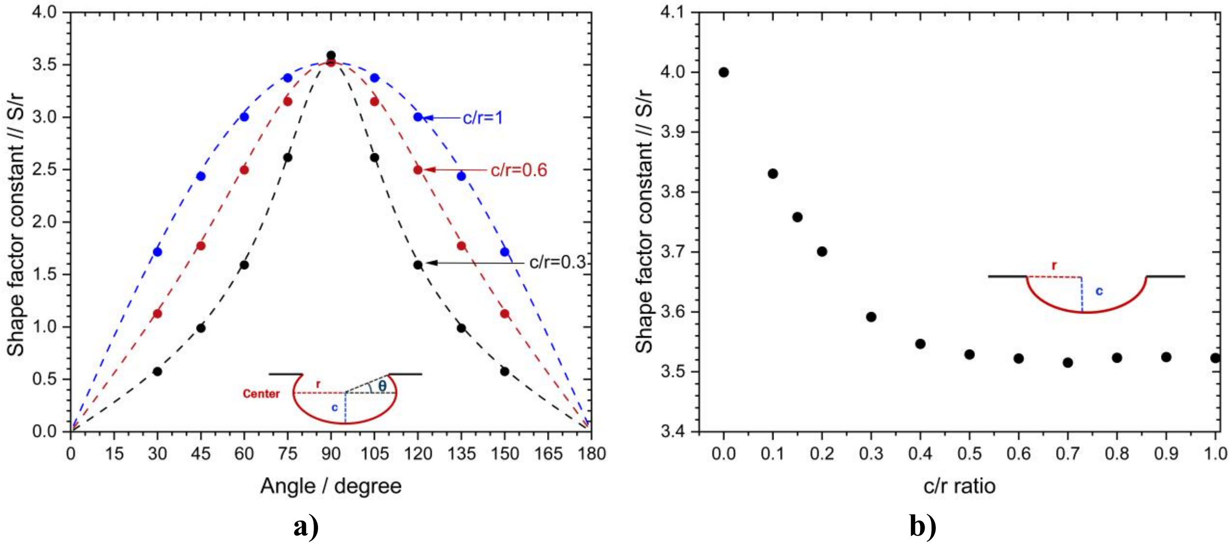

Figure 4.5. a) Shape factor constant as a function of angle θ for c/r ratios of 1 (blue), 0.6 (red), and 0.3 (black) obtained via FEM (dots) and the fitting of the FEM data through Equation 4.15 and **b)** Shape factor constant as a function of c/r ratio for θ=90°.

Figure 4.5b presents the shape factor constant as a function of *c/r* ratio for $\theta = 90°$. It can be noted that the shape factor constant decreases by increasing the *c/r* ratio until a *c/r* ratio of around 0.3 is reached for which the shape factor constant remains between 3.5 and 3.6. Note that for *c/r*=0, the shape factor is 4, corresponding to the analytical solution of a thin disk in a semi-infinite medium.

4.4.3. Bispherical bodies

In this section, we investigate the shape factor constant of a bispherical pit geometry, which is particularly relevant for cases of pitting corrosion where a pit may develop beneath another pit, whether the initial pit has passivated or is active. The configuration considered involves a smaller spherical body with radius r and a constant inner surface concentration c_1, connected at the base of a larger spherical body with radius R. The larger sphere's inner surface is either insulated or set to the same concentration c_1. The angle θ for both spherical bodies is defined consistently with the previous cases of spherical and spheroidal geometries. Three specific cases are explored. In all cases, we consider a hemispherical body with radius r and constant inner surface concentration c_1, placed at the center-bottom of another hemispherical body with radius R:

1. Both pits active: both hemispherical bodies have a constant inner surface concentration c_1. An arbitrary chosen ratio of 0.2 of *r/R* is selected for the demonstration. The angle $90° \leq \theta \leq 150°$ applies to both spheres (Figure 4.6a). The geometrical dimension connected to the shape factor constant is the radius of the small spherical body, *r*.
2. New pit within repassivated pit: the inner surface of the (larger) hemispherical body with radius R is insulated. The ratio of 0.2 of *r/R* is chosen arbitrarily for this case, as well. The angle $90° \leq \theta \leq 150°$ applies to both spheres (Figure 4.7a). The geometrical dimension connected to the shape factor constant is the radius of the small spherical body, *r*.

3. Identical to number 2 above, but $\theta = 90°$ for both spherical bodies. Calculations are for a range of ratios $0.05 \leq r/R \leq 1$ (Figure 4.8a). The geometrical dimension connected to the shape factor constant is the radius of the small spherical body, *r*.

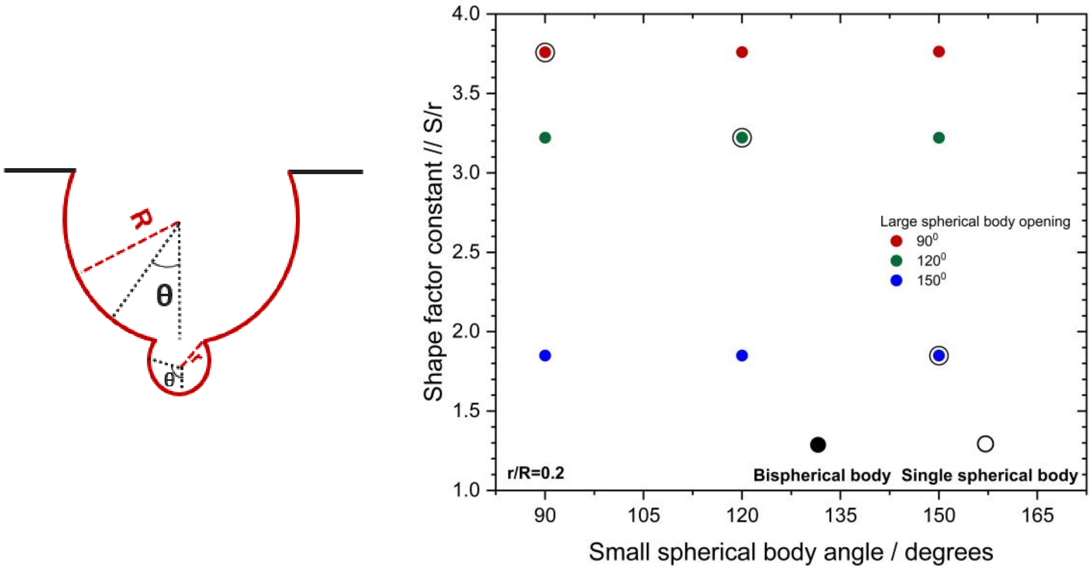

a) **b)**

Figure 4.6. **a)** Geometry of the bispherical body utilized in case 1 (red color symbolizes that the surfaces are set at a constant concentration c_1 and black symbolizes an insulated surface) and **b)** results for the shape factor constant for different angles of the small and large spherical body (filled circles) and the comparison with the single spherical geometry (empty circles). Note the *r/R* ratio is 0.2.

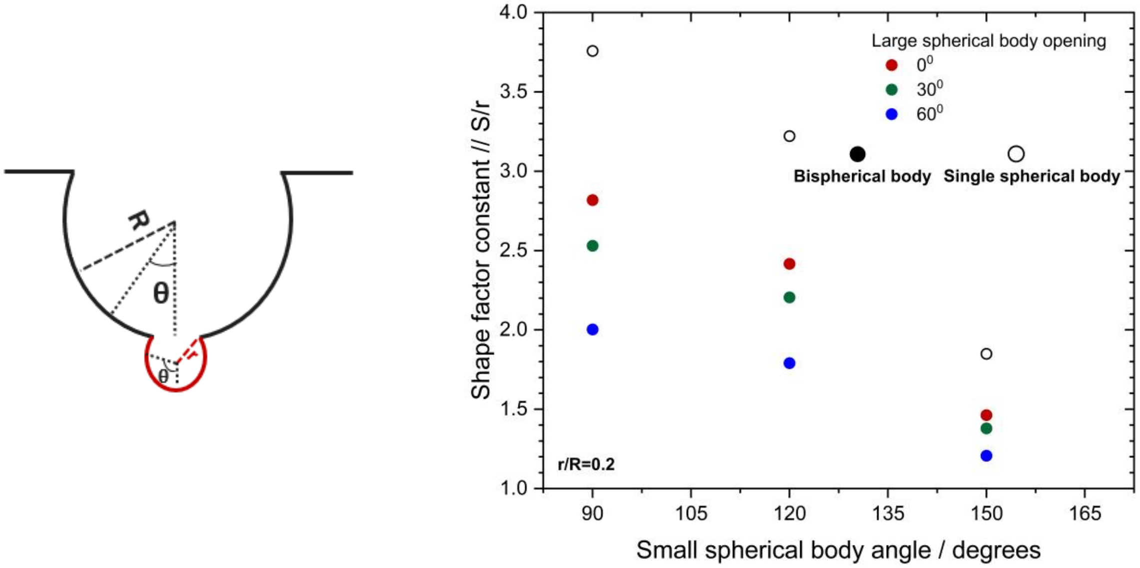

a) **b)**

Figure 4.7. a) Geometry of the bispherical body utilized in case 2 (red color symbolizes that the surfaces are set at a constant concentration c_1 and black symbolizes an insulated surface) and **b)** results for the shape factor constant for different angles of the small and large spherical body (filled circles) and the comparison with the single spherical geometry (empty circles). Note the *r/R* ratio is 0.2.

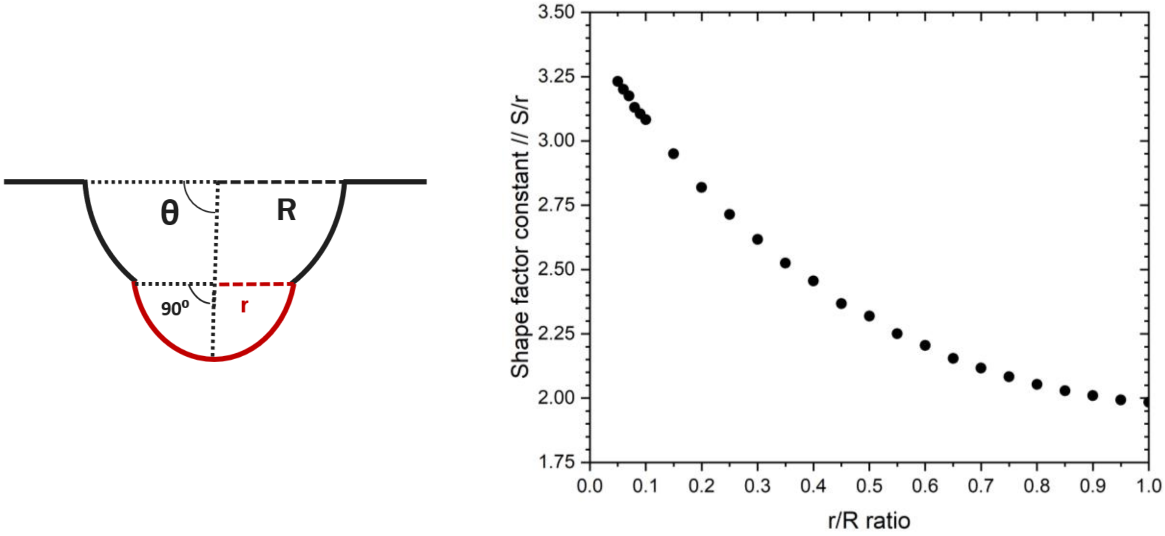

a) b)

Figure 4.8. a) Geometry of the bispherical body utilized in case 3 (red color symbolizes that the surfaces are set at a constant concentration c_1 and black symbolizes an insulated surface-note that the red spherical body is hemisphere) and **b)** results for the shape factor constant for *r/R* ratios where the surface of the small hemisphere with radius *r* is set at a constant concentration and the large spherical body surface with radius *R* is insulated.

The corresponding shape factor constant results for cases 1 and 2 are presented in Figures 4.6b and 4.7b for a representative ratio of *r/R*=0.2, chosen arbitrarily. For Figure 4.6b, case 1, the shape factor constant depends solely on the angle θ of the larger sphere and remains independent of the angle θ of the smaller sphere. Note that the shape factor constant for the spherical body presented in case 1 matches identically to that of a single spherical body. In Figure 4.7b, case 2, the shape factor constant is influenced by the angles θ of both the smaller and larger spheres, decreasing as angle θ increases for both spheres. The shape factor constant of the bispherical body is lower than that of a single spherical geometry, with the difference diminishing as the angle of the smaller sphere increases. Lastly, Figure 4.8b, case 3, the shape factor constant decreases with increasing *r/R*, illustrating a dependency on the relative size of the two spheres.

4.4.4. Presence of an insulating layer partially covering the mouth opening

The transport-of species between surfaces can be influenced by the presence of obstacles along the path. One relevant example is the growth of pits beneath a thin metallic sheet or remnant oxide film containing perforations at the pit opening. This sheet, commonly referred to as a lacy cover, introduces geometric constraints that impact species flux. A schematic representation of this geometry is provided in Figure 4.9a. This section investigates the influence of the lacy cover by examining how the location and radius, *a*, of a circular hole relative to the hemispherical body radius, R, affects the overall transport characteristics. Additionally, the relationship between the number and size of circular holes on the lacy cover is analyzed. For consistency, all results presented here consider a hemispherical geometry.

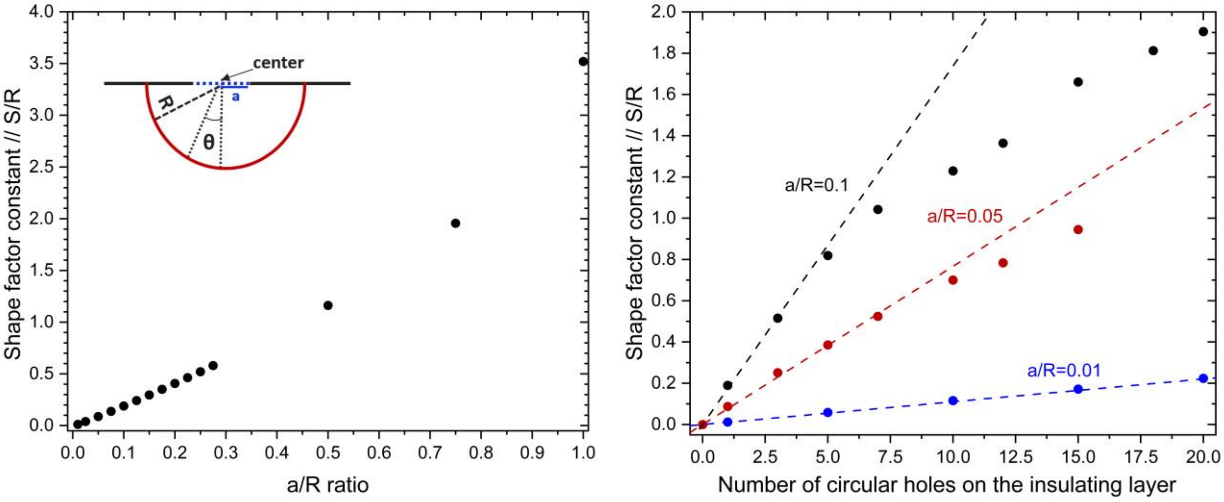

a) **b)**

Figure 4.9. a) Variations of the shape factor constant as a function of the *a/R* ratio for a hemispherical geometry and **b)** variations of the shape factor constant as a function of the number of circular holes in the insulating layer of a hemispherical geometry for *r/R* ratios of 0.01 (blue), 0.05 (red), 0.1 (black). In both cases, shape factors correlate to the radius *R* of the hemispherical body.

Figures 4.9a and 4.9b assess the impact of two parameters affecting the shape factor constant: the size of the circular hole on the insulating layer relative to the hemispherical radius (*a/R*) and the number of circular holes of varying sizes. Figure 4.9a reveals a power law relationship between the shape factor constant and *a/R*, suggesting that a lower *a/R* ratio can decrease the shape factor constant substantially. For example, for an *a/R* ratio of 0.1 the shape factor constant is approximately 0.19; this value is about 5.4% of the shape factor constant of the same hemispherical body with an entirely open mouth. Note that the findings in Figure 4.9a remain invariant with changes in the hemispherical body radius. While not shown in the results of Figure 4.9a, our observation is that the shape factor constant remains independent of the circular hole's location.

Conversely, Figure 4.9b shows that the shape factor constant depends on the number of circular holes on the insulating layer, increasing with an increasing number of holes. Interestingly, for small *a/R* values (*e.g.*, *a/R*=0.01), Figure 4.9b shows that the shape factor constant of the final configuration scales approximately with the number of small circular holes through Equation 4.11:

$$S_n = n * S_a \tag{4.11}$$

where S_n is the overall shape factor of the final configuration, *n* is the number of circular holes, and S_a is the shape factor for a single circular hole in the insulating layer. The relationship presented in Equation 4.11 is found to hold with a relatively high accuracy if S_a does not exceed approximately 10% of the shape factor for the hemispherical body without the insulating cover (the constant of which was determined to be 3.52 in this study).

Furthermore, an additional equation can be derived to calculate the shape factor for a hemispherical body with circular holes of varying sizes on the insulating layer. Provided the resulting shape factor remains below around 10% of the hemispherical body's open-mouth shape factor, the total shape factor can be expressed through Equation 4.12 as:

$$S_T = n_1 S_{a_1} + n_2 S_{a_2} + \cdots \tag{4.12}$$

Results from some selected cases are summarized in Table 4.2 below.

Table 4.2. Shape factors constant for various combinations of circular holes on the insulating layer, calculated using Equation 4.12 and FEM simulations.

Case	Shape factor from FEM	Shape factor from Equation.4.12	Percent error, %
1 hole *a/R*=0.1, **13 holes *a/R*=0.01**	0.33	0.34	3.03
1 hole *a/R*=0.2, **10 holes *a/R*=0.01**	0.51	0.53	3.92
1 hole *a/R*=0.1, **1 hole *a/R*=0.05,** **6 holes *a/R*=0.01**	0.33	0.35	6.25

The results in Table 4.2 show excellent agreement between Equation 4.12 and FEM calculations, with the percentage error remaining below 6.25%.

4.4.5. Shape factor of bodies with a variation in transport properties of electrolyte

This section examines cases in which the transport properties of the medium inside the spherical body differ from those in the bulk, a scenario commonly encountered in localized corrosion. In localized corrosion, significant differences in species concentrations inside and outside pits often lead to variations in conductivity and diffusion coefficients. Schematics relevant to this section are shown in Figure 4.10a, 4.10b, and 4.11. In these cases, a first approximation is used in which the transport properties undergo a step change at the pit/exterior boundary. We focus on spherical and spheroidal geometries with a *c/r* ratio of 0.3 and opening angles $\theta \geq 90°$. A case of a hemispherical geometry with an insulating layer and circular holes of radius a is also explored.

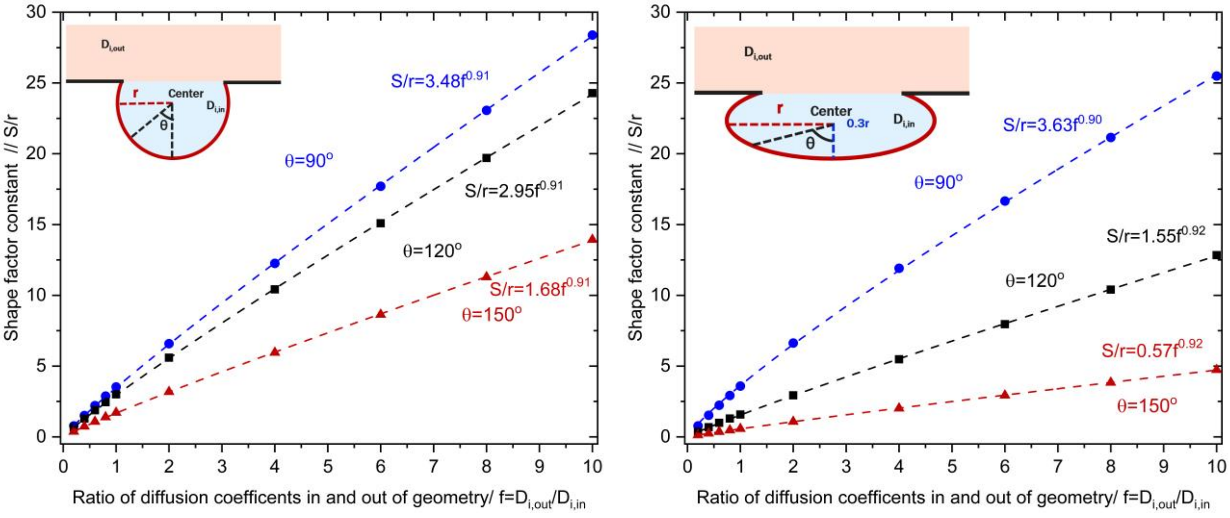

a) **b)**

Figure 4.10. Shape factor constant as a function of the diffusion coefficients between inside and outside of the **a)** spherical geometry and **b)** oblate spheroidal geometry with *c/r*=0.3 for *θ*=90° (blue),120° (black), and 150° (red). The dashed lines and the equations refer to the fit equation for each case. The geometrical dimension connected to the shape factor constant is the radius of the geometry, *r*.

Figure 4.10a illustrates the variations in the shape factor constant for a spherical body as a function of $\theta \geq 90°$. The results indicate that the shape factor depends on the ratio of the diffusion coefficients inside and outside the spherical geometry. This relationship follows a power-law behavior, described by Equation 4.13:

$$S_f = S_{f=1} \cdot f^q \tag{4.13}$$

where f is the ratio of the diffusion coefficient of species i in the bulk to the diffusion coefficient of the same species inside the spherical medium, S_f is the shape factor at a given fraction f, $S_{f=1}$ is the shape factor when $f=1$(values provided in Figure 3 for spherical bodies), and q is a fitting parameter determined to be approximately 0.91, independent of angle θ.

Figure 4.10b extends this analysis to oblate spheroidal geometries with angles θ of 90°, 120°, and 150°. Like spherical geometries, the shape factor variation adheres to Equation 4.13. Notably, the fitting parameter q consistently remains around 0.91 across these cases independent of angle θ.

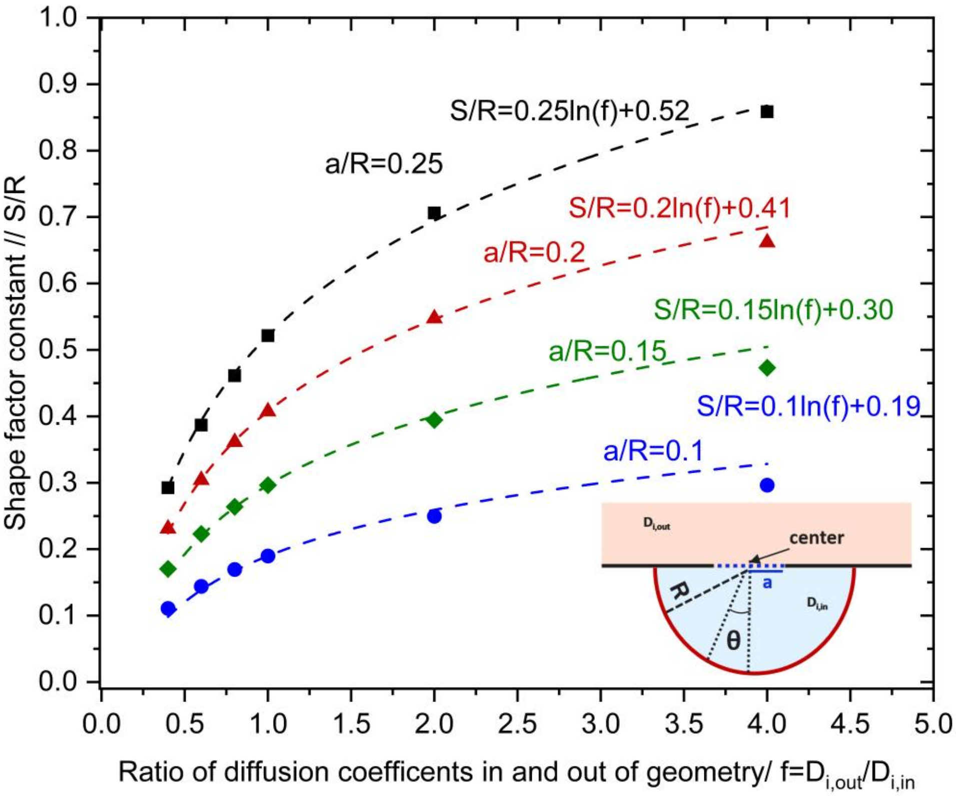

Figure 4.11. Shape factor constant as a function of the ratio of the diffusion coefficients outside and inside the hemispherical geometry with an insulation along its diameter and one circular hole on its center with radius *a*=0.25*R*(black), *a*=0.2*R*(red), *a*=0.15*R*(green), and *a*=0.1*R*(blue). The fitted dotted line and the pertaining equations are also shown. The geometrical dimension connected to the shape factor constant is the radius of the spherical body, *R*.

Figure 4.11 depicts the variation of the shape factor constant as a function of the diffusion coefficient ratio, *f*, between the interior and exterior of a hemispherical body with a lacy cover spanning its diameter and a central circular hole of radius *a*. Four cases are presented, where the *a/R* ratio varies between 0.1 and 0.25, with *R* representing the radius of the hemispherical body. Across all cases, a logarithmic relationship is observed between the shape factor and *f*. The fitted equation, represented by dashed lines in Figure 4.11, indicates that the shape factor for this configuration can be expressed by Equation 4.14:

$$S_{c,f} = \frac{a}{R} ln(f) + S_{c,f=1} \tag{4.14}$$

Here, $S_{c,f}$ denotes the shape factor of the hemispherical geometry (with radius *R*) that includes an insulating cover with a hole of radius a, while $S_{c,f=1}$ corresponds to the shape factor for the case where the diffusion coefficients of species *i* are identical inside and outside the geometry.

4.4.6. Location of the sink surface

To simulate and calculate the flux of species i between the inner surface of a given geometry and a distant boundary ideally placed at infinity, for the FEM calculations the distance between these two surfaces is typically chosen to be over 10^5 times larger than the size of the geometry of interest (*e.g.*, radius of a hemisphere or oblate spheroid). In this section, however, we investigate scenarios where the sink surface for the species is located adjacent to the geometry of interest.

This configuration is relevant in cases where metallic ionic species generated within a pit migrate toward a nearby cathode. Here, the cathode effectively acts as a "sink" for these metallic cations. In the first part of this section, we examine the case of varying c/r ratio between 0.1 and 1 and θ=90°,with and without an insulating layer at the mouth with a circular opening at the center of radius $a=0.1r$ Then we examine the shape factor for spherical and spheroidal geometries with a c/r ratio of 0.3, 0.6 and 1 and opening angles $\theta \geq 90°$, with the sink surface positioned adjacent to the geometry. Schematics of geometry of geometries of interest with the boundary conditions are shown along the corresponding results in Figure 4.12a.

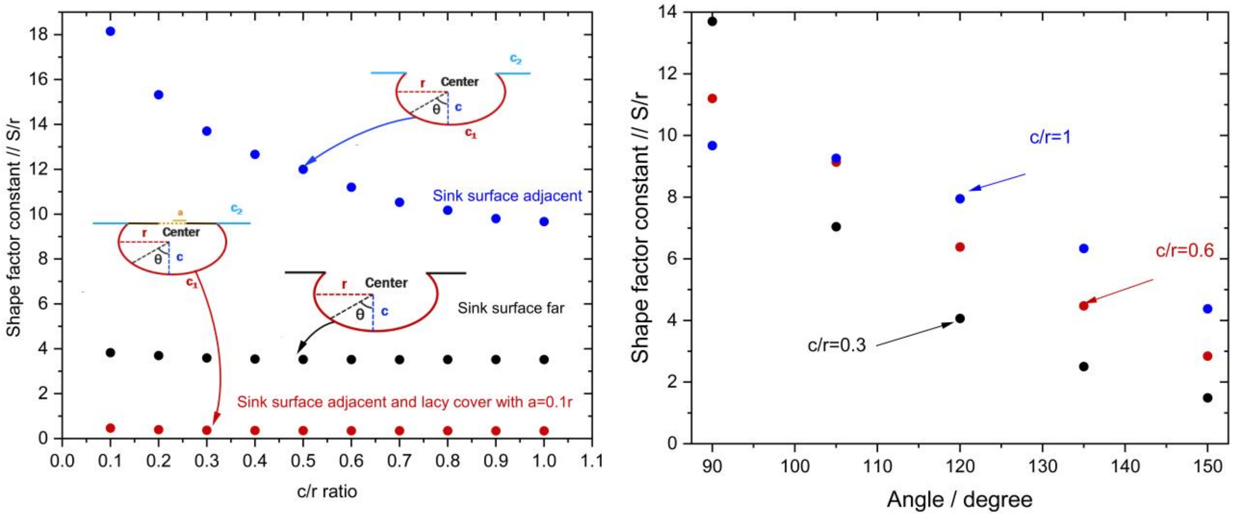

a) **b)**

Figure 4.12.a) Shape factor constant calculations and the pertaining schematics for c/r ratio between 0 and 1 and θ=90° for different locations of the sink surface (base case in black is for the sink far away from the spheroidal body (base case in black). Sink adjacent without an insulating layer (blue) and placed adjacent with an insulating layer at the mouth with a circular opening of radius $a=0.1r$(red) and **b)** variations of the shape factor constant as a function of the angle θ for various c/r ratios and the sink surface adjacent to the spherical/spheroidal body without a lacy cover. The geometrical dimension connected to the shape factor constant is the radius of the geometry, r.

Figure 4.12a compares the variations in the calculated shape factor constant for θ=90° and $0 \leq \frac{c}{r} \leq 1$ for the cases where the sink surface is effectively infinitely far away (10^5 times larger than r-in black), adjacent to the other surface (in blue), and adjacent with and without the presence of a lacy cover of radius a (in red). The findings suggest that the shape factor constant is significantly higher (between 3 to 4 times) than when the sink surface is placed at large distance without the presence of the lacy cover (base case). When an insulating layer with a circular opening of radius a is placed at the mouth, the shape factor constant decreases to approximately 10 % of the base case.

Figure 4.12b illustrates the influence of the *c/r* ratio and the angle *θ* on the shape factor constant of the spherical/spheroidal body when the sink surface for the species is positioned adjacent to the body, as depicted in Figure 4.12a. Similar to the scenario where the sink surface was located at large distances (Figure 4.5a), the shape factor constant in this configuration also decreases as angle *θ* increases from 90^o to 150^o. However, it is notable that the shape factor constant is consistently higher when the sink surface is adjacent to the body compared to when it is placed at large distances, across all tested *c/r* ratios. Additionally, the results shown in Figure 4.12b are not normalized using Equation 4.10, as no fitting equation was identified that could accurately capture the combined effects of *c/r*. Finally, as observed in the findings in Figure 4.5a, the data in Figure 4.12b reveal that for $\theta \neq 90°$ the shape factor constant corresponding to *c/r*=1 is consistently larger than those associated with other *c/r* ratios.

4.4.7. Effect of other geometrical constraints

The results from the previous section indicate that the location of the sink surface significantly impacts the shape factor. Building on this, we explore additional scenarios for spherical and oblate spheroidal geometries (*c/r*=0.3) with angles *θ*=90°, *θ*=120°,and *θ*=150°. Results are presented to show the impacts of the electrolyte thickness, *L*, the diameter of the surrounding surface, *D*, and the interaction between them.

The following cases are considered:

1. *H* is varied, with the sink surface not adjacent to the geometry. A schematic representation of this setup is provided with the results in Figure 4.13a and 4.13b.
2. *L* is varied while keeping its location adjacent to the geometry of interest. In this configuration, the far boundary, distance *H* from the geometry interest, is insulated. A wide range of *L/r* is considered, from 0.3 to 10^5. A schematic for this case is shown with the results in Figure 4.14a. Only results for ratio of *c/r*=0.3 are shown.

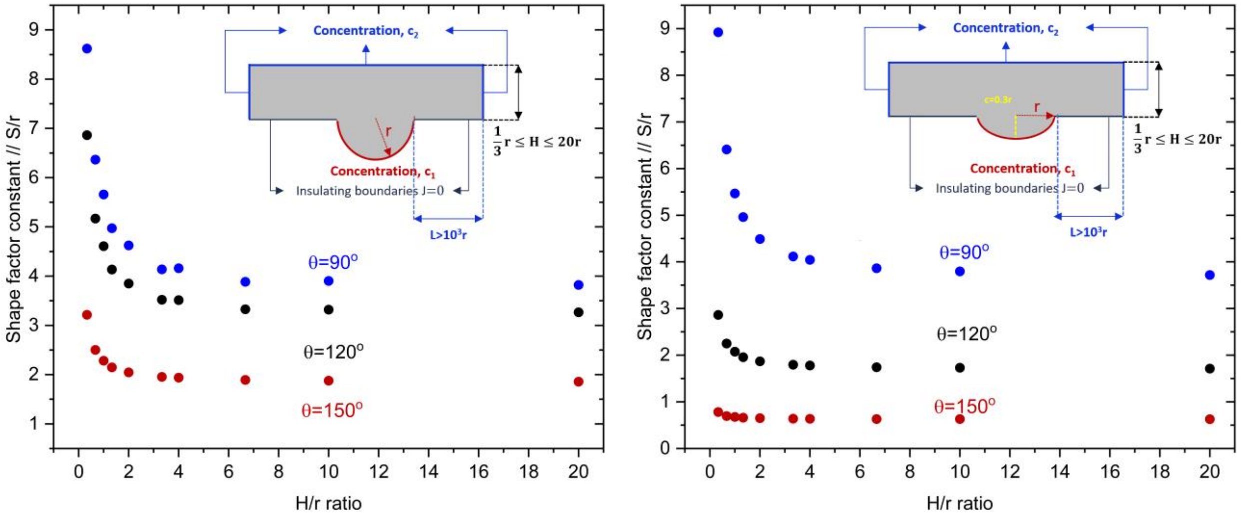

a) **b)**

Figure 4.13. Shape factor constant as a function of *H/r* ratio for **a)** *c/r*=1 (spherical) and **b)** *c/r*=.3 (oblate spheroidal for three different angle *θ*=90° (blue), *θ*=120° (black), and *θ*=150° (red). 2D schematics of the pertaining geometry and the boundary conditions are shown in each one of the figures. The geometrical dimension connected to the shape factor constant is the radius of the geometry, *r*.

Figures 4.13a and 4.13b present the results for case 1, corresponding to *c/r*=1 and *c/r*=0.3, respectively, across the three angles of interest: 90°,120°, and 150°. As shown in Figure 4.13a, H is the distance between the geometry of interest and sink surface toward which the species *i* travel. In both cases and for all angles, increasing the *H/r* ratio causes the shape factor constant to decrease, approaching the value observed for an infinitely large *H/r*. This trend is consistent across all tested angles. As previously noted, the shape factor decreases as *θ* increases from 90° to 120°, and further to 150°.

For *c/r*=1, the reduction in shape factor constant is more pronounced when angle *θ* increases from 90° to 120° compared to the change from 120° to 150°. Conversely, for *c/r*=0.3, the reduction in shape factor is more significant between 120° and 150° than between 90° and 120°. Finally, for both *c/r* ratios and all angles, the shape factor constant exhibits minimal further decrease once *H/r*≈6 is reached.

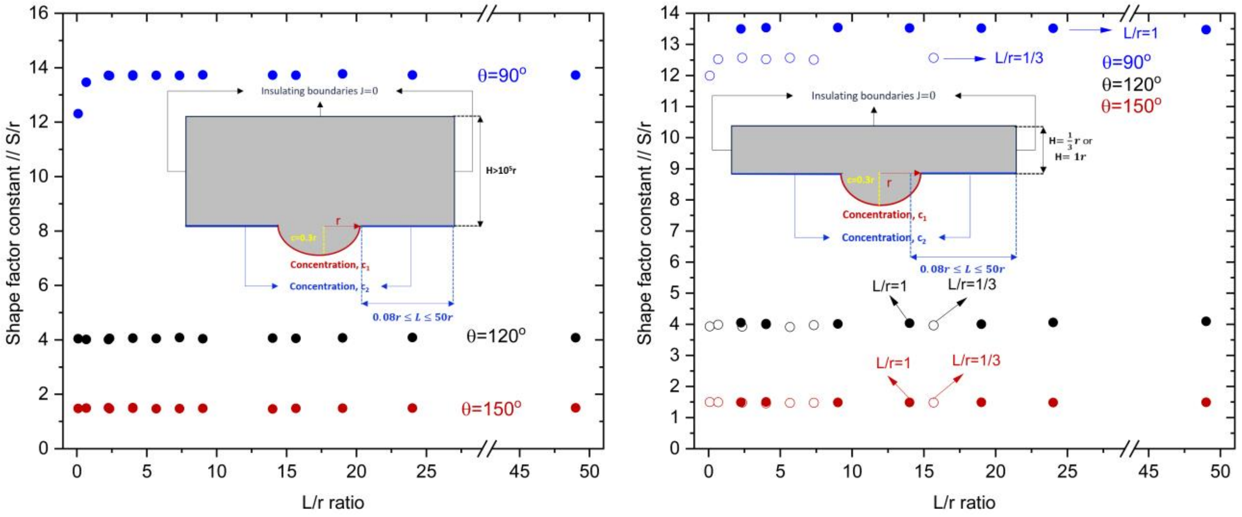

a) **b)**

Figure 4.14. Shape factor constant as a function of *L/r* ratio for *c/r*=0.3 for case 2: **a)** large *H/r* and **b)** small *H/r* for three different angle *θ*=90° (blue), *θ*=120° (black), and *θ*=150° (red). For small *H/r*, the results for two different *H/r* ratio of 0.3 (empty circles) and 1 (full circles) are shown. The geometrical dimension connected to the shape factor constant is the radius of the geometry, *r*.

Figures 4.14a and 4.14b present the results of shape factor constant as a function of *L/r* ratio when *c/r*=0.3 and angle *θ* is 90°, 120°, and 150°, for case 2. In Figure 4.14b, the effects of the *H/r* ratios of 1/3 and 1 on the shape factor are also explored. These conditions were used to isolate the influence of *H* size from that of *L* when the sink surface is adjacent to the geometry of interest.

The results presented in Figure 4.14a demonstrate that when the sink surface for the species is positioned adjacent to the mouth of the geometry and *H* is large, the shape factor constant for *c/r*=0.3 is generally independent of the *L/r*. Deviations from this trend are observed only in the case of *θ*=90º and *L/r*<2. Figure 4.14b shows that under the same scenario, when *H* is reduced to *H/r*=1 or *H/r*=1/3, and for angles of 120º and 150º, the shape factor constant remains independent of both the *L/r* and *H/r* ratios. However, for *θ*=90º the shape factor for *H/r*=1 is slightly higher (by approximately one) than that for *H/r* = 1/3 across all *L/r* ratios. Additionally, a minor decrease in the shape factor constant is observed for of *θ*=90º *L/r*<2, and *H/r*=1/3.

4.4. Discussion

The utility of the shape factor is its ability to adjust the flux obtained under one-dimensional conditions (*i.e.*, 1D pit experiments with the cathode effectively at infinity) to 3D shapes with the cathode at different locations. In this way, the relative stability of different pit geometries can be assessed based on the assumption that the value of $(i \cdot x)_{crit}$ extracted from the 1D pit measurements captures the critical conditions necessary for continued pit growth. This section places the results described above into the context of the pitting characteristics commonly observed.

To focus on the impact of pit shape, the calculations presented above assumed that the pitting process was under either primary (ohmic control) or Tertiary (diffusion control) current distribution. Multiple characteristics of pit shape were shown to be important, including the general shape of the pit, the dimensions, the presence of a lacy cover (or other impediment to flux at the pit mouth), the location of the cathode, the water layer thickness, and the decrease in the mass transport properties of the concentrated solution within the pit relative to the bulk solution outside.

The section begins with discussion of the strong dependence of shape factor constant on the details of pit shape. Next, the large impact of having the cathode (*i.e.*, the sink surface for the flux) adjacent to the pit is considered along with the limited impact of water layer thickness and the change in transport properties within the pit. Finally, the impact of pit shape on pit stability is demonstrated by consideration of the effects of shape factor constant on the size of pits that can be grown for a given cathode with limited current capacity.

4.5.1. Pit geometries observed in service can lead to very low shape factor constant

A key result of this work is the demonstration that pit geometry can have a very large effect on pit stability. Recall that shape factor constant can be thought of as an ease of mass transport through a medium. Thus, it indicates how much current would be needed to maintain the same chemistry at the surface of that shape, as shown in Equation 4.5 reproduced below:

$$I = SzFD\Delta C \tag{4.5}$$

The easier mass transport is, the higher the current needed. In the case of localized corrosion, that is the metal dissolution current which determines the local chemistry. One utility of S comes in its ability to allow translation of 1D pit experiments to 3D shapes:

$$I_{crit} = S(i \cdot x)_{crit} \tag{4.6}$$

One can consider S to be the multiplier of the flux needed to maintain the critical chemistry and/or potential at the surface of the pit for a given shape relative to a 1D pit. An alternative framework for understanding S is that it represents the overall conductance of the medium measured between the source and sink. Higher values of shape factor constants indicate easier species transport, making it more challenging to maintain critical pit conditions. Consequently, only smaller pits of that shape remain stable.

Values for the constant of shape factor constant for a hemispherical pit in the literature have clustered around three[27,32,33], including by one of the authors.[29] The present work shows unequivocally that the actual value of shape factor constant for that geometry is 3.52. This higher shape factor constant would indicate that hemispherical pits have a more difficult time remaining stable than for previously reported shape factors as they would need ~17% more current. Of course, shallow, dish-shaped pits have higher *S*, approaching 4 as shown in Figure 4.5.

This work has also shown that more occluded pits can have a shape factor constant significantly less than 1 due to increased resistance to mass transport. The shape factor constant decreases as the degree of occlusion increases. Lacy covers, commonly observed in service,[5,34] can dramatically impact the shape factor constant. For instance, a single hole in the cover with $a/R = 0.3$ can reduce the shape factor constant to 0.7-an 80% decrease- with the impact scaling linearly with the number of identically sized holes for small holes (*e.g.*, hole radius = 0.01 × pit radius) (Figure 4.9b). Pits-within-pits show little effect from a second pit if the first remains active (Figure 4.8). However, if the primary pit repassivates, the second pit can reduce the shape factor constant by approximately 40% (Figure 4.8). Similarly, occluded spheroids exhibit lower shape factor constants than hemispheroids, and can drop *S* below 1 for ink-well shapes (*i.e.*, $\theta > 135°$), as shown in Figure 4.4. Oblate spheroids also demonstrate decreased shape factor constants compared to hemispheres, with the rate of decrease depending on the occlusion angle and increasing as c/r decreases (*i.e.*, as the shape becomes more ellipsoidal), as shown in Figure 4.5.

4.5.2. Adjacent cathodes of equivalent size compared to a remote cathode reduce the stability of pit

As explained in the case addressing the pit occlusion, the location of the cathode relative to the pit significantly influences the shape factor and, consequently, pit stability. A cathode positioned adjacent to the pit substantially increases the shape factor constant, reducing pit stability for any given pit geometry. When the cathode is so close, mass transport occurs more easily, making it more difficult to retain the critical chemistry due to the minimal IR drop in the bulk electrolyte. Figure 4.12 illustrates this impact. When the sink surface is remote, the pit's oblateness (*i.e.*, its c/r) has no effect on the shape factor constant. However, when the sink surface is adjacent, the shape factor constant increases dramatically. For a hemispherical pit, the shape factor constant is approximately three times larger, and as c/r decreases, the difference compared to a remote sink increases, reaching nearly six times larger.

This effect of an adjacent cathode has interesting ramifications for the use of laboratory-derived pitting data for prediction of service performance. The most common laboratory pitting testing involves the use of a potentiostat to control the potential (or current) with a counter electrode well away from the surface of the working electrode (*WE*) where pitting will occur. This arrangement represents an L/r approaching infinity with a remote cathode. A lower shape factor constant would be expected with an adjacent cathode. This lower shape factor constant would imply that one could create/maintain pits in a potentiostatic test that would not be stable with an adjacent cathode.

Note that the discussion in this section assumed that the electrolyte layer was very large relative to the pit size, *i.e.*, $H > 10^5 r$. This assumption removes any impact of the size of the electrolyte on the results.

4.5.3. Impact of water layer thickness

The previous section of this discussion focused on the impact of the cathode or sink surface position relative to the pit. However, in atmospheric pitting, not only is the cathode surface adjacent to the pit, but also the electrolyte solution volume is limited, as defined by *H* and *L*. The thickness of this water layer is known to have a significant effect on localized corrosion.[3,35]

Figure 4.13 presents results for cases where *L* is very large but insulating, while *H* varies relative to *r* from 0.3 to 20. In Figure 4.13a, the pit is hemispherical (*i.e.*, a spheroidal pit with $c/r = 1$), whereas in Figure 13b, the pit is an oblate spheroid with $c/r = 0.3$, making it more dish-like. In both scenarios, a small water layer results in very high shape factor constant values. This result aligns with the expectation that a thin *H* causes a large ohmic drop, forcing more current to remain close to the pit and hindering the growth of larger pits. However, once the *H* exceeds ~4*r*, the shape factor becomes constant, with its value dictated by the occlusion angle (θ). Higher angles lead to lower shape factor constants, as demonstrated in Figures 4.3-4.5 and discussed above.

The limited impact of *L* on the shape factor for a range of spheroidal pits is shown in Figure 14 in which the cathode is adjacent to the pit, and the *H* ranges from very small ($H/r = 0.3$) to very large ($H/r > 10^5$). For all *H/r*, the shape factor quickly plateaus at small L. In all cases of the spheroidal pit, from hemispherical ($\theta = 90°$) to quite occluded ($\theta = 150°$), the level of occlusion of the pit completely dominates the shape factor, as shown in Figures 4.3-4.5. This result is due to the assumption of the current distribution being either primary or Tertiary, making interfacial electrochemical kinetics irrelevant.

4.5.4. Slower transport properties within pits have a more limited impact in stabilizing pits

It is well known that the concentrated solutions present in localized corrosion sites have lower transport properties, such as *D*, so the impact on shape factor is of interest. Ianuzzi et al.[36] showed that in moving from a highly diluted solution (*e.g.*, 0.05 M [Cl^-]) to near saturation (*i.e.*, 9 M [Cl^-]), the diffusion coefficients of all ions studied including Na^+, Cl^-, $FeCl^+$, and Fe^{2+}, decreased by approximately a factor of two. Considering Figure 4.11, if $D_{i,out}/D_{i,in} = 2$, then the shape factor constant would increase from 3.53 to ~6, making it more difficult to maintain pit stability, as one might think, as the slower transport within the pit would aid in the retention of the critical solution composition. These results also show that as the degree of occlusion of the pit increases, the impact of the ratio of diffusivities between the outside and inside the pit lessens.

4.5.5. Overall implications for pit stability

This work has developed a methodology for assessing the relative stability of the range of pit shapes observed in practice. Although this information alone can be of use, when the different pit shapes are coupled to a cathode that can supply only a finite current in support of pit growth, a more intuitive appreciation of the impact of pit shape can be had. Figure 4.15 shows plots of the maximum cathodic current as a function of pit size. The shape of the curve has been discussed elsewhere.[29] Superimposed on the maximum cathode current line are seven different cases for the minimum anodic current needed to maintain the pit stability. In Figure 4.15, the change in shape factor constant can change the expected maximum pit size from 27μm (S=6.59r) to as much as 374μm (S=0.75r). The conditions used are reasonable for atmospheric pitting of stainless steel, but they are arbitrary as the goal of the cases selected is to simply illustrate the engineering impact of pit shape.

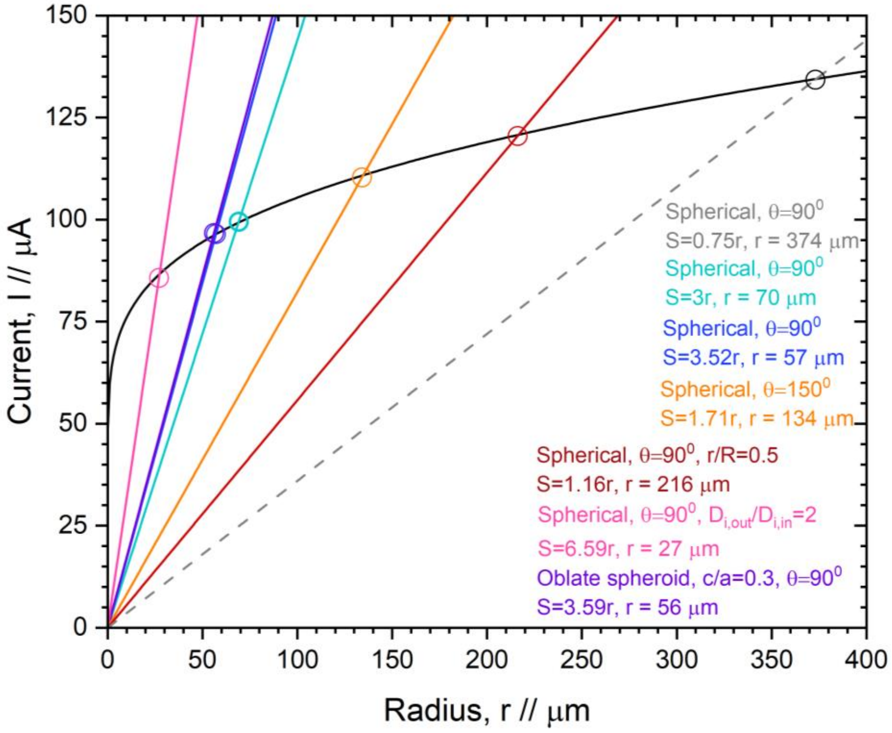

Figure 4.15. Maximum pit size calculations for SS304 in 0.6M NaCl. Current for the anodic (linear lines) and cathodic (curved black line) are shown as a function of radius of pit. Anodic curves are extracted from the artificial pit experiments while the cathodic line is generated in surrogate solution of 0.73M NaBr in accordance with work from Katona et.al[11]

The base case of a hemispherical pit has an $S = 3.52r$ and a predicted maximum pit size of 57μm. If one were to account for lowered diffusion coefficients within the pit, an $S = 6.59r$ would lead to a pit size of 27μm. The impact of occlusion is clear for the other cases considered. An undercutting hemisphere (*i.e.*, an “inkwell”) with an opening angle of 150° would lead to a decreased S (1.71r) and a substantial increase in the pit size to 134μm. A lacy pit cover with a single perforation with radius half that of the pit radius is a strong stabilizing force, leading to a pit size of 216μm. The most severe case shown has an S of 0.75r. This shape factor would result from either a single perforation lacy cover with a radius 35% that of the pit radius, or a lacy pit cover in which each hole had a radius of just 5% of the pit radius, but there were ten of them perforating the cover.

The significance of this exercise lies in the depth of understanding required to accurately estimate potential pit size in a pitting system. If one assumes an open hemispherical pit but fails to account for a lacy cover or other mass transport impediments, such as dust,[37] the maximum pit size would be severely underestimated. Although the foundation of the maximum pit size model is simply the Law of Charge Conservation, its predictive accuracy depends on the quality of the input data, as with any model. The key challenge in pit prediction is the need for a reasonable *a priori* estimate of pit shape, as any assumed geometry could lead to either conservative or non-conservative predictions. The range of pit shapes discussed above, though extreme, remain plausible.

4.5.6. Limitations and their implications

The assumptions used to derive shape factors in general should be emphasized and the limitations they impose appreciated. The shape factor is only defined when the conditions along the pit surface are constant. Shape factor constants can be considered the ratio of flux to the driving force. For primary current distribution, the shape factor constant represents the conductance as the ratio of the ionic current to the potential. For Tertiary current distribution, the shape factor constant represents the diffusion coefficient for the medium as the ratio of the flux to the concentration gradient. This definition of shape factor is that used in other fields.[26,31] For pits under mixed control, the shape factor s undefined for, as the driving force is a function of position, and it thus affects the kinetics inside and outside the pit. Mixed control may well describe the conditions under which pitting occurs in some systems.

An additional characteristic of these analyses is the assumption of steady state conditions. Pit stability has always been considered in terms of a steady state, that is, the conditions under which the critical conditions of potential/chemistry can be maintained at the pit surface. Such an assumption is made to simplify the mathematics as well as focus on the propagation of pitting as it is generally of most concern for engineering structures. That said, the FEM results discussed here can be used to gain insight into the relative stability of portions of a pit by considering the current distribution within the pit shape. That relative stability reveals the conditions required for pits to retain their shape during propagation.

Recall that the shape factor constants are calculated under the assumption of constant conditions (*i.e.*, potential or concentration) at all positions along the pit surface. Because of differences in the transport path, this assumption leads to a distribution of current densities along the pit surface with the highest current densities near the mouth. The higher current densities are captured in Figure 4.4a which demonstrates that as the degree of occlusion increases, the amount of current from the upper portion of the pit increases. Figure 4.4b presents the data in a different framework, that of the shape factor constant of the upper vs. lower portions of the pit.

For a hemispherical pit, the current density is the same along the entire pit surface, and thus it can continue to grow as a hemisphere as long as the conditions remain constant. A more occluded pit, such as a spheroidal pit with $\theta = 135°$, would not be stable in shape if the conditions were constant along its surface. Instead, the higher current densities near the mouth would lead to the pit shape moving towards a hemisphere, but if and only if the conditions were constant along the pit surface. To maintain a non-hemispherical pit shape, there must be a distribution in surface concentration or potential that impacts the current density in such a way that it impacts dissolution near the mouth. Otherwise, for any $c/r > 1$, the pit would evolve towards a hemisphere, and for any $c/r < 1$, the shape would become more dish-like.

In reality, however, pit stability is a dance between potential and concentration distributions. These distributions lead to the range of pit shapes observed. One example of such is the fact that most lacy covers have pits that are far closer to oblate spheroids than they are to hemispheres.[5,34] Just under the lacy cover the current density is very high due to high potential and a relatively low surface concentration. Deeper in the pit, the potential drop makes the condition less aggressive despite what must be higher surface concentrations.

Note that none of the discussion in this section impacts any of the conclusions reached given the underlying assumptions under which the results were generated.

4.6. Conclusions

In this study, FEM was employed to predict the shape factor constant of various geometries and configurations relevant to localized corrosion. Using a 3D steady state diffusion physics interface, the chapter showed the shape factor values for spherical and oblate spheroidal geometries, including undercutting features (spherical and disk-shaped pits), bispherical bodies (pit-within-pit structures), and covered pits with perforated (lacy) covers. Additionally, differences in transport conditions between the pit interior and exterior, as well as the cathode's location, were shown to influence the shape factor. Based on these analyses, the following conclusions were drawn:

1. Pits with undercuts (occluded pits) generally exhibit lower shape factor values (sometimes below 1) compared to open pits.
2. Disk-shaped pits have a smaller shape factor constant than spherical ones, with the value decreasing as the c/r ratio and occlusion angle (θ) increase, except when $\theta = 90°$.
3. A predictive method for the shape factor, and consequently the maximum size, of a pit-within-a-pit is presented. Results indicate that a second pit has minimal effect if the first pit remains active.
4. An empirical equation was presented to quantify the effect of a lacy cover on the shape factor, demonstrating that its presence significantly reduces the shape factor value.
5. Elevated salt concentration within pits, leading to slower ionic transport, have a limited role in stabilizing pits compared to geometrical factors. Additionally, as pit occlusion increases, the influence of the diffusivity ratio of ions between the pit interior and exterior diminishes.

6. Certain pit geometries observed in service can result in very low shape factor values. Specifically, a thin electrolyte layer and the presence of an adjacent cathodic sink increase the shape factor, thereby reducing pit stability.

4.7. References

1. Tester, J. W. & Isaacs, H. S. Diffusional Effects in Simulated Localized Corrosion. *J. Electrochem. Soc.* **122**, 1438–1445 (1975).
2. Steinsmo, U. & Isaacs, H. S. Dissolution and Repassivation Kinetics of Fe-Cr Alloys in Pit Solutions: I . Effect of the Surface Salt Layer. *J. Electrochem. Soc.* **140**, 643–653 (1993).
3. Laycock, N. J. & Newman, R. C. Localised dissolution kinetics, salt films and pitting potentials. *Corros. Sci.* **39**, 1771–1790 (1997).
4. Ernst, P. & Newman, R. C. Pit growth studies in stainless steel foils. I. Introduction and pit growth kinetics. *Corros. Sci.* **44**, 927–941 (2002).
5. Srinivasan, J., McGrath, M. J. & Kelly, R. G. A High-Throughput Artificial Pit Technique to Measure Kinetic Parameters for Pitting Stability. *J. Electrochem. Soc.* **162**, C725–C731 (2015).
6. Srinivasan, J. & Kelly, R. G. Evaluating the Critical Chemistry for Repassivation at the Corroding Surface Using Mass Transport Model-Based Artificial Pit Experiments. *J. Electrochem. Soc.* **163**, C768–C777 (2016).
7. Li, T., Scully, J. R. & Frankel, G. S. Localized Corrosion: Passive Film Breakdown vs Pit Growth Stability: Part II. A Model for Critical Pitting Temperature. *J. Electrochem. Soc.* **165**, C484–C491 (2018).
8. Li, T., Scully, J. R. & Frankel, G. S. Localized Corrosion: Passive Film Breakdown vs. Pit Growth Stability: Part IV. The Role of Salt Film in Pit Growth: A Mathematical Framework. *J. Electrochem. Soc.* **166**, C115–C124 (2019).
9. Li, T., Wu, J. & Frankel, G. S. Localized corrosion: Passive film breakdown vs. Pit growth stability, Part VI: Pit dissolution kinetics of different alloys and a model for pitting and repassivation potentials. *Corros. Sci.* **182**, 109277 (2021).
10. Katona, R. M., Carpenter, J., Schindelholz, E. J. & Kelly, R. G. Prediction of Maximum Pit Sizes in Elevated Chloride Concentrations and Temperatures. *J. Electrochem. Soc.* **166**, C3364–C3375 (2019).
11. Marshall, R. S., Katona, R. M., Melia, M. A. & Kelly, R. G. Pit Stability Predictions of Additively Manufactured SS316 Surfaces Using Finite Element Analysis. *J. Electrochem. Soc.* **169**, 021506 (2022).
12. Carslaw.H.S. *Introduction to the mathematical theory of the conduction of heat in solids*. (Macmillan and Co., 1921).
13. Crank, J. *The Mathematics of Diffusion*. *Journal of the American Chemical Society* (Clarendon pRESS, 1957).
14. Vetter, K. J. *Electrochemical Kinetics, Theoretical and Experimental Aspects*. (Academic Press Inc., 1967).
15. Beck, T. R. & Grens, E. A. An Electrochemical Mass Transport-Kinetic Model for Stress Corrosion Cracking of Titanium. *J. Electrochem. Soc.* **116**, 177–184 (1969).
16. Frankenthal, R. P. & Pickering, H. W. On the Mechanism of Localized Corrosion of Iron and Stainless Steel. *J. Electrochem. Soc.* **119**, 1304 (1972).

17. Galvele, J. R. Transport Processes and the Mechanism of Pitting of Metals. *J. Electrochem. Soc.* **123**, 464–474 (1976).
18. Galvele, J. R. Transport processes in passivity breakdown-II. Full hydrolysis of the metal ions. *Corros. Sci.* **21**, 551–579 (1981).
19. Gravano, S. M. & Galvele, J. R. Transport processes in passivity breakdown—III. Full hydrolysis plus ion migration plus buffers. *Corrosion* **24**, 517–534 (1984).
20. Newman, R. Pitting Corrosion of Metals. *Electrochem. Soc. Interface* **19**, 33–38 (2010).
21. Srinivasan, J., Liu, C. & Kelly, R. G. Geometric Evolution of Flux from a Corroding One-Dimensional Pit and Its Implications on the Evaluation of Kinetic Parameters for Pit Stability. *J. Electrochem. Soc.* **163**, C694–C703 (2016).
22. Li, T., Scully, J. R. & Frankel, G. S. Localized Corrosion: Passive Film Breakdown vs Pit Growth Stability: Part V. Validation of a New Framework for Pit Growth Stability Using One-Dimensional Artificial Pit Electrodes. *J. Electrochem. Soc.* **166**, C3341–C3354 (2019).
23. Alwitt, R. S., Uchi, H., Beck, T. R. & Alkire, R. C. Electrochemical Tunnel Etching of Aluminum. *Electrochem. Soc. Ext. Abstr.* **82–2**, 108–109 (1982).
24. Hebert, K. & Alkire, R. Growth and Passivation of Aluminum Etch Tunnels. *J. Electrochem. Soc.* **135**, 2146–2157 (1988).
25. Hebert, K. R. A Mathematical Model for the Growth of Aluminum Etch Tunnels. *J. Electrochem. Soc.* **148**, B236 (2001).
26. Yovanovich, M. A general expression for predicting conduction shape factors. in *11th Aerospace Sciences Meeting* (American Institute of Aeronautics and Astronautics, 1973). doi:doi:10.2514/6.1973-121.
27. Pistorius, P. C. & Bustein, G. T. Metastable pitting corrosion of stainless steel and the transition to stability. *Philos. Trans. R. Soc. London. Ser. A Phys. Eng. Sci.* **341**, 531–559 (1992).
28. Faraday, M. On Static Electrical Inductive Action. *Philos. J.* **22**, 200–2004 (1844).
29. Chen, Z. Y. & Kelly, R. G. Computational Modeling of Bounding Conditions for Pit Size on Stainless Steel in Atmospheric Environments. *J. Electrochem. Soc.* **157**, C69 (2010).
30. Chen, Z. Y., Cui, F. & Kelly, R. G. Calculations of the Cathodic Current Delivery Capacity and Stability of Crevice Corrosion under Atmospheric Environments. *J. Electrochem. Soc.* **155**, C360 (2008).
31. Warren, R. M., James, H. P. & I.Young, C. *Handbook of Heat Transfer*. *Computer Vision* (McGraw-Hill, 1998). doi:10.1007/978-3-030-63416-2_844.
32. Williams, D. E., Stewartt, J. & Balkwill~, P. H. The nucleation, growth and stability of micropits in stainless steel. *Corros. Sci.* **36**, 1213–1235 (1994).
33. Pride, S. T., Scully, J. R. & Hudson, J. L. Metastable Pitting of Aluminum and Criteria for the Transition to Stable Pit Growth Metastable Pitting of Aluminum and Criteria for the Transition to Stable Pit Growth. *J. Eectrochemical Soc.* **141**, 3028–3040 (1994).
34. Ernst, P., Laycock, N. J., Moayed, M. H. & Newman, R. C. The mechanism of lacy cover formation in pitting. *Corros. Sci.* **39**, 1133–1136 (1997).

35. Katona, R. M. *et al.* Editors' Choice—Natural Convection Boundary Layer Thickness at Elevated Chloride Concentrations and Temperatures and the Effects on a Galvanic Couple. *J. Electrochem. Soc.* **168**, 031512 (2021).
36. Wang, K., Salasi, M. & Iannuzzi, M. A Comprehensive Numerical Model for One-Dimensional Pit Growth of 316L SS under a Salt Film. *J. Electrochem. Soc.* **168**, 121504 (2021).
37. Schaller, R. F. *et al.* Observations of Atmospheric Corrosion Testing on Heated Austenitic Stainless Steel Surfaces: Exploring the Role of Inert Dust Particulates and Seawater. *Nucl. Technol.* **210**, 1658–1671 (2024).

A4. Appendix

Pistorius and Burstein[27] proposed an analytical solution to determine the shape factor of a three-dimensional hemispherical pit under conditions of ohmic control. In summary, their approach involves considering a hemispherical pit of radius r, as shown in Figure A4.1, where the pit surface is maintained at a constant potential E_1. The resistance (R_2) of the current flux from the surface at E_1 to a counter electrode located at infinity, maintained at a constant potential E_2, is modeled by subtracting the resistance (R_3) associated with the outer portion of the hemispherical pit from the combined resistances (R_1 + R_2) of current flow between two thin disks: one at potential E_3 and the other at the counter electrode surface at E_1.

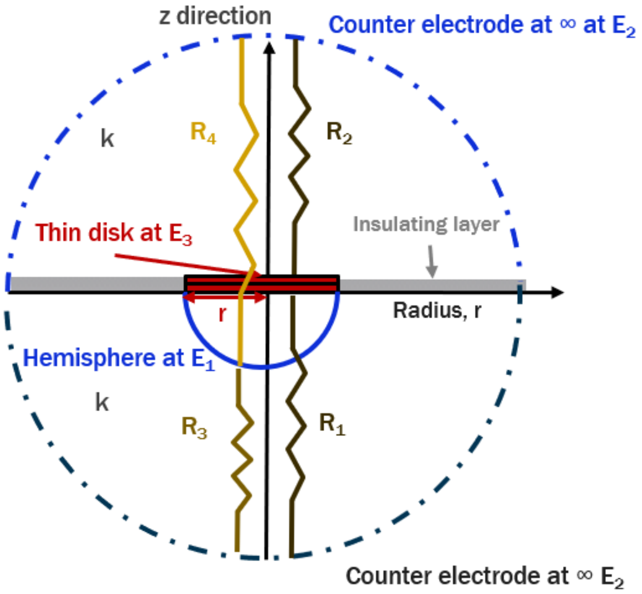

Figure A4.1. Two-dimensional schematic representation of three-dimensional geometry utilized in the analytical approach from Pistorius and Burstein [27] in calculating the shape factor from the inner region of hemispherical geometry (solid blue) to a counter electrode at infinity (dashed blue and black). Two thin disks (red) were considered between two insulated thin layers (gray). Lines in zig-zag fashion represent the resistances between the surfaces at which their lines start and finish.

The total resistance, R_T, can be expressed as:

$$R_T = R_1 + R_2 = R_4 + R_5 - R_3 = \frac{1}{4ur} + \frac{1}{4ur} - \frac{1}{2\pi ur} = \frac{1}{2ur}\frac{\pi-1}{\pi} \qquad \text{(A4.1)}$$

here, $R_4 = R_5 = \frac{1}{4kr}$ are the resistances of two thin disk in an infinite medium, and $R_3 = \frac{1}{2\pi kr}$ is the resistance from the outer region of the hemisphere to an infinite medium. Using the definition of the shape factor in Equation A4.1, the shape factor for a hemispherical pit is approximately:

$$S = \frac{2\pi}{\pi - 1} r = 2.934r \approx 3r \qquad \text{(A4.2)}$$

Building on the methodology outlined by Pistorius and Burstein[27] the approach from Figure A4.1 above can be extended to various pit geometries, including hemispherical pits with varying degrees of undercutting, dish-shaped pits, and pits with lacy covers. The resistance R_3 for various geometrical configurations was obtained from the work of Yovanovich.[26]

A summary of the derived equations is presented in Table A4.1 below. The geometries presented in Table A4.1 are shown as a cross section of a three-dimensional geometry. In each one of these geometries, r is the radius of the sphere or the width from the center of spheroidal geometry, c is the depth from the center of the spheroidal geometry, and θ is the angle measured consistently as shown in each one of the schematics of Table A4.1. For the case of oblate spheroid $c/r<1$ (case of a sphere pressed uniformly from the top and bottom) while for the case of prolate spheroid $c/r>1$ (case of a sphere pressed uniformly from its sides).

Table A4.1. Summary of the shape factor for various geometries following an analytical solution.

Geometry	**Schematic**	**Shape factor, *S***
Case 1. Hemispherical pits with different degrees of undercutting	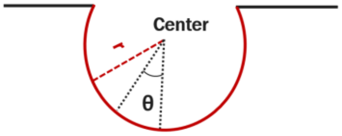	$\frac{2\pi sin(\theta)(1-cos(\theta))}{\pi(1-cos(\theta))-sin(\theta)} r$ A4.3
Case 2. Oblate spheroid (disk shaped) pits with undercutting	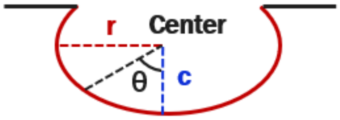	$\frac{2\pi sin(\theta)\sqrt{1-\left(\frac{c}{r}\right)^2}(1-cos(\theta))}{\pi(1-cos(\theta))\sqrt{1-\left(\frac{c}{r}\right)^2}-sin(\theta)\left(\frac{\pi}{2}-tan^{-1}\left[sinh\left(tanh^{-1}\left(\frac{c}{r}\right)\right)\right]\right)} r$ A4.4
Case 3. Prolate spheroid (deep) pits with undercutting	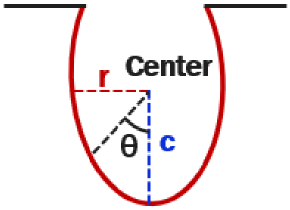	$\frac{2\pi sin(\theta)\sqrt{\left(\frac{c}{r}\right)^2-1}(1-cos(\theta))}{\pi\sqrt{\left(\frac{c}{r}\right)^2-1}-sin(\theta)ln\left(tan\left(\frac{1}{4}ln\left(\frac{\frac{c}{r}+1}{\frac{c}{r}-1}\right)\right)\right)} r$ A4.5
Case 4. Oblate spheroid-shaped pits	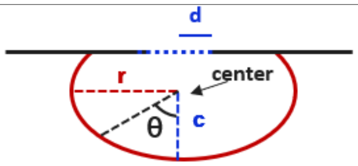	$\frac{4\pi(1-cos(\theta))}{\pi(1-cos(\theta))+2\,tan^{-1}\left[sinh\left(tanh^{-1}\left(\frac{c}{r}\right)\right)\right]} d$ A4.6

with a lacy cover	Same as above where $d=\sqrt{r^2-c^2}$	$\frac{4\pi\sqrt{1-\left(\frac{c}{r}\right)^2}(1-cos(\theta))}{\pi(1-cos(\theta))+2tan^{-1}[sinh(tanh^{-1}\left(\frac{c}{r}\right))]}r$ A4.7

θ: angle of the geometry $0^0 < \theta < 180^0$; r: radius of the geometry; *c/r*: ratio of depth to radius; d: opening of the lacy cover.

Knowing the parameters pertaining to each equation, the shape factor can be easily calculated for any of the presented geometries above. The derivations of the equations given in Table A4.1 are provided in the following section of this Appendix. For the interested reader, Equations A4.8 through A4.12 are also plotted as functions of *r, c*, and θ. Briefly, for hemispherical pits with different degrees of undercutting, dish-shaped pits (θ < 90°) exhibit larger shape factors compared to those with undercut geometries (θ > 90°). Oblate spheroid pits with undercutting exhibit shape factors that are larger for small θ and decrease with increase in the angle θ but are weakly dependent on *c/r* ratio. For prolate spheroid (high depth-to-width ratios) pits with undercutting, the shape factor is also weakly dependent on *c/r* but is not single valued as a function of angle θ, showing a maximum at ~120°. Finally, oblate spheroid-shaped pits with a lacy cover have a shape factor that decreases with increasing *c/r* but is weakly dependent on angle θ.

Hemispherical pits with different degrees of undercutting

For a spherical geometry of radius r and a given angle θ, the resistance from the outer surface of the sphere to infinity is given by:

$$R=\frac{1}{u2\pi r(1-cos\theta)} \qquad \text{(A4.8)}$$

The resistance from the inner surface of the spherical body to a location infinity is then given as:

$$R_T=\frac{1}{2ursin(\theta)}-\frac{1}{u2\pi r(1-cos\theta)}=\frac{\pi(1-cos\theta)-sin(\theta)}{2ur\pi sin(\theta)(1-cos\theta)} \qquad \text{(A4.9)}$$

Thus, the shape factor S for this case can be given as:

$$S=\frac{2\pi sin(\theta)(1-cos\theta)}{\pi(1-cos\theta)-sin(\theta)}r \qquad \text{(A4.3)}$$

Using Equation A4.3, the shape factor for both shallow and undercut hemispherical pits can be calculated. Figure A4.2 illustrates these results, showing that the shape factor constant decreases significantly with increasing angle θ. At θ=90°, the geometry forms a hemisphere. Shallow spherical (also known as dish-shaped) pits exhibit larger shape factors compared to those with undercut geometries.

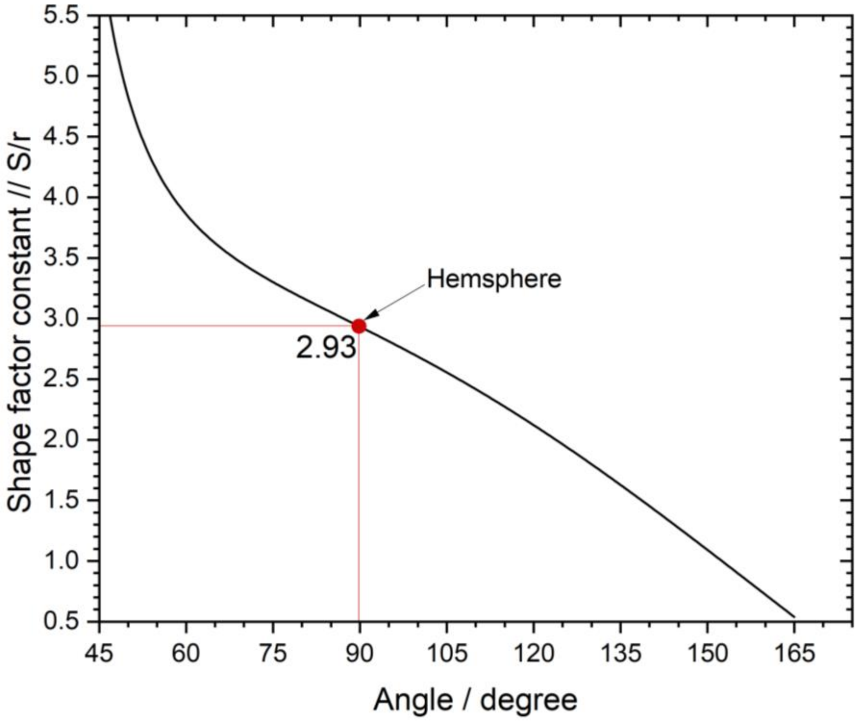

Figure A4.2. Shape factor constant as a function of angle for a spherical pit utilizing the analytical approach of Equation A4.3. Red dot highlights the shape factor for a hemisphere geometry.

Oblate spheroid (dish-shaped) pits with undercutting

Case 2 of Table A4.1 shows a sketch of a typical oblate spheroid pit under which $a = b \neq c$. Under such case, we will define $a = b = r$ and the ratio of "radius" *r* to depth *c* given as *c/r* will serve as a measurement of the flatness of the geometrical body. In addition, the angle θ parameter of an angle is also considered as a variable parameter. Under the assumptions that *c/r*<1, resistance, therefore, from the outer surface of an oblate spheroid to a surface in infinity is given by:

$$R = \frac{\frac{\pi}{2} - \tan^{-1}[\sinh(\tanh^{-1}\left(\frac{c}{r}\right))]}{2u\pi\sqrt{r^2 - c^2}(1 - \cos\theta)} \tag{A4.10}$$

Then, utilizing the approach from Pistorius and Burstein outlaid in Equation A4.2, the total resistance can be calculated as:

$$R_T = \frac{1}{2ursin(\theta)} - \frac{\frac{\pi}{2} - tan^{-1}[sinh(tanh^{-1}\left(\frac{c}{r}\right))]}{2u\pi\sqrt{r^2 - c^2}(1 - cos\theta)} = \frac{\pi\sqrt{r^2 - c^2} - rsin(\theta)\left(\frac{\pi}{2} - tan^{-1}[sinh(tanh^{-1}\left(\frac{c}{r}\right))]\right)}{2\pi ursin(\theta)\pi\sqrt{r^2 - c^2}(1 - cos\theta)} \tag{A4.11}$$

The shape factor for the case of dish-shaped pits can be given as:

$$S = \frac{2\pi sin(\theta)\sqrt{1 - \left(\frac{c}{r}\right)^2}(1 - cos(\theta))}{\pi(1 - cos\theta)\sqrt{1 - \left(\frac{c}{r}\right)^2} - sin(\theta)\left(\frac{\pi}{2} - tan^{-1}[sinh(tanh^{-1}\left(\frac{c}{r}\right))]\right)} \tag{A4.4}$$

The results from Equation A4.4 are plotted for the *c/r*<1 ratios and various angles θ. The results are shown in Figure A4.3 below and indicate that the shape factor constant is larger for small θ and decreases with increase in the angle and *c/r* ratio.

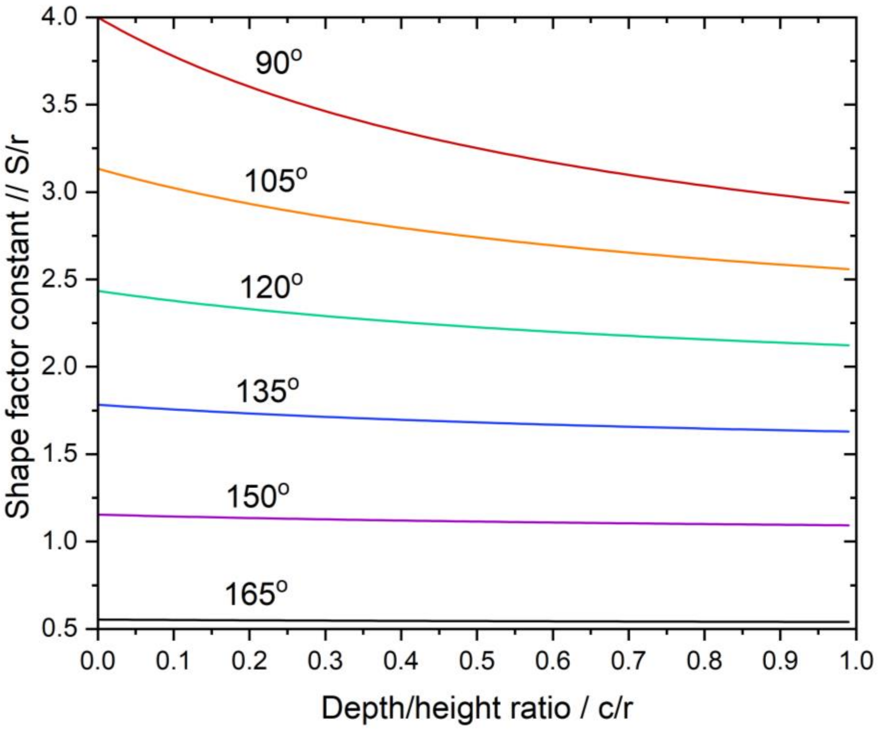

Figure A4.3. Shape factor constant as a function of c/r ratio for an oblate spheroid geometry utilizing the analytical approach of Equation A4.4. Different angles are explored.

Prolate spheroid (deep) pits with undercutting

Deep pits, in which the depth is larger than the width (*c/r*>1) can also be treated through this approach. A schematic of the parameters for such geometries is shown in Table A4.1. Defining, again, $a = b \neq c,\ a = b = r$ and the angle θ, the resistance from the outer surface of the prolate spheroid to a surface at infinity is given by:

$$R = \frac{ln\left(tan\left(\frac{1}{4}ln\left(\frac{c+r}{c-r}\right)\right)\right)}{2u\pi\sqrt{c^2-r^2}(1-cos\theta)} \qquad \text{(A4.12)}$$

The total resistance from the inner surface of the pit to the infinity and the corresponding shape factor are given by Equations A4.13 and A4.5 below:

$$R_T = \frac{1}{2ursin\theta} - \frac{ln\left(tan\left(\frac{1}{4}ln\left(\frac{c+r}{c-r}\right)\right)\right)}{2u\pi\sqrt{c^2-r^2}(1-cos\theta)} = \frac{\pi\sqrt{c^2-r^2} - rsin\theta\ ln\left(tan\left(\frac{1}{4}ln\left(\frac{c+r}{c-r}\right)\right)\right)}{2u\pi rsin\theta\sqrt{c^2-r^2}(1-cos\theta)} \qquad \text{(A4.13)}$$

$$S = \frac{2\pi r sin\theta\sqrt{c^2-r^2}(1-cos\theta)}{\pi\sqrt{c^2-r^2}-rsin\theta\, ln\left(tan\left(\frac{1}{4}ln\left(\frac{c+r}{c-r}\right)\right)\right)} \, or \, \frac{2\pi sin\theta\sqrt{\left(\frac{c}{r}\right)^2-1}(1-cos\theta)}{\pi\sqrt{\left(\frac{c}{r}\right)^2-1}-sin\theta ln\left(tan\left(\frac{1}{4}ln\left(\frac{\frac{c}{r}+1}{\frac{c}{r}-1}\right)\right)\right)} r \qquad (A4.5)$$

The variations of the shape factor constant, *S/r*, as a function of *c/r* and the angle θ is depicted in Figure A4.4.

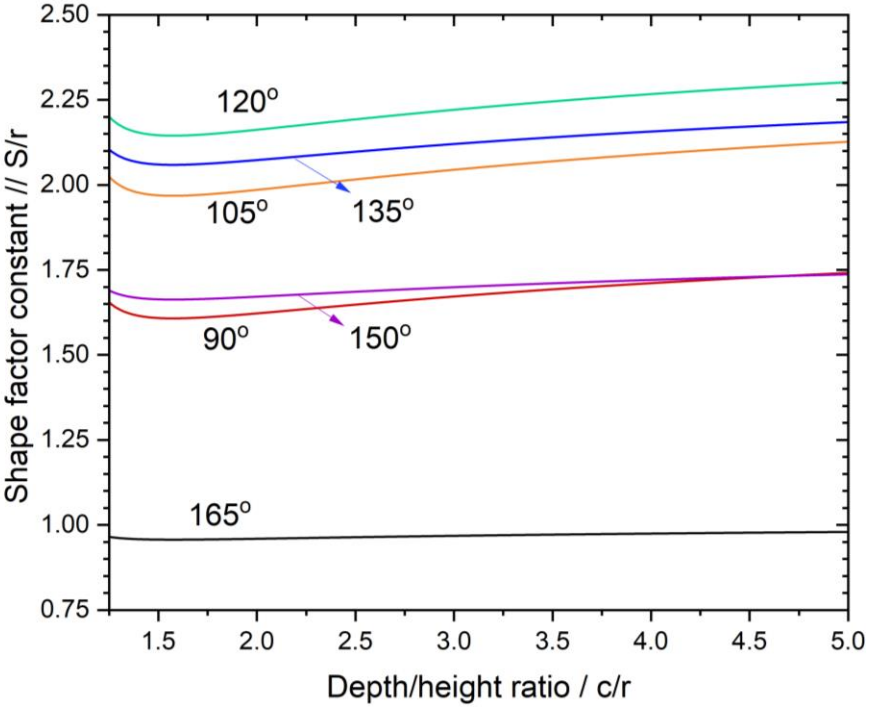

Figure A4.4. Shape factor constant as a function of *c/r* ratio for a prolate spheroid geometry utilizing the analytical approach of Equation A4.5. Different θ are explored.

Pits with a lacy cover

During pit propagation, the presence of a lacy cover-a thin metal layer with openings-modifies the resistance of species' flux. For the general case presented in case 4 of Table A4.1 of an oblate spheroid pit with $a = b \neq c$, $a = b = r$, *c/r*<1, angle θ, and an opening, *d* in the lacy cover, the resistance from pit mouth to the bottom of the pit can be given as:

$$R = \frac{tan^{-1}[sinh(tanh^{-1}\left(\frac{c}{r}\right))]}{2u\pi a(1-cos\theta)} \qquad (A4.14)$$

Note that the region *d*<*x*<*b* is a perfectly insulated surface which would represent the thin metal layer remanence on the pit mouth. Following the work from Pistorius and Burstein, the total resistance from the bottom of the pit to a surface at infinity can be found by adding to Equation A4.14 the resistance of a thin disk in a semi-infinite medium:

$$R = \frac{1}{4ud} + \frac{\tan^{-1}[\sinh(\tanh^{-1}\left(\frac{c}{r}\right))]}{2u\pi d(1-\cos\theta)} = \frac{\pi(1-\cos\theta)+2\tan^{-1}[\sinh(\tanh^{-1}\left(\frac{c}{r}\right))]}{4u\pi d(1-\cos\theta)} \quad \text{(A4.15)}$$

The shape factor then can be calculated as following:

$$S = \frac{4\pi(1-\cos\theta)}{\pi(1-\cos\theta)+2\tan^{-1}[\sinh(\tanh^{-1}\left(\frac{c}{r}\right))]} d \quad \text{(A4.6)}$$

In Equation A4.6, the value of the shape factor S can be identified as a function of radius d for various *c/r* ratios, or the d value can be substituted for $\sqrt{r^2 - c^2}$ in which case the shape factor is given by:

$$S = \frac{4\pi\sqrt{1-\left(\frac{c}{r}\right)^2}(1-\cos\theta)}{\pi(1-\cos\theta)+2\tan^{-1}[\sinh(\tanh^{-1}\left(\frac{c}{r}\right))]} r \quad \text{(A4.7)}$$

In such cases, the shape factor can be identified for different values of *c/r*<1 ratios. Equation A4.6 and Equation A4.7 are plotted in Figures A4.5a and A4.5b respectively.

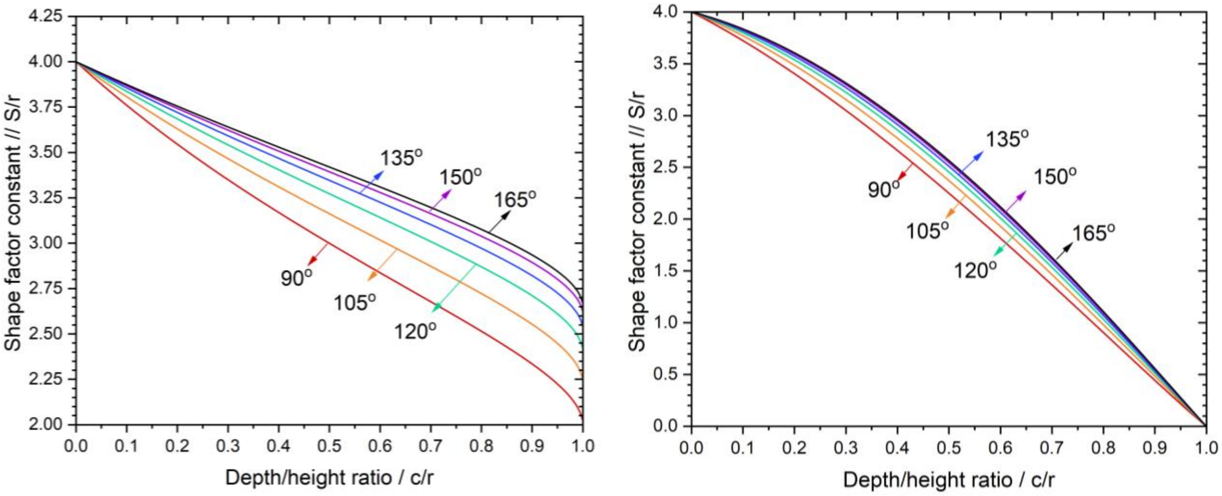

a) **b)**

Figure A4.5. Shape factor constant as a function of *c/r* ratio for an oblate spheroid geometry utilizing the analytical approach of **a)** Equation A4.6 and **b)** Equation A4.7. Different angles θ are explored.

Chapter 5. From 1D to 3D: Maximum pit size predictions with different levels of complexity

A. Shehi, R. G. Kelly
[1]Center for Electrochemical Science and Engineering, Department of Materials Science and Engineering, University of Virginia, Charlottesville, VA 22904

Contributions: A. Shehi - Conceptualization, Data curation, Formal analysis, Investigation, Methodology, Visualization, Writing - original draft, Writing-review and editing, **R. G. Kelly** - Conceptualization, Funding acquisition, Data curation, Formal analysis, Project administration, Resources, Project administration, Investigation, Methodology, Visualization, Writing - original draft, Writing – review and editing

5.1. Summary

This study evaluates the conservatism of Chen and Kelly's model for predicting pit growth in localized corrosion using FEA with Secondary and Tertiary current distributions. The investigation incorporates artificial 1D pit experiments and thermodynamic modeling to determine electrochemical boundary conditions for shallow pits. Key experimental data, including the equilibrium constants for Cr^{3+} hydrolysis and chlorination reactions, were integrated into the model. Results show that Chen and Kelly's model tends to underestimate maximum pit size by approximately 40%, primarily due to idealized assumptions regarding cathodic processes. The omission of electrolyte chemistry in the model leads to an underprediction of cathodic limitations. Additionally, incorporating Tafel kinetics into the model improves realism but introduces increased uncertainty in predictions. Time-dependent hydrolysis reactions, significant in the context of localized corrosion, challenge equilibrium-based models. Finally, simplifying reaction location to electrode-electrolyte boundaries reduces computational complexity without sacrificing accuracy. These findings underscore the need for more sophisticated models that account for the dynamic behavior of localized corrosion processes.

5.2. Introduction

Several modeling approaches have been developed in the field of localized corrosion, particularly pitting corrosion.[1–9] One of the main challenges in predicting the maximum damage associated with pitting corrosion in engineering structures is the difficulty in defining input boundary conditions for the dynamic and highly aggressive environment inside the pit. One such model that has aimed to simplify this prediction process is the Chen and Kelly model.[2]

Pitting corrosion is characterized by the initiation and propagation of pits in a very localized region of an alloy, which is typically covered by a passive film.[10,11] Throughout all stages of pitting corrosion, a pit remains active as long as it continues to receive current from the adjacent cathode, which remains passive. Chen and Kelly leveraged this fundamental principle to develop an analytical solution that avoids the complex input boundary conditions typically required by other localized corrosion models, such as Finite Element Analysis (FEA). As described in the introduction of this dissertation, their model solves the equations governing the total anodic current demand and total cathodic current supply separately, with the pit size (*e.g.,* radius for hemispherical pits) as the key variable.

However, the conservatism of the Chen and Kelly model has been acknowledged by its authors both at the time of its publication and in subsequent years.[2] While this conservative approach may be beneficial in ensuring safety in engineering design, it has been noted that the model tends to over-predict pit size compared to real-world in-service observations. The model's conservatism is not so much related to the input parameters, or the pitting features it considers, but rather in the predicted total pit size.

In this work, we investigate the level of conservatism inherent in the Chen and Kelly model by comparing its predictions with FEA results. Specifically, we examine Secondary current distribution (*i.e.,* potential and current special variations) and Tertiary current distribution (*i.e.,* potential, current, and species distribution). Experimental input boundary conditions are used to solve the model and interpret the data. Additionally, a reduced-order model (ROM) based on the Tertiary current distribution approach is presented, offering a more efficient solution for localized corrosion problems by saving both time and computational resources.

5.3. Methodology

This study incorporates both experimental and computational approaches. In the experimental component, the input parameters required for the modeling were obtained. In contrast, computational work is divided into two main components: analytical solutions and FEA.

5.3.1. Solution preparation for pH measurement and modeling

The first part of the experimental work consisted of solution pH measurements. Electrolytes with different concentrations of $CrCl_3$ in deionized water, $CrCl_3$ in 1M NaCl, $CrCl_3$ in 2M NaCl, $CrCl_3$ in 3M NaCl, and $CrCl_3$ in 1.5M $NiCl_2$ were prepared utilizing reagent grades salts of NaCl, $CrCl_3 \cdot 6H_2O$ and $NiCl_2$. First the base solution (DI water, NaCl in DI water, or $NiCl_2$ in DI water) was prepared and fully dissolved. Then appropriate measurements of $CrCl_3 \cdot 6H_2O$ were mixed into the base solutions to achieve the desired $CrCl_3$ concentration. The solution pH was measured and recorded before the addition of the $CrCl_3 \cdot 6H_2O$ salt, around 10s after the salt was added and mixed, and around 10min after the addition.

5.3.2. Artificial pit experiments

Artificial one-dimensional pits from a SS304 wire with a diameter of 50.8μm (cross -sectional area $2.0268 \cdot 10^{-5}$ cm^2) were utilized to carry on the experiments. Details of the schematic of the cell are shown elsewhere. The certified compositions of SS304 utilized in this study is presented in Chapter 2 of this work.

SS304 wires were embedded in epoxy, ensuring that only the cross-section of the wire was exposed to the electrolyte. All samples were metallographically prepared to a 320-grit surface finish, followed by cleaning in deionized water and air drying. Electrolyte solutions were prepared using 0.6M NaCl solutions at 25°C. All electrochemical experiments were conducted on an in-house made electrochemical cell containing a total of 100mL solution utilizing a commercially available potentiostat.

A series of electrochemical techniques were applied cyclically to the artificial pit in the following order: (1) a 30s open circuit potential (OCP), (2) potentiostatic polarization to -0.75V vs. SCE for 2min to attempt to remove any protective layer therefore ensuring an easy pit initiation, (3) potentiostatic polarization to +0.75 V vs. SCE to initiate the pit, (4) potentiostatic polarization to +0.55V vs. SCE to propagate the pit to the desired depth, (5) a linear sweep voltammetry (LSV) at a scan rate of 5mV/s from +0.55V vs. SCE to $^-$0.65 V vs. SCE.

5.3.3. Maximum pit size modeling

Modeling of the maximum pit size was conducted for hemispherical pit utilizing two different approaches: analytical solution through Chen and Kelly's model, Secondary and Tertiary current distribution through COMSOL Multiphysics Version 6.3.

5.3.3.1. Chen and Kelly's model

The details on the equations behind Chen and Kelly's model are explained in Chapter 1 of this work. The following boundary conditions for SS304 in 0.6M NaCl were utilized to solve for the maximum hemispherical pit size: $(i \cdot x)_{sf}$ =0.85 A/m, f=0.35 shape factor n=3.52 (from Chapter 4),

E_{rp}=-0.19V vs. SCE (from Chapter 2) as well additional E_{rp} values extracted from the 1D experiments corresponding to shorter pit depths and explained in the results section of this work The water layer thickness (WL) was chosen arbitrarily to be 100μm and the electrolyte conductivity was selected to be 6 S/m. Lastly activation controlled kinetics for oxygen reduction reaction (ORR) in 0.6M NaCl and pH = 7 obtained through OLI Studio version 12.0 with reversible potential, E^o= 0.1 V vs. SCE, exchange current density, i_o=$4.47 \cdot 10^{-9}$ A/cm^2 and β_c=-0.12V/decade. Note that the cathodic kinetics presented above to not affect the main objective and the goal of this paper. The cathodic kinetics can be replaced by any experimentally measured one, if needed.

5.3.3.2. FEA modeling

COMSOL Multiphysics version 6.3 was utilized to carry on the maximum pit calculations through Secondary and Tertiary current distribution.

The Secondary current distribution module of COMSOL Multiphysics version 6.3 was employed to perform potential and current distribution calculations for a hemispherical pit with a radius adjacent to a cathode of radius R and a WL of 100 μm. The electrolyte conductivity was set to 6 S/m. Anode boundary conditions were defined as a constant current density, using the same input parameters as in the study by Chen and Kelly. The constant current density on the surface of the hemispherical pit can be calculated using the following Equation 5.1:

$$i_{hemispherical} = f \cdot n \cdot \frac{(i \cdot x)_{sf}}{2\pi \cdot r} \tag{5.1}$$

In this equation, f is the fraction of saturation, n is the shape factor constant, r is the radius of the hemispherical pit, and $(i \cdot x)_{sf}$ is the pit stability product under a salt film as measured from artificial 1D pit experiments. The cathode boundary conditions were set to be consistent with those in Chen and Kelly's approach, as described earlier. It is important to note that during the simulations, both the current density and potential at the edge of the cathode were constrained to remain equal to or below the exchange current density and the reversible potential for ORR mentioned previously.

To determine the maximum pit size, stationary simulations were conducted for various pit radii r and cathode radii R. A pit was considered repassivated if the potential at the pit's bottom matched the experimentally obtained values for the same pit depth, as further detailed and derived in the results section of this work.

Tertiary current distribution simulations were performed using two distinct approaches. In the first approach, the current density within the pit was assumed to be constant, based on the pit radius according to Equation 5.1 above, or the first equation in the second row of Table 5.1. In the second approach, the input boundary conditions were based on Tafel kinetics, following Equation 5.2 in the second row of Table 5.1. All other electrochemical parameters and chemical reactions in Table

5.2 remained unchanged between the two approaches used for the Tertiary current distribution simulations.

Table 5.1. Input electrochemical parameters for the Tertiary current distribution pit model.

Variable	Value/Equation	Citation
$E_{o,M}$	$-0.128V_{SCE}$	This work
$i_{,M}$	1. $3.52 \cdot 0.35 \cdot 0.85/(2\pi r)$ [A/m^2] for constant pit current density simulations 2. if ($E<E_{rp,\ pit\ size}$, $((0.069) \cdot 10^{((E+0.128[V])/0.06[V])})$[A/cm^2] else, $3.52 \cdot 0.85/(2\pi r)$ [A/m^2])) for Tafel kinetics simulations	This work
β_M	0.06V/decade	This work
$i_{lim,M}$	$3.52 \cdot 0.85/(2\pi r)$ [A/m^2]	This work
$E_{o,HER,}$ inside pit	-0.49093 V_{SCE}	This work
$i_{o,HER}$ inside pit	$3.21 \cdot 10^{-2}$ [A/cm^2]	This work
β_{HER} inside pit	-0.15V/decade	This work
$E_{o,ORR}$ cathode	0.759 V_{SCE}	OLI Studio
$i_{o,ORR}$ cathode	Interpolated based on cathode pH – see Appendix for data	OLI Studio
β_{ORR}	-0.12V/decade	OLI Studio
$i_{lim,ORR}$	$5 \cdot 10^{-5}$ [A/cm^2]	[12]
$E_{o,HER,}$ cathode	-0.141 V_{SCE}	This work
$i_{o,HER}$ cathode	Interpolated based on cathode pH – see Appendix for data	OLI Studio
$i_{pass,M}$	0.05[μA/cm^2]	OLI Studio
i_{act}	$i_{act}=i_o \cdot 10^{\eta/\beta}$	-

All hydrolysis and chlorination reactions in Table 5.2 have been defined as equilibrium reactions. The precipitation reactions were defined utilizing a step reaction according to Equation 5.2 below:

$$r_{Me(OH)_{x,s}} = k_f(C_{Me^{n+}} \cdot C_{OH^-}^n - K_{sp}) \cdot H(x) \tag{5.2}$$

Where k_f is a rate constant chosen arbitrarily to be as 1/s, C_x is the concentration of the metal or hydroxyl species, and H(x) is a Heaviside step function defined as:

$$x = \frac{C_{Me^{n+}} \cdot C_{OH^-}^n}{K_{sp}} - 1 \tag{5.3}$$

Table 5.2. Input reactions for the Tertiary current distribution pit model. All equilibrium constant units are in molarity, M.

Reactions	Equilibrium/solubility constant	k_f	Citation
$Fe_{aq}^{2+} + H_2O_l \leftrightarrow \mathrm{FeOH}_{aq}^+ + \mathrm{H}_{aq}^+$	$1 \cdot 10^{-9.34}$	-	OLI Studio

$Fe_{aq}^{2+} + Cl_{aq}^{-} \leftrightarrow \mathrm{Fe}Cl_{aq}^{+}$	$1 \cdot 10^{-0.168}$	-	OLI Studio
$Ni_{aq}^{2+} + H_2O_l \leftrightarrow \mathrm{NiOH_{aq}^{+}} + \mathrm{H_{aq}^{+}}$	$1 \cdot 10^{-9.49}$	-	OLI Studio
$Ni_{aq}^{2+} + Cl_{aq}^{-} \leftrightarrow \mathrm{Ni}Cl_{aq}^{+}$	$1 \cdot 10^{0.1256}$	-	OLI Studio
$Cr_{aq}^{3+} + H_2O_l \leftrightarrow \mathrm{CrOH_{aq}^{2+}} + \mathrm{H_{aq}^{+}}$	$1 \cdot 10^{-3.5}$	-	[13,14]
$Cr_{aq}^{3+} + 2H_2O_l \leftrightarrow \mathrm{Cr(OH)_{2,aq}}^{+} + 2\mathrm{H_{aq}^{+}}$	$1 \cdot 10^{-9.38}$	-	[13,14]
$Cr_{aq}^{3+} + Cl_{aq}^{-} \leftrightarrow \mathrm{Cr}Cl_{aq}^{2+}$	This work	-	
$Fe_{aq}^{2+} + 2OH_{aq}^{-} \rightarrow \mathrm{Fe(OH)_{2(s)}}$	$6.61 \cdot 10^{-15}$	1 [1/s]	[15]
$Ni_{aq}^{2+} + 2OH_{aq}^{-} \rightarrow Ni\mathrm{(OH)_{2(s)}}$	$9.33 \cdot 10^{-18}$	1 [1/s]	OLI Studio
$Cr_{aq}^{3+} + 3OH_{aq}^{-} \rightarrow \mathrm{Cr}OOH_{3\mathrm{(s)}} + H_2O_l$	$4.22 \cdot 10^{-36}$	1 [1/s]	[16]
$H_2O_l \leftrightarrow H_{aq}^{+} + OH_{aq}^{-}$	$1.01 \cdot 10^{-14}$	-	OLI Studio

Lastly, diffusion coefficients for each one of the species were taken from OLI Studio MSE database. Figure 5.1 shows a typical meshed geometry of cathode (blue) and anode (red) utilized during the FEA simulations.

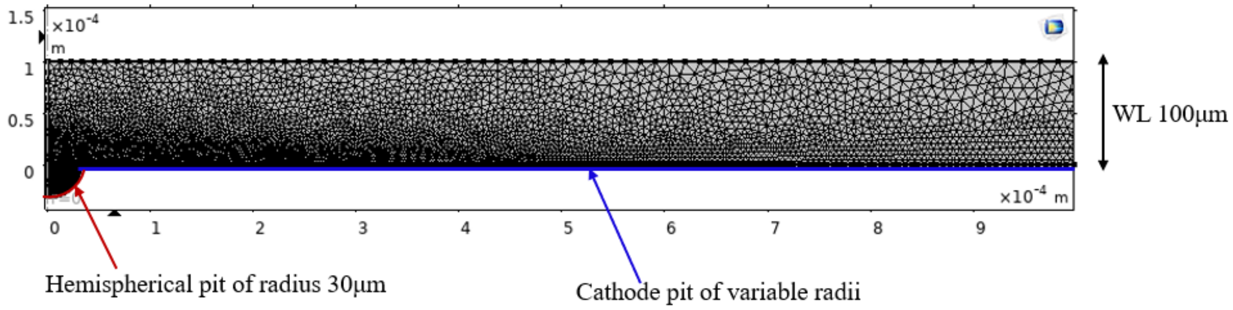

Figure 5.1. Visual representation of the pit model utilized for Secondary current distribution and the Tertiary current distribution in COMSOL Multiphysics version 6.3.

5.4. Results

The results section is divided into several key components, each addressing different aspects of modeling and predicting the maximum pit size at varying levels of complexity. The first part presents experimental data demonstrating the influence of electrolyte concentration and exposure time on the equilibrium constants governing Cr^{3+} hydrolysis. This is followed by experimental findings that extrapolate E_{rp} values for short pits under different saturation conditions.

Subsequently, the focus shifts to the simulation aspect of this study. The method for calculating the maximum pit size using Chen and Kelly's approach is not explicitly detailed here, as has been described elsewhere.[2,3] Instead, a comparative analysis is conducted between the maximum pit size obtained via Secondary current distribution modeling and experimental results. The study then progresses to Tertiary current distribution modeling. First, we validate a newly proposed approach aimed at reducing computational time and resource usage by restricting hydrolysis, chlorination, and water equilibrium reactions to the electrode-electrolyte boundary instead of placing them as homogenous reactions occurring throughout the electrolyte. Finally, we present simulation results obtained using a constant current density within the pit, as well as an alternative approach where current and potential are correlated through a Tafel relationship. A comparison of the maximum pit size obtained through the three approaches: Chen and Kelly method, Secondary current distribution, and Tertiary current distribution is then conducted.

5.4.1. Experimental results and fitting

Figures 5.2a and 5.2b present the pH of the solution as a function of $CrCl_3$ concentration, measured after 10 seconds and 10 minutes, respectively, in various background electrolytes, including DI H_2O, 1M NaCl, 2M NaCl, 3M NaCl, and 1.5M $NiCl_2$. The results indicate a slight decrease in pH after 10 minutes of mixing. However, distinct differences in pH are observed across different background electrolytes, particularly between $CrCl_3$ in DI H_2O and in 3M NaCl.

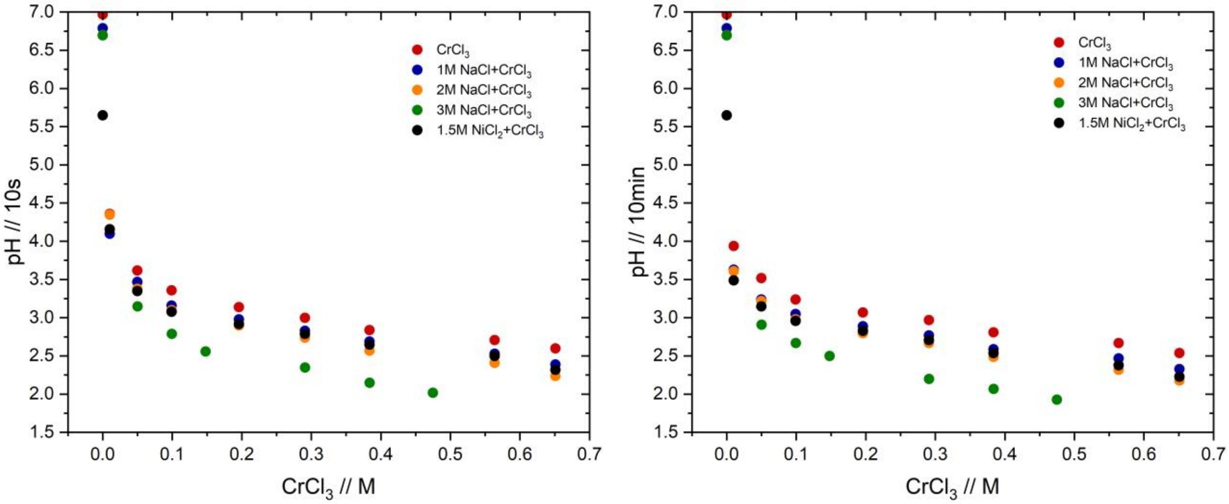

(a) **(b)**

Figure 5.2. Solution pH versus $CrCl_3$ concentration in M for electrolytes containing only $CrCl_3$ (red), $CrCl_3$ in 1M NaCl (blue), $CrCl_3$ in 2M NaCl (orange), $CrCl_3$ in 3M NaCl (green), and $CrCl_3$ in 1.5M $NiCl_2$ (black) measured after **a)**10s and **b)**10min after mixing.

An increase in Cl^- concentration correlates with a decrease in measured pH at both time intervals. Notably, the $NiCl_2$ background electrolyte results in a pH that falls between those of the 1M NaCl and 2M NaCl solutions, rather than aligning with 3M NaCl, despite having the same Cl^- content. These findings suggest that the pH of the solution is influenced not only by Cr^{3+} concentration but also by Cl^- concentration, highlighting the role of chloride ions in modulating solution acidity.

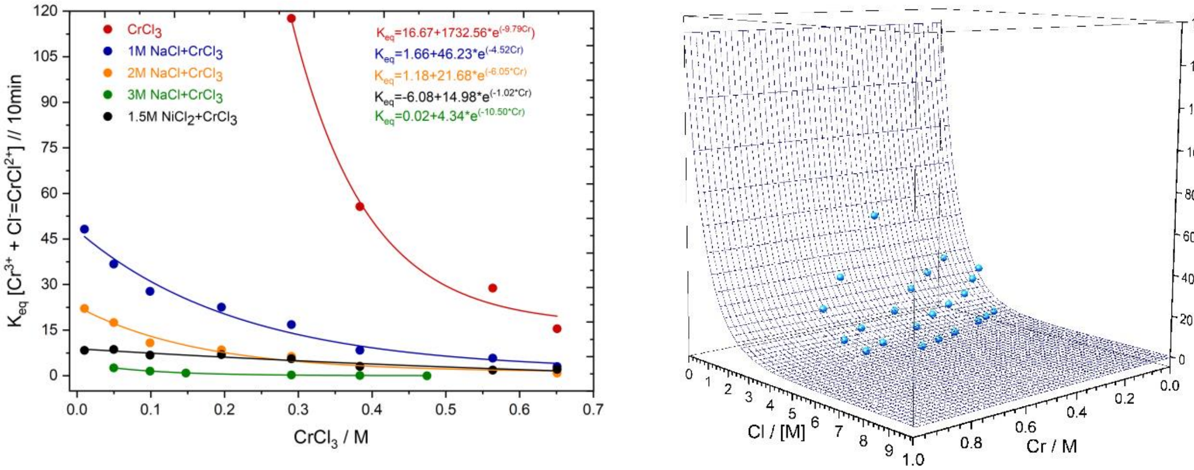

(a) **(b)**

Figure 5.3. a) Extracted equilibrium constant for $CrCl^{2+}$ formation as a function of $CrCl_3$ concentration measured at different base solutions and **b)** Mapping for experimentally extracted equilibrium constants after 10min of $CrCl_3$ in a three-dimensional graph and surface fitting of the data.

Figure 5.3a shows the equilibrium constant determined by fitting for the formation of $CrCl^{2+}$ as a function of $CrCl_3$ concentration in different electrolyte media. The fitting is conducted by solving simultaneously two equations: In one, the first hydrolysis of Cr^{3+} is considered based on its widely reported equilibrium constant $10^{-3.5}$.[13,14]

$$Cr_{aq}^{3+} + H_2O_l = CrOH_{aq}^{2+} + H^+ \qquad K_{eq} = 10^{-3.5} = \frac{[CrOH_{aq}^{2+}][H^+]}{[Cr_{aq}^{3+}]} \tag{5.2}$$

In the derived Equation 5.2, the concentration of Cr^{3+}consumed is adjusted to ensure that the solution to the equilibrium reaction aligns with the experimentally recorded values after 10 minutes. This timeframe is selected to allow for uniform mixing of the electrolyte, ensuring consistency in the recorded data.

Simultaneously, the chlorination reaction of Cr^{3+} is formulated based on the total chloride concentration in the solution and the remaining unreacted Cr^{3+} from Equation 5.2. This approach accounts for the dynamic interaction between Cr^{3+} and Cl^-, providing a more accurate representation of the system's chemical behavior.

$$Cr_{aq}^{3+} + Cl_{aq}^{-} = CrCl_{aq}^{2+} \qquad K_{eq} = \frac{[CrCl_{aq}^{2+}]}{[Cr_{aq}^{3+}][Cl_{aq}^{-}]} \tag{5.3}$$

The fitted K_{eq} from Equation 5.3 is recorded and presented in Figure 5.3a. The results indicate that K_{eq} for the chlorination of Cr^{3+} is strongly dependent on the concentrations of both Cr^{3+} and Cl^-.

To visualize this relationship, a three-dimensional (3D) map of the data was constructed, along with the best-fitted surface, as shown in Figure 5.3b. The equation describing the best-fitted surface is provided in Equation 5.4 below:

$$K_{eq}(Cr^{3+}, Cl^{-}) = -36.84 + 37.11 \cdot e^{-0.01014 \cdot [Cr^{3+}]} + 152.2 \cdot e^{-1.111 \cdot [Cl^{-}]} \tag{5.4}$$

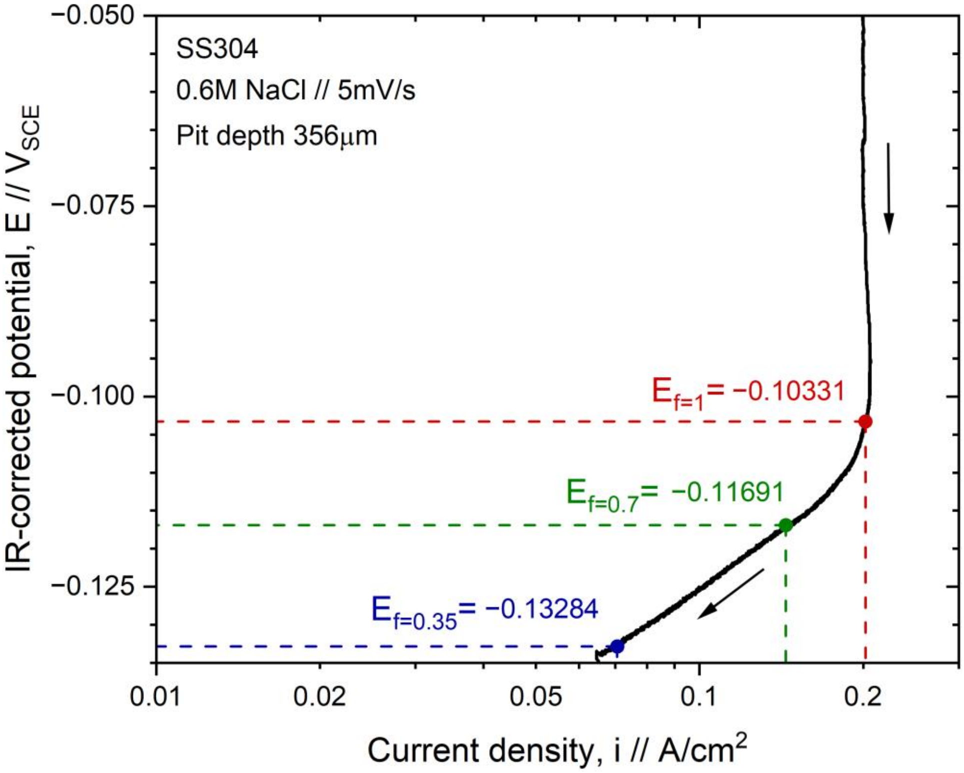

Figure 5.4. Potential versus current density (in logarithmic scale) of an LSV scan of SS304 artificial pit at 5mV/s in 0.6M NaCl at a pit depth of 356μm. Extracted potentials at different fractions of saturation: 1 (red), 0.7(green), and 0.35(blue). Arrows indicate the direction of the scan

Figure 5.4 presents a representative LSV curve of SS304 recorded in 0.6M NaCl at a scan rate of 5 mV/s, with a pit depth of 356 μm through an artificially generated 1D pit. The potential has been IR-corrected based on the previously reported dependence of pit and solution resistance on pit depth for this alloy in the given electrolyte per the results presented in Appendix of Chapter 2 of this dissertation.

Along the activation-controlled region of the LSV curve, potentials corresponding to current densities representing a fraction (*f*) of the limiting (saturation) current were extracted. These data are used to establish the potential dependence on different saturation fractions for short pit depths, as shown in Figure 5.5.

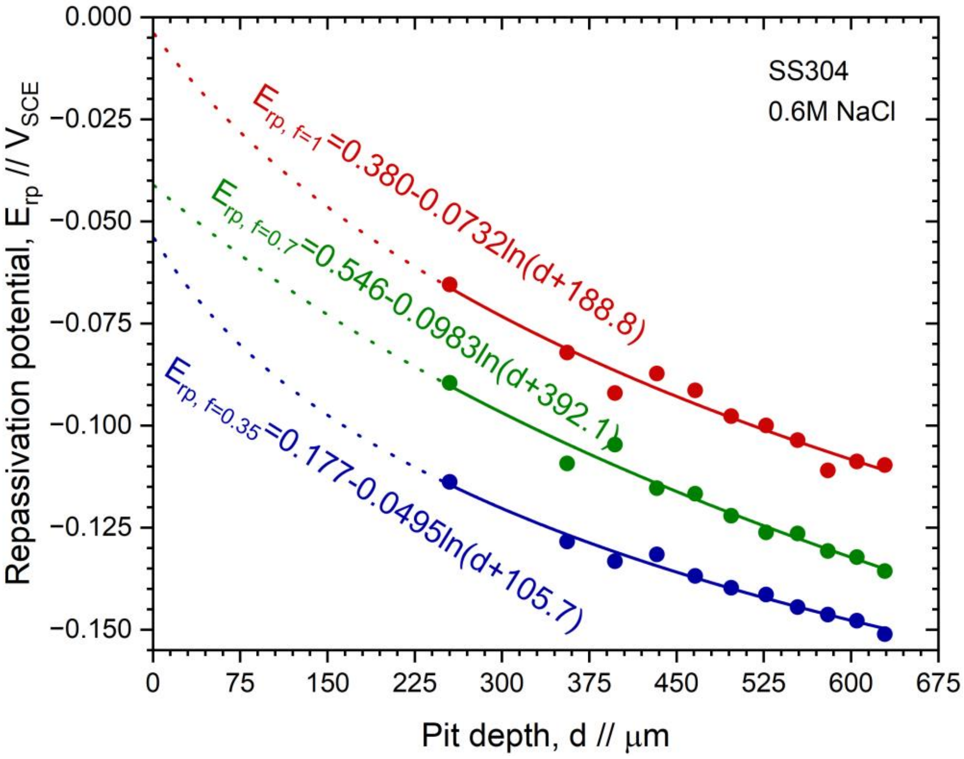

Figure 5.5. Repassivation potential (E_{rp}) from the LSV scans extracted at different pit depths and different fractions of saturation: 1 (red), 0.7(green), and 0.35(blue). Logarithmic fitted curve extrapolated at shorter pit depths is also shown for each *f*.

Figure 5.5 illustrates the dependence of the potential at the bottom of the pit on the pit depth (filled symbols), along with extracted logarithmic fitted curves. A logarithmic fit was chosen due to the well-established logarithmic relationship between potential and current density in the activation-controlled region, as described by the Tafel equation, and the inverse correlation between current density and pit depth, as previously derived. [17]

It is important to note that accurately extracting the experimental relationship between potential and pit depth at lower pit depths is challenging due to the risk of pit dilution at shallow pits.[18–20] The recorded potentials are labeled as E_{rp}, as they represent the potential at the pit bottom after IR correction, effectively eliminating pit and electrolyte resistance.

The results in Figure 5.5 indicate that increasing *f* values from 0.35 to 1 leads to an increase in E_{rp} for a given pit depth. This trend aligns with the expected potential versus current distribution. Notably, this trend is also preserved in the extracted values obtained through the fitted curves. For the analysis of maximum pit size predictions, E_{rp} values extracted for $f = 0.35$ (blue curve) in Figure 5.5 are used in subsequent sections. A similar *f* value of approximately 0.35 has been previously reported for this alloy in the given electrolyte from Chapter 2 of this work.

5.4.2. Maximum pit through Secondary current distribution

In this section, we present the data on the maximum pit size obtained through the Secondary current distribution analysis. Various cathode sizes and pit radius values were tested. A pit was considered repassivated if the potential at the bottom of the pit reached the experimentally extracted E_{rp} values, as previously discussed. These reference values are depicted by the black line in Figure 5.6 below.

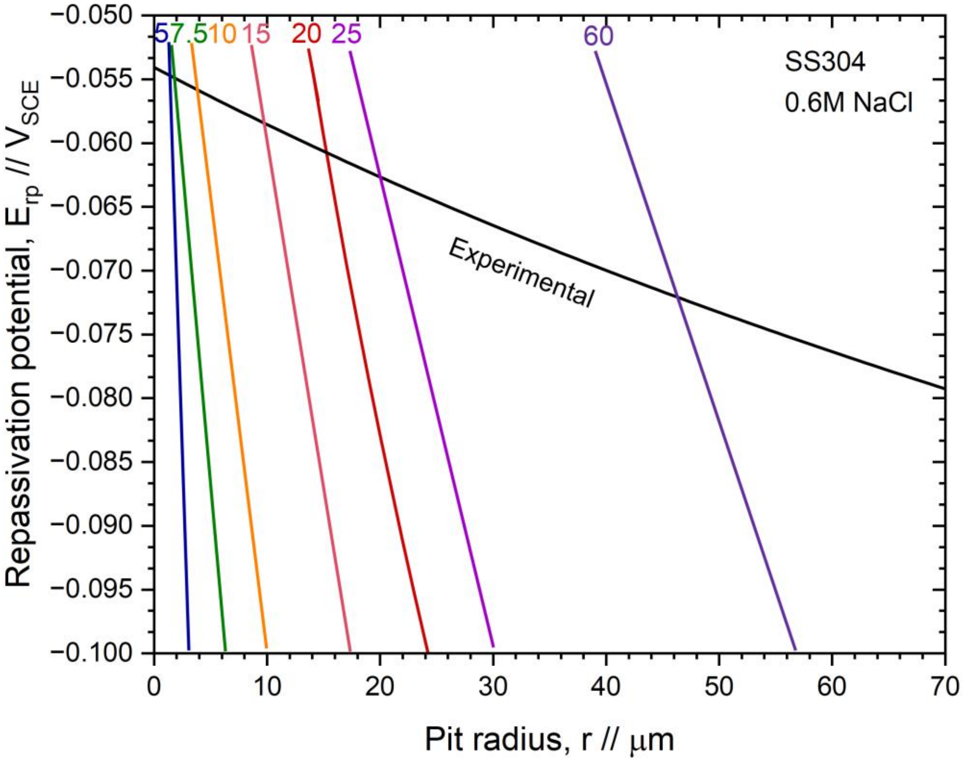

Figure 5.6. Repassivation potential (E_{rp}) measured from the bottom of the hemispherical pit from simulations resulting from Secondary current distribution simulations in FEM with $(i \cdot x)_{sf}$ = 0.85A/m, *f*=0.35. and shape factor of 3.52. Numbers next to each curve symbolize the radius of the cathode in cm. The black represented the extracted E_{rp} values from LSV scants from 1D artificial pits at *f*=0.35.

Figure 5.6 illustrates the relationship between cathode size and the predicted maximum pit size based on the Secondary current distribution. The results indicate that increasing the cathode size leads to larger predicted pit sizes. The recorded hemispherical pit sizes ranged from less than 1 µm for a 5 cm cathode to approximately 48 µm for a 60 cm cathode. However, for the given input boundary conditions, further increasing the cathode size beyond 60 cm did not result in a significant increase in pit size.

5.4.3. Comparison of models with reactions taking place throughout the electrolyte and only at the electrode-electrolyte interface.

Before presenting the results from the Tertiary current distribution, a novel ROM will be introduced. As previously mentioned, the Tertiary current module will be utilized to compare the potential and current distribution obtained by placing the equilibrium reactions only at the electrode-electrolyte boundary versus throughout the electrolyte. The primary objective of this section is to verify whether confining the equilibrium reactions to the boundary yields similar results to conventional methods, which typically require equilibrium reactions to occur throughout the electrolyte.

To establish this comparison, we first examine the pH variations at the pit mouth over time after a 60-second simulation. The decision to start with the pH vs. time dependence at the pit mouth, as shown in Figure 5.7, is based on two key factors: (1) pH is a logarithmic scale of H^+ concentration, making pH variations not only widely reported in the literature but also crucial for determining the input potential and current distribution in this model, and (2) the pH at the pit mouth exhibits more drastic changes than inside the pit, as it serves as the boundary between the highly acidic environment inside the pit and the more alkaline cathodic region.

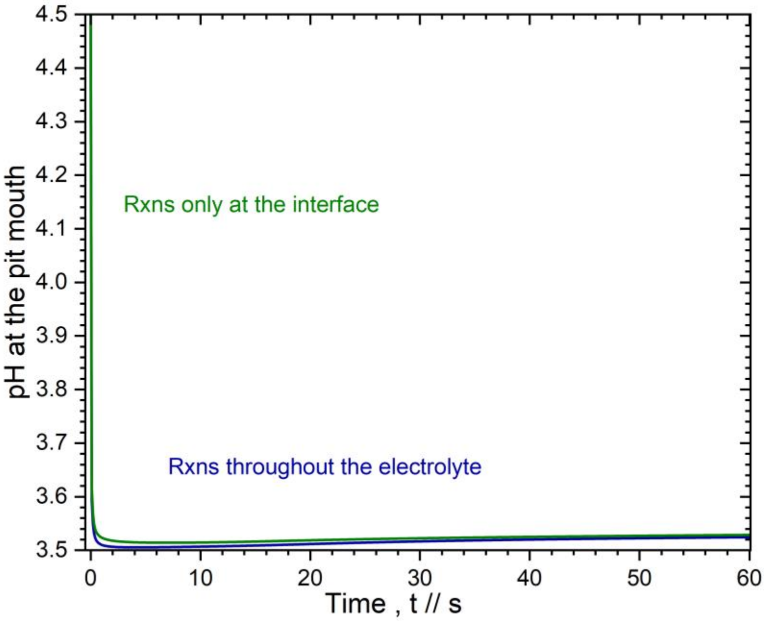

Figure 5.7. pH versus time at the pit mouth recorded for the two Tertiary current distribution techniques with reactions being placed throughout the electrolyte and at the boundary (green) and only at the electrode-electrolyte boundary.

The results from Figure 5.7 indicate that a pseudo-steady state is reached approximately 2 seconds into the simulation, as evidenced by the minimal changes in pH over time. Additionally, the results demonstrate excellent agreement between the two calculation methods.

A significant difference in computational efficiency is observed between the two approaches. The simulation in which equilibrium reactions were allowed throughout the electrolyte and at the electrode-electrolyte boundary required a total of 47,457 seconds to complete, with a memory usage of 8.59 GB. In contrast, the model that restricted equilibrium reactions to the electrode-electrolyte boundary completed in just 279 seconds, using 5.89 GB of memory. These findings highlight the substantial computational savings achieved by limiting the reaction zone to the electrode-electrolyte boundary without compromising accuracy.

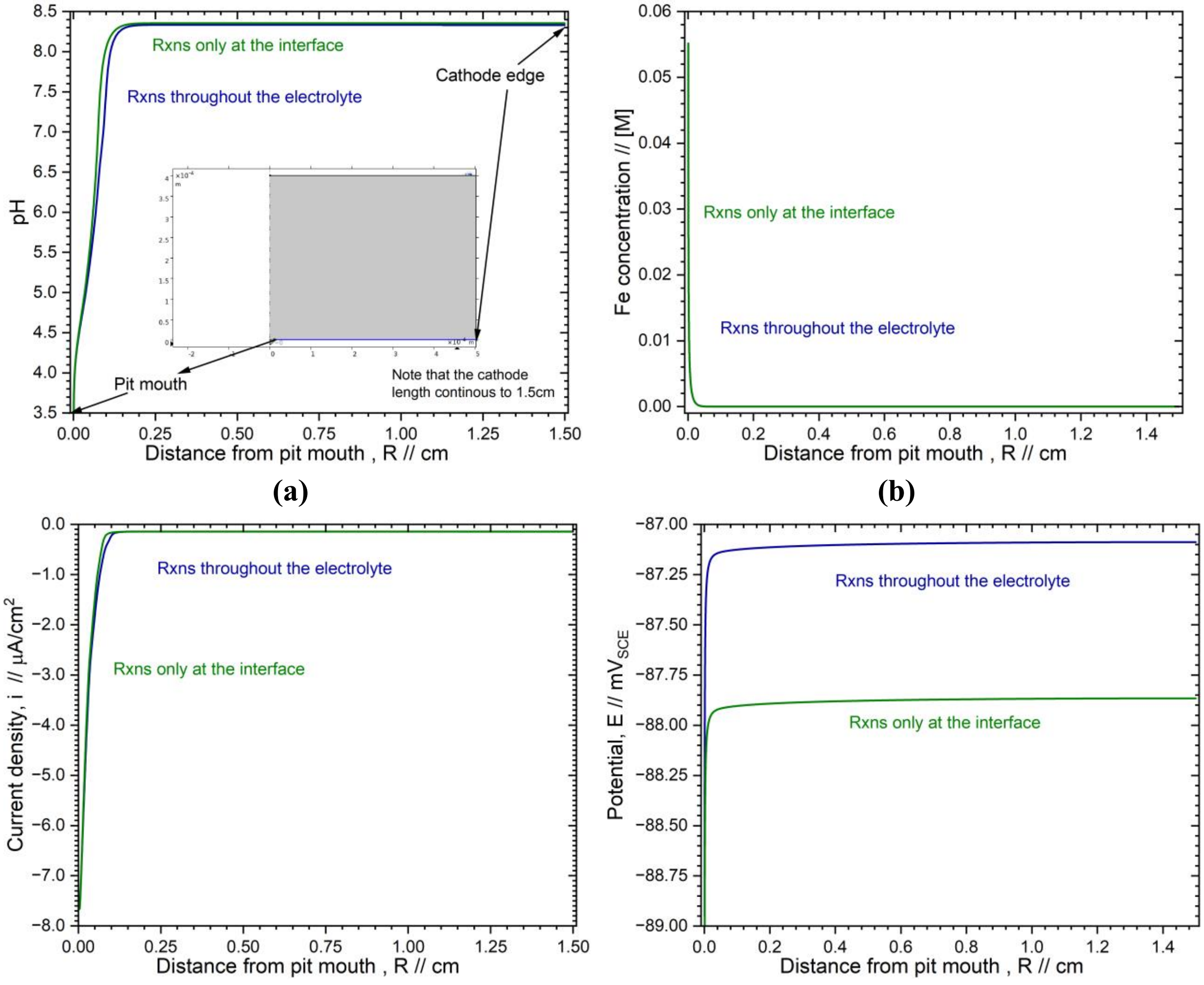

(a) (b)

(c) (d)

Figure 5.8. Simulations utilizing Tertiary current distribution with reactions throughout the electrolyte and at the boundary (blue) and only at the boundary (green) obtained at the cathode after 60s for **a)** pH, **b)** Fe concentration, **c)** current density, and **d)** potential.

The results from Figure 5.8 indicate excellent agreement between the two calculation methods across all variables compared. While certain parameters, such as potential, may appear to show notable differences at first glance, this is largely due to the scale of the ordinate axis. When considering the actual numerical values, the discrepancies remain minimal.

Furthermore, the strong agreement between the two methods is consistent across the entire anode length and throughout the electrolyte, from the bottom of the pit to the center of the pit mouth, as further illustrated in the Appendix. These findings reinforce the validity of the reduced-order model implemented here in accurately capturing the electrochemical behavior while significantly improving computational efficiency.

5.4.4. Maximum pit through Tertiary current distribution-constant $(i{\cdot}x)_{crit}$ at pit surface

In the previous section, we demonstrated the utility of simplifying the system by assuming that equilibrium reactions only occur at the electrode-electrolyte surface. This approach was shown to significantly reduce both simulation time and resource usage compared to the conventional methods, and it has been effectively utilized for the Tertiary current distribution comparisons discussed below.

In the first part of this work, we will employ a technique similar to that of Chen and Kelly, applied to the Secondary current distribution. Specifically, the inside of the pit will be modeled with a constant current density corresponding to the critical current density $(i{\cdot}x)_{crit}$, based on the hemispherical pit size. The cathode kinetics will be pH-dependent, with the cathode current also placed inside the pit, and an anodic limiting current will be applied to the cathode. All simulations will be conducted for a cathode size of 60 cm in radius.

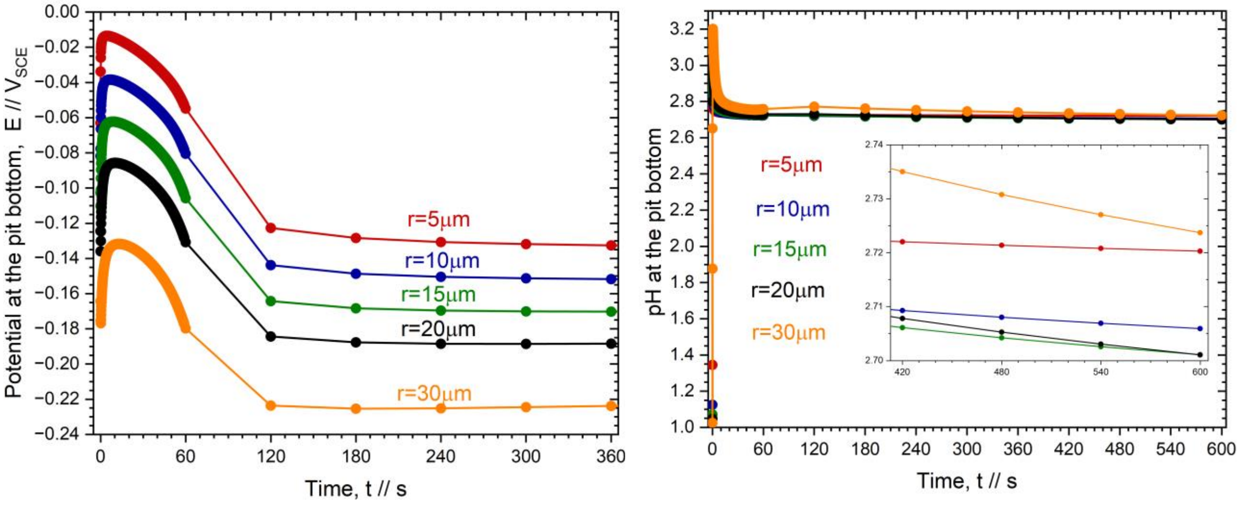

(a) **(b)**

Figure 5.9. a) Potential vs. time and **b)** pH vs. time at the bottom of the pit obtained through Tertiary current distribution for hemispherical pits of radius 5µm (red), 10µm (blue), 15µm (green), 20µm (black) and 30µm (orange). The data obtained with the current density fixed at the pit surface and cathode radius of 60cm.

The results from Figure 5.9a and 5.9b demonstrate the potential and pH at the bottom of the pit as a function of time, respectively. Figure 5.9a shows that upon initiation, the potential increases by around 40mV within less than a second and then stabilizes at a more constant value around 120s, remaining steady for the duration of the simulation. At the end of the simulation, the trend in the potential at the bottom of the pit indicates that increasing the pit radius leads to a decrease in the measured potential.

Figure 5.9b shows that the stabilization of the pH to a near steady state occurs in less than 60s of simulation time, which is much faster than the potential stabilization. No significant trends were observed after 600s on the pH at the bottom of the pit across the different pit radii, with the pH varying from 2.70 to 2.725. Regarding the initial pH being near 1 for all the pit sizes in Figure 9b, it is important to note that these were the initial values intentionally set to better understand the timeline of the dilution phenomenon in such small pits. The results indicate that within less than a second, the dilution of the pit occurs, as evidenced by the sudden increase in pH shown in Figure 9b.

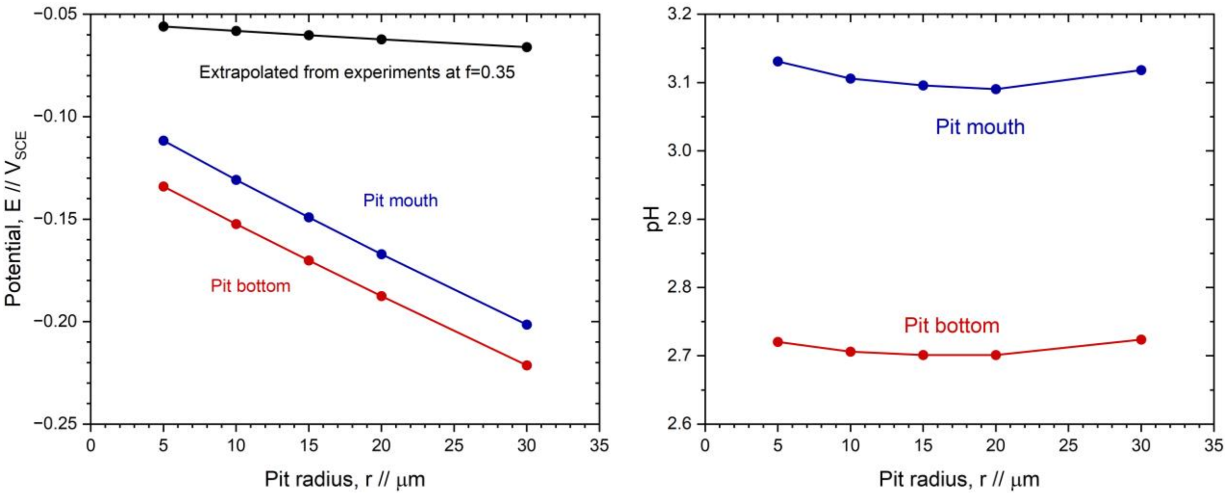

(a) **(b)**

Figure 5.10. a) Potential vs. hemispherical pit radius and **b)** pH vs. hemispherical pit radius after 600s at the bottom of the pit (red) and pit mouth (blue) obtained through Tertiary current distribution for hemispherical pits of radius from 5µm-30µm. The data obtained with the current density is fixed at the pit surface and cathode radius of 60cm.

Figure 5.10a and 5.10b show the potential and pH at the bottom of the pit and at the pit mouth after 600s of simulation time. Figure 5.10a demonstrates that the potential at both the bottom of the pit and the pit mouth decreases with an increase in pit radius at a rate of 4mV/μm. The difference in potential between the pit mouth and the bottom of the pit remains constant, around 25mV, across different pit sizes. The potential at the pit mouth and bottom remains considerably lower, by 75mV-150mV, than the experimentally extracted values.

Figure 5.10b shows that the pH at both the pit bottom and the pit mouth remain relatively constant across different pit sizes. On average, the pH at the pit bottom stays around 2.71, while that at the pit mouth is around 3.15.

The results from Figure 5.9a indicate that the only pit radii that remained active, at a potential above the experimentally extrapolated E_{rp} (black line in Figure 5.10a), are the pits with a radius of 5μm and 10μm. Therefore, the analysis in the following sections focuses only on pits of those sizes.

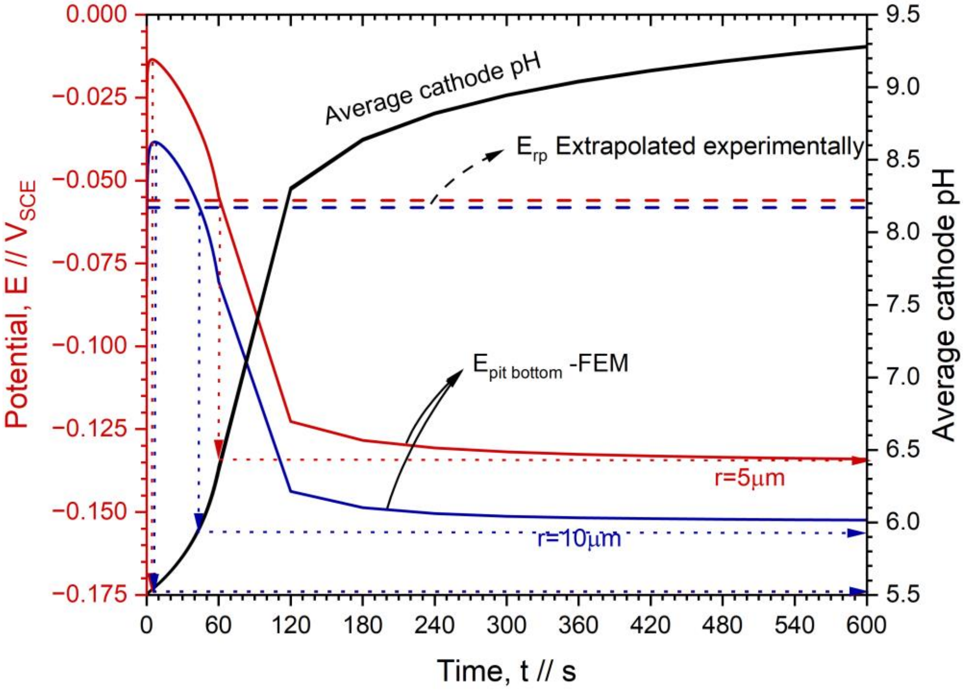

Figure 5.11. Potential at the pit bottom versus time (left ordinate) for pits of 5um (red) and 10um(blue) obtained through FEM (solid) and extrapolated from experiments (dashed). The right ordinate represents the average cathode pH evolution over time for each pit radius. (black solid lines-same for both pit sizes). Results obtained through Tertiary current distribution with constant current density on the pit surface and cathode radius of 60cm.

Figure 5.11 shows the variations in potential at the pit bottom for pits of radius 5μm and 10μm (solid red and blue lines, respectively) on the left ordinate axis and the corresponding average cathode pH (black solid line) on the right ordinate axis, as a function of time. Both pit radii exhibit the same average cathode pH over time, so only one solid black line appears in the graph. Additionally, the dashed lines represent the E_{rp} values from the extrapolated experimental data.

Whenever the dashed lines intersect with the solid lines (corresponding to the same pit size), dotted arrows are projected onto the line corresponding to the average cathode pH and ultimately onto the right ordinate axis. These values correspond to the range of average cathode pH that can support an active pit of the given radius before the bottom of the pit reaches the E_{rp}.

The results indicate that, in order for the cathode to support pits of 5μm and 10μm, the average pH on its surface must be below 6.4 and 5.9, respectively.

5.4.5. Maximum pit through Tertiary current distribution-Tafel kinetics at pit surface

In this section of the work, we investigate the evolution of pit chemistry as well as the potential and current distribution, with the inside of the pit following Tafel relationships between potential and current densities. No changes to the cathode input or other boundary conditions have been made.

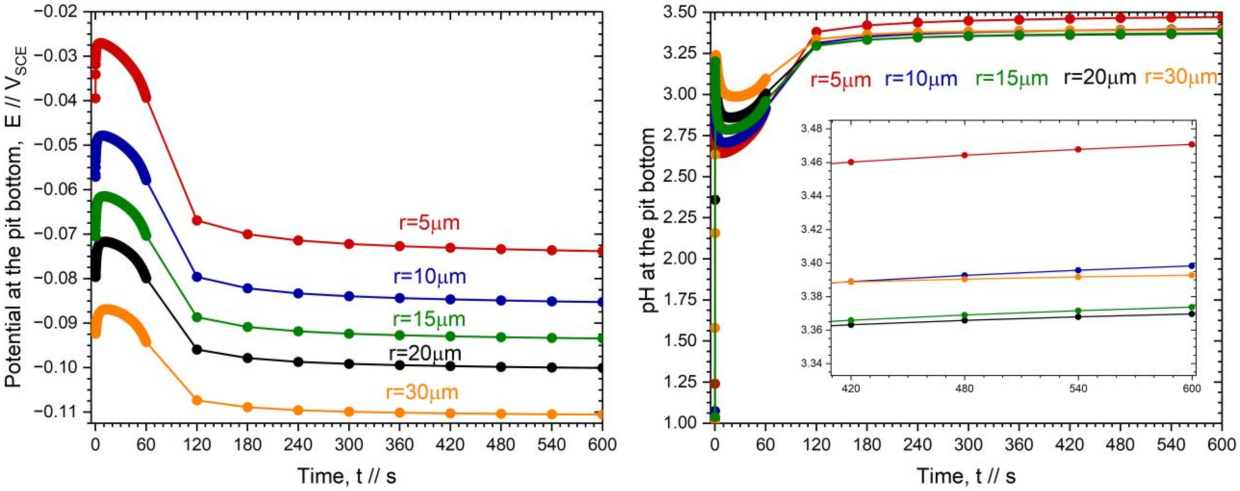

(a) **(b)**

Figure 5.12. a) Potential vs. time and **b)** pH vs. time at the bottom of the pit obtained through Tertiary current distribution for hemispherical pits of radius 5μm (red), 10μm (blue), 15μm (green), 20μm (black), and 30μm (orange). The data obtained with a Tafel relationship between the current density and potential on the pit surface and cathode radius of 60cm.

Figure 5.12a and 5.12b show the evolution of the potential and pH at the pit bottom as a function of time for pits with radii ranging from 5μm to 30μm. Overall, similar trends to those presented in Figure 5.9a and 5.9b for the case of a constant current density at the bottom of the pit are observed. However, for the case presented here, the potential at the bottom of the pit is about two times higher than those in Figure 5.9a for the same pit size. On the other hand, the results in Figure 5.12b show that after 600s, the pH at the bottom of the pits is higher than those in Figure 5.9b by about 0.5-0.7 pH units after the same amount of time.

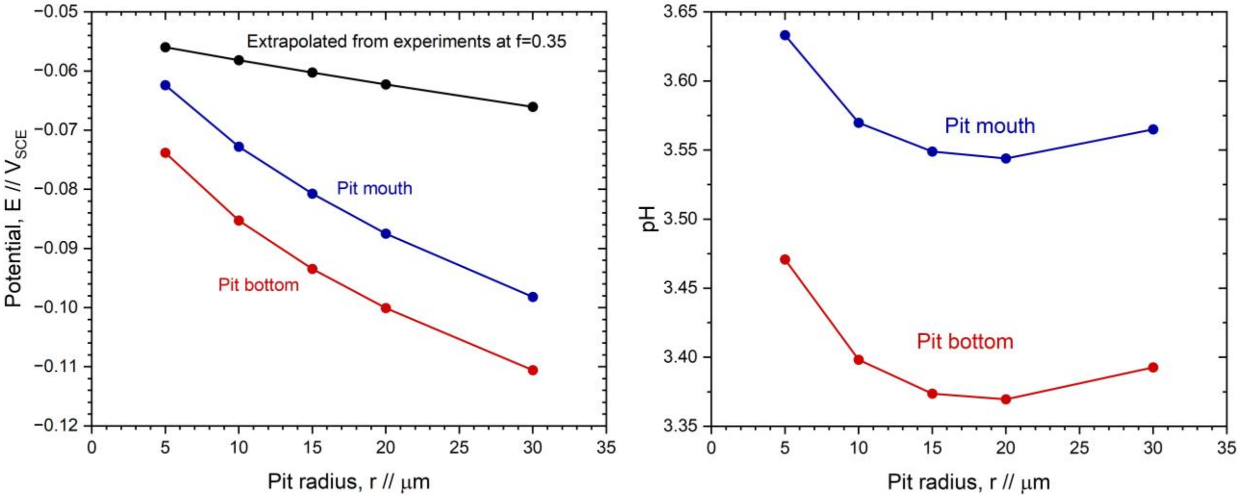

(a) **(b)**

Figure 5.13. a) Potential vs. hemispherical pit radius and **b)** pH vs. hemispherical pit radius at the bottom of the pit (red) and pit mouth (blue) obtained through Tertiary current distribution for hemispherical pits of radius from 5μm-30μm. The data obtained with a Tafel relationship between the current density and potential on the pit surface and cathode radius of 60cm.

The results presented in Figure 5.12a and 5.12b are further clarified in Figures 5.13a and 5.13b. The data in Figure 5.12a indicate that as pit depth increases, the potential at both the pit bottom and pit mouth decreases. However, unlike the linear decrease observed in Figure 5.10a, the decrease in potential with increasing pit radius follows a logarithmic trend. The difference in potential between the pit mouth and the pit bottom varies slightly as the pit radius increases from 5μm to 30μm, with an average difference of approximately 15mV. Overall, after 600s, the potential at both the pit bottom and pit mouth remains lower than the experimentally extrapolated values for *f*=0.35. Conversely, the pH at the pit bottom and pit mouth after 600s does not exhibit a clear trend with changing pit radius. However, these pH values are significantly higher-by approximately 0.5-0.7 pH units-compared to those observed in the constant current density case presented in Figure 5.10b.

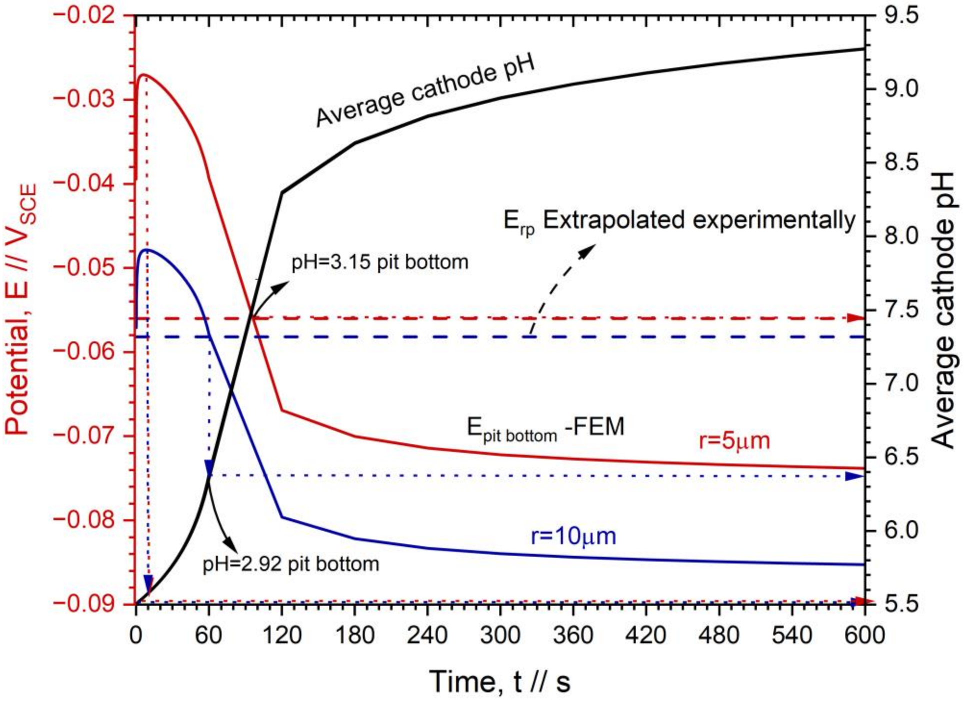

Figure 5.14. Potential at the pit bottom versus time (left ordinate) for pits of 5um (red) and 10um(blue) obtained through FEM (solid) and extrapolated from experiments (dashed). The right ordinate represents the average cathode pH evolution over time for each pit radius. (black solid lines-same for both pit sizes). Results obtained through Tertiary current distribution with a Tafel relationship between current and potential on the pit surface and cathode radius of 60cm.

Figure 5.14 presents a graph similar to Figure 5.11, illustrating the relationship between pit stability and cathode pH. As observed in the constant current density case (Figure 5.11), only the pits with radii of 5μm and 10μm exhibited an increase in potential above the E_{rp} during the dilution phase. The results in Figure 5.14 indicate that for a hemispherical pit with a radius of 5μm, the average cathode pH required to sustain its activity must remain below 7.45. For a hemispherical pit with a radius of 10μm, this threshold decreases to a pH below 6.4. Additionally, the pH at the bottom of the pit at the point of repassivation was approximately 3.15 for the 5μm pit and around 2.92 for the 10μm pit.

5.4.6. Summary graph

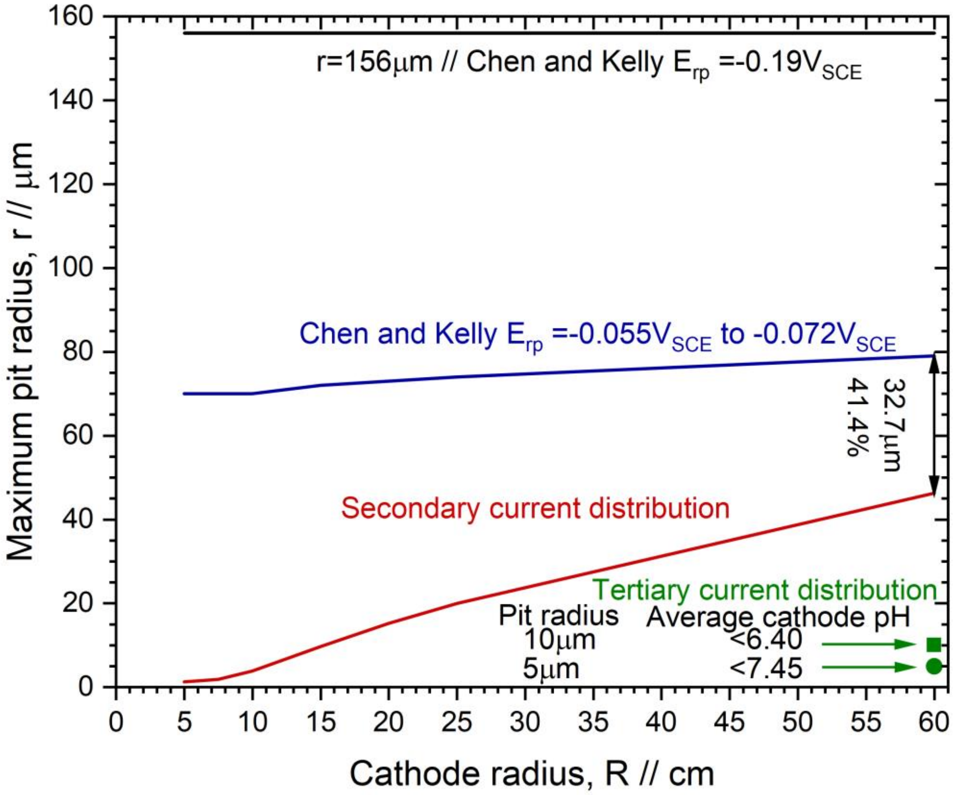

Figure 5.15. Maximum pit size predictions for a SS304 hemispherical pit through 3 different methods as a function of cathode radius, R: Chen and Kelly's model with E_{rp} values of -0.19V vs. SCE (black) and -0.055V vs. SCE to -0.072V vs. SCE (blue), Secondary current distribution (red), and Tertiary current distribution at different average cathode pH value and cathode radius of 60cm (green symbols).

The final results in Figure 5.15 present maximum pit size predictions for a hemispherical pit of SS304 in 0.6M NaCl using three different methods: Chen and Kelly (black and blue lines), Secondary current distribution (red line), and Tertiary current distribution (green symbols). The findings indicate that the Chen and Kelly model provides more conservative predictions compared to both the Secondary (by 41.4%) and Tertiary current distributions.

The E_{rp} value of -0.19V vs. SCE corresponds to data from our previous study[21] while the blue line represents E_{rp} values extracted from experimental results in this study at f=0.35. In the Secondary current distribution model, the predicted maximum pit size increases with cathode size until further increases result in negligible changes. Conversely, Tertiary current distribution results predict smaller hemispherical pit sizes than both the Chen and Kelly model and the Secondary current distribution, primarily due to limitations imposed by cathode pH. The largest hemispherical pit radius that remained active in the Tertiary current distribution simulations was 10µm, sustained by an average cathode pH below 6.40 for a 60cm radius cathode.

5.5. Discussion

The primary goal of this paper is to quantify and establish, through varying levels of complexity, the conservatism of Chen and Kelly's model in predicting the maximum hemispherical pit size on a given alloy, provided a necessary set of input parameters. This assessment is achieved by comparing results for a hemispherical pit in SS304 exposed to 0.6M NaCl, using Chen and Kelly's model, Secondary current distribution, and Tertiary current distribution. In the case of the Tertiary current distribution, the implications of incorporating solution chemistry into the obtained calculations for maximum pit are also discussed.

5.5.1. Chen and Kelly's model is conservative in the maximum pit size predictions due to idealized assumptions

The conservatism of Chen and Kelly's model arises from several fundamental assumptions that treat the system as ideal, particularly in terms of maximizing the total cathodic current available. More detailed discussions of the system's assumptions can be found in Chen and Kelly's original work[2,3] but here, we highlight some of the most important ones. To start, Chen and Kelly's method considers the total cathodic current available for the system by integrating the current from the OCP (which would typically be located at the cathode edge) to the E_{rp} (taken at this model to be at the pit mouth). To circumvent the need for a cathode size, then, Chen and Kelly's model utilizes an equivalent cathode assuming a uniform current density (and hence ohmic drop) across its infinite length. The implications of this assumption become evident when comparing the results from Secondary and Tertiary current distribution models in terms of potential and current distribution along the cathode.

For example, as shown in Figure 5.8c and 5.8d the majority of the current supplied by the cathode to the pit is concentrated very close to the pit mouth, where the rate of potential drop is largest. This concentration is reflected in the sharp increase in current density and potential on the cathode region near the pit mouth. As the distance from the pit mouth increases, the magnitude of the current density gradually decreases until it reaches the cathode edge. However, in the FEM model, the potential at each individual point does not exactly match the input boundary condition of OCP, meaning that the total cathodic current is not maximized. The asymptotic nature of the current density profile is due to the fact that as OCP is reached, the low current densities result in small ohmic drop.

To maximize the cathodic current in the FEM model, one could increase the cathode size. However, since the cathodic current density near the OCP is typically very low, increasing the cathode size results in only a modest increase in the total current and, consequently, a slight increase in the predicted maximum pit size. This effect explains the behavior observed in Figure 5.14, where the slope of the red line decreases with an increase in cathode size, leading to diminishing changes in the predicted maximum pit size. In this study, the means of calculating the maximum cathodic current possible is the difference between Chen and Kelly's model and the Secondary current distribution is the key factor to the discrepancies in the predicted maximum pit size between the models.

5.5.2. Excluding electrolyte chemistry underpredicts cathode limitations

Another key assumption from the Chen and Kelly's model is the neglect of electrolyte chemistry and reactions inside the pit and around the cathode that could influence the electrochemical boundary conditions. When comparing Chen and Kelly's model with the Tertiary current distribution model, which assumes a constant current density inside the pit, the primary difference between the two models lies in the incorporation of hydrolysis, precipitation, chlorination, and water equilibrium reactions at both the pit surface and the cathode on the later one. The exchange current density for these reactions is a function of pH. Although the current density distribution inside the pit remains the same for both models, it is important to note that the potential on the anode surface decreases after approximately 60 s in the Tertiary current distribution model (Figure 5.9). The potential of the anode surface is not calculated or considered in the Chen and Kelly model as the minimum anode current density required for pit growth as determined by the pit stability product is not a function of potential.

In the Tertiary current distribution model, the current density inside the pit is independent of any input boundary conditions related to the potential. Therefore, the potential distribution depends on the cathode's ability to adjust its potential and current distribution based on the electrolyte chemistry to satisfy the constant current density demand from the anode (pit). These adjustments on the cathode affect the potential distribution inside the pit. Specifically, the decrease in potential observed on the cathode (and by default due to the boundary conditions on the anode) is due to the pH dependence of the exchange current density (and consequently the potential) on the cathode surface. As time progresses, the pH on the cathode increases, and in order for the cathode to satisfy the same total current demand from the anode (pit) at higher pH, the overpotential must rise, leading to a reduction in potential - not only on the cathode surface but also inside the pit.

Therefore, in addition to the limited cathode size, the Tertiary current distribution model further reduces the cathode's capacity by decreasing its reduction reaction current due to the increasing pH on its surface, which is a direct result of the reduction reaction occurring from the ORR reaction boundary condition.

This phenomenon helps clarify another observation from Figures 5.10a and 5.10b. For example, it may seem paradoxical that the potential at the bottom of the pit in Figure 5.10a is as low as -0.2V vs. SCE, while the pH at the same location is around 2.7. The low potential suggests the pit would passivate, while the low pH would typically indicate an active pit. However, it is essential to emphasize that in this model, the pH inside the pit remains low as long as the cathode continues to supply the current demand from the anode. As the cathode experiences an increase in pH, the only way to meet the current demand from the pit is by further increasing the driving force/overpotential for the cathodic reaction, which results in a more negative potential on the cathode surface. The cathode and anode are interdependent, meaning that the decrease in potential on the cathode surface must be matched by a decrease in potential on the anode.

In the case of the Tertiary current distribution model, with a constant current density inside the anode, the potential inside the pit can be driven to unreasonably low values while maintaining a high dissolution rate (low pH), making it appear as though the pit is active. However, to determine whether the pit is active or passive in this model, the pH inside the pit should be disregarded in this model where the current density inside of the pit is constant because that constant current density will always result in a low pH. However, the potential which the cathode and anode current match can occur at very low potentials because of the disregard for the connection between the current density and potential. Instead, the potential should be considered in determining stability. Once it is below E_{rp}, the pit must passivate.

5.5.3. Introducing Tafel kinetics inside the pit improves model realism and decreases conservativism while increasing uncertainty.

One of the most critical comparisons in this study is between Chen and Kelly's model and a Tertiary current distribution model that incorporates Tafel kinetics within the pit, alongside the previously mentioned boundary conditions. The primary implication of this setup is that the potential and current distribution on the cathode surface are influenced not only by the pH but also by the potential and current distribution within the pit. Essentially, both the anode (pit) and cathode must "work" together to achieve steady-state conditions for potential, current, and chemical species' distribution.

In this model, the anode (pit) does not have a fixed, predetermined total current that must be matched by the cathode. Instead, the current density and potential at the pit surface can adjust dynamically in response to changes at the cathode. This connection means that the current and potential distribution inside the pit will vary, typically decreasing from the pit mouth to the pit bottom. The reference potential, E_{rp}, can therefore be defined either as the potential at the pit mouth or at the pit surface, depending on the experimental methods used to measure the potential. In this study, the IR-corrected potential was used to match the experimentally determined E_{rp}, with repassivation occurring once the extrapolated experimental E_{rp} for a given pit depth was reached.

However, unlike the previous case, the pH inside the pit at the moment of repassivation should also be considered when evaluating the model's validity and predictive capability. In this case, the pH at repassivation point was found to be consistent with values often reported in the literature for the alloy.[21]

Lastly, we address how the Tafel kinetic relationship for potential and current distribution inside the pit predicts a broader range of average cathode pH values that can support an active pit, compared to the more rigid constant current density model. As shown in Figures 5.11 and 5.13, this difference arises because the total current density within the pit, when using the Tafel relationship, is lower than in a Tertiary current distribution model with a constant current density. This effect is evidenced by the higher potential at the pit bottom, which reflects a corresponding increase in the potential values on the cathode surface, and it is shown more explicitly in Figure A5.6 in the Appendix.

It is important to note that while upgrading to the Tertiary current distribution model offers significant improvements, it also involves trade-offs, particularly in the increased complexity and understanding required for the input boundary conditions which can lead to uncertainties. For instance, the results of this study clearly demonstrate that the input conditions for hydrolysis and chlorination reactions can substantially influence the outcomes. Additional challenges arise from factors such as the rate of precipitation reactions, diffusion coefficients, the mobility of species, and ionic interaction parameters. Few of the needed parameters are available for most alloy systems.

For example, considering the interaction parameters between ions, as well as the changes in diffusivity and mobility due to the increased viscosity within the pit and surrounding pit mouth area, it is unlikely that the total cathodic capacity would increase (in fact a decrease in the cathode capacity is expected under such situations). Therefore, despite the added complexities of the Tertiary current distribution model, the idealized assumptions of Chen and Kelly's model remain the most conservative approach for predicting a single maximum pit size.

5.5.4. Hydrolysis reactions are time dependent on the time scale important to localized corrosion, hence, challenging equilibrium-based models

The hydrolysis time of Cr^{3+} is a critical factor, as it raises another important question: how long does a single Cr^{3+} ion remain near the pit surface after being released into the electrolyte? If the Cr^{3+} ion exits the pit before hydrolysis can occur, then it does not contribute to the pit pH. To gain insight into this question, the pH versus time graphs in Figures 5.9b and 5.12b clearly show that the dilution time for all the small pits examined through FEM is extremely short - less than a second. However, it is known that Cr^{3+} hydrolysis is a slow process due to the exchange rate of the waters of hydration. Therefore, the duration for Cr^{3+} to hydrolyze near the surface during localized corrosion is expected to be minimal. These results suggest that the pH inside the pit could be considerably higher than the pH predicted by thermodynamic simulations that assume complete hydrolysis or by time-dependent FEM models that use thermodynamic K_{eq}-based reactions as boundary conditions.

For instance, Figure A5.4b and A5.5 in the Appendix illustrates that when the equilibrium constant between Cr^{3+} and Cl^- is not considered in the model, the resulting pH and potential distributions differ significantly, assuming all other boundary conditions remain constant. This discrepancy arises from the fact that the K_{eq} for Cr^{3+} hydrolysis and chlorination reactions are typically modeled separately rather than in conjunction with the mass transport calculations. This separation can lead to variations in results, particularly in cases in which both ions are present in significant concentrations, thus influencing the outcome of the simulation.

5.5.5. Placing the reactions only at the electrode-electrolyte boundaries reduces computational complexity while maintaining accuracy

In the final part of this study, we examine the ROM presented here and utilized it to provide time-dependent solutions of a complicated localized corrosion system. The results demonstrate that for a complex Tertiary current distribution system incorporating precipitation, hydrolysis, chlorination, and water equilibrium reactions, the distributions of current, potential, and species concentrations remain largely consistent whether these reactions are applied as boundary conditions throughout the entire electrolyte and electrode-electrolyte interface or only at the electrode-electrolyte interface. These similarities extend across the pit surface, cathode surface, and throughout the electrolyte, as shown in Figures 5.7, 5.8, A5.2 and A5.3.

Notably, restricting these reactions to the electrode-electrolyte boundary yields significant computational advantages, including reduced simulation time and memory usage, as well as improved model initialization and convergence stability. In the context of localized corrosion, the results suggest that most reactions occur near the electrode-electrolyte interface, while dilution effects in the bulk electrolyte have a minimal impact on the overall simulation outcome. This phenomenon can be attributed to the high local concentrations of reactive species near the interface, which drive rapid solution property changes, such as shifts in pH and Cl^- concentration. Given the relatively low K_{eq} of these reactions, most reactive species immediately undergo transformation into their respective products. Consequently, by the time species diffuse or migrate into the bulk electrolyte, they have already reached near-equilibrium concentrations, resulting in negligible further changes in concentration.

5.5.6. Limitations

The present study operates under several assumptions, including ideal solution behavior. Some of the limitations of the work were mentioned briefly in the discussion sections above. However, three key limitations and their potential impact on the findings are addressed below.

The first limitation concerns the influence of additional cations, such as Ni^{2+} and Fe^{2+}, on the dissolution of SS304 and the subsequent hydrolysis of Cr^{3+}. As demonstrated in Figures 5.2a and 5.2b, when the Cl^- concentration is held constant at 3M, replacing Na^+ with Ni^{2+} results in measurable pH changes. This suggests that Ni^{2+} actively participates in hydrolysis and chlorination reactions, which, in turn, influence the hydrolysis and chlorination of Cr^{3+} due to complex ion interactions.

Secondly, this study assumes that precipitation reactions act as sinks for ionic species involved in the reaction process. Within the Tertiary current distribution model, once the K_{sp}/K_{eq} is reached, precipitating species are effectively removed from the system, preventing the formation of solid products on the cathode surface. This assumption is significant because cathodic precipitation can reduce the active cathode area available for electrochemical reactions as well as impose effectively lower conductivity in the solution, ultimately decreasing cathode capacity and limiting maximum pit size. While incorporating precipitation effects into the Tertiary current distribution model is possible, it introduces computational challenges related to convergence. Notably, prior work by Chen and Kelly[2,3] has incorporated modifications to account for reduced cathode capacity due to precipitation reactions.

Finally, this study employs cathodic reaction kinetics for the ORR obtained from OLI Studio to model the cathode surface behavior. Although OLI Studio provides high-fidelity, semi-empirical data, experimental cathodic boundary conditions may enhance model accuracy. In particular, the cathodic kinetics of alloys with specific surface finishes relevant to the studied conditions could yield more precise results.

Conclusions

In this work, the conservatism of Chen and Kelly's model was evaluated using FEA techniques, incorporating both Secondary and Tertiary current distributions. Through a combination of artificial 1D pit experiments and thermodynamic modeling, input electrochemical boundary conditions for shallow pits were determined. Experimental data on the equilibrium constant for Cr^{3+} hydrolysis and chlorination reactions were also obtained and used as input for the Tertiary current distribution model. The following conclusions were drawn:

1. Chen and Kelly's model tends to be conservative in predicting the maximum pit size, underestimating it by approximately 40% compared to predictions based on Secondary current distribution. This discrepancy is primarily due to idealized assumptions about the total cathodic current.
2. Excluding electrolyte chemistry and associated reactions results in an underestimation of cathodic limitations, particularly when the same anode input boundary conditions from Chen and Kelly's model are applied.

3. Introducing Tafel kinetics within the pit environment improves the model's realism, reducing conservatism but also increasing uncertainty in predictions.
4. Hydrolysis reactions are time-dependent, with timescales significant to localized corrosion, thus challenging equilibrium-based models that do not account for this time dependency.
5. Simplifying the reactions by placing them solely at the electrode-electrolyte boundaries reduces computational complexity while still maintaining model accuracy.

A5. Appendix

Table A5.1. Dependence on pH of the pseudo exchange current density for HER and ORR in 0.6M NaCl and reversible potential of -0.141 V vs. SCE and 0.759 V vs. SCE obtained through OLI Studio version 12.0.

pH	**HER // i_o(ma/cm^2)**	**ORR // i_o(ma/cm^2)**
0	$1.32\cdot10^{-6}$	$8.13\cdot10^{-11}$
1	$4.91\cdot10^{-7}$	$2.31\cdot10^{-10}$
2	$1.58\cdot10^{-7}$	$3.20\cdot10^{-8}$
3	$5.00\cdot10^{-8}$	$1.13\cdot10^{-9}$
4	$1.58\cdot10^{-8}$	$6.52\cdot10^{-10}$
5	$5.00\cdot10^{-9}$	$2.31\cdot10^{-10}$
6	$1.58\cdot10^{-9}$	$8.03\cdot10^{-11}$
7	$5.00\cdot10^{-10}$	$3.21\cdot10^{-11}$
8	$1.58\cdot10^{-10}$	$1.68\cdot10^{-11}$
9	$5.00\cdot10^{-11}$	$1.20\cdot10^{-11}$
10	$1.59\cdot10^{-11}$	$1.04\cdot10^{-11}$
11	$5.22\cdot10^{-12}$	$9.95\cdot10^{-12}$
12	$2.28\cdot10^{-12}$	$9.80\cdot10^{-12}$
13	$2.67\cdot10^{-12}$	$9.76\cdot10^{-12}$
14	$6.50\cdot10^{-12}$	$9.86\cdot10^{-12}$

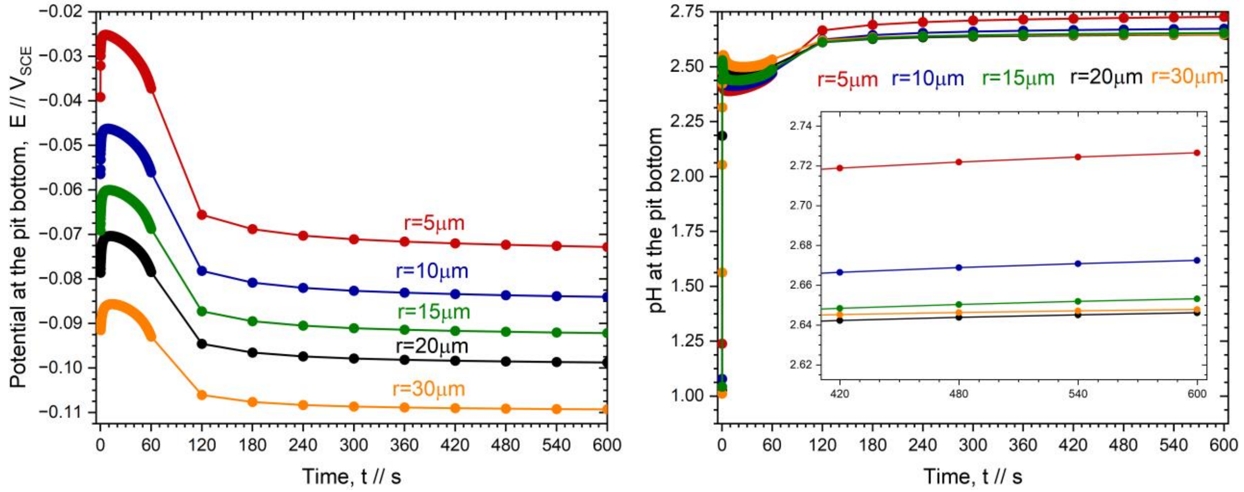

(a) **(b)**

Figure A5.1. a) Potential vs. time and **b)** pH vs. time at the bottom of the pit obtained through Tertiary current distribution for hemispherical pits of radius 5μm (red), 10μm (blue), 15μm (green), 20μm (black), and 30μm (orange). Results obtained through Tertiary current distribution with a Tafel relationship between current and potential on the pit surface without the $CrCl^{2+}$ equilibrium reaction taking place and cathode size of radius 60cm.

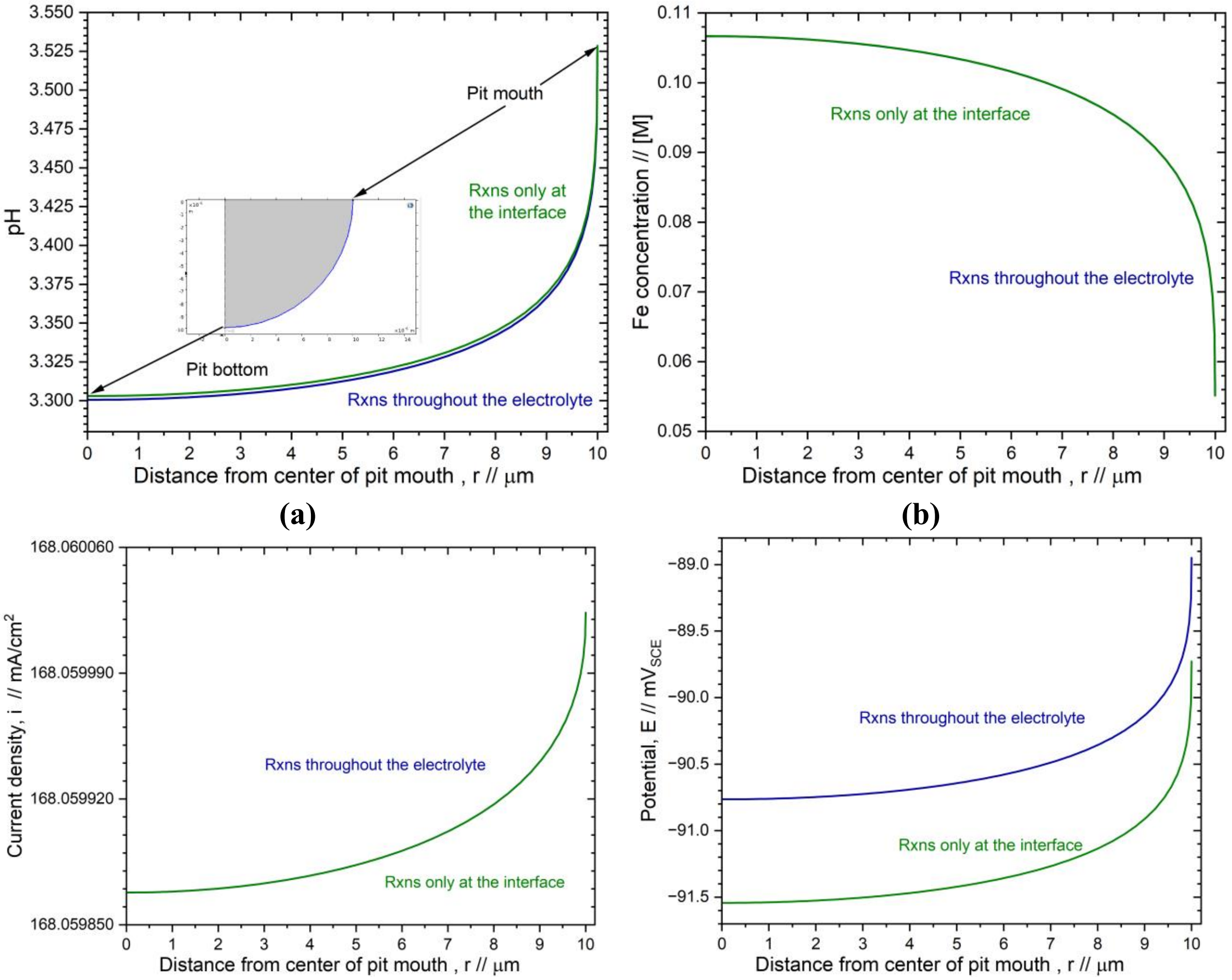

(a) **(b)**

(c) **(d)**

Figure A5.2. Simulations utilizing Tertiary current distribution with reactions throughout the electrolyte and at the boundary (blue) and only at the boundary (green) obtained at the pit surface after 60s for **a)** pH, **b)** Fe concentration, **c)** current density, and **d)** potential

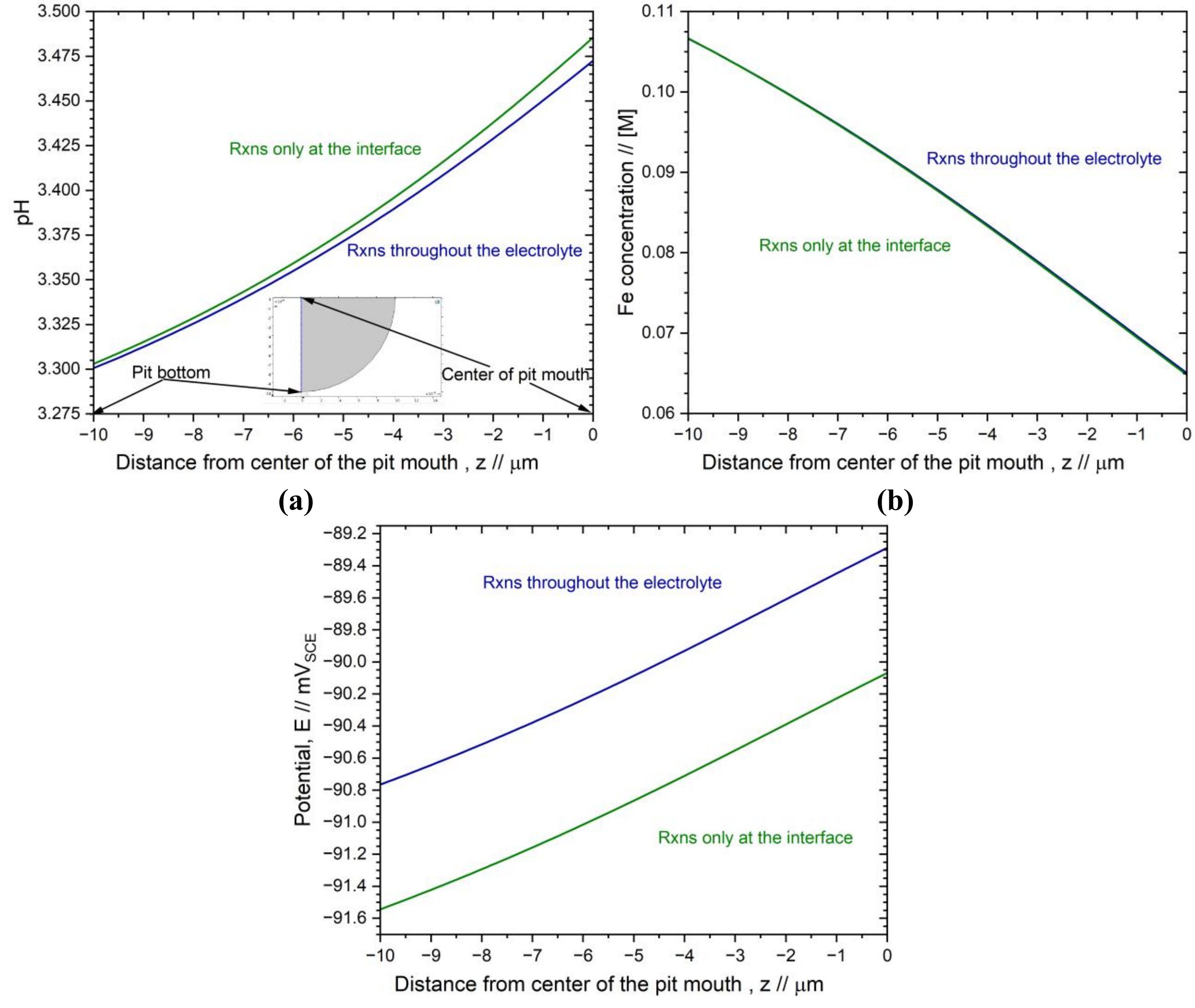

(a) **(b)**

(c)

Figure A5.3. Simulations utilizing Tertiary current distribution with reactions throughout the electrolyte and at the boundary (blue) and only at the boundary (green) obtained throughout the electrolyte from the center bottom of the pit to pit mouth after 60s for **a)** pH, **b)** Fe concentration, and **c)** potential.

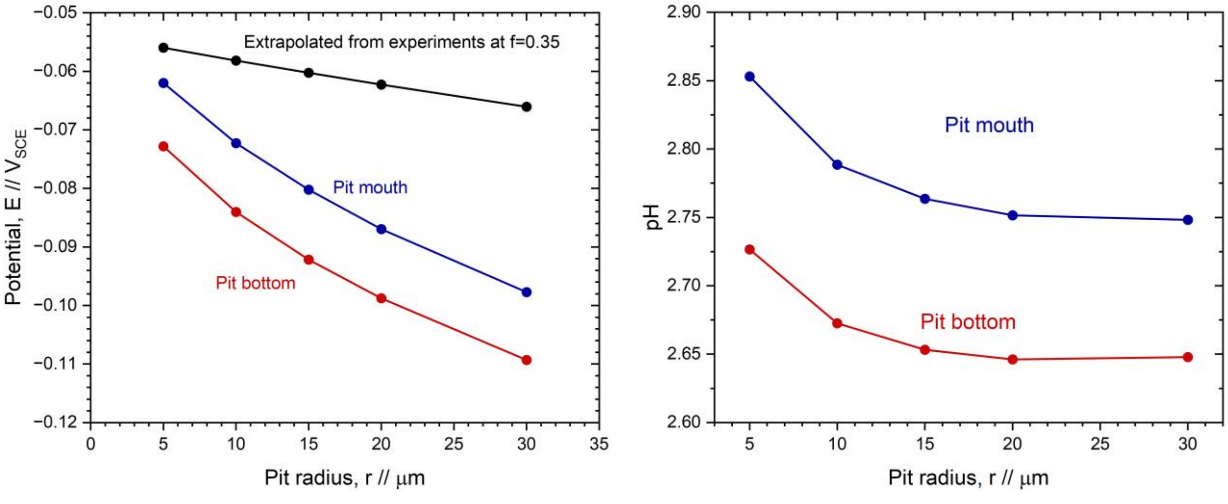

(a) **(b)**

Figure A5.4. a) Potential vs. hemispherical pit radius and **b)** pH vs. hemispherical pit radius at the bottom of the pit (red) and pit mouth (blue) obtained through Tertiary current distribution for hemispherical pits of radius from 5μm-30μm. Results obtained through Tertiary current distribution with a Tafel relationship between current and potential on the pit surface without the $CrCl^{2+}$ equilibrium reaction taking place and cathode size of radius 60cm.

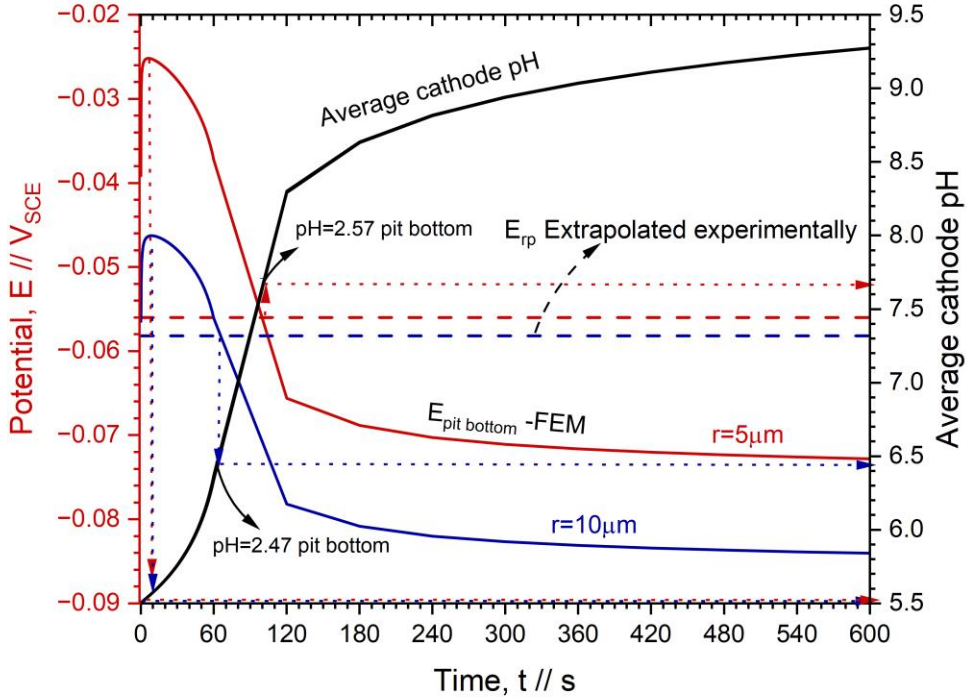

Figure A5.5. Potential at the pit bottom versus time (left ordinate) for pits of 5um (red) and 10um(blue) obtained through FEM (solid) and extrapolated from experiments (dashed). The right ordinate represents the average cathode pH evolution over time for each pit radius. (black solid lines-same for both pit sizes). Results obtained through Tertiary current distribution with a Tafel relationship between current and potential on the pit surface without the $CrCl^{2+}$ equilibrium reaction taking place and cathode size of radius 60cm.

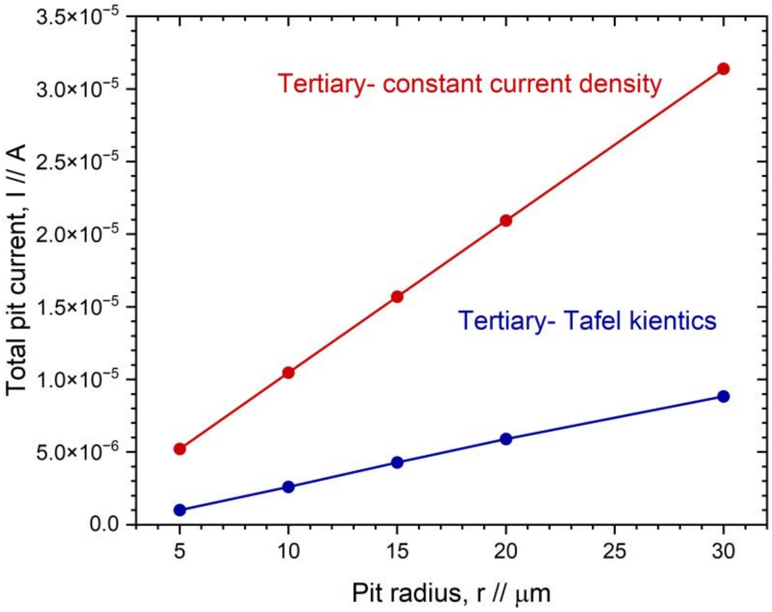

Figure A5.6. Total pit current versus pit radius for Tertiary current distribution with constant current density inside the pit (red) and Tafel kinetics relationship between current and potential (blue).

5.7. References

1. Nakata, M., Ono, N. & Usuda, Y. State of Stainless Steels Roofing in Okinawa and Characteristics of Corrosion Resistance in Atmosphere of Various Stainless Steels. *Zairyo-to-Kankyo* **46**, 559–564 (1997).
2. Chen, Z. Y. & Kelly, R. G. Computational Modeling of Bounding Conditions for Pit Size on Stainless Steel in Atmospheric Environments. *J. Electrochem. Soc.* **157**, C69 (2010).
3. Chen, Z. Y., Cui, F. & Kelly, R. G. Calculations of the Cathodic Current Delivery Capacity and Stability of Crevice Corrosion under Atmospheric Environments. *J. Electrochem. Soc.* **155**, C360 (2008).
4. Scheiner, S. & Hellmich, C. Finite Volume model for diffusion- and activation-controlled pitting corrosion of stainless steel. *Comput. Methods Appl. Mech. Eng.* **198**, 2898–2910 (2009).
5. Liu, C. & Kelly, R. G. A review of the application of finite element method (FEM) to localized corrosion modeling. *Corrosion* **75**, 1285–1299 (2019).
6. Nguyen, V. A., Newman, R. C. & Laycock, N. J. 2-Dimensional Simulations of Pit Propagation and Multi-Pit Interactions. *J. Electrochem. Soc.* **169**, 081503 (2022).
7. Krouse, D., Laycock, N. & Padovani, C. Modelling pitting corrosion of stainless steel in atmospheric exposures to chloride containing environments. *Corros. Eng. Sci. Technol.* **49**, 521–528 (2014).
8. Laycock, N. J. & White, S. P. Computer Simulation of Single Pit Propagation in Stainless Steel under Potentiostatic Control. *J. Electrochem. Soc.* **148**, B264 (2001).
9. Laycock, N. J., Krouse, D. P., Hendy, S. C. & Williams, D. E. Computer simulation of pitting corrosion of stainless steels. *Electrochem. Soc. Interface* **23**, 65–71 (2014).
10. Sato, N. The Stability of Pitting Dissolution of Metals in Aqueous Solution. *J. Electrochem. Soc* **129**, 260–264 (1982).
11. Sato, N. A theory for breakdown of anodic oxide films on metals. *Electrochim. Acta* **16**, 1683–1692 (1971).
12. Katona, R. M. *et al.* Editors' Choice—Natural Convection Boundary Layer Thickness at Elevated Chloride Concentrations and Temperatures and the Effects on a Galvanic Couple. *J. Electrochem. Soc.* **168**, 031512 (2021).
13. Baes, C. & Mesmer, R. Charles Frederick Baes, Robert Eugene Messmer - The Hydrolysis of Cations-John Wiley & Sons Inc (1976). (1976).
14. Paul, B. L. & Ekberg, C. *Hydrolysis of Metal Ions*. (Wiley-VCH Verlag GmbH & Co. KGaA, 2016). doi:10.1002/9783527656189.
15. Katona, R. M., Burns, J. T., Schaller, R. F. & Kelly, R. G. Insights from electrochemical crack tip modeling of atmospheric stress corrosion cracking. *Corros. Sci.* **209**, 110756 (2022).
16. Ziemniak, S. E., Jones, M. E. & Combs, K. E. S. Solubility and phase behavior of Cr(III) oxides in alkaline media at elevated temperatures. *J. Solution Chem.* **22**, 601–623 (1993).
17. Galvele, J. R. Transport Processes and the Mechanism of Pitting of Metals. *J. Electrochem.*

Soc. **123**, 464–474 (1976).

18. Srinivasan, J., Liu, C. & Kelly, R. G. Geometric Evolution of Flux from a Corroding One-Dimensional Pit and Its Implications on the Evaluation of Kinetic Parameters for Pit Stability. *J. Electrochem. Soc.* **163**, C694–C703 (2016).
19. Srinivasan, J. & Kelly, R. G. One-Dimensional Pit Experiments and Modeling to Determine Critical Factors for Pit Stability and Repassivation. *J. Electrochem. Soc.* **163**, C759–C767 (2016).
20. Srinivasan, J. A Quantitative Framework Connecting the Critical Factors Determining the Stability of Localized Corrosion. (University of Virginia, Materials Science - School of Engineering and Applied Science, PHD (Doctor of Philosophy), 2016, 2016).
21. Shehi, A., Choudhary, S. & Kelly, R. . Repassivation of stainless steels : A unifying quantitative framework. *Corros. Sci.* (2025).

Chapter 6. A comparison of FEM results from the use of different governing equations in a galvanic cell part III: Localized corrosion case-impact of high current density, supporting electrolyte concentration, and diffusion coefficient of electrochemically active species.

A. Shehi[1], C. V. Moraes[2], R. G. Kelly[1]
[1]Center for Electrochemical Science and Engineering, Department of Materials Science and Engineering, University of Virginia, Charlottesville, VA 22904
[2]Arconic Technology Center, 100 Technical Drive New Kensington, PA 15068 USA

Contributions: A. Shehi - Conceptualization, Data curation, Formal analysis, Investigation, Methodology, Visualization, Writing – original draft, Writing – review and editing, **C.V. Moraes** - Conceptualization, Investigation, Writing – review and editing, **R. G. Kelly** - Conceptualization, Funding acquisition, Data curation, Formal analysis, Project administration, Resources, Project administration, Investigation, Methodology, Visualization, Writing – original draft, Writing – review and editing

6.1. Summary

This study investigates the influence of diffusion potential and current on the accuracy of reduced-order electrochemical models based on the Laplace equation. The findings reveal the conditions under which diffusion potential and current significantly impact key electrochemical parameters, offering guidance on selecting the appropriate governing equation Overall, this work shifts attention to the electrolyte and incorporates localized corrosion scenarios characterized by high current densities and varying supporting electrolyte concentrations. Using a simplified electrochemical model with unidirectional transport, we demonstrate that a reduced-order method can yield results identical to the more rigorous method under conditions of zero total diffusion current and does so with impactful improvements in speed and a lessening of computing resources required. In the presence of a diffusion potential/current, its accuracy remains high in the bulk solution, but at and near the electrochemical interface, its accuracy improves as the migration current of electrochemically active species decreases at the electrolyte interface. The work also shows that the diffusion current density of electrochemically active species near the electrode-electrolyte interface is consistently dominant unless its concentration gradient is fixed. Additionally, the total diffusion current remains significant except in rare cases where all electrolyte species have identical diffusion coefficients or even in more rare scenarios when the diffusion currents of the supporting electrolyte and electrochemically active species cancel out. Lastly, this study also shows that the diffusion current from the supporting electrolyte precisely balances the migration current at the electrode-electrolyte interface.

6.2. Introduction

In electrochemical systems, several key parameters require accurate spatiotemporal distribution analysis, including current, potential, the concentration of reactive species involved in electrochemical or chemical reactions, and the concentration of supporting electrolyte ions. However, in many cases, direct experimental measurement of these parameters is challenging. Consequently, computational modeling has become an increasingly valuable tool for gaining insights into the governing parameters and interpreting the limited experimental data available.[1-18]

As described in detail elsewhere [1], computing these distributions in electrolytes bounded by electrochemically active surfaces requires solving systems of partial differential equations. Mass transport is dictated by the flux of all species in response to electrochemical potential gradients. These fluxes are most commonly described using the Nernst-Planck Equation, 6.1, which accounts for transport through diffusion, migration, and convection.

$$\frac{dc_i}{dt} = -\nabla(-D_i\nabla c_i - z_i u_i c_i F\nabla\varphi + c_i u) + R_i \tag{6.1}$$

These i equations (one for each species) separate the electrochemical potential gradients into the three transport modes. This artificial separation implies that the three modes are independent of one another. Ignoring convection, the Nernst-Planck Equation divides the driving force into potential and concentration gradients, which we interpret as representing mass transport by migration and diffusion, respectively. A key result of this artificial division of the electrochemical potential is that the potential gradient in solution contains two terms, the first describing the electrolyte as an ohmic conductor, and a second term, called the “diffusion potential”, as shown in Equation 6.2.

$$\nabla\phi = \frac{-i}{\kappa} - \frac{F}{\kappa}\sum_i z_i D_i \nabla c_i \tag{6.2}$$

The diffusion potential is the summation of the potential gradients resulting from differences in the diffusion coefficients of the ionic species and the influence of their concentration gradients. In other words, concentration gradients of charged species result in electrolytes that are more complicated than simple ohmic conductors. Instead, the concentration gradients lead to a diffusive flux of charged species (a diffusion current, the numerator if second term of Equation 6.2 which creates a potential gradient (the diffusion potential-the complete second term of Equation 6.2 that adds algebraically to the potential gradient caused by the flux of charged species through a finite conductivity medium (the first term) to generate a total potential gradient.

Well away from the electrode surface, there are no concentration gradients, and we define this region as the bulk solution. There, the diffusion potential term, and the resulting diffusion current, are nil, or small enough to be neglected. Near the electrode surface, however, the existence of a diffusion current, arising from concentration gradients of electrochemically active species produced from the electrode, is often an important part of the current.

One impact of our artificial separation of the mass transport modes in the Nernst-Planck Equations is on the governing equations used in computational modeling to solve for the distributions of the desired parameters referred to above. The key decision in the computational modeling of mass transport modes is the selection of the approach to defining an $i^{th}+1$ equation to combine with the set of i Nernst-Planck Equations for the species to have the same number of equations as variables, *i.e.,* the concentrations of all species and the potential. The different choices (*i.e.,* the Poisson Equation, electroneutrality, or the Laplace Equation) rely on different assumptions. Reduced-order (ROM) approaches such as the widely used Nernst-Planck Electroneutrality (**NPE)** approach and the more recently developed Laplace with variable conductivity (**Lvk**) [1,2] approach lead to much faster and more efficient solutions than the Nernst-Planck-Poisson (**NPP**) approach, but at the expense of accuracy.

This work follows the work of Parts I and II [1,2] in which the accuracy of several reduced-order models was assessed over a range of supporting electrolyte ratios (SER is the ratio between the sum of the concentration of the inert species and the sum of the concentration of the electrochemically active species). In Part I and II [1,2], an Al-Mg galvanic system in a thin electrolyte was considered. Current densities in that system are small (~10^{-5} A/cm) and the [Mg^{2+}] is constrained by solubility to < 1 mM. Similar conditions are encountered in many corrosion scenarios.

In that work [1,2] it was shown that **Lvk** can provide reasonably accurate (within ~ 5% of **NPP**, which was in excellent agreement with **NPP**) calculations of potential, current, and chemical distributions for a galvanic system in which (Case I) there is no homogeneous chemical reactions to consider and the electrochemically-active species are at low concentrations relative to the non-reactive species (*i.e.,* the supporting electrolyte). When homogeneous reactions are considered (Case II), there is a loss of accuracy, especially at lower SER. It was proposed that this loss in accuracy is due to the increased importance of the diffusion potential that develops. The diffusion potential is exacerbated by homogenous reactions involving the electroactive species. Case III is when all diffusivities are the same, so no diffusion potential exists. These comparisons were made at the center of the cathode, at the interface. Errors do tend to be higher in the center of the cathode there for parameters of interest, and they can be largest there for some parameters of interest.

The present work addresses two questions that arose from the earlier work: a) can the hypothesis that the diffusion potential and current are the root cause of the disagreements between **Lvk** and **NPE** as the SER decreases be confirmed, and b) how do these errors change when the electrochemical active species is not limited in concentration by solubility and current densities are higher, such as occurs in localized corrosion sites, batteries, fuel cells, and electrochemical processing. In these cases, the SER are low, although the absolute concentrations of the supporting electrolyte may be high.

6.3. Computational Methods

Partial differential equations were solved using COMSOL Multiphysics™ (v.6.2), incorporating the PARDISO direct linear solver and a modified Newtonian method nonlinear solver. The Backward Differential Formula (BDF) method was used for time-step generation. Detailed descriptions of model geometries and meshing techniques can be found in the referenced papers. When mesh details were not provided, the mesh was refined until the results stabilized. For further information on meshing techniques, refinement, and solvers, refer to the COMSOL Multiphysics user manual. Simulations were performed on a system with an Intel Core i9 3.70 GHz processor, 64 GB of RAM, and Windows 10.

6.3.1. Explanation of the computational methods utilized

The study aims to compare the accuracy, efficiency, and benefits of various computational methods for FEM electrochemical systems. The following methods were employed:

1. **Nernst-Planck with Electroneutrality (NPE):** This Tertiary current distribution module in COMSOL Multiphysics solves for the distributions of all species, current, and potential based on the selection of a user-defined make-up ion, maintaining energy conservation. Of note, because of the use of a user-defined make-up ion to maintain charge neutrality at all positions, **NPE** does not conserved mass. Detailed equations and descriptions can be found in the COMSOL user manual and all the equations utilized for the **NPE** method are presented in Figure 6.1a.
2. **Laplace with variable conductivity (Lvk):** A reduced order modeling technique by Moraes and Kelly [1,2] which solves the Laplace Equation and species transport in two separate steps. The spatial variations of electrolyte conductivity, solved using the Transport of Dilute Species module, are used to determine potential distribution via the Laplace Equation in the Secondary Current Distribution module, as shown in Equation 6.3:

$$i = -\nabla\varphi F^2 \sum_i z_i^2 u_i c_i \tag{6.3}$$

Notably from Equation 6.3, in calculating the total electrode current (from Secondary Current Distribution module) the **Lvk** method neglects any current rising from the diffusion of charged species in the Transport of Dilute Species module. In addition, the **Lvk** method does not impose electroneutrality. Multiphysics potential coupling exists between the Secondary Current Distribution and species transport modules. Through this, the potential solved from the Laplace Equation serves to solve the migration flux of the species in the Transport of Dilute Species module. A schematic of this is shown in Figure 1b.

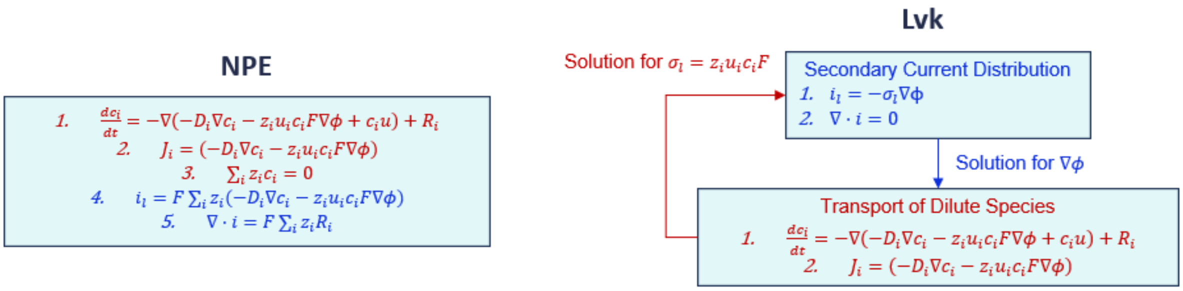

a) **b)**

Figure 6.1. A schematic of the computational flow utilized by the **a)** NPE method and **b)** Lvk method.

Note that for the **NPE** method, all of the equations related to mass transport, potential and current distribution are all solved simultaneously.

6.3.2. System description

The system utilized in this chapter was originally developed by Fu and Chan [19] to compare the simulated and experimental data for the one-dimensional diffusion of a silver ions (Ag^+) produced by galvanostatic dissolution of an Ag wire in a 0.1M potassium nitrate (KNO_3) solution. FEM was employed to simulate the dissolution of a 2 mm diameter Ag wire in 0.1M KNO_3. The original authors did not provide details on the cell geometry or electrochemical boundaries used in the simulation. The decision for the length of the Ag wire to be 10 cm was obtained from the simulation results section of Fu and Chan's paper [19] while the 10 cm x 10 cm portion of the cell geometry was chosen arbitrarily. Neither in the simulation, nor in the experimental section of the paper did the authors provide the location of a counter electrode, as such its location being 20 cm away from the anode was also chosen arbitrarily. No difference in the obtained results was noted if the cathode was placed near the 2 mm x 10 cm cylindrical section of the geometry. The geometry and general electrochemical boundary conditions for this model are depicted in Figure 6.2.

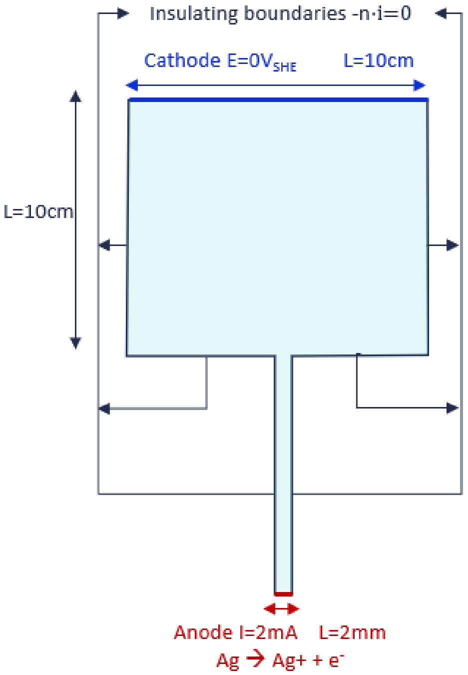

Figure 6.2. Schematic representation and general boundary conditions utilized for Fu and Chan model.[19]

According to Fu and Chan [19], the numerical methods employed by them involved a subroutine procedure in which the potential distribution was first used to calculate ionic fluxes in the solution. This solution step was followed by a hydrolysis reaction:

$$Ag_{(aq)}^{+} + H_2O_{(l)} \leftrightarrow AgOH_{(s)} + H_{(aq)}^{+} \tag{6.4}$$

After this, the updated ionic concentrations were used to recalculate conductivity and boundary conditions for the subsequent step. This iterative process was repeated until a steady state was reached.

In the simulation presented in the current chapter, dilute solution theory was assumed, with the activity coefficients of each species automatically set to 1. Diffusion coefficients were obtained from OLI Studio version 12.0 using the Mixed Solvent Electrolyte (MSE) database for a 0.1M KNO_3 and 1×10^{-6} M $AgNO_3$ solution, as detailed in Table 6.1.

Table 6.1. Parameters used for Fu and Chan model.

Parameter	Description	Value	Reference
i_a	Anodic current	1 mA	Fu and Chan[19]
$E_{0,a}$	Reverse potential for anodic reaction	-1 V vs.SHE	Arbitrary*
$E_{0,c}$	Reverse potential for cathodic reaction	-0 V vs.SHE	Arbitrary*

D_{Ag^+}	Diffusion coefficient of Ag^+	1.53×10^{-9} m^2/s	OLI Studio (v.12.0)
$D_{NO_3^-}$	Diffusion coefficient of NO_3^-	1.77×10^{-9} m^2/s	OLI Studio (v.12.0)
D_{H^+}	Diffusion coefficient of H^+	8.24×10^{-9} m^2/s	OLI Studio (v.12.0)
D_{OH^-}	Diffusion coefficient of OH^-	4.74×10^{-9} m^2/s	OLI Studio (v.12.0)
D_{K^+}	Diffusion coefficient of K^+	1.82×10^{-9} m^2/s	OLI Studio (v.12.0)
D_{AgOH}	Diffusion coefficient of AgOH	1.59×10^{-9} m^2/s	OLI Studio (v.12.0)
k_f	Forward reaction rate constant	1.82×10^{-5} 1/s	Arbitrary[#]
K_{eq}	Hydrolysis equilibrium constant for Ag^+	3.2×10^{-11} mol/dm^3	Fu and Chan[19]

[*] Chosen to be consistent with measured electrochemical kinetics but not calculated via the Nernst Equation.
[#] Selected to be consistent with the Ag^+ hydrolysis constant

A constant current of 1 mA, based on the experimental procedure from the Fu and Chan [19], was applied to the anode. This current represents a current density of approximately 31.83 mA/cm^2. The cathode potential was set to arbitrary potential 0 V vs. SHE and positioned at the electrolyte/air boundary. Note that the value chosen for the reversible potential did not have any effect on the results. No reduction reaction occurred at the cathode, and the water hydrolysis reaction was imposed throughout the geometry. The equilibrium constant for the Ag^+ hydrolysis reaction was maintained at 3.2×10^{-11} mol/dm^3. An arbitrary forward reaction rate constant, $k_f=1.0\times10^{-5}\ s^{-1}$, was used, with the backward rate constant, defined as $k_b=k_f/K_{eq}$.

To explore a range of conditions, several input parameters for the model were adjusted from the original case. First, the effect of the concentration of the supporting electrolyte, KNO_3, was studied by changing its concentration from 0.1 M to 1M. Next, the anode input current density was studied at 31.83 mA/cm^2, 0.3183 mA/cm^2, and 3.183 μA/cm^2. Finally, the original diffusion coefficient ratio between Ag^+ and NO_3^- ions, given as 0.84 in Table 6.1, was modified to consider other scenarios. The diffusion coefficient ratio between Ag^+ and NO_3^- ions was defined as 0.5, 0.84, 1, or 5, reflecting realistic ranges for the concentration ratio between the reactive cation and the makeup ion in an electrochemical system.[20]

The model was solved using the **NPE** module from the Tertiary Current Distribution module with NO_3^- as the makeup ion. The previously described **Lvk** approach was also applied as a comparison. Mesh refinement was performed uniformly across all methods, with element sizes ranging from 6.1×10^{-5} m to 5.1×10^{-3} m, resulting in a total of 55,019 elements. The model was run for an arbitrarily chosen simulation time of 5h, with a 1min time step.

6.4. Results

The results first present the outcomes of the **NPE** method, comparing them with both the experimental data and computational results of Fu and Chan.[19] This comparison validates the assumptions made in this study and assesses the accuracy of replicating the results reported by the original authors. Next, the computational time and memory usage of each method are evaluated for a base case with input parameters similar to those used by Fu and Chan [19], aiming to highlight the computational advantages of a ROM such as **Lvk**. Subsequently, the effects of varying the supporting electrolyte (KNO_3) concentration and input current density are examined to compare the **NPE** and **Lvk** methods on a broader scale - considering results for current, potential, and concentration distributions while also analyzing the individual contributions of diffusion and migration to current and potential (*i.e.,* concentration gradient, conductivity, and potential gradient). Finally, the impact of current increases due to ionic species diffusion is explored, along with the diffusion-to-migration current ratio.

6.4.1. A comparison with Fu and Chan's results

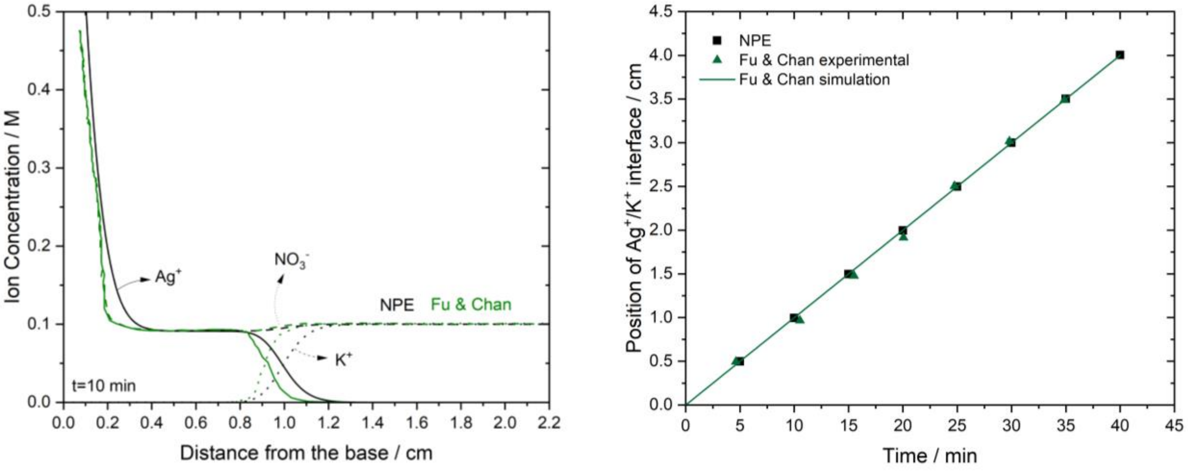

a) **b)**

Figure 6.3. Comparison of the results obtained for various parameters obtained using the **NPE** method and the Fu and Chan [19] experimental and simulation data for 0.1M KNO_3 solution and 31.83 mA/cm^2 input current density. Comparison of the ionic species concentration as a function of distance away from the base (anode) after 10 min in **a)** position of the Ag^+/K^+ interface as a function of time in **b)**.

Figure 6.3a and 6.3b highlight the similarities between the FEM model developed in this study and the results from both the FEM model and experimental data presented in the Fu and Chan publication.[19] The results shown are for the case of 0.1M KNO_3 electrolyte, 31.83 mA/cm^2 current density, and a value of 0.84 for $D_{Ag^+}/D_{NO_3^-}$. Figure 3a shows that the concentrations of Ag^+, NO_3^-, and K^+ ions after 10 minutes, as obtained through the **NPE** method, closely match the results from Fu and Chan.[19] Figure 6.3b further demonstrates the accuracy of these models in capturing the movement of the Ag^+/K^+ interface over time, aligning well with the experimental data.

It is important to note that the exact method Fu and Chan [19] used to extract the movement of the Ag^+/K^+ boundary experimentally is unclear. To address this, the authors will refer the reader to Figure 6.2 and 6.3 in the original paper, noting slight discrepancies in the concentration versus position data at the 10 min mark. In this study, however, the Ag^+/K^+ interface was identified as the point where the concentrations of Ag^+ and K^+ are the same.

6.4.2. Computational time and memory between calculations methods

Table 6.2 presents the computation time and physical memory required for a total simulation time of 5 h for $D_{Ag^+}/D_{NO_3^-}$=0.84. For both calculations methods, increasing the concentration of KNO_3 and decreasing the input current resulted in a decrease in computational time and a modest decrease in the physical memory utilized. The results demonstrate that the **Lvk** method requires significantly less simulation time and computational memory than the **NPE** method. Specifically, the **Lvk** method reduces simulation time by approximately 2-4 times compared to the **NPE** approach. Additionally, the **Lvk** method lowers computational memory usage by a factor of 2-3 relative to the **NPE** method.

It's important to note that Table 6.2 does not include computational expenses related to variations in the diffusion coefficient ratios between Ag^+ and NO_3^-. The same trends in computational time and memory observed for the $D_{Ag^+}/D_{NO_3^-}$=0.84 are also seen for other $D_{Ag^+}/D_{NO_3^-}$ ratios and are presented in Appendix A6 of this chapter.

Table 6.2. Comparison between the computational time and physical memory of different governing equations after 5hr simulation time for $D_{Ag^+}/D_{NO_3^-}$=0.84.

KNO_3 concentration / M and input current density / mA·cm^{-2}	**NPE**		**Lvk**	
	Time / s	Memory / GB	Time / s	Memory / GB
0.1 and 31.83	5,607	8.75	1,428	3.98
1 and 31.83	951	8.50	311	3.92
1 and 0.3183	295	8.32	182	3.92
1 and 0.003183	293	8.11	125	3.91

6.4.3. Comparison of current density, potential, and Ag^+ concentration distributions between the NPE and Lvk methods with variations in concentration of supporting electrolyte.

Figure 6.4a through 6.4d show the ratio of the total vertical electrolyte current density obtained through the **Lvk** methods to that from the **NPE** method across varying parameters, including $D_{Ag^+}/D_{NO_3^-}$ values, input currents, and KNO_3 concentrations. For all cases discussed in this section, the contribution of the horizontal component is disregarded in these analyses due to its value being over six orders of magnitude smaller compared to the vertical component. It is important to note that the original simulation by Fu and Chan [19] utilized a 0.1M KNO_3

concentration and a 31.83 mA/cm^2 input current density, with a $D_{Ag^+}/D_{NO_3^-}$ ratio of 0.84 as provided by OLI Studio version 12 MSE database.

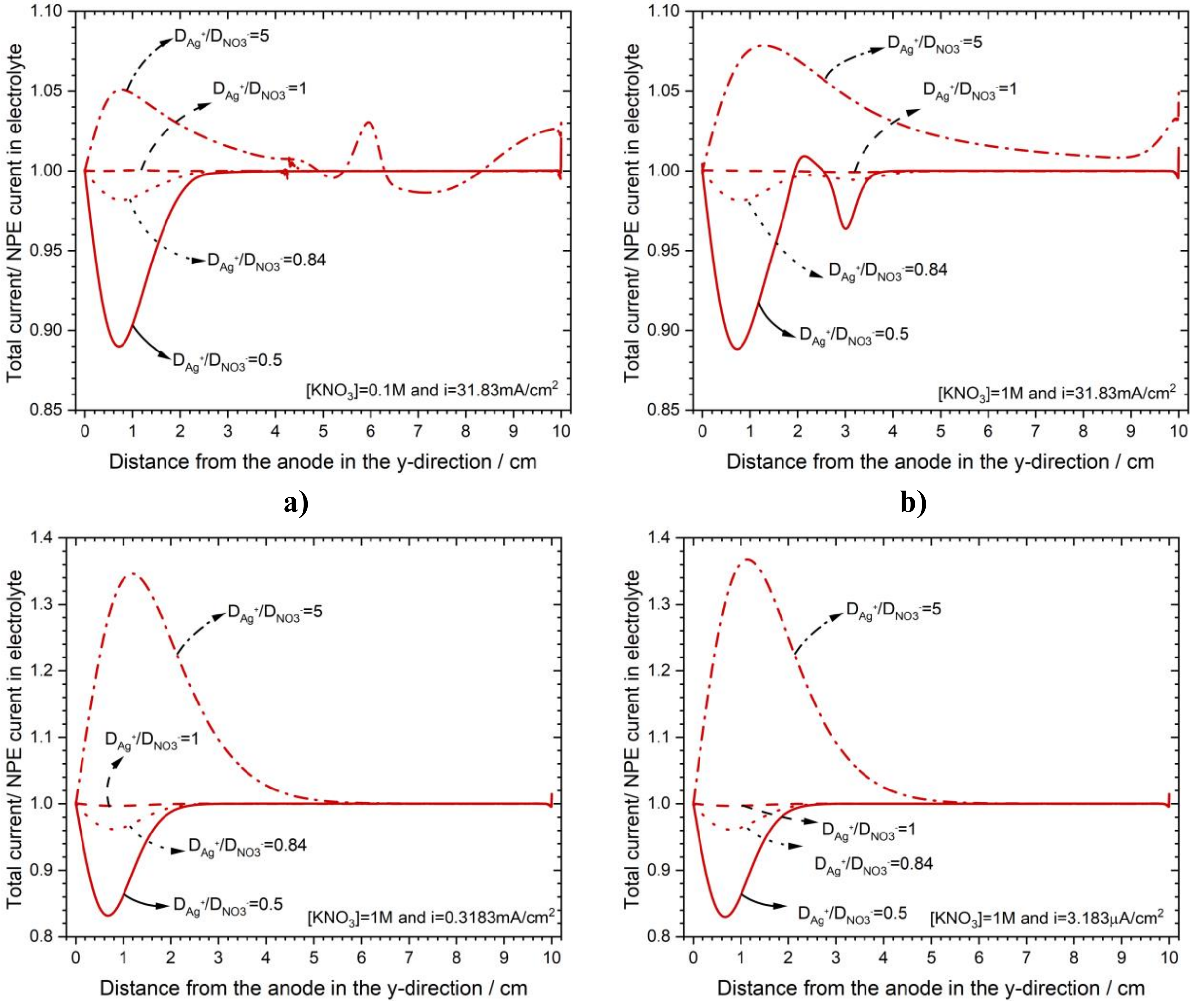

a) **b)**

c) **d)**

Figure 6.4. Ratio of the total current between **Lvk** and **NPE** as a function of distance orthogonal to the anode for various ratios of Ag$^+$ and NO$_3^-$ diffusion coefficients at **a)** 0.1M KNO$_3$ and 31.83 mA/cm^2, **b)** 1M KNO$_3$ and 31.83 mA/cm^2, **c)** 1M KNO$_3$ and 0.3183 mA/cm^2, and **d)** 1M KNO$_3$ and 3.183 μA/cm^2. Results obtained after a 5h simulation time. Line style of the arrows matches the line style of the current ratio for each $D_{Ag^+}/D_{NO_3^-}$ value.

The results presented in Figure 6.4a-6.4d demonstrate excellent (less than 0.1%) agreement between the **Lvk** and **NPE** methods at the electrode-electrolyte interface (y=0 cm) across all tested input current densities, KNO$_3$ concentrations, and $D_{Ag^+}/D_{NO_3^-}$ ratios. Notably, the **Lvk** method maintains high accuracy in predicting total current density when $D_{Ag^+}/D_{NO_3^-}$=1, despite variations in the diffusion coefficients of other ionic species in the electrolyte.

Figure 6.4a and 6.4b indicate that even at high input current densities, the **Lvk** method remains highly accurate when $D_{Ag^+}/D_{NO_3^-}$<1, provided the distance from the electrode exceeds a certain threshold (between 4-5 cm). This observation also holds true for lower current densities (Figure 4c and 4d) across all $D_{Ag^+}/D_{NO_3^-}$ ratios. Closer to the electrode, the error in total current density does not exceed 11% for the two higher current densities, although it was over 30% at lower current densities for the largest $D_{Ag^+}/D_{NO_3^-}$ ratio of 5.

Additionally, across all tested current densities and KNO_3 concentrations, the current density ratio between the **Lvk** and **NPE** methods fluctuates between positive and negative values along the tube length, depending on the $D_{Ag^+}/D_{NO_3^-}$ ratio. However, the error in current density predictions using the **Lvk** method extends over a larger distance as the $D_{Ag^+}/D_{NO_3^-}$ ratio increases. For instance, in Figure 4a and 4b, for the extreme case when $D_{Ag^+}/D_{NO_3^-}$=5, the **Lvk** method struggles to maintain accuracy over the full 10 cm electrolyte length. This error decreases as the difference between D_{Ag^+} and $D_{NO_3^-}$ narrows, indicating an improved predictive capability of the **Lvk** method under these conditions.

Furthermore, the sensitivity of the **Lvk** method to the $D_{Ag^+}/D_{NO_3^-}$ ratio is further explored in terms of electrolyte current density. When $D_{Ag^+}/D_{NO_3^-}$>1 (*e.g.,* $D_{Ag^+}/D_{NO_3^-}$=5), the peak error in total current density predicted by the **Lvk** method increases with higher KNO_3 concentrations and lower input current densities. However, this trend is not observed when $D_{Ag^+}/D_{NO_3^-}$<1, suggesting that the **Lvk** method's accuracy is more sensitive to diffusion coefficient disparities when D_{Ag^+} is greater than $D_{NO_3^-}$.

Figure 6.5a through 6.5d compare the vertical component of the potential distribution perpendicular to the anode across all the varied parameters after a period of 5h obtained with the two computational techniques for high and low concentrations and current densities. In all these cases, a magnified region from 0 to 4.5 cm is depicted to highlight the differences between the **Lvk** and the **NPE** for all the considered $D_{Ag^+}/D_{NO_3^-}$ ratios. In this and later figures, the color of the line represents the solution method (red for **Lvk**, black for **NPE**) whereas the line style represents the ratio of the diffusivities of silver and nitrate ions (i.e., solid for $D_{Ag^+}/D_{NO_3^-}$=0.5, dotted for 0.84, dashed for 1, and dotted-dashed for 5). In cases where only one line style exists, the data for the two methods are identical.

In general, for distances larger than 4.5 cm from the electrode, no significant differences in predicted electrolyte potential between the **Lvk** and **NPE** were noted for any of the cases studied. The potential distribution in the electrolyte exhibits two main characteristics across all tested conditions: (1) the potential decreases from the mouth of the cylinder towards the anode-electrolyte interface, initially linearly and then, depending on $D_{Ag^+}/D_{NO_3^-}$, with a smaller or larger slope near the anode surface, (2) the lower the $D_{Ag^+}/D_{NO_3^-}$ the greater the potential drop across the cylinder, resulting in a lower potential near the surface, and (3) the lower the input current densities and the higher the KNO_3 concentration, the more positive the potential at the interface (*i.e.,* the smaller the potential drop).

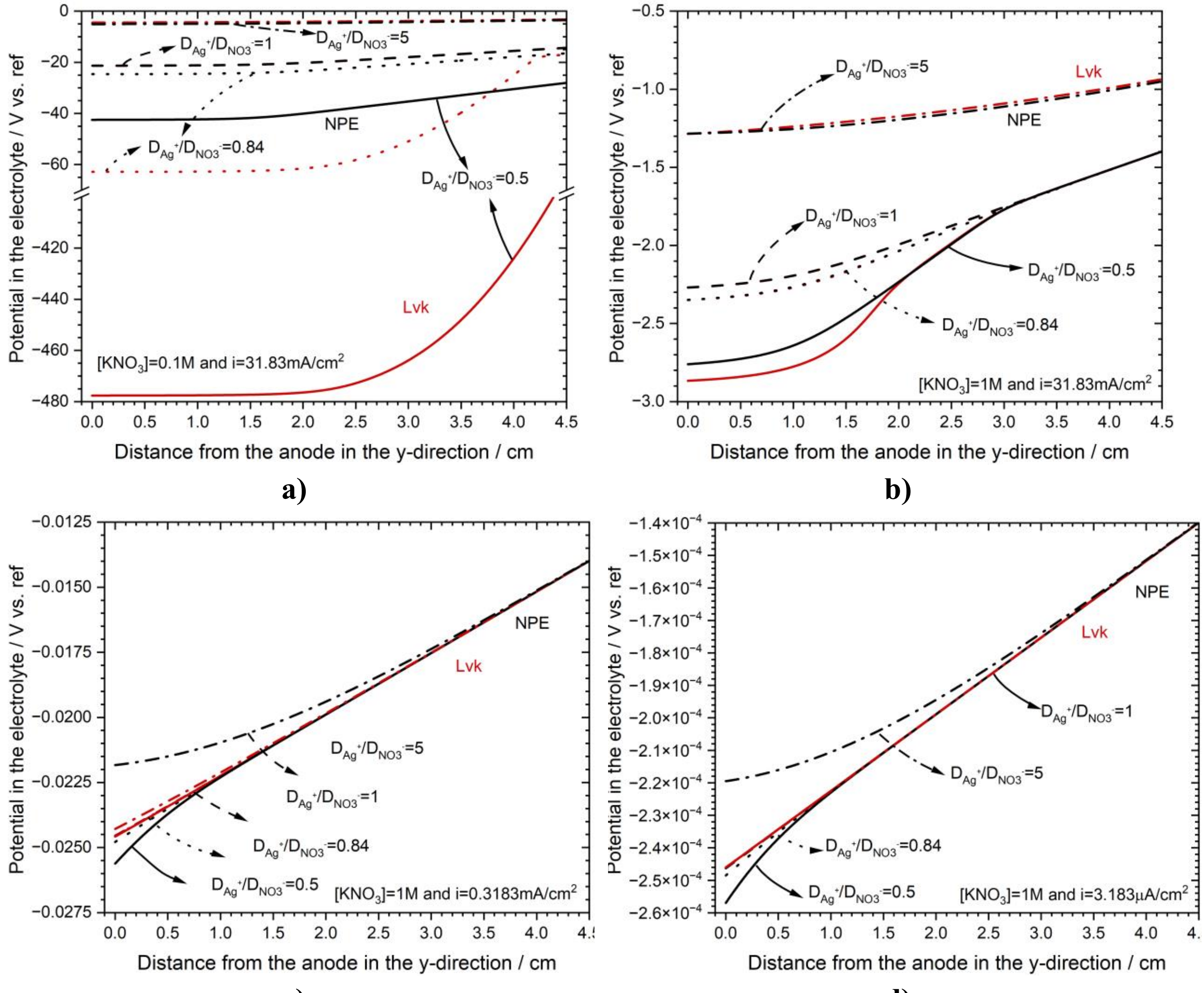

a) **b)**

c) **d)**

Figure 6.5. Variations in potential (V vs. ref) as a function of distance orthogonal to the anode for various ratios of Ag^+ and NO_3^- diffusion coefficients at **a)** 0.1M KNO_3 and 31.83 mA/cm^2, **b)** 1M KNO_3 and 31.83 mA/cm^2**, c)** 1M KNO_3 and 0.3183 mA/cm^2, and **d)** 1M KNO_3 and 3.183 µA/cm^2. Results obtained for the **NPE** (black) and **Lvk** (red) methods of calculations after a 5h simulation time. Line style of the arrows matches the line style of the potential for each $D_{Ag^+}/D_{NO_3^-}$ value.

In the scenarios presented in Figure 6.5a and 6.5b, the **Lvk** method provides a reasonable prediction of the potential at the interface compared to the NPE method when $D_{Ag^+}/D_{NO_3^-} > 1$. Consistent with the total current density results discussed earlier, no differences in potential are observed throughout the electrolyte when $D_{Ag^+}/D_{NO_3^-}$=1. However, the largest discrepancies between the **Lvk** and **NPE** methods occur at the electrode-electrolyte interface when $D_{Ag^+}/D_{NO_3^-}$ <1, particularly for $D_{Ag^+}/D_{NO_3^-}$ =0.5 in the presence of 0.1M KNO3. The extremely large potential drops, especially in Figure 6.5a, should be noted, including for $D_{Ag^+}/D_{NO_3^-}$ =0.84, the ratio applicable to the actual Fu and Chan [19] experiments.

For all the explored current densities and KNO3 concentrations, the **NPE** method reveals a highly nonlinear dependence of potential on distance near the electrode-electrolyte interface. This nonlinearity is strongly influenced by the $D_{Ag^+}/D_{NO_3^-}$ ratio, with larger ratios resulting in a more pronounced nonlinear potential dependence. Notably, this effect can be dramatic, as seen in Figure 6.5b for $D_{Ag^+}/D_{NO_3^-}$=0.5. A similar nonlinear relationship between potential and distance is also observed in the **Lvk** method predictions near the electrode. In particular, the **Lvk** method shows a sharp potential drop for $D_{Ag^+}/D_{NO_3^-}$=0.84 and 0.50 in Figure 6.5a, as well as for $D_{Ag^+}/D_{NO_3^-}$=0.5 in Figure 6.5b. These two cases exhibit the largest differences in potential between the **Lvk** and **NPE** methods.

As the input current density decreases (Figure 6.5c and 6.5d), the **Lvk** method continues to produce potential values similar to those of the **NPE** method. In particular, the largest difference in potential at the electrode-electrolyte interface is obtained when the $D_{Ag^+}/D_{NO_3^-}$=5 with values of 2.45 mV and 0.026 mV for input current densities of 0.3183 mA/cm^2 and 3.183 µA/cm^2, respectively. However, across all input current densities and $D_{Ag^+}/D_{NO_3^-}$ratios, the **Lvk** method consistently predicts an almost-linear potential on distance dependence from the electrode-insulated boundary interface to the electrode-electrolyte interface.

Figure 6.6a through 6.6d illustrate the variations in Ag$^+$ concentration along the vertical direction perpendicular to the anode after a period of 5h obtained with **NPE** and **Lvk** computational techniques. Additionally, to highlight the accuracy of the **Lvk** method, the focus is limited to the region between positions 0 and 4 cm along the cylinder, as the results were identical for positions farther from the electrode surface. In all cases, the concentration of the Ag$^+$ decreases with increasing distance from the electrode surface with the higher concentration at the electrode-electrolyte boundary. Notably, for all cases, a higher $D_{Ag^+}/D_{NO_3^-}$ ratio corresponds to a higher Ag$^+$ concentration for distances from the electrode greater than approximately 1 cm. As expected, when $D_{Ag^+}/D_{NO_3^-}$=5, the Ag$^+$ concentration remains low near the electrode-electrolyte interface but stays higher than for any other diffusion coefficient ratio as the distance from the electrode surface increases beyond ~1 cm.

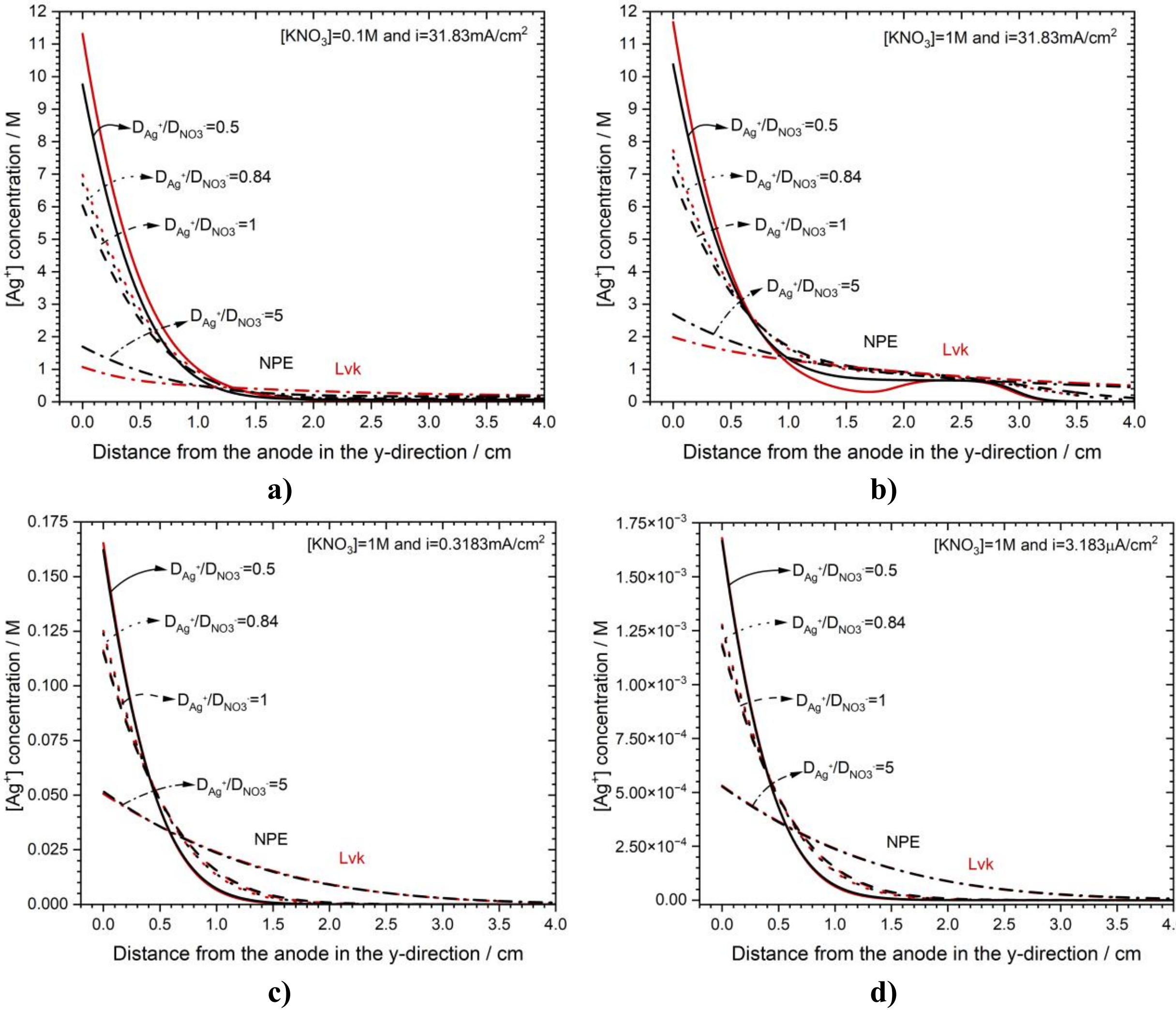

Figure 6.6. Variations in Ag^+ concentration as a function of distance orthogonal to the anode for various ratios of Ag^+ and NO_3^- diffusion coefficients at **a)** 0.1M KNO_3 and 31.83 mA/cm^2, **b)** 1M KNO_3 and 31.83 mA/cm^2, **c)** 1M KNO_3 and 0.3183 mA/cm^2, and **d)** 1M KNO_3 and 3.183 μA/cm^2. Results obtained for the **NPE** (black), and **Lvk** (red) methods of calculations after a 5h simulation time. Line style of the arrows matches the line style of the potential for each $D_{Ag^+}/D_{NO_3^-}$ value.

Overall, the results indicate that the **Lvk** method predicts Ag^+ concentration distribution trends that closely match those of the **NPE** method across all tested KNO_3 concentrations, input current densities, and $D_{Ag^+}/D_{NO_3^-}$ratios. The primary focus remains on the electrode-electrolyte interface, as it is both a critical region of interest and the area with the highest percentage error.

For low input current densities of 0.3183 mA/cm^2 and 3.183 μA/cm^2 **(**Figure 6.6c and 6.6d), the **Lvk** method demonstrates excellent agreement with the **NPE** method across all $D_{Ag^+}/D_{NO_3^-}$ ratios. Specifically, at 0.3183 mA/cm^2**,** the highest observed percent error is 2.08%**,** while at 3.183 μA/cm^2**,** this error decreases further to 0.72% (both for $D_{Ag^+}/D_{NO_3^-}$= 5). However, for high input current densities (Figure 6.6a and 6.6b), the largest percentage error in Ag^+ concentration at the electrode-electrolyte interface occurs when $D_{Ag^+}/D_{NO_3^-}$= **0.5**, with values reaching 38.5% for 0.1M KNO_3 and 28.8% for 1M KNO_3**.**

An interesting case is observed in Figure 6.6b for both the **Lvk** and **NPE** methods when $D_{Ag^+}/D_{NO_3^-}$=0.5. In this scenario, the Ag^+ concentration initially decreases, then plateaus at approximately 1.5 cm from the electrode surface before dropping to nearly zero at around 3 cm. This behavior is similar to the base case presented in Figure 6.3a for Fu and Chan [19] after 10 min. However, in Figure 6.6b, the results are taken after 5 h. These similarities underscore the complexities of localized corrosion systems and their sensitivity to input parameters.

6.4.4. Comparison of diffusion and migration components of current and potential between Lvk and NPE.

Figure 6.7a and 6.7b illustrate the contributions of migration and diffusion components to the electrolyte current density as a function of distance from the anode for the case of 1M KNO_3, an input current density of 0.3183 mA/cm^2, and $D_{Ag^+}/D_{NO_3^-}$=5, using the **NPE** and **Lvk** methods, respectively. In this analysis, current densities are calculated separately for Ag^+, NO_3^-, and K^+ species, as the effects of H^+ and OH^- are considered negligible due to their low concentrations. Additionally, the Appendix section of this work presents a similar analysis for other input current densities and KNO_3 concentrations examined in this study, while maintaining $D_{Ag^+}/D_{NO_3^-}$=5.

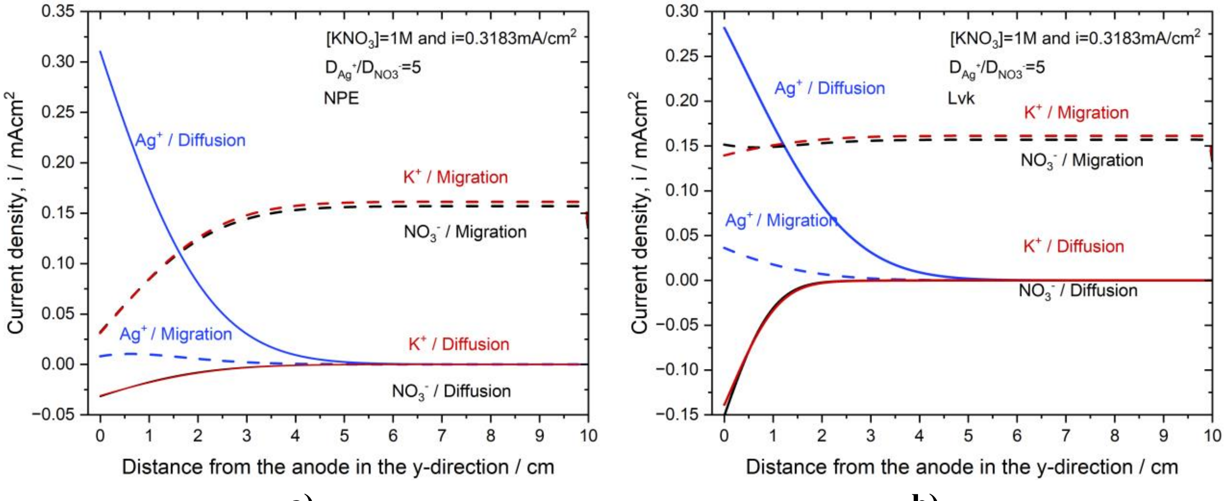

a) **b)**

Figure 6.7. Variations in diffusion current density (solid line) and migration current density (dashed line) as a function of distance orthogonal to the anode for $D_{Ag^+}/D_{NO_3^-} = 5$ diffusion coefficients at 1M KNO_3 and 0.3183 mA/cm^2 for: Ag^+ (blue), NO_3^- (black), and K^+ (red). Results obtained for **a) NPE** and **b) Lvk** methods of calculations after a 5h simulation time. Note that the

effects of other elements are not shown as their impact is deemed negligible compared to the ones presented.

Overall, at any point within the electrolyte, the sum of the current densities of all species remains 0.3183 mA/cm^2 which equals the total input electric current density and ensures compliance with the law of charge conservation.

Figure 6.7a illustrates nonzero diffusion and migration current density components at the electrode-electrolyte boundary for each ion through the **NPE** method. Notably, the migration of NO_3^- and K^+ constitutes the entire electrolyte current density at approximately 5 cm and beyond from the electrode. As the distance to the electrode decreases, the migration current density declines, while the diffusion component increases. At the electrode-electrolyte boundary, the sum of the diffusion and migration components for NO_3^- and K^+ individually equals zero, consistent with the physical limitation that supporting electrolyte ions cannot cross this boundary.

Conversely, Ag^+ exhibits a significant diffusion current density at the interface, accompanied by a relatively small migration component. The results from Figure 6.7a combined with Figure A6.2 A6.3 and A6.4 in the Appendix as well as additional unpublished simulations, indicate that the diffusion component of Ag^+ at the electrode-electrolyte interface is always greater than or equal to its corresponding migration current density depending on the input parameters. Both the diffusion and migration components of Ag^+ diminish as the distance from the electrode increases. That said, as can be seen in Figure A6.2 in the Appendix, at any distance $y > 0$ cm, the migration component of the current density from Ag^+ is larger than the Ag^+ diffusion current density.

Figure 6.7b presents the diffusion and migration current densities of major ionic species throughout the electrolyte under the same conditions as Figure 6.7a, using the **Lvk** method. Notably, both methods show identical trends in the bulk electrolyte (far from the electrode), where migration solely carries the electrolyte current. However, as the distance to the electrode surface decreases, the migration current density of NO_3^- and K^+ slightly decreases to accommodate the migration component arising from Ag^+. At the electrode-electrolyte interface and throughout the electrolyte, the sum of all migration currents must equal the total input current-a boundary condition imposed by the **Lvk** method. In contrast, the **NPE** method sets the boundary condition that the total current density (sum of migration and diffusion) must equal the input electric current density at the electrode.

This behavior is accompanied by an increase in the diffusion current densities of these species near the electrode. As in the **NPE** method, the sum of the diffusion and migration components of the supporting electrolyte species (NO_3^- and K^+) must equal zero at the electrode-electrolyte interface, as these species cannot cross the boundary. However, Figure 6.7b shows slight differences in the diffusion and migration components of Ag^+ compared to Figure 6.7a (**NPE** method), with both components decreasing as the distance from the electrode increases.

A key distinction in the **Lvk** method, as derived in the Appendix, is that the imposed boundary conditions lead to a total diffusion current density of zero at the electrode-electrolyte interface. While this condition, which is not necessarily true for the **NPE**, does not hold throughout the entire electrolyte length, it can introduce calculation errors, as discussed later.

The results from Figure 6.4-6.7 reveal interesting phenomena: while the **Lvk** method can, under certain electrolyte conditions, produce results nearly identical to those of the **NPE** method, in other cases, significant differences arise. In the following two sections, the **Lvk** and **NPE** methods are compared in detail by examining the parameters used to solve the Nernst-Planck Equation. For the given system, the Nernst Planck Equation is only divided into species transport effects arising from diffusion and migration. Here, we analyze the contributions of both components.

The first aspect examined is the diffusion term. Although the diffusion coefficients remain constant throughout the electrolyte, variations in concentration gradients lead to changes in both current and potential. To explore this, we compare the total diffusion current across the electrolyte, followed by the diffusion gradient of the electrochemically active species, Ag^+. Although all ionic species contribute to the total diffusion current, this section aims to provide a deeper understanding of electrochemically active species (often of interest in many applications) while comparing the **Lvk** and **NPE** calculation methods.

Next, we investigate the electrolyte's conductivity and potential gradient to evaluate how migration contributes to current and potential, again comparing both methods. Finally, we analyze the ratio of diffusion to migration current throughout the electrolyte for both the **Lvk** and **NPE** approaches.

6.4.6. Diffusion effects

Figure 6.8a through 6.8d illustrate the diffusion current density in the vertical direction (*i.e.,* perpendicular to the anode) as a function of distance from the electrode for different diffusion coefficient ratios, KNO_3 concentrations, and input currents after 5 h, as obtained using the **NPE** and **Lvk** methods. Overall, it is noted that increasing the KNO_3 concentration (Figure 6.8a to 6.8b) results in a mild increase in the diffusion current for all the $D_{Ag^+}/D_{NO_3^-}$ ratios except for $D_{Ag^+}/D_{NO_3^-}$=1. As expected, however, decreasing the input current density decreases the diffusion current density for constant KNO_3 concentration (Figure 6.8b to 6.8c to 6.8d).

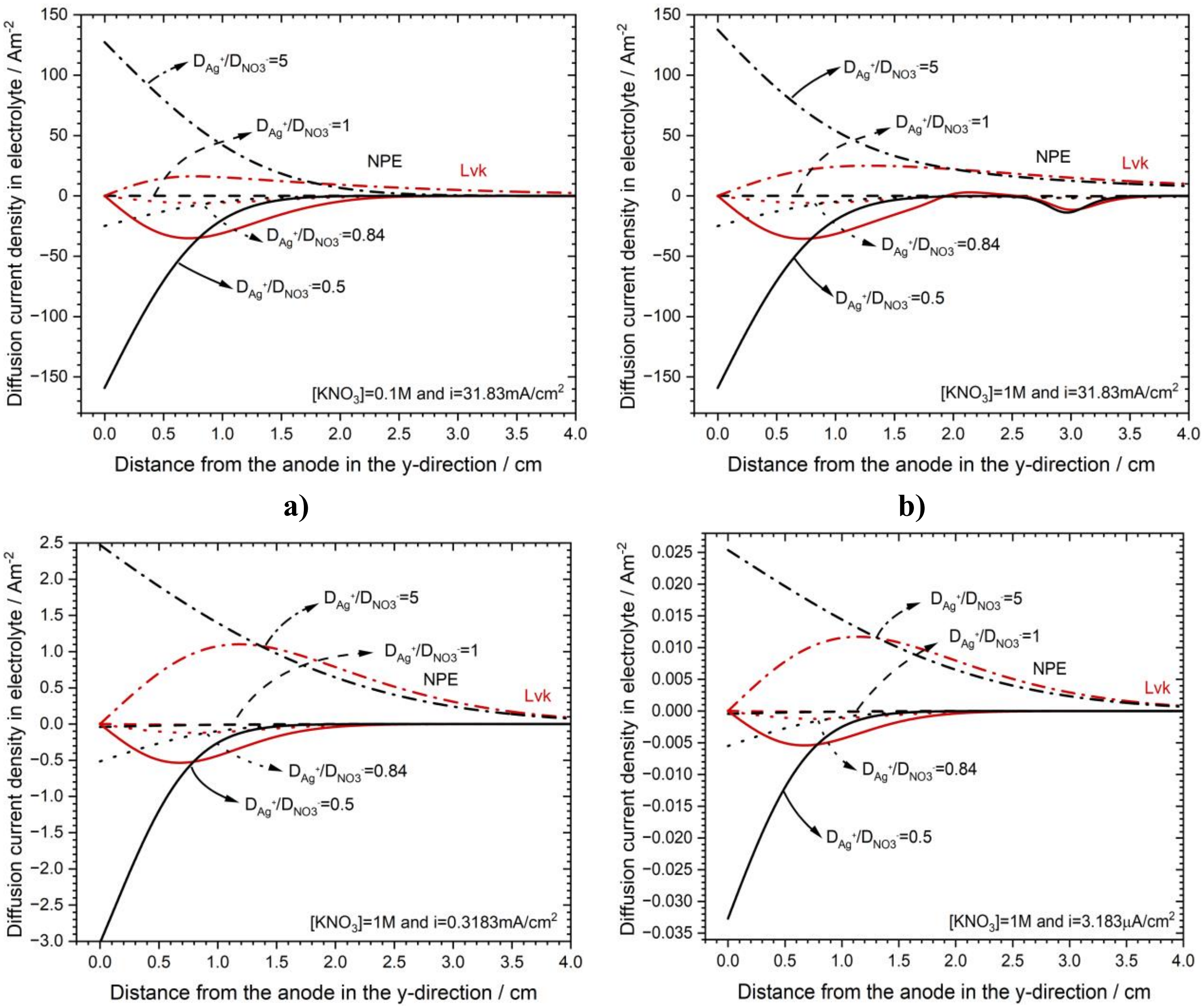

a) **b)**

c) **d)**

Figure 6.8. Variations in diffusion current density as a function of distance orthogonal to the anode for various ratios of Ag^+ and NO_3^- diffusion coefficients at **a)** 0.1M KNO_3 and 31.83 mA/cm^2, **b)** 1M KNO_3 and 31.83 mA/cm^2, **c)** 1M KNO_3 and 0.3183 mA/cm^2, and **d)** 1M KNO_3 and 3.183 μA/cm^2. Results obtained for the **NPE** and **Lvk** methods of calculations after a 5h simulation time. Line style of the arrows matches the line style of the diffusion current density for each $D_{Ag^+}/D_{NO_3^-}$ value.

The **NPE** results indicate that diffusion current is highest near the electrode-electrolyte interface and decreases with distance from the electrode. These variations, both in magnitude and sign, strongly depend on the $D_{Ag^+}/D_{NO_3^-}$ratio. Specifically, when $D_{Ag^+}/D_{NO_3^-}<1$, the total diffusion current in the electrolyte is negative, whereas for $D_{Ag^+}/D_{NO_3^-}>1$, it is positive. However, when $D_{Ag^+}/D_{NO_3^-}= 1$, the diffusion current remains zero throughout the electrolyte. Notably, for all examined current densities and KNO_3 concentrations, a ratio of $D_{Ag^+}/D_{NO_3^-}=0.5$ has a greater impact on diffusion current density at the electrode-electrolyte boundary compared to $D_{Ag^+}/D_{NO_3^-}$

=5, despite the latter having a larger difference in diffusion coefficients. However, in all explored cases, the diffusion current for $D_{Ag^+}/D_{NO_3^-}$=5 extends farther from the electrode than for other ratios. Apart from the $D_{Ag^+}/D_{NO_3^-}$=1 case, the **Lvk** method predicts diffusion currents at the electrode-electrolyte surface and throughout the electrolyte that differ from the **NPE** results. As further explored in the discussion section of this chapter, an interesting result is that the **Lvk** method predicts zero diffusion current at the electrode-electrolyte interface across all input current densities, KNO_3 concentrations, and diffusion coefficient ratios. However, as distance from the electrode increases, the diffusion current transitions to negative or positive values, similar to the **NPE** predictions. In general, the diffusion current in the **Lvk** method also approaches zero at approximately the same distance from the electrode as in the **NPE** results.

Figure 6.9a through 6.9d illustrate the variations in the vertical concentration gradient of Ag^+ as a function of distance from the electrode base for both the **Lvk** and **NPE** methods across all examined parameters. This study focuses specifically on the concentration gradient of the electrochemically active species, Ag^+.

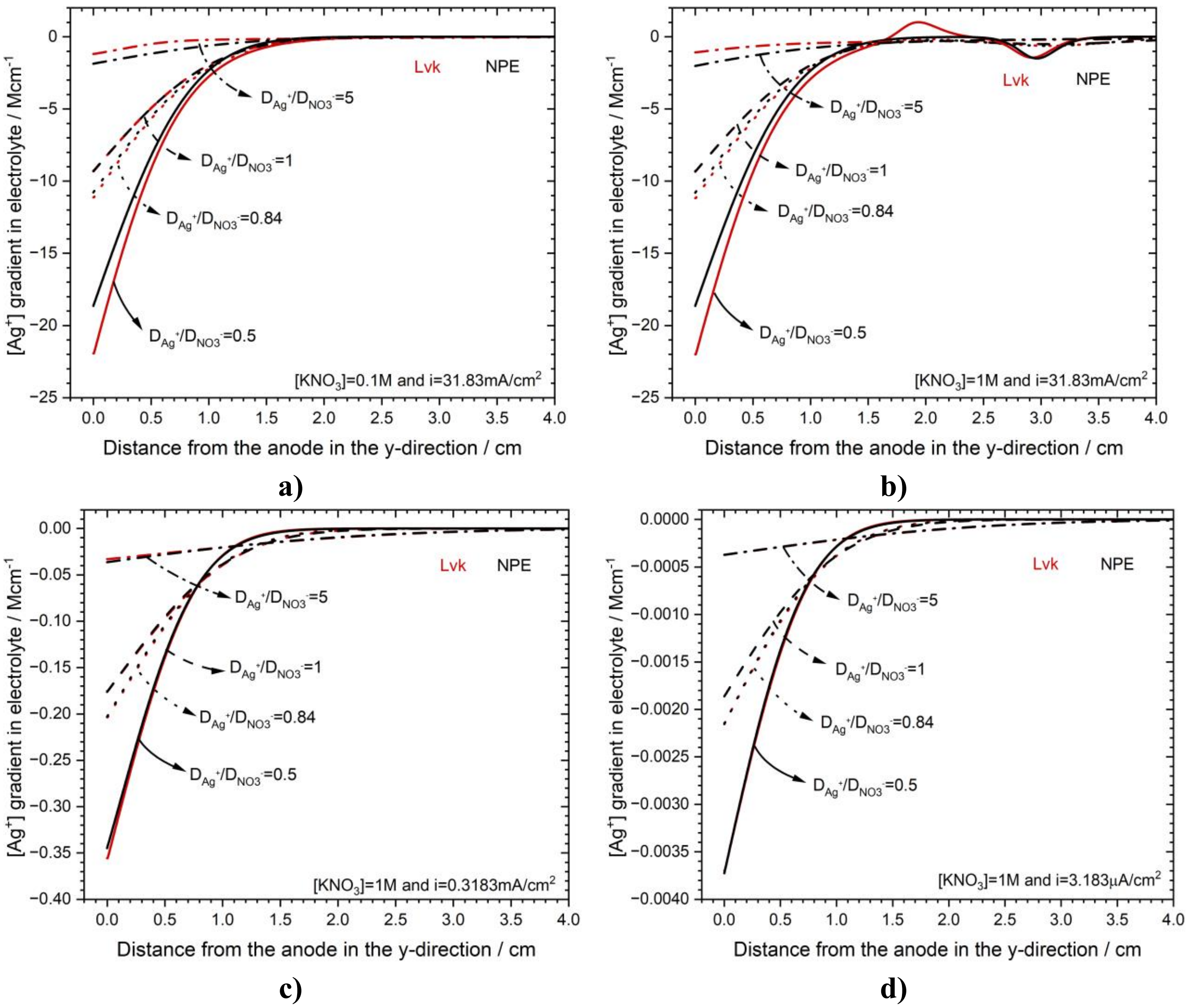

a) **b)**

c) **d)**

Figure 6.9. Variations in Ag^+ concentration gradient as a function of distance orthogonal to the anode for various ratios of Ag^+ and NO_3^- diffusion coefficients at **a)** 0.1M KNO_3 and 31.83 mA/cm^2, **b)** 1M KNO_3 and 31.83 mA/cm^2, **c)** 1M KNO_3 and 0.3183 mA/cm^2, and **d)** 1M KNO_3 and 3.183 µA/cm^2. Results obtained for the **NPE** and **Lvk** methods of calculations after a 5h simulation time. Line style of the arrows matches the line style of the Ag^+ concentration gradient for each $D_{Ag^+}/D_{NO_3^-}$ value.

Across all input current densities, KNO_3 concentrations, and $D_{Ag^+}/D_{NO_3^-}$ratios, the Ag^+ concentration gradient is negative at the electrode-electrolyte interface and approaches near-zero values as the distance from the electrode increases. Notably, the lower the $D_{Ag^+}/D_{NO_3^-}$ratio, the higher (in magnitude) the concentration gradient. Additionally, there are no significant differences between the two calculation methods when $D_{Ag^+}/D_{NO_3^-}$=1. As with the diffusion current density case explored above, Figure 6.9a and 6.9b indicate that an increase in KNO_3 concentration leads to a slight increase in the Ag^+ concentration gradient, while a decrease in total input current density reduces the gradient, as seen in Figure 6.9b through 6.9d.

A comparison of the **Lvk** and **NPE** results reveals good agreement across all $D_{Ag^+}/D_{NO_3^-}$ ratios, particularly for 1M KNO_3 at 0.3183 mA/cm^2 (Figure 6.9c) and 3.183 µA/cm^2 (Figure 6.9d). The largest differences are observed at the electrode-electrolyte interface in Figure 6.9c for $D_{Ag^+}/D_{NO_3^-}$ =5 and $D_{Ag^+}/D_{NO_3^-}$= 0.5, with percent errors of 9.0% and 3.1%, respectively.

The **Lvk** method also shows strong agreement with **NPE** for high input current densities and $D_{Ag^+}/D_{NO_3^-}$ratios of 1 and 0.84, as seen in Figure 6.9a and 6.9b. However, similar to low input current density cases, the largest discrepancies in Ag^+ concentration gradient predictions occur at the electrode-electrolyte interface for $D_{Ag^+}/D_{NO_3^-}$5 and $D_{Ag^+}/D_{NO_3^-}$=0.5. In Figure 9a, the errors are 17.7% for $D_{Ag^+}/D_{NO_3^-}$=0.5 and 36.4% for $D_{Ag^+}/D_{NO_3^-}$=5. In Figure 9b, these errors increase to 18.0% and 46.5%, respectively.

6.4.7. Migration effects

Figure 6.10a through 6.10d present the conductivity values as a function of distance from the electrode for different KNO_3 concentrations, input current densities, and $D_{Ag^+}/D_{NO_3^-}$ratios using the **Lvk** and **NPE** methods. In most cases, the conductivity is highest near the anode surface and decreases with distance until it reaches a plateau of the bulk conductivity. The only exception to this trend occurs in Figure 6.10b for $D_{Ag^+}/D_{NO_3^-}$=0.5, where conductivity initially decreases with distance from the electrode before increasing at approximately 3 cm. This behavior is observed in both the **Lvk** and **NPE** methods.

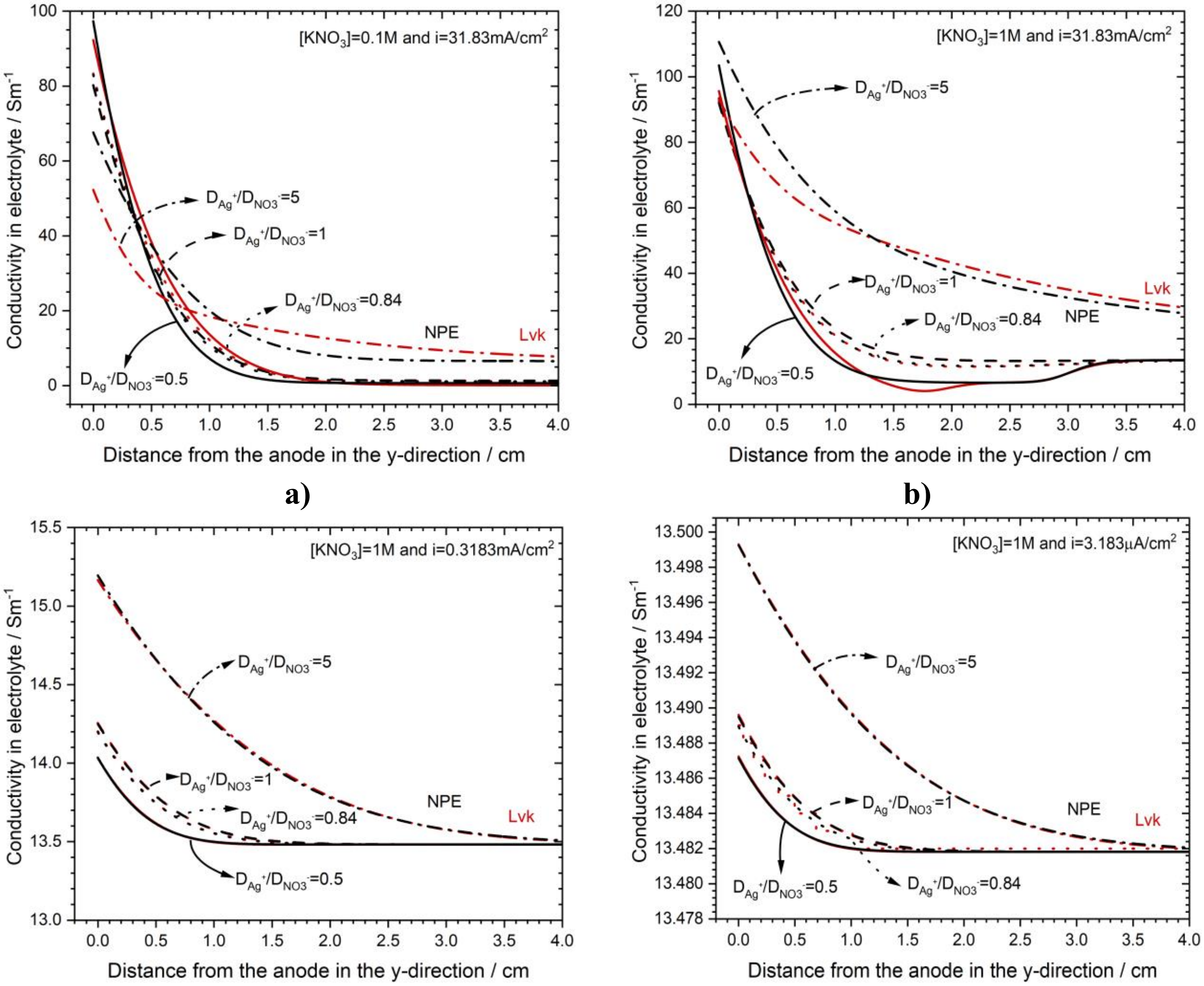

a) b) c) d)

Figure 6.10. Variations in conductivity as a function of distance orthogonal to the anode for various ratios of Ag^+ and NO_3^- diffusion coefficients at **a)** 0.1M KNO_3 and 31.83 mA/cm^2, **b)** 1M KNO_3 and 31.83 mA/cm^2, **c)** 1M KNO_3 and 0.3183 mA/cm^2, and **d)** 1M KNO_3 and 3.183 μA/cm^2. Results obtained for the **NPE** and **Lvk** methods of calculations after a 5h simulation time. Line style of the arrows matches the line style of the conductivity for each $D_{Ag^+}/D_{NO_3^-}$ value.

For lower current densities, higher $D_{Ag^+}/D_{NO_3^-}$ ratios generally correspond to higher electrolyte conductivity throughout the system (Figure 6.10c and 6.10d). However, this trend does not hold when the current density input is high, as seen in Figure 6.10a and 6.10b. In these cases, near the electrode-electrolyte interface, a lower $D_{Ag^+}/D_{NO_3^-}$ratio results in higher conductivity, but this trend reverses as the distance from the electrode increases.

Overall, increasing the KNO_3 concentration increases the solution conductivity (Figure 6.10a and 6.10b), while decreasing the input current density leads to lower overall conductivity in the electrolyte (Figure 6.10b through 6.10d).

When comparing the **Lvk** and **NPE** methods, **Lvk** demonstrates excellent agreement with **NPE** across the entire electrolyte for all $D_{Ag^+}/D_{NO_3^-}$ ratios in cases of 0.3183 mA/cm^2 (Figure 6.10c) and 3.183 μA/cm^2 (Figure 6.10d) input current densities. Significant differences in conductivity predictions between the two methods only appear at high current densities, particularly in Figure 6.10a and 6.10b for $D_{Ag^+}/D_{NO_3^-}$=0.5 and $D_{Ag^+}/D_{NO_3^-}$=5, respectively. These discrepancies are most prominent near the electrode surface. In Figure 6.10a, the percent error in conductivity at the electrode-electrolyte interface is 5.2% for $D_{Ag^+}/D_{NO_3^-}$=0.5 and 22.7% for $D_{Ag^+}/D_{NO_3^-}$= 5. In Figure 6.10b, these errors change to 7.6% and 15.8%, respectively.

Figure 6.11a through 6.11d illustrate the potential gradients in the vertical direction across various input parameters and computational methods. Notably, Figure 6.11a and 6.11b show significant variations in the potential gradient. To effectively capture these drastic changes, the potential gradient is shown across the entire 10 cm of the electrolyte. In particular, Figure 6.11a includes two breaks in the ordinate to accommodate the extrema of the potential drop calculated using the **Lvk** method. The results from these Figure indicate that increasing the KNO_3 concentration and the $D_{Ag^+}/D_{NO_3^-}$ ratio reduces the potential drop. When $D_{Ag^+}/D_{NO_3^-}$=1, no differences in potential drop are observed between the **Lvk** and **NPE** methods across the entire electrolyte length. Excellent agreement between the two methods is also observed for 1M KNO_3 at an input current density of 31.83 mA/cm² with $D_{Ag^+}/D_{NO_3^-}$=0.84, as shown in Figure 6.11b. However, in all other cases, the agreement between **Lvk** and **NPE** is poor for the Ag$^+$ concentration gradient.

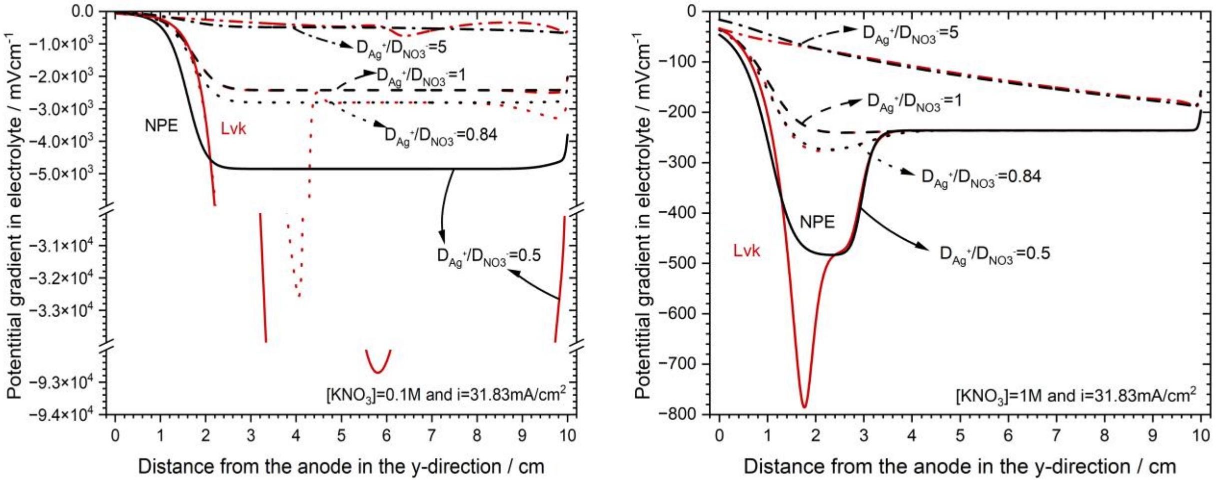

a) **b)**

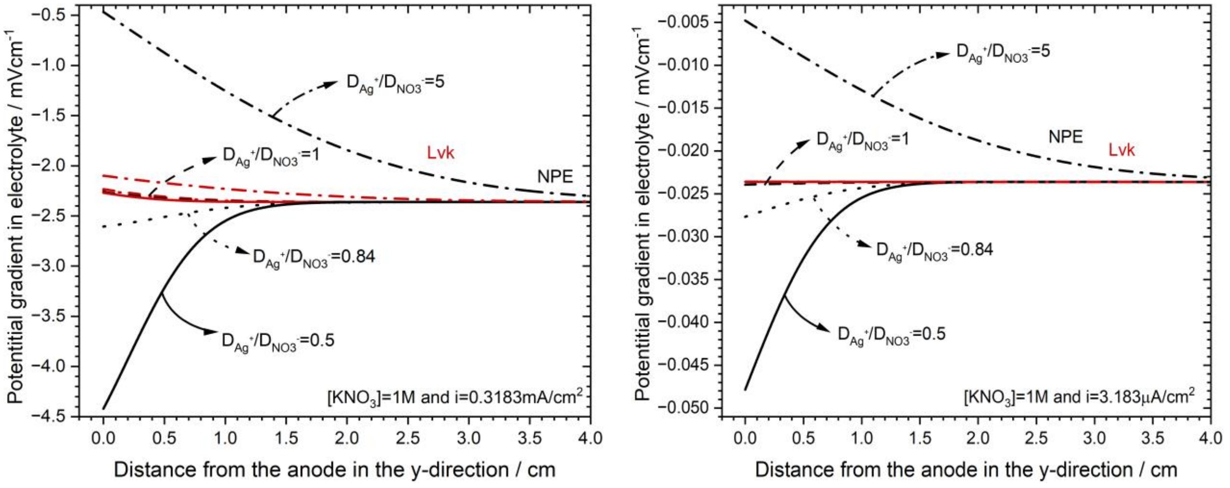

c) **d)**

Figure 6.11. Variations in potential gradient as a function of distance orthogonal to the anode for various ratios of Ag^+ and NO_3^- diffusion coefficients at **a)** 0.1M KNO_3 and 31.83 mA/cm^2, **b)** 1M KNO_3 and 31.83 mA/cm^2, **c)** 1M KNO_3 and 0.3183 mA/cm^2, and **d)** 1M KNO_3 and 3.183 μA/cm^2. Results obtained for the **NPE** and **Lvk** methods of calculations after a 5h simulation time. Line style of the arrows matches the line style of the conductivity for each $D_{Ag^+}/D_{NO_3^-}$ value.

An interesting trend observed in Figure 6.11a and 6.11b is that for $D_{Ag^+}/D_{NO_3^-}$<1, the potential gradient initially decreases with distance from the electrode surface before increasing to a constant value.

Figure 6.11c and 6.11d focus on the first 4 cm of the electrolyte to highlight differences in potential gradients near the electrode-electrolyte surface for smaller current densities. Unlike the high current density cases (Figure 11a and 11b), when $D_{Ag^+}/D_{NO_3^-}$<1, the potential gradient is initially low at the electrode-electrolyte interface before increasing to a constant value with distance. The opposite trend is observed for $D_{Ag^+}/D_{NO_3^-}$>1, while for $D_{Ag^+}/D_{NO_3^-}$=1, the potential gradient remains constant throughout the electrolyte.

For both cases, except when $D_{Ag^+}/D_{NO_3^-}$=1, the **Lvk** and **NPE** methods show poor agreement. Interestingly, the **Lvk** method predicts that for 1M KNO_3 at 3.183 μA/cm^2, the potential gradient in the electrolyte remains nearly unchanged across all $D_{Ag^+}/D_{NO_3^-}$ratios.

The final part of the results section examines the comparison between diffusion and migration fluxes, as presented in Figure 6.12a-6.12d. These Figure illustrate the ratio of diffusion to migration current density in the electrolyte perpendicular to the anode for both the **Lvk** and **NPE** methods across all varied input parameters. The observed trends closely resemble those reported for diffusion current densities in Figure 6.8a-6.8d.

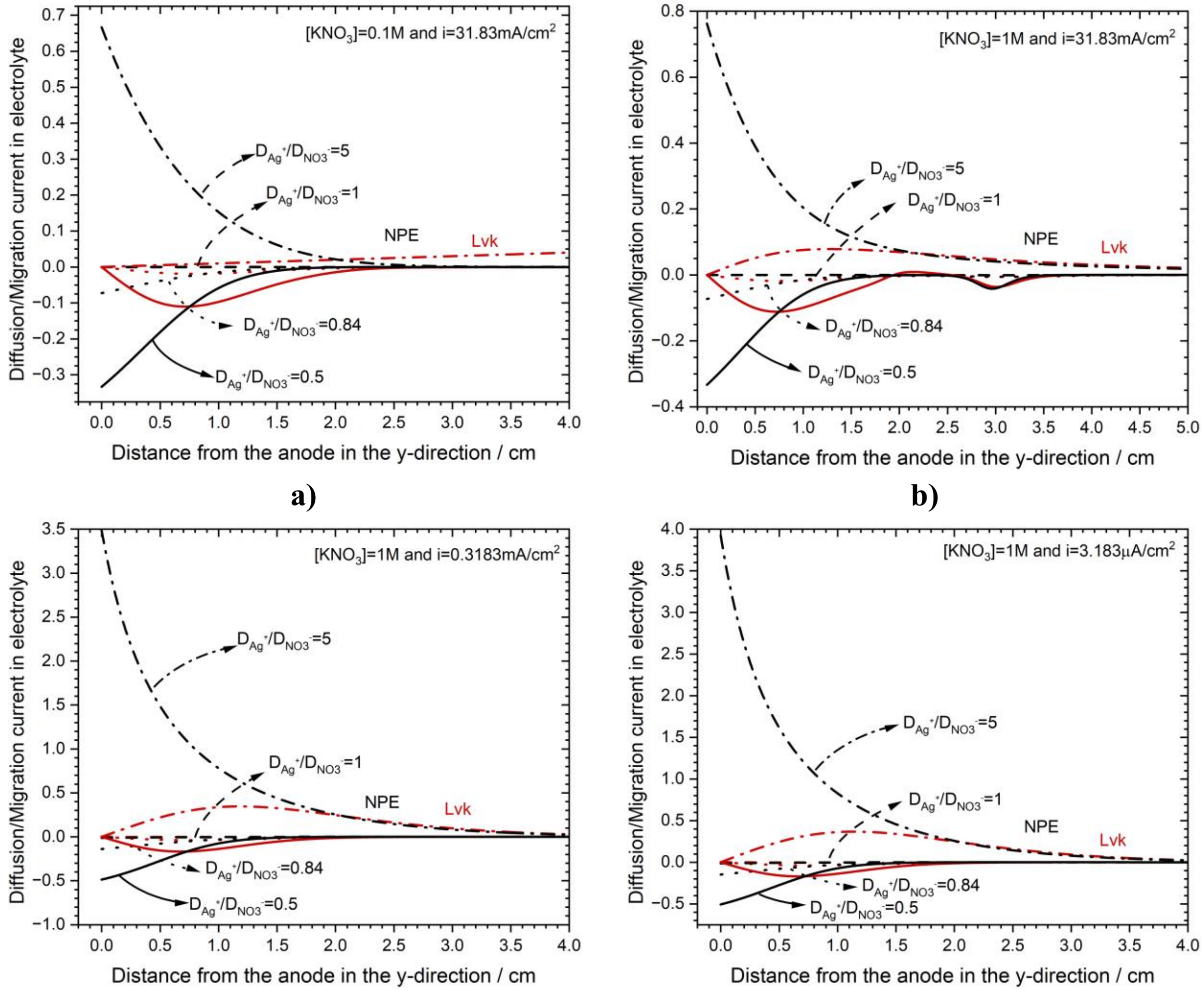

a) b)

c) d)

Figure 6.12. Variations in the ratio of diffusion-to-migration current density as a function of distance orthogonal to the anode for various ratios of Ag^+ and NO_3^- diffusion coefficients at **a)** 0.1M KNO_3 and 31.83 mA/cm^2, **b)** 1M KNO_3 and 31.83 mA/cm^2, **c)** 1M KNO_3 and 0.3183 mA/cm^2, and **d)** 1M KNO_3 and 3.183 µA/cm^2. Results obtained for the **NPE** and **Lvk** methods of calculations after a 5h simulation time. Line style of the arrows matches the line style of the diffusion-to-migration for each $D_{Ag^+}/D_{NO_3^-}$ value.

However, Figure 6.12a-6.12d emphasize the significance of the diffusion current (and consequently, the diffusion potential) near the electrode-electrolyte boundary, as demonstrated by the **NPE** method. The results indicate that a higher $D_{Ag^+}/D_{NO_3^-}$ ratio leads to an increased diffusion-to-migration current density ratio at and near this boundary. Additionally, the magnitude of this ratio decreases with increasing distance from the electrode surface. As mentioned previously, because the diffusion current density is calculated to be zero at the electrode-electrolyte boundary for all examined parameters, it follows that the ratio of diffusion to migration current in the **Lvk** method is also expected to be zero at this location.

6.5. Discussion

Calculation of the spatiotemporal distributions of current, potential, and species concentrations within an electrolyte domain is computationally demanding, particularly when homogeneous chemical reactions are also considered. These distributions are described by sets of partial differential equations (PDEs) coupled to boundary conditions including the kinetics of the interfacial electrochemical reactions. Solving these sets of PDEs requires a numerical approach in all but the simplest of systems. The highly non-linear relationships between potential and current for electrochemical reactions along with the very different time scales on which migration and diffusion operate as mass transfer modes leads to long computation times to solve the Nernst-Planck Poisson Equation for all chemical species. Although it is tempting to simply rely on Moore's Law to increase the computational power available to address these long computation times, modelers will simply be interested in modeling more complex systems as computational power increases.

To address these challenges and enhance efficiency and flexibility, modelers frequently turn to reduced-order modeling techniques (ROMs). These techniques are grounded in the principle that a lower-dimensional system or a reduced set of governing equations can adequately represent complex systems. In such scenarios, ROMs offer a more robust and time-efficient solution while maintaining a certain level of accuracy. Previous studies have demonstrated that implementing ROMs in corrosion studies can significantly enhance computational efficiency. However, the accuracy and the acceptable error margins of these methods can be highly dependent on the input boundary conditions, and these have only recently been explored.[1,2]

In this section, the galvanostatic dissolution of Ag in KNO_3 system of Fu and Chan [19] is used as the exemplar to study the parameter space in which the most advanced ROM for these systems described to date, **Lvk**. can provide accurate solutions for some or all the parameters listed above. Fu and Chan's system [19] was selected for this study due to several advantageous features that make it particularly suitable for our analysis. First, the system is elegantly simple, incorporating only six species: Ag^+, NO_3^-, K^+, H^+, OH^-, and AgOH. This minimalistic approach reduces computational complexity while still capturing the range of essential electrochemical behaviors.

One of the significant advantages of this system is that, under the specified electrochemical parameters, species transport within the cylindrical portion of the model geometry occurs almost exclusively in the vertical direction. This directional transport simplifies the analysis by eliminating the need to account for horizontal components of the diffusion and migration currents, which are otherwise near zero but can become significant near the mouth of the cylinder. By focusing on unidirectional (vertical, y) transport, we can more accurately assess the behavior of species within the system without the added complexity of multi-directional fluxes.

The geometry of the model is another crucial aspect of its relevance to this study. It closely resembles the physical characteristics of localized corrosion sites, such as pitting corrosion, where dissolution is confined to a narrow region. In such regions, the diffusion and migration components of the electrolyte current are in direct competition, creating a dynamic environment that is ideal for studying the interplay between the two. Furthermore, the simplicity and robustness of the system make it an excellent platform for exploring the effects of varying species' mobilities. By adjusting the diffusion coefficients of anions and cations within the model, we can systematically investigate how each component of the Nernst-Planck Equation contributes to the overall current in the electrolyte.

Moraes and Kelly [1,2] have shown the effectiveness of the **Lvk** approach utilizing a galvanic couple simulating a Mg-rich primer coated Al alloy and Mg for conditions which describe well many corrosion scenarios. The current density was low (~10^{-5} A/cm^2) and Tafel kinetics were imposed for the anodic and cathodic reactions. Nevertheless, there remains a need to quantify the practicality of this ROM in capturing localized corrosion settings as well as provide a detailed understanding of the electrochemical phenomena occurring at the electrode-boundary interface as well as throughout the electrolyte. In fact, it is this one of the main advantages offered by a simple model such as the one from Fu and Chan.[19]

In this section, the origin of errors that do occur when outside that parameter space and their dependence on location relative to the dissolving surface is established to explain the types and magnitudes of the errors. Specifically, we identify the key role of the diffusion potential and current and show the parameter space in which their influence can be ignored, and thus ROMs such as **Lvk** can be used with a minimum loss in accuracy. We then discuss the portion of parameter space in which **Lvk** loses accuracy and explain the role of position, diffusion coefficient ratio, supporting electrolyte concentration, and current density.

6.5.1. Impact of diffusion potential on errors associated with Laplace-based ROMS

The underlying tenet of all Laplace-based models is that the electrolyte always acts as an ohmic conductor at all locations. The strict Laplace approach requires that the electrolyte be homogeneous and of constant conductivity, hence it requires the system to be under steady-state conditions. Although useful in many cases [6,8–10,16,17], those requirements are limitations. The **Lvk** approach addressed those limitations by requiring that the Laplace Equation conditions be met locally, but as chemical, electrochemical reactions, and mass transport by diffusion occurred, the conductivity of that element is recalculated based on the new chemical composition. Essentially, it considers the electrolyte domain to be a set of interconnected resistors with their resistance varying both spatially and temporally.

Equation 6.2 is the general expression for the total potential distribution, containing potential change due to migration and that due to diffusion. If all the D_i are equal, the second term in Equation 6.2 further simplifies because the diffusivities can be factored out of the summation. The remaining portion of the term represents electroneutrality, meaning there is no diffusion potential. Under these conditions, both at the electrode-electrolyte boundary and throughout the electrolyte, the governing equations of the **NPE** reduce to those of the **Lvk** approach, leading to identical solutions for the studied parameters-such as current densities, potential, concentrations, and gradients. This is a particularly useful case where the previously discussed time and computational savings [1,2] can be leveraged without sacrificing accuracy.

Interestingly, Figure 6.4-6.6 and 6.8-6.12 show that when $D_{Ag^+}/D_{NO_3^-}$=1, all calculated parameters from **Lvk** match those from **NPE** under all conditions of current density and supporting electrolyte concentration. This equality of results includes potential profiles and concentration gradients of all species. However, it is important to note that in this scenario, the diffusivities of other ionic species do not match those of Ag^+ or NO_3^- (as indicated in Table 6.1). The key reason for this excellent agreement is the absence of diffusion current, as seen in Figure 6.8a-6.8d.

A detailed analysis of the governing equations is provided in the Appendix, but a summary is given here. Assuming the concentration gradients of H^+ and OH^- are negligible due to their low concentrations, electroneutrality implies that the concentration gradient of K^+ (d_{K^+}/dy) is directly proportional to $-z_{NO_3^-}c_{NO_3^-} - z_{Ag^+}c_{Ag^+}$, as shown in Equation A6.14 Appendix Consequently, the total diffusion current density in the electrolyte is expressed as Equation A6.8 in the Appendix, which simplifies to Equation 6.4:

$$-F\left(D_{Ag^+} - D_{K^+}\right)\left(\frac{d_{Ag^+}}{dy} - \frac{d_{NO_3^-}}{dy}\right) \tag{6.4}$$

For $D_{Ag^+}/D_{NO_3^-}$=1, we find that $D_{Ag^+} - D_{K^+} \approx 10^{-11}$ m²/s (see Table 1). To make the diffusion current density at least 10% of the total input current density (and hence provide significant and notable variations between **NPE** and **Lvk**) the term $\left(\frac{d_{Ag^+}}{dy} - \frac{d_{NO_3^-}}{dy}\right)$ in Equation 6.4 must reach values of ~100 M/cm for an input current density of 31.83 mA/cm^2, ~1 M/cm for 0.3183 mA/cm^2, and ~10^{-2} M/cm for 3.183 μA/cm^2. However, Figure 6.9a–6.9d indicate that such differences in concentration gradient near the electrode-electrolyte boundary are highly unlikely. Given the similar near-surface concentrations of NO_3^- and Ag^+, the concentration gradient of NO_3^- is unlikely to exceed that of Ag^+ by more than two orders of magnitude. Therefore, when $D_{Ag^+}/D_{NO_3^-}$=1, the total diffusion current density in the electrolyte (rather than the diffusion current density of individual species) is negligible, and charge transport is dominated by migration. As highlighted in the Appendix, as long as the total diffusion current density in the electrolyte remains negligible compared to the total current density, the **Lvk** and **NPE** methods yield identical results for all parameters-current density, potential, concentrations, and concentration gradients. This result applies specifically to the dilute system studied here, where a single electrochemically active species is produced and hydrolyzed in a two-ion supporting electrolyte, with one ion having the same mobility (u_i) and D$_i$ as the electrochemically active ion.

However, in more complex systems, such as within pitting corrosion, where multiple electrochemically active species are involved, u_i and D_i vary more significantly. That said, the diffusivities of most ionic species fall within a factor of two of one another [20] which limits deviations to some extent. Notably, H^+ and OH^- have much higher diffusivities than other ions-by factors of 5.4 and 3.1, respectively, compared to Ag^+ (as seen in Table 1). While this could introduce larger deviations, their typically low concentrations in certain applications mean their impact is often minor. Such changes could affect pH profile, which could, in turn, can influence the speciation of other ionic, pH dependent electrochemical boundary conditions, and hence potential, current density, and concentration of species.

6.5.2. Accuracy of Lvk depends on current density, electrolyte concentration, and diffusion coefficient ratio

For systems with low current densities (10^{-6} to 10^{-4} A/cm^2) and high supporting electrolyte concentrations (1 M), the errors in total current density (Figure 6.4c and 6.4d), potential distributions (Figure 6.5c and 6.5d), Ag^+ concentration (Figure 6.6c and 6.6d), concentration gradients (Figure 6.9c and 6.9d), and conductivity (Figure 6.10c and 6.10d) using the **Lvk** method are minimal. These conditions are relevant to many corrosion scenarios. Notably, Figure 6.12a-6.12d demonstrate that the diffusion current density is not negligible compared to the migration current density (except when $D_{Ag^+}/D_{NO_3^-}$=1). However, as discussed in Parts I and II [1,2] for high SER values and demonstrated here, the results from the **Lvk** and **NPE** methods show strong agreement-particularly in the distribution of all ionic species at the electrode-electrolyte boundary and now shown here to also hold true for their concentration throughout the electrolyte. This raises an important question: can we analytically demonstrate the underlying reasons for this agreement between the **Lvk** and **NPE** methods of calculation for high SER ratios?

To explain this observation, in the Appendix of this chapter we have provided a detailed analysis and explanation behind this observation. In summary, the accuracy of the **Lvk** method improves as the migration component of the electrochemically active species' current density decreases. When this migration component is negligible, the **Lvk** method assumption that all current density (and, by extension, potential) is carried by the migration of the supporting electrolyte species, throughout the electrolyte, including the electrode-electrolyte interface is highly accurate. Conversely, in the **NPE** method, the total current density arises from both diffusion and migration of all electrochemically active species. However, even in the **NPE** approach, the concentration of Ag^+ is primarily determined by its gradient, which depends on the amount of Ag^+ produced at the electrode-electrolyte interface and its diffusion coefficient. As a result, under conditions where $D_{Ag^+}/D_{NO_3^-}$=1 but the migration current density of Ag^+ remains negligible compared to its diffusion current density (*e.g.,* at 1 M KNO_3 with input current densities of 0.3183 mA/cm^2 and 3.183 μA/cm^2), the concentration profiles of Ag^+ calculated by **Lvk** and **NPE** remain highly consistent.

For these low-current-density, high supporting electrolyte concentration cases, the impact of $D_{Ag^+}/D_{NO_3^-}$ deviations from unity are generally small for potential distributions, Ag^+ concentration profiles, and conductivity. However, errors become more pronounced within the diffusional boundary layer (*i.e.,* y<4 cm in this study) and are particularly significant for total and diffusion current densities. Because of the phenomena explained in the above paragraph, the largest discrepancies between the **NPE** and **Lvk** in concentration profiles primarily occur in the supporting electrolyte species (*e.g.,* NO_3^- and K^+ profile, as shown in the Appendix). However, given the high concentration of these species relative to the electrochemically active species, small variations in their concentration can often be neglected.

Figure 6.4a-6.4d illustrate that the ratio of total current density between **Lvk** and **NPE** deviates significantly in regions where diffusion current density is large (approximately y<4, except at y=0 cm). This discrepancy arises because, while **Lvk** uses diffusion to recalibrate conductivity, it does not include diffusion current in the total current density calculation within the Secondary Current Distribution module (Figure 6.1b). As a result, **Lvk** enforces a condition where diffusion current is zero at the electrochemical interface, requiring all current to be carried by migration to maintain continuity with the galvanostatic boundary condition. Note that in the **Lvk** method, the Secondary Current Distribution is solved separately from the Transport of Dilute Species module. As a result, **Lvk** can only enforce the condition that the total diffusion current density remains zero at x=0 cm, where electric current transitions to electrolytic current. However, this strict condition is not imposed throughout the entire electrolyte. In contrast, **NPE** accounts for diffusion current when solving for current and potential within the Tertiary Current Distribution module. Consequently, when $D_{Ag^+}/D_{NO_3^-}$ deviates significantly from 1 (*e.g.,* $D_{Ag^+}/D_{NO_3^-}$=0.5 or 5), large diffusion current densities arise, sometimes exceeding the migration current density (Figure 6.12a-6.12d). Although **Lvk** effectively captures the overall trends in current densities, these differences can introduce discrepancies in potential and potential gradients. While these discrepancies remain small, their significance depends on the accuracy requirements of the specific modeling application.

Despite these differences, both **Lvk** and **NPE** must impose another mandatory boundary condition at the electrode-electrolyte interface that prevents supporting electrolyte species from crossing this boundary. This condition ensures that the total diffusion and migration current densities of the supporting electrolyte sum to zero at y=0 cm. As a result, at y=0 cm, all electrolyte current is carried by the electrochemically active species Ag^+. It is this the reason why the ratio of the total current density between **Lvk** and **NPE** is 1 for all the conditions at y=0 cm regardless of the magnitude of the diffusion current density or the presence of a migration current density of Ag^+ species.

6.5.3. Accuracy depends on position relative to dissolving surface

Outside the diffusional boundary layer, there are no concentration gradients so no diffusion potential can exist, thus the electrolyte behaves in accordance with Ohm's law (ohmically).

Laplace-based methods work well here, and their speed and lower computational power needs can be exploited. Note that in many cases it is distributions of parameters away from the electrode interface that are of primary interest. The fact that errors in parameters near the electrode does not influence values farther away is notable and of value.

As discussed in the Introduction, it is expected that the regions closest to the electrode surface would be those which pose the largest challenge to ROMs such as **Lvk** because it is these regions that the largest concentration gradients will exist in the system as ionic species are being produced (and/or consumed). Here the second term of Equation 6.2, the diffusion potential, will have its impact. The fraction of the charge that is moved by concentration gradients replaces some of that moved by potential gradients, so the solution in this region is not an ohmic conductor. This characteristic is the direct source of errors in Laplace-based methods.

In the system of interest here, Laplace-based methods require that all the current be migration current as that is what is used in the governing equation. Diffusion processes occur and can be evaluated from **Lvk** analyses, but the diffusion current is not used to conserve charge. The migration of K^+ and NO_3^- are considered in the Laplace calculation, but because these species cannot cross the interface, their respective diffusion current densities must algebraically cancel the migration current density of each. The Ag^+ does carry the charge, but its diffusion current is not used in the calculation of the potential.

This analysis finds that ROMs such as the **Lvk** approach, which account only for migration effects in the electrolyte, can yield results identical to those from standard methods like the **NPE** provided that the total diffusion current density in the electrolyte sums to zero. When this is not possible, these models maintain high accuracy when the migration contribution of electrochemically active species is negligible compared to their diffusion current density. A zero total diffusion current density occurs when the diffusion coefficients of the ionic species are nearly identical. On the other hand, minimizing the migration effects near the interface for electrochemically active species can be achieved by reducing the potential gradient in the electrolyte, which can be accomplished through the use of a highly concentrated supporting electrolyte, low current densities, or geometries that limit additional potential drop beyond the intrinsic electrolyte resistance.

6.5.4. Advantages and limitations of Laplace-based methods

In computational modeling in general there is an inherent trade-off among speed, computing resources needed, and accuracy. **NPE** has speed and computing resource requirements that are advantageous relative to solution to of full Nernst-Planck-Poisson Equation[1] The standard Laplace Equation approach is highly limited in terms of the conditions to which it can be applied as it requires the conductivity to be constant in space and time, and it does not include any impact of diffusion processes. That said, the success of cases in which it has been used show that it has utility even under conditions in which the requirements are not strictly met.[6,8–10,16] A critical limitation is the constraint that the system be at steady state. **Lvk** was developed as a bridge between standard Laplace methods and **NPE** in that it is faster and uses less computing resources than **NPE**. Its use allows one to consider more complex systems than can currently be studied with **NPE** for any given set of computing resources. The present work has shown that many parameters can be accurately modeled over a wide range of conditions. That said, the impact of the simplifications inherent in **Lvk** have not been fully assessed.

Previous work [1,2] showed that **Lvk** can bridge the gap described for many conditions of interest, albeit for one electrochemical system of interest to corrosion scientists and engineers, galvanic corrosion in a thin electrolyte. That work also showed that when the supporting electrolyte concentration decreased, particularly relative to the concentration of the electrochemically produced species, large errors in the parameters of interest can result. The present chapter demonstrates that these errors were due to the presence and importance of a diffusion potential and current density.

As shown above, the accuracy of **Lvk** depends on a combination of current density, supporting electrolyte concentration, and differences in diffusivity amongst ionic species. In addition, close proximity to the dissolving interface presents the greatest challenge for **Lvk** accuracy. Differences in ionic diffusivities are important because they are the heart of the reason diffusion potentials exist, as shown directly in Equation 6.2. If all of the diffusivities are the same, the diffusion potential is zero by definition. Although the range of diffusivities of ionic species is limited by the range of ionic mobilities, the high mobilities of OH^- and H^+ will have an impact that amplifies their concentrations, which are typically low in most corrosion cases, in particular. That said, for situations where one of these is a major species, errors can be large. Within a localized corrosion site is one of those instances. High current densities and high concentrations of H^+ are endemic to localized corrosion sites, so FEM calculations aimed at areas within pits, crevices, and cracks should use the **NPE** method. That said, if interactions between localized corrosion sites and other regions of a domain are of interest, **Lvk** should work well, as the current densities and H^+ concentration are much lower in solution on that spatial scale.

6.6. Conclusions

This chapter presents a comprehensive analysis of the **NPE** and **Lvk** calculation methods for current, potential, and species distribution, employing computational approaches and supported with an analytical component. The primary objective of this study is to investigate the influence of diffusion potential and current on the accuracy of reduced-order models based on the Laplace Equation. This study highlights the conditions under which diffusion potential and current significantly impact key parameters at specific locations, providing critical guidance on selecting the appropriate governing equation. The work presented here compliments Part I and Part II[1,2] by shifting the attention to the electrolyte itself and by exploring localized corrosion scenarios characterized by high current densities and varying supporting electrolyte concentrations. To achieve this, we adopted a simplified electrochemical model with unidirectional transport from Fu and Chan.[19]

The key findings are as follows:

1. At the electrolyte interface, the diffusion current from the supporting electrolyte ions is substantial, precisely balancing the migration current in magnitude but with an opposite sign.
2. Near the electrode-electrolyte interface, the diffusion current density of the electrochemically active species is consistently high and dominates its migration current density.
3. The total diffusion current (and potential) at the electrode-electrolyte interface remains significant under most conditions, except in rare cases where all electrolyte species have identical diffusion coefficients or more extremely rare situations when the total diffusion current of the supporting electrolyte offsets that of the electrochemically active species.
4. The **Lvk** model can produce identical results to the **NPE** method throughout the electrolyte if the total diffusion current in the electrolyte is zero. Its accuracy remains high in the bulk solution (i.e., outside the diffusional boundary layer).
5. In more general scenarios, the accuracy of the **Lvk** model in capturing electrochemical behavior at the electrode-electrolyte interface improves as the migration current of the electrochemically active species decreases-a condition often achieved by increasing the concentration of the supporting electrolyte in high-current-density environments.

6.7. References

1. Moraes, C. V. & Kelly, R. G. A comparison of FEM results from the use of different governing equations in a galvanic cell part II: Impact of low supporting electrolyte concentration. *Electrochim. Acta* **468**, 143153 (2023).
2. Moraes, C. V. & Kelly, R. G. A comparison of FEM results from the use of different governing equations in a galvanic cell part I: In the presence of a supporting electrolyte. *Electrochim. Acta* **469**, 143146 (2023).
3. Moraes, C. V., Santucci, R. J., Scully, J. R. & Kelly, R. G. Finite Element Modeling of Chemical and Electrochemical Protection Mechanisms Offered by Mg-Based Organic Coatings to AA2024-T351. *J. Electrochem. Soc.* **168**, 051505 (2021).
4. Charles-Granville, U.-E. *et al.* Application of Finite Element Modeling to Macro-Galvanic Coupling of AA7050 and SS316: Validation Using the Scanning Vibrating Electrode Technique. *J. Electrochem. Soc.* **169**, 031502 (2022).
5. Alkire, R., Bergh, T. & Sani, R. L. Predicting Electrode Shape Change with Use of Finite Element Methods. *J. Electrochem. Soc.* **125**, 1981–1988 (1978).
6. Liu, C. & Kelly, R. G. A review of the application of finite element method (FEM) to localized corrosion modeling. *Corrosion* **75**, 1285–1299 (2019).
7. Katona, R. M., Burns, J. T., Schaller, R. F. & Kelly, R. G. Insights from electrochemical crack tip modeling of atmospheric stress corrosion cracking. *Corros. Sci.* **209**, 110756 (2022).
8. Marshall, R. S., Kelly, R. G., Goff, A. & Sprinkle, C. Galvanic corrosion between coated Al alloy plate and stainless steel fasteners, Part 1: FEM model development and validation. *Corrosion* **75**, 1461–1473 (2019).
9. Marshall, R. S., Goff, A., Sprinkle, C., Britos, A. & Kelly, R. G. Estimating the Throwing Power of SS316 when Coupled with AA7075 Through Finite Element Modeling. *Corrosion* **76**, 476–484 (2020).
10. Cocke, C. *et al.* The Effect of Corrosion Location Relative to Local Stresses on the Fatigue Life of Geometrically Complex, Galvanically Corroded AA7075-T6. *Corrosion* **78**, 152–162 (2022).
11. Abodi, L. C. *et al.* Modeling localized aluminum alloy corrosion in chloride solutions under non-equilibrium conditions: Steps toward understanding pitting initiation. *Electrochim. Acta* **63**, 169–178 (2012).
12. Topa, V., Demeter, A. S., Hotoiu, L., Deconinck, D. & Deconinck, J. A transient multi-ion transport model for galvanized steel corrosion protection. *Electrochim. Acta* **77**, 339–347 (2012).
13. Demeter, A. S. *et al.* Multi-ion transport and reaction model used to improve the understanding of local current density measurements in presence of concentration gradients around a point current source. *Electrochim. Acta* **127**, 45–52 (2014).
14. Thébault, F., Vuillemin, B., Oltra, R., Allely, C. & Ogle, K. Modeling bimetallic corrosion under thin electrolyte films. *Corros. Sci.* **53**, 201–207 (2011).

15. Thébault, F., Vuillemin, B., Oltra, R., Allely, C. & Ogle, K. Reliability of numerical models for simulating galvanic corrosion processes. *Electrochim. Acta* **82**, 349–355 (2012).
16. Harris, Z. D., Marshall, R. S., Kelly, R. G. & Burns, J. T. Coupling Fracture Mechanics Experiments and Electrochemical Modeling to Mitigate Environment-Assisted Cracking in Engineering Components. *Corrosion* **79**, 363–375 (2023).
17. Marshall, R. S. *et al.* A materials selection framework for fastener-in-panel geometries using FEM and LEFM, to mitigate coating degradation and environmentally assisted cracking. *Corros. Sci.* **227**, 111788 (2024).
18. Liu, C., Srinivasan, J. & Kelly, R. G. Editors' Choice—Electrolyte Film Thickness Effects on the Cathodic Current Availability in a Galvanic Couple. *J. Electrochem. Soc.* **164**, C845–C855 (2017).
19. Fu, J. W. & Chan, S. K. Finite Element Method for Modeling Localized Corrosion Cells. *Corrosion* **40**, 540–544 (1984).
20. Newman, J. & Thomas-Alyea, K. E. *Electrochemical Systems*. *Electrochemical Science Series* (John Wiley & Sons, Inc., 2004).

A6. Appendix

Table A6.1. Comparison between the computational time and physical memory of different governing equations after 5hr simulation time for $D_{Ag^+}/D_{NO_3^-}$=0.5.

KNO$_3$ concentration / M and input current density / mA·cm^{-2}	**NPE**		**Lvk**	
	Time / s	Memory / GB	Time / s	Memory / GB
0.1 and 31.83	13,418	9.06	5,246	3.72
1 and 31.83	1203	8.74	341	3.90
1 and 0.3183	293	8.28	190	3.94
1 and 0.003183	284	8.03	125	3.97

Table A6.2. Comparison between the computational time and physical memory of different governing equations after 5hr simulation time for $D_{Ag^+}/D_{NO_3^-}$=1.

KNO$_3$ concentration / M and input current density / mA·cm^{-2}	**NPE**		**Lvk**	
	Time / s	Memory / GB	Time / s	Memory / GB
0.1 and 31.83	2495	8.56	1,428	3.98
1 and 31.83	623	8.36	311	3.92
1 and 0.3183	293	8.03	182	3.92
1 and 0.003183	294	8.10	125	3.91

Table A6.3. Comparison between the computational time and physical memory of different governing equations after 5hr simulation time for $D_{Ag^+}/D_{NO_3^-}$=5.

KNO$_3$ concentration / M and input current density / mA·cm^{-2}	**NPE**		**Lvk**	
	Time / s	Memory / GB	Time / s	Memory / GB
0.1 and 31.83	745	8.69	477	3.95
1 and 31.83	485	8.82	320	3.94
1 and 0.3183	293	8.19	195	3.95
1 and 0.003183	294	8.15	130	3.94

Extended comparison between the diffusion and migration current density rising in the electrolyte for major ionic components through NPE and Lvk

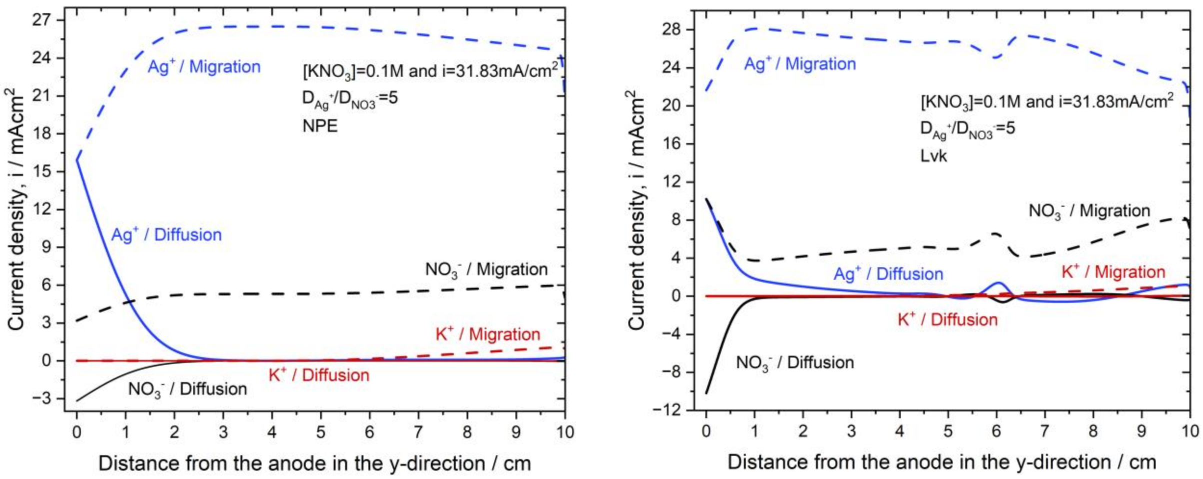

a) **b)**

Figure A6.1. Variations in diffusion current density (solid line) and migration current density (dashed line) as a function of distance orthogonal to the anode for $D_{Ag^+}/D_{NO_3^-} = 5$ diffusion coefficients at 0.1M KNO_3 and 31.83mA/cm^2 for: Ag^+ (blue), NO_3^- (black), and K^+ (red). Results obtained for **a) NPE** and **b) Lvk** methods of calculations after a 5h simulation time. Note that the effects of other elements are not shown as their impact is deemed negligible compared to the ones presented.

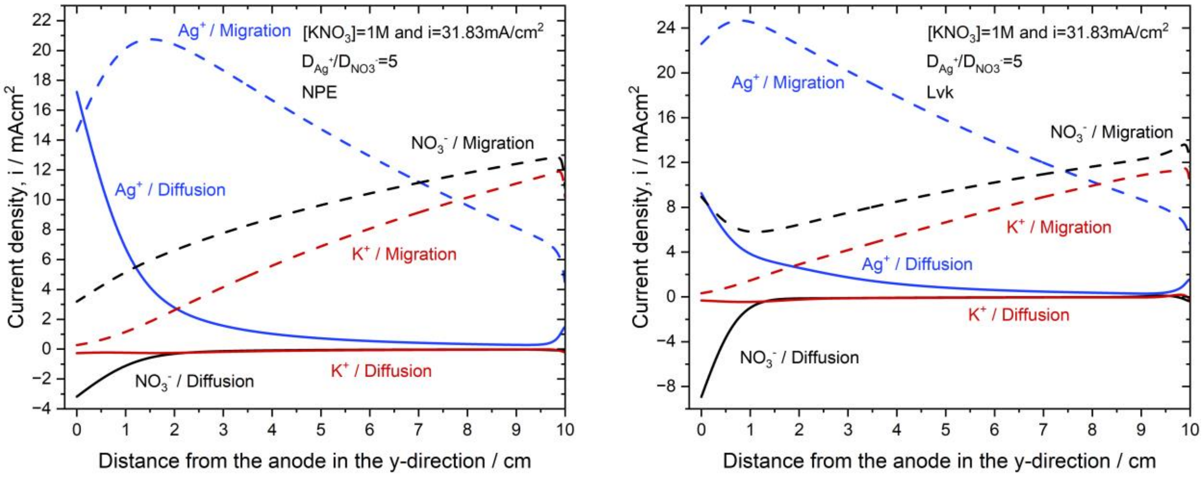

a) **b)**

Figure A6.2. Variations in diffusion current density (solid line) and migration current density (dashed line) as a function of distance orthogonal to the anode for $D_{Ag^+}/D_{NO_3^-} = 5$ diffusion coefficients at 1M KNO_3 and 31.83mA/cm^2 for: Ag^+ (blue), NO_3^- (black), and K^+ (red). Results obtained for **a) NPE** and **b) Lvk** methods of calculations after a 5h simulation time. Note that the effects of other elements are not shown as their impact is deemed negligible compared to the ones presented.

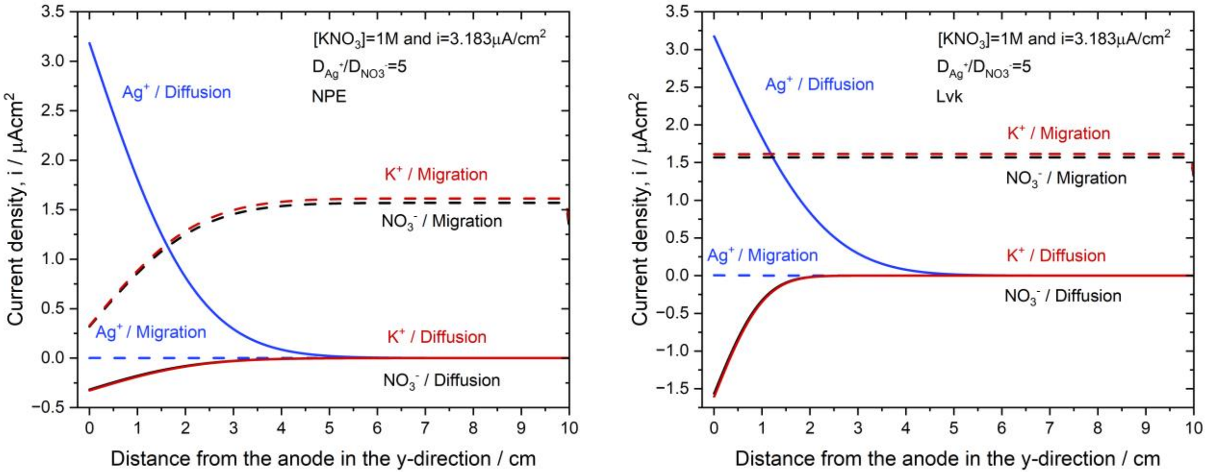

a) **b)**

Figure A6.3. Variations in diffusion current density (solid line) and migration current density (dashed line) as a function of distance orthogonal to the anode for $D_{Ag^+}/D_{NO_3^-} = 5$ diffusion coefficients at 1M KNO$_3$ and 3.183μA/cm^2 for: Ag$^+$ (blue), NO$_3^-$ (black), and K$^+$ (red). Results obtained for **a) NPE** and **b) Lvk** methods of calculations after a 5h simulation time. Note that the effects of other elements are not shown as their impact is deemed negligible compared to the ones presented.

Analytical derivation of the solutions for NPE and Lvk for the 1D Ag wire dissolution in KNO_3 solution.

In the scenario pertaining to this chapter, the transport of species is limited to a single direction, *y*. Thus, all variables referenced in the following steps pertain to their respective vertical components. The species considered will be Ag^+, NO_3^-, and K^+, as the effects of other components (OH^- and H^+) are negligible in quantity and do not contribute to electrochemical reactions. From now on, the concentration of species i is noted as c_i. The reader is suggested to refer to Figure 6.7 and Appendix for any graphical information, especially for the electrode-electrolyte area region, to ease the visual understanding of diffusion and migration current rising from each of the ionic species considered in this analysis. No additional chemical reactions are considered in this section.

NPE

For the case of the **NPE**, at the electrode-electrolyte interface, the following equations must be true at all times:

1. $$i = \left(z_{Ag^+}F\right)(-Fz_{Ag^+}u_{Ag^+}c_{Ag^+}\frac{\partial\phi}{\partial y} - D_{Ag^+}\frac{\partial c_{Ag^+}}{\partial y}) \quad \text{(A6.1)}$$
2. $$0 = \left(z_{NO_3^-}F\right)(-Fz_{NO_3^-}u_{NO_3^-}c_{NO_3^-}\frac{\partial\phi}{\partial y} - D_{NO_3^-}\frac{\partial c_{NO_3^-}}{\partial y}) \quad \text{(A6.2)}$$
3. $$0 = (z_{K^+}F)(-Fz_{K^+}u_{K^+}c_{K^+}\frac{\partial\phi}{\partial y} - D_{K^+}\frac{\partial c_{K^+}}{\partial y}) \quad \text{(A6.3)}$$
4. $$c_{NO_3^-} = \frac{-z_{K^+}c_{K^+} - z_{Ag^+}c_{\mathrm{Ag+}}}{z_{NO_3^-}} \quad \text{(A6.4)}$$

Equation A6.1-A6.4 are true at all times at the interface. Equation A6.1 converts the electric charge into electrolyte current carried by Ag^+ species through diffusion and migration. At the electrode boundary, NO_3^- and K^+ are not produced, hence, the total current is zero, Equation A6.2 and A6.3. Lastly, Equation A6.4 imposes electroneutrality with NO_3^- selected to be the makeup specie, as in the FEM simulations provided in this chapter. Note that K^+ can also be chosen to be the make-up ionic species as it does not partake in any electrochemical reaction but caution must be exercised as in certain cases its concentration can be extremely low as shown below in Figure A6.4 and A6.5. By definition, then, Equation A6.4 can be used to approximate the gradient in K^+ in Equation A6.5:

5. $$\frac{\partial c_{K^+}}{\partial y} = \frac{\partial}{\partial y}\left(\frac{-z_{NO_3^-}c_{NO_3^-} - z_{Ag^+}c_{Ag^+}}{z_{K^+}}\right) \text{ and } \frac{\partial c_{K^+}}{\partial y} = -\frac{z_{NO_3^-}}{z_{K^+}}\frac{\partial c_{NO_3^-}}{\partial y} - \frac{z_{Ag^+}}{z_{K^+}}\frac{\partial c_{Ag^+}}{\partial y} \quad \text{(A6.5)}$$

An important finding arises from Equation A6.2 and A6.3: at the boundary, there cannot be a net flux of supporting electrolyte species. Thus, at all times, the diffusion and migration flux of these species (NO_3^- or K^+) must be equal in magnitude but opposite in direction. If this condition is not met, part of the input current would be consumed by the supporting electrolyte, violating Faraday's law. This principle consistently applies to the supporting electrolyte.

This condition leads to another significant aspect: near the electrode surface, the diffusion current of the supporting electrolyte *cannot* be zero. Since the migration current from the supporting electrolyte must equal the diffusion current of these species, a diffusion flux-and therefore current-for each supporting electrolyte species must increase in the electrolyte until its absolute value matches that of absolute value of the migration current at the electrode boundary.

The total diffusion current at the electrode-electrolyte boundary can be found by adding second term of Equation A6.3 and substituting Equation A6.5:

$$6.\quad i_D = F(-z_{Ag^+}D_{Ag^+}\frac{\partial c_{Ag^+}}{\partial y} - z_{NO_3^-}D_{NO_3^-}\frac{\partial c_{NO_3^-}}{\partial y} - z_{K^+}D_{K^+}(-\frac{z_{NO_3^-}}{z_{K^+}}\frac{\partial c_{NO_3^-}}{\partial y} - \frac{z_{Ag^+}}{z_{K^+}}\frac{\partial c_{Ag^+}}{\partial y}) \tag{A6.6}$$

The total migration current at the electrode-electrolyte boundary can be found by adding first term of Equation A6.3 and substituting Equation A6.4:

$$7.\quad i_M = F^2\frac{\partial \phi}{\partial y}(-z_{Ag^+}^2 u_{Ag^+}c_{Ag^+} - z_{NO_3^-}u_{NO_3^-}(-z_{K^+}c_{K^+} - z_{Ag^+}c_{\mathrm{Ag+}}) - z_{K^+}^2 u_{K^+}c_{K^+}) \tag{A6.7}$$

For the species case when $D_{Ag^+}/D_{NO_3^-} = 1$, Equation A6.6 deduces to:

$$8.\quad i_D = F\left(z_{Ag^+}\frac{\partial c_{Ag^+}}{\partial y} + z_{NO_3^-}\frac{\partial c_{NO_3^-}}{\partial y}\right)\left(D_{K^+} - D_{Ag^+}\right) \tag{A6.8}$$

Moreover, under the influence of the supporting electrolyte, the migration component of the electrochemically active species, Ag$^+$, becomes negligible.[20] This is logical because, in the presence of a strong supporting electrolyte with high conductivity, the potential gradient diminishes. Additionally, given the low concentration of the Ag species (due to low currents and therefore low c_{Ag^+}), the term $-F^2 z_{Ag^+}^2 u_{Ag^+}c_{Ag^+}\frac{\partial \phi}{\partial y}$approaches zero. In fact, one of the purposes of adding supporting electrolytes in many experiments is to facilitate the study of minor species and their diffusion.[20] Consequently, Equation A6.1 becomes:

$$9.\quad i = -Fz_{Ag^+}D_{Ag^+}\frac{\partial c_{Ag^+}}{\partial y} \tag{A6.9}$$

On the other hand, solving Equation A6.1-A6.5 simultaneously, while knowing that $u_i = \frac{D_i}{RT}$ and $Fz_{Ag^+}u_{Ag^+}c_{Ag^+}\frac{\partial \phi}{\partial y} \approx 0$ yields:

$$10.\ \frac{\partial c_{NO_3^-}}{\partial y} = (\frac{-z_{Ag^+}}{z_{NO_3^-}-z_{K^+}})\frac{\partial c_{Ag^+}}{\partial y} \tag{A6.10}$$

$$11.\ \frac{\partial c_{K^+}}{\partial y} = (\frac{z_{Ag^+}z_{K^+}}{z_{K^+}\left(z_{NO_3^-}-z_{K^+}\right)})\frac{\partial c_{Ag^+}}{\partial y} \tag{A6.11}$$

Equation A6.10 and Equation A6.11 suggest that in scenarios with high concentrations of supporting electrolyte and low input current densities at the electrode boundary, the diffusion (and consequently the migration) flux of the supporting electrolyte is constrained by the concentration gradient of the electrochemically active species, Ag$^+$. From Equation A6.10 and Equation A6.11, it can be inferred that the absolute value of the concentration gradients of NO_3^- and K^+ are always half that of Ag^+ (opposite in value).

Lvk

In the **Lvk** approach, the conductivity calculated from the Transport of Dilute Species module is inserted into the Laplace Equation in the Secondary current distribution module of COMSOL. This way, the module solves the potential and current distribution with an updated/variable conductivity of the present species. For small potential changes from one-time step to another, one can generalize this statement by saying that only the migration current from the transport of dilute species is considered in solving for potential and current distribution. Note that the current rising from the diffusion current is not considered when solving for current and potential distribution. Still, the same main equations as in the **NPE** shall apply, except for the ones arising for electroneutrality:

1. $$i = \left(z_{Ag^+}F\right)\left(-Fz_{Ag^+}u_{Ag^+}c_{Ag^+}\frac{\partial\phi}{\partial y} - D_{Ag^+}\frac{\partial c_{Ag^+}}{\partial y}\right) \quad \text{(A6.11)}$$
2. $$0 = \left(z_{NO_3^-}F\right)\left(-Fz_{NO_3^-}u_{NO_3^-}c_{NO_3^-}\frac{\partial\phi}{\partial y} - D_{NO_3^-}\frac{\partial c_{NO_3^-}}{\partial y}\right) \quad \text{(A6.12)}$$
3. $$0 = \left(z_{K^+}F\right)\left(-Fz_{K^+}u_{K^+}c_{K^+}\frac{\partial\phi}{\partial y} - D_{K^+}\frac{\partial c_{K^+}}{\partial y}\right) \quad \text{(A6.13)}$$

Equation A6.11 must always hold true. The input current is a boundary condition on the left side of the equation and is satisfied on the right side by the surface and potential coupling within the transport of dilute species module. Essentially, this equation ensures that all input current is used for the production of Ag^+ and this current is divided between diffusion and migration components.

The second and third equations must also be upheld. These indicate that the supporting electrolyte does not consume any input current at the boundary. Instead, the current is evenly distributed between the diffusion and migration components of each species, with equal magnitudes but opposite signs, as with **NPE**. This situation represents a *no-flux* boundary condition, as implemented in COMSOL Multiphysics.

For high *supporting electrolytes and low input current* densities, the $-F^2z_{Ag^+}^2u_{Ag^+}c_{Ag^+}\frac{\partial\phi}{\partial y}$ term of Equation A6.11 is close to zero.[20] Therefore Equation A6.11 becomes:

4. $$i = -Fz_{Ag^+}D_{Ag^+}\frac{\partial c_{Ag^+}}{\partial y} \quad \text{(A6.14)}$$

5.

In fact, in the case of **NPE**, the total current in the electrolyte must match that of the electric current. Simply, Kirchoff's law must be obeyed between electrolyte current and electric current. As such, one can simply write the total current as:

6. $$i = -F^2 z_{Ag^+}^2 u_{Ag^+} c_{Ag^+} \frac{\partial \phi}{\partial y} - F z_{Ag^+} D_{Ag^+} \frac{\partial c_{Ag^+}}{\partial y} - F^2 z_{NO_3^-}^2 u_{NO_3^-} c_{NO_3^-} \frac{\partial \phi}{\partial y} - F z_{NO_3^-} D_{NO_3^-} \frac{\partial c_{NO_3^-}}{\partial y} - F^2 z_{K^+}^2 u_{K^+} c_{K^+} \frac{\partial \phi}{\partial y} - F z_{K^+} D_{K^+} \frac{\partial c_K}{\partial y} \tag{A6.15}$$

Equation A6.15 is a fundamental electrochemical equation which when multiplied by the gradient, gives the statement of the Conservation of Charge: $\nabla \cdot i = 0$. In the case of the **Lvk**, the electrolyte current from the diffusion component is disregarded under the assumption of a negligible diffusion potential. As such, for the case of the **Lvk**, Equation A6.15 converts into:

7. $$i = -F^2 z_{Ag^+}^2 u_{Ag^+} c_{Ag^+} \frac{\partial \phi}{\partial y} - F^2 z_{NO_3^-}^2 u_{NO_3^-} c_{NO_3^-} \frac{\partial \phi}{\partial y} - F^2 z_{K^+}^2 u_{K^+} c_{K^+} \frac{\partial \phi}{\partial y} \tag{A6.16}$$

From Equation A6.16, the total current in the electrolyte, driven by the migration of NO_3^- and K^+ species, must equal the input current.

At the electrode-electrolyte boundary the current is directed toward the production of Ag^+. The Ag^+ species dissipate in the solution solely through diffusion, as described by Equation A6.14. At the same time, this input current at the boundary must be balanced by the migration current from the supporting electrolyte, in accordance with Equation A6.16. Using the **Lvk** method, for high *supporting electrolytes and low input current* densities we expect that, based on Equation A6.16:

8. $$-F^2 z_{NO_3^-}^2 u_{NO_3^-} c_{NO_3^-} \frac{\partial \phi}{\partial y} - F^2 z_{K^+}^2 u_{K^+} c_{K^+} \frac{\partial \phi}{\partial y} = 3.183 \mu A/cm^2 \tag{A6.17}$$

At the boundary, as well:

9. $$-F^2 z_{NO_3^-}^2 u_{NO_3^-} c_{NO_3^-} \frac{\partial \phi}{\partial y} - F z_{K^+} D_{K^+} \frac{\partial c_{K^+}}{\partial y} = -3.183 \mu A/cm^2 \tag{A6.18}$$

As in the case of the **NPE**, this rule gives rise to the diffusion potential from the supporting electrolyte, where for each species, its magnitude is equal to ohmic potential (migration effect) but opposite in sign. Throughout this process, the current carried by the Ag^+ produced near the electrode surface is primarily due to diffusion, with no significant migration expected. Ag^+ moves through the electrolyte by diffusion, driven by the concentration gradients the dissolution creates. This diffusion current carried by supporting electrolyte species equals that of the diffusion current carried by Ag^+, but opposite in sign. Hence, the total diffusion current from the electrolyte species at the electrode-electrolyte boundary is always zero for the **Lvk**. This is a consequence of the modified boundary conditions that only consider the electrolyte current rising from migration of the ionic species. This imposed condition does not exist in the case of the **NPE**.

In the case when $-F^2 z_{Ag^+}^2 u_{Ag^+} c_{Ag^+} \frac{\partial \phi}{\partial y} \neq 0$ an analytical solution from the **Lvk** is complicated. On one side, the production of the Ag^+ is defined at the electrode electrolyte boundary and its mass transport must be separated between diffusion and migration. At the boundary, once again, no net current can rise from the NO_3^- or K^+ (Equation A6.12 and A6.13). At the same time, for the **Lvk**, Equation A6.16 is true as it is an imposed boundary condition.

Comparing it to the case from a lower input current densities the right side of Equation A6.16 has an additional term that now can be significant $(-F^2 z_{Ag}^2 u_{Ag} c_{Ag} \frac{\partial \phi}{\partial y})$. However, the total current density imposed at the electrode-electrolyte interface must be say 0.3183 mA/cm^2. In order to do so the current must be split between $-F^2 z_{Ag^+}^2 u_{Ag^+} c_{Ag^+} \frac{\partial \phi}{\partial y}$, $-F^2 z_{NO_3^-}^2 u_{NO_3^-} c_{NO_3^-} \frac{\partial \phi}{\partial y}$ and $-F^2 z_{K^+}^2 u_{K^+} c_{K^+} \frac{\partial \phi}{\partial y}$ to satisfy Equation A6.12 and A6.13. We emphasize that, if the electrolyte was extremely conductive, the current density would be split between NO_3^- and K^+ based on the ratio of their mobilities/diffusion coefficients.

In the present case, part of the 0.3183 mA/cm^2 current must be attributed to the migration component of Ag^+. As a result, at the electrode boundary, the migration current density components of K^+ and NO_3- must decrease to accommodate the migration current density of Ag^+. Analyzing the system to ensure that every current component is accounted for can be complex. However, it is expected that the changes in the diffusion and migration of K^+ and NO_3^- near the surface, compared to their behavior in the bulk electrolyte, will closely correspond to the migration current associated with Ag^+. Naturally, a diffusion current density for K^+ and NO_3^- will also arise near the boundary to satisfy Equation A6.12 and A6.13, as previously mentioned.

It's important to highlight that Equation A6.11-13 in this section lead to an interesting challenge in the solution, which stems from the simplifications inherent in reduced-order modeling. On the one hand, Equation A6.15 is always true in the **Lvk** method when considered the electrolyte current solved from the Transport of Dilute Species module. On the other hand, the total current calculated through Equation A6.16 is utilized to solve for current and potential in the Secondary Current Distribution module of the **Lvk**. In simple terms, Equation A6.15 gives electric current while Equation A6.16 is the electrolyte current. In order to close the circuit and apply Kirchoff's law, Equation A6.16 can be substituted into Equation A6.15 to give Equation A6.19:

10. $$i = (-Fz_{Ag^+}D_{Ag^+}\frac{\partial c_{Ag^+}}{\partial y} - Fz_{NO_3^-}D_{NO_3^-}\frac{\partial c_{NO_3^-}}{\partial y} - Fz_{K^+}D_{K^+}\frac{\partial c_K}{\partial y}) + i \qquad \text{(A6.19)}$$

In Equation A6.19, the current densities cancel, proving that the total diffusion current at the electrode-electrolyte boundary is always zero for the **Lvk**. If the current density, *i*, on the right side of Equation A6.19 is substituted for Equation A6.11, it gives rise to Equation A6.20 below:

11. $$i = \left(-Fz_{Ag^+}D_{Ag^+}\frac{\partial c_{Ag^+}}{\partial y} - Fz_{NO_3^-}D_{NO_3^-}\frac{\partial c_{NO_3^-}}{\partial y} - Fz_{K^+}D_{K^+}\frac{\partial c_K}{\partial y}\right) - F^2 z_{Ag^+}^2 u_{Ag^+} c_{Ag^+}\frac{\partial \phi}{\partial y} - Fz_{Ag^+}D_{Ag^+}\frac{\partial c_{Ag^+}}{\partial y} \qquad \text{(A6.20)}$$

Two important conclusions can be drawn from Equation A6.20. The first is that the identity of Equation A6.20 is always valid if the first part of the right-hand side equals zero, which would imply that there is no diffusion potential in the electrolyte. This scenario has significant implications and can occur in very specific, albeit rare, combinations of species' concentration gradients, charges, and diffusion coefficients all-together, or if all species have identical diffusion coefficients. Logically, the latter one does not imply that the concentration gradient of each individual species is zero but rather the net diffusion of species in the solution cancels one another. This effect has been previously demonstrated in Part I and Part II[1,2] and will be briefly shown below. *This case is particularly noteworthy, as in the absence of diffusion current the solutions from both the* ***Lvk*** *and* ***NPE*** *methods become identical in every aspect, even when comparing the internal components of the Nernst-Planck Equation, such as potential gradients and species concentration gradients.* In the situation of zero diffusion potential, Equation A6.20 simplifies to Equation A6.16. Note that in this case, the migration current rising from the electrochemically active species does not need to be zero.

The second conclusion relates to the earlier discussion in this section, where the migration component of the Ag$^+$ *species must be zero for Equation A6.20 to hold true and for* ***Lvk*** *to yield similar answers to that of* ***NPE***. In this instance, the input current is a boundary condition that must be matched with the migration component of the electrolyte current density, Equation A6.16. We will now evaluate each term in Equation A6.20 and demonstrate, for the system considered, that the elimination of a particular term makes Equation A6.20 a valid identity and subsequently, reduced-ordered models such as **Lvk** extremely useful.

We continue our discussion will retain our focus at the electrode-electrolyte interface. To begin, the diffusion current arising from Ag$^+$ at the surface cannot be set to zero unless the dissolution of Ag$^+$ is governed by the chemical dissolution of a deposited Ag$^+$ layer at the surface which fixes the concentration of Ag$^+$. This is not the case here. Regarding the diffusion current from the supporting electrolyte species, its value at the surface cannot be zero because the net flux current must equal zero at the electrode surface for the supporting electrolyte. Therefore, the most plausible term to be set to zero is the migration current of the electrochemically active species, Ag$^+$. In such cases, the current in Equation A6.11 can be described purely in terms of the diffusion current from Ag$^+$, allowing us to utilize Equation A6.12 and Equation A6.13 to simplify Equation A6.20 into Equation A6.21:

$$12. \quad i = -F^2 z_{NO_3^-}^2 u_{NO_3^-} c_{NO_3^-} \frac{\partial \phi}{\partial y} - F^2 z_{K^+}^2 u_{K^+} c_{K^+} \frac{\partial \phi}{\partial y} = k \frac{\partial \phi}{\partial y} \qquad (A6.21)$$

where k is the conductivity of the solution.

Equation A6.21 is equivalent to Equation A6.16, which also serves as a boundary condition in reduced order modeling. In this case, the potential and current distributions, along with the spatial concentration of the electrochemically active species, are very similar between the **Lvk** and **NPE** methods, especially near the surface. However, other factors, such as the potential gradient or the concentration of the supporting electrolyte species, may still vary.

These adjustments, like the ones presented above, can introduce variations in the obtained solutions from **Lvk** when compared to the **NPE** method. Generally, the higher the migration current density of the electrochemically active species, the more pronounced these deviations may become (see Figure 6.8-6.12). As demonstrated in Part I and Part II[1,2], lower electrolyte conductivity tends to result in larger discrepancies between the **NPE** and **Lvk** methods. Adjustments to the input currents in the boundary conditions through solely adjusting the electrolyte conductivity, such as **Lvk**, cannot always ensure an accurate distribution of species (unless migration of electrochemically active species is negligible, all species electrolyte diffusion coefficient are the same, hence, the total electrolyte diffusion potential is zero, or diffusion current occurs), as the solutions for potential gradients may differ, which can, in turn, affect concentration gradients and other factors.

An important consideration is that the calculations of the diffusion potential using the **Lvk** method can be influenced by factors such as boundary conditions and species distribution and its value is deemed to always be zero at y=0, corresponding to electrode-electrolyte interface. While there may be variations near the surface, overall, the **NPE** has shown that a diffusion current/potential near the surface is to be expected and can be significant across all the conditions as shown above. It’s important to recognize that the **Lvk** method still provides valuable insights into the system's behavior. For greater precision, implementing the diffusion current of all the species throughout the entire calculation process can lead to more accurate results.

Comparison of the supporting electrolyte concentration species, NO_3^- and K^+, as a function of distance from the electrode surface, after 5h, for NPE and Lvk

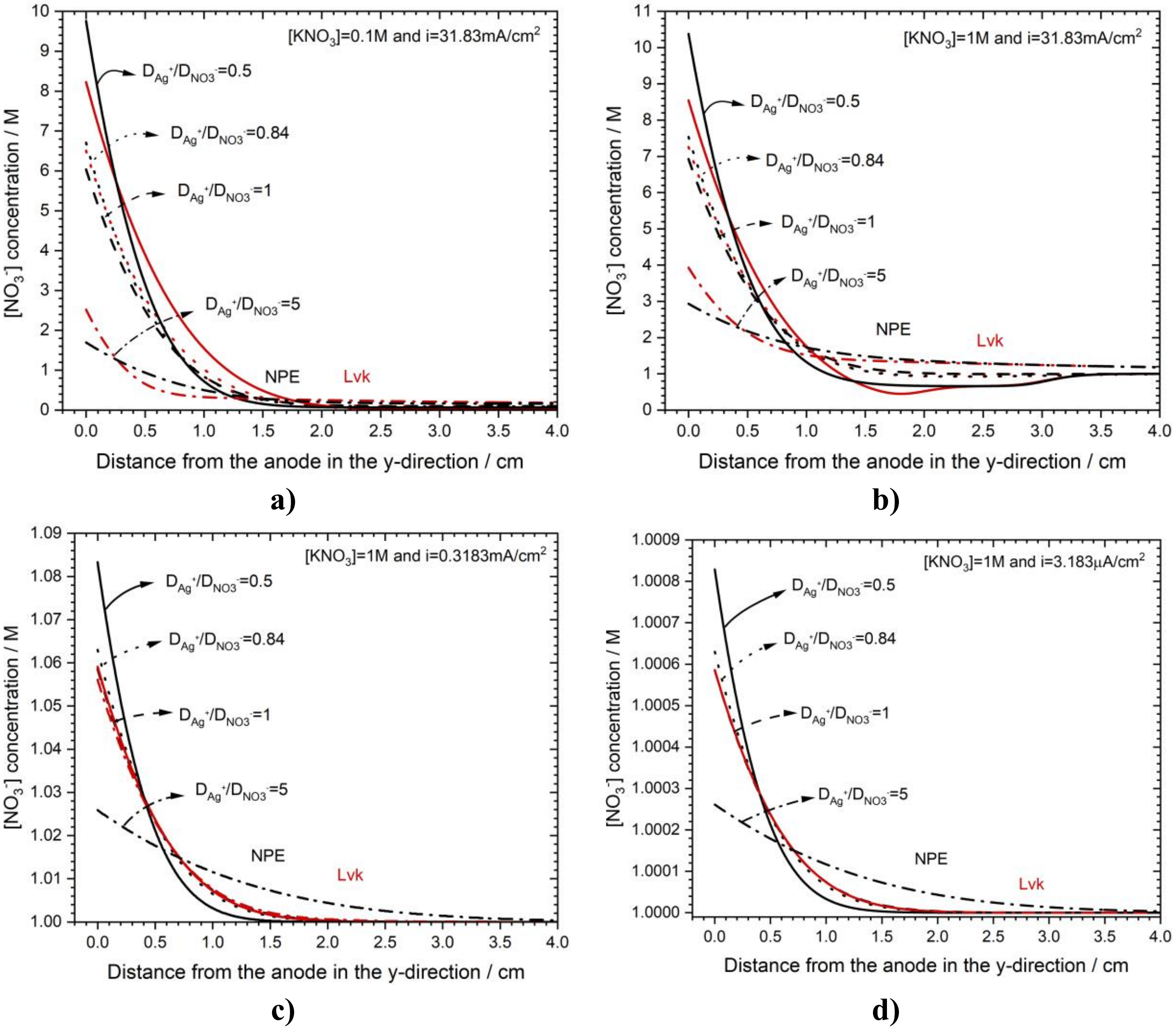

a) **b)**

c) **d)**

Figure A6.4. Variations in NO_3^- concentration as a function of distance orthogonal to the anode for various ratios of Ag^+ and NO_3^- diffusion coefficients at **a)** 0.1M KNO_3 and 31.83 mA/cm^2, **b)** 1M KNO_3 and 31.83 mA/cm^2, **c)** 1M KNO_3 and 0.3183 mA/cm^2, and **d)** 1M KNO_3 and 3.183 μA/cm^2. Results obtained for the **NPE**, and **Lvk** methods of calculations after a 5h simulation time. Line style of the arrows matches the line style of the potential for each $D_{Ag^+}/D_{NO_3^-}$ value.

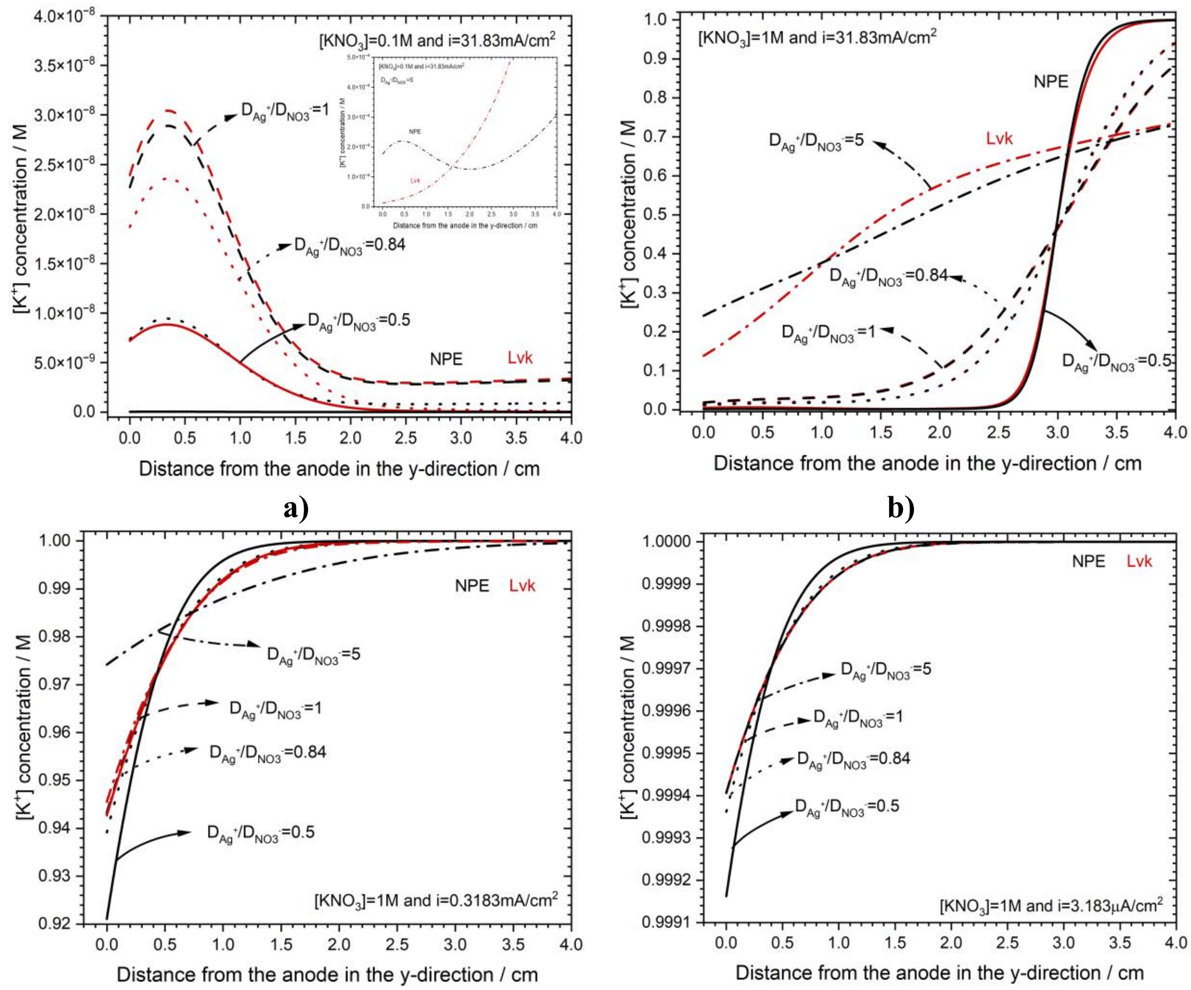

a) b)

c) d)

Figure A6.5. Variations in K$^+$ concentration as a function of distance orthogonal to the anode for various ratios of Ag$^+$ and NO$_3^-$ diffusion coefficients at **a)** 0.1M KNO$_3$ and 31.83 mA/cm^2, **b)** 1M KNO$_3$ and 31.83 mA/cm^2, **c)** 1M KNO$_3$ and 0.3183 mA/cm^2, and **d)** 1M KNO$_3$ and 3.183 μA/cm^2. Results obtained for the **NPE**, and **Lvk** methods of calculations after a 5h simulation time. Line style of the arrows matches the line style of the potential for each $D_{Ag^+}/D_{NO_3^-}$ value.

Chapter 7. Conclusion and future work

7.1. Conclusion

This work provided a quantitative approach to identifying and analyzing the critical factors surrounding pit propagation and repassivation and localized processes that happen near the electrode-electrolyte interface during pitting corrosion.

In *Chapter 2* of this thesis we presented a unifying quantitative framework for understanding repassivation behavior of SS316L and SS304 by integrating key parameters, including pH, anodic and cathodic kinetics within the pit, repassivation potential, and electrode-electrolyte interactions. The findings indicate that integrating thermodynamic modeling with kinetic data allows for the prediction of critical pH and concentration thresholds, further enhancing the understanding of repassivation mechanisms. One significant observation is that repassivation potential decreases with increasing pit depth, stabilizing at approximately -0.15 to -0.165 V vs. SCE for SS316L and -0.18 to -0.2 V vs. SCE for SS304 in the given electrolyte. Molybdenum in SS316L enhances repassivation by suppressing anodic kinetics and accelerating cathodic kinetics. Local cathodic kinetics play a crucial role, with i_c/i_a values of 2-4.5% for SS316L and ≤1% for SS304. Despite differences in individual kinetic parameters, the critical pit stability product ($(i\cdot x)_{rp}$) remains similar for both alloys at around 0.32 A/m, with the supporting factor (f) ranging between 0.35 and 0.4.

In *Chapter 3* we examined the repassivation behavior of SS316L in varying SO_4^{2-}/Cl^- ratios within a 0.6M NaCl solution using kinetic and thermodynamic parameters. Findings show that SO_4^{2-} increases the pH at the pit bottom, with a more pronounced effect as the fraction of saturation rises. Sulfate ion addition promotes the formation of primary stable salt precipitates (prior to the anticipated $FeCl_2 \cdot 4H_2O$ salt), such as $FeCl_2 \cdot 7H_2O$ and $NiCl_2 \cdot 6H_2O$, which can be linked to current oscillations during potentiostatic holds in mass-transfer-controlled regions and even repassivation under high applied potentials. In activation-controlled regions, sulfates inhibit corrosion by reducing anodic kinetics, increasing cathodic kinetics at anodic potentials, and lowering $(i_c/i_a)_{crit.}$ Compared to pure chloride solutions, sulfate-containing environments show a lower $(i\cdot x)_{sf}$ but a significantly higher f (~88%), with increased $(i\cdot x)_{crit}$ and E_{rp}, enhancing repassivation in SS316L.

In *Chapter 4* we looked into the role of transport conditions and cathode location in influencing shape factor values. Key findings indicate that occluded pits generally exhibit lower shape factor values than open pits, with some values falling below 1. Among different pit shapes, disk-shaped pits have smaller shape factor constants compared to spherical ones, and their shape factor decreases with increasing c/r ratio and occlusion angle, except at 90°. The study also presents a predictive method for determining the shape factor of a pit-within-a-pit structure, concluding that a secondary pit has minimal impact if the primary pit remains active. Furthermore, an empirical equation was introduced to quantify the impact of a lacy cover on shape factor, showing that such covers significantly reduce shape factor values. The study also found that while higher salt concentrations within pits slow down ionic transport, their role in pit stabilization is relatively limited compared to geometrical factors. As pit occlusion increases, the impact of ionic diffusivity differences between the interior and exterior diminishes. Finally, the chapter highlights that certain corrosion pit geometries, particularly those with thin electrolyte layers or adjacent cathodic sinks, can lead to very low shape factor values, reducing pit stability.

In *Chapter 5* we assessed the conservativism of Chen and Kelly's maximum pit size model with other FEA analysis techniques employing Secondary and Tertiary current distributions. The findings indicate that Chen and Kelly's model is conservative, underestimating maximum pit size by approximately 40% compared to Secondary current distribution predictions. This discrepancy arises primarily due to idealized assumptions about total cathodic current. Furthermore, neglecting electrolyte chemistry and its associated reactions leads to an underestimation of cathodic limitations, particularly when using the same anode boundary conditions as the original model. Introducing Tafel kinetics within the pit environment enhances model realism, reducing its conservatism but also increasing prediction uncertainty. Additionally, the study highlights the time-dependent nature of hydrolysis reactions, challenging equilibrium-based models that do not account for reaction kinetics over time. To balance accuracy and computational efficiency, the research suggests simplifying reaction modeling by confining them to the electrode-electrolyte boundaries, which maintains accuracy while reducing computational complexity.

In *Chapter 6* we looked closer into the ROMs, specifically the Lvk one, to try to help us understand the electrochemical processes near the electrode-electrolyte boundary for a localized corrosion cell and provide to us insights as to when and why such ROMs can prove to be useful even in such highly aggressive environments. Key findings reveal that at the electrode-electrolyte interface, the diffusion current from supporting electrolyte ions is substantial, precisely counterbalancing the migration current. Near the electrode-electrolyte interface, the diffusion current density of electrochemically active species remains consistently high and dominates migration current density. The study further indicates that the total diffusion current and potential at the electrode-electrolyte interface remain significant under most conditions, except in rare cases where all electrolyte species have identical diffusion coefficients or when the diffusion current of the supporting electrolyte offsets that of the active species. Additionally, the results show that the Lvk model can produce identical outcomes to the NPE method throughout the electrolyte if the total diffusion current is zero, maintaining high accuracy in the bulk solution beyond the diffusional boundary layer. However, in more general scenarios, the Lvk model's accuracy at the electrode-electrolyte interface improves as the migration current of electrochemically active species decreases. This condition is often met by increasing the concentration of the supporting electrolyte in high-current-density environments.

In an additional *Appendix i* we showed the third ROM developed by the authors of this dissertation, called FST. The study highlights the high precision and accuracy of the FST method in replicating the behavior and results of the NPE method. The results demonstrated the FST method's ability to achieve comparable accuracy while also showcasing its advantages over the NPE method. Furthermore, an emphasis was placed on the computational efficiency of the FST method, requiring fewer resources and less time compared to the NPE method.

Beyond traditional parameters such as potential, current, and concentration distribution-often the primary focus in FEM electrochemical models-the FST method also delivers high accuracy in predicting electrolyte conductivity, species concentration gradients, and diffusion and migration currents. This broader applicability makes it a valuable tool depending on specific electrochemical modeling needs. The accuracy of the FST method stems from its approach of solving potential distribution and species flux using the same governing equations as the NPE method, but in two sequential steps rather than a single step. An additional advantage of the FST method is its ease of initialization and convergence. Unlike the NPE method, which simultaneously solves current and transport equations-posing challenges in finding a solution to all the shape function equations as well as the computational demand-the FST model simplifies this process, making it a more efficient and user-friendly alternative for electrochemical simulations.

7.2. Future work and recommendations

While several recommendations for future research are provided in the limitations sections of the previous chapters, the following additional avenues of investigation are proposed:

1. *Controlled Study of Ionic Species Impact:* A controlled study should investigate the effects of other ionic species, such as Fe^{2+} and Ni^{2+}, on the hydrolysis of mixed salts. This study has shown that the time-dependent hydrolysis of Cr^{3+} significantly impacts simulation predictions. Preliminary findings suggest that the presence of ions like Ni^{2+} might slow down these processes. Therefore, there is a clear need for an experimental database followed by thermodynamic modeling of highly concentrated electrolytes often present in localized corrosion environments.
2. *Sulfate-to-Chloride Ratio in Pitting Corrosion:* While the influence of the sulfate-to-chloride ratio on the E_{rp} and f during pitting corrosion of SS316L has been studied, the investigations focused primarily on solutions with 0.6M chloride. It is essential to assess whether these effects are consistent across a range of chloride concentrations, which would provide broader applicability to various corrosive environments.
3. *Application to SNF Canisters:* The techniques used to evaluate the E_{rp} of SS316L and SS304 should be extended to more relevant environmental conditions, particularly those associated with pitting corrosion in SNF canisters. Specifically, the temperature range between 45°C and 65°C and relative humidity between 55% and 75% should be considered. While this study has demonstrated a combined experimental and computational approach, it is recommended that the methods be applied to electrolytes and environments that are more directly relevant to SNF canister surfaces.

4. *Validation of Pit Shape Factors:* Further experimental work is needed to validate the pit shape factors developed in Chapter 4. This validation will help improve the accuracy of models related to localized corrosion and enhance their predictive capabilities.
5. *Exploration of FST Method:* Additional research into the details of the FST method is recommended. This includes investigating other modes where the ROMs can be applied, such as fully coupled versus decoupled models, as well as exploring different discretization methods.
6. *FEA for Current Density Contributions:* The utilization of FEA to better understand the primary contributors to electrolyte current densities in localized corrosion environments is suggested. This will help translate these findings into more accurate shape factors and improve the modeling of localized corrosion processes.
7. *Study of Additional Corrosion Inhibitors on SNF Canisters:* Future work should focus on studying other inhibitors that might be present on the surface of SNF canisters, such as NO_3^-. A combined thermodynamic and experimental approach should be developed to study their effect on time-dependent repassivation of SS316L and SS304, which is crucial for understanding long-term corrosion behavior.
8. *In Situ Characterization of Pit Propagation:* In situ optical microscopy characterization of the 1D pit experiments during sulfate addition is recommended to visually assess how sulfate influences salt film properties during pit propagation. Comparing these results with pure chloride solutions would provide valuable insights into the role of sulfate in the corrosion process.

Section i. Additional information on another ROM developed from this work.

i1. Introduction

Over the past few years, the Finite Element Method (FEM) has emerged as an indispensable tool in engineering and the sciences due to its robust capability to analyze intricate structures and complex environments.[1–6] FEM empowers modelers by discretizing continuous domains into smaller elements, thereby facilitating the numerical solutions of partial differential equations (PDEs). However, solving these complicated environments, which often entail complex and highly non-linear PDEs, can be computationally intensive, especially for large-scale systems demanding high accuracy.

To address these challenges and enhance efficiency and flexibility, modelers frequently turn to reduced-order modeling techniques (ROMs). These techniques are grounded in the principle that a lower-dimensional system or a reduced set of governing equations can adequately represent complex systems. However, this simplification is not without trade-offs, as it can impact the accuracy of the results obtained.

In the field of electrochemistry, particularly concerning corrosion, solving PDEs necessitates consideration of potential distributions, ohmic drop, charge and species transport, and both homogeneous and heterogeneous chemical reactions. Consequently, solutions to these systems can become exceedingly complex and computationally demanding. In such scenarios, ROMs offer a more robust and time-efficient solution while maintaining a certain level of accuracy. Previous studies have demonstrated that implementing ROMs in corrosion studies can significantly enhance computational efficiency. However, the accuracy and the acceptable error margins of these methods can be highly dependent on the input boundary conditions.

The development of computational methods that are both efficient and accurate in the field of electrochemistry is of paramount importance for various applications. This is especially true where complications arise from highly complex and non-linear governing equations and when the computational powers are limited.

i2. Governing equations

In the field of electrochemistry, the electrochemical reactions occurring at the electrolyte/electrode interface, along with the transport of species within the electrolyte, govern the current and potential distribution. The interactions between ions in an electrolyte, and between the ions and the solvent, can be intricate and challenging to model accurately. To simplify these complexities, one common assumption is that the fluxes of ionic species are not independent from one another. This is often referred to as the dilute solution approximation, which also assumes that the activity and the concentration of a given species are equal. Under these conditions, the general equation that describes mass transport is given by:

$$\frac{dc_i}{dt} = -\nabla(-D_i\nabla c_i - z_i u_i c_i F\nabla\varphi + c_i u) + R_i \qquad \text{(B.1)}$$

here c_i is the concentration of species i, D_i is the diffusion coefficient of species i, z_i is the species charge of species i, u_i is the species mobility of species i, u is the bulk electrolyte velocity, φ is the electrostatic potential, and R_i represents the consumption or production of species i from homogeneous reactions in the electrolyte.

The aim of this study is to develop a more efficient yet accurate subroutine method for solving complex partial differential equations in electrochemistry, particularly the Nernst-Planck Equation with electroneutrality as a constraint (**NPE**). Both simple and complex models, considering the effects of diffusion, migration, and chemical reactions on mass transport, were analyzed. It is important to note that this study does not aim to validate the findings of the referenced studies; hence, no comments on their scientific conclusions are provided. Parameters utilized in each model are discussed individually in subsequent sections. Modifications to some input geometrical and rate constants were made for ease of convergence, and any such changes are clearly noted in the respective sections. These modifications do not impact the primary objective of this paper, which is to evaluate the outcomes of a new modeling approach rather than compare with previously published results.

i3. Computational Methods

This study builds on the models developed by Moraes and Kelly[1,2], as well as Fu and Chan.[7] Partial differential equations were solved using COMSOL Multiphysics (v.6.2), incorporating the PARDISO direct linear solver and a modified Newtonian method nonlinear solver. The Backward Differential Formula (BDF) method was used for time-step generation. Detailed descriptions of model geometries and meshing techniques can be found in the referenced papers. When mesh details were not provided, the mesh was refined until the results stabilized. For further information on meshing techniques, refinement, and solvers, refer to the COMSOL Multiphysics user manual. Simulations were performed on a system with an Intel Core i9 3.70 GHz processor, 64 GB of RAM, and Windows 10.

Explanation of the computational methods utilized

The study aims to evaluate the accuracy, efficiency, and benefits of various computational methods for FEM electrochemical systems. The following methods were employed:

3. **Nernst-Planck with Electroneutrality (NPE):** This Tertiary current distribution module in COMSOL Multiphysics solves for species, current, and potential distribution based on a make-up ion, maintaining energy and mass conservation. Detailed equations and descriptions can be found in the COMSOL user manual.

4. **Modified Laplace (Lvk):** A reduced order modeling technique by Moraes and Kelly[1,2], which solves the Laplace Equation and species transport in two separate steps. The spatial variations of electrolyte conductivity, solved using the Transport of Dilute Species module, are used to determine potential distribution via the Laplace Equation in the Secondary Current Distribution module, as shown in Equation B.2:

$$i = -\nabla\varphi F^2 \sum_i z_i^2 u_i c_i \tag{B.2}$$

The model neglects current from species diffusion and does not impose electroneutrality. Multiphysics potential coupling exists between the Secondary Current Distribution and species transport modules. Through this, the potential solved from the Laplace Equation serves to solve the flux migration of the species in the Transport of Dilute Species module.

5. **Full Secondary+Transport (FST):** Another reduced order model introduced in this study. This method extends the **Lvk** approach by including diffusion current and applying electroneutrality. The migration and diffusion fluxes from the Transport of Dilute Species module are used in the Secondary Current Distribution module according to Equation B.3. Multiphysics potential coupling is also applied, and electroneutrality is maintained using Equations B.4 and B.5.

$$i = F \sum_i z_i(-D_i\nabla c_i - z_i u_i c_i F\nabla\varphi) \tag{B.3}$$

$$\sum_i z_i c_i = 0 \tag{B.4}$$

$$c_j = -\frac{\sum_{i\neq j} z_i c_i}{z_j + eps} \tag{B.5}$$

Model 1: Galvanically-Driven Dissolution of Mg in Various NaCl Solutions

The first model, originally developed by Moraes and Kelly, examines a galvanic couple between aluminum (Al) and magnesium (Mg), originally designed to investigate the protection offered by Mg-rich primers (MgRp). The model consists of a 2D cross-sectional representation of a 10 mm long scratch that exposes the bare Al surface, on the two sides of which 5 mm long MgRp-coated surfaces are located. A schematic of the geometry and the general boundary conditions are shown in Figure i.1. This setup follows the methodology described in previous publications by Moraes and Kelly.

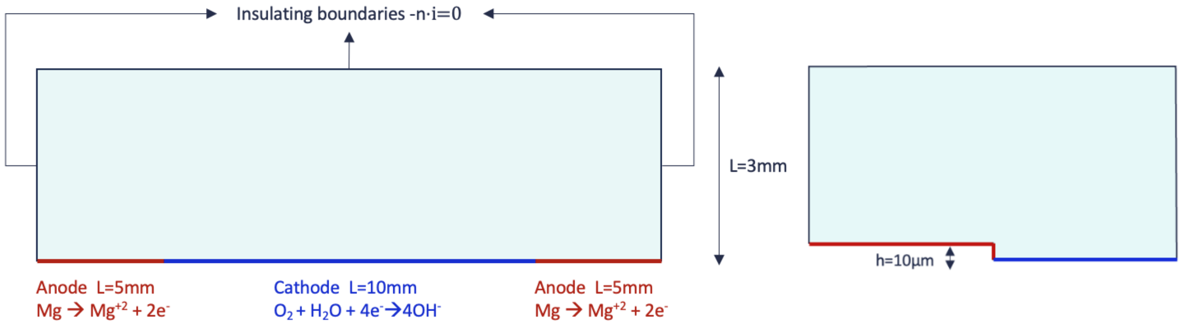

Figure i.1. Schematic representation of the geometry of the galvanic couple from Moraes and Kelly[1,2] **a)** general view with input geometrical and electrochemical boundary conditions b) a zoomed view of the 10um step separating the anode and the cathode.

The transport and kinetic parameters used in the model are summarized in Table i.1. The study was conducted with a quiescent electrolyte of 3 mm thickness and NaCl concentrations ranging from 1×10^{-4} M to 1 M. Electrochemical surface kinetics followed a Tafel relation for both the anode and cathode. For the Al surface, acting as the cathode, only the hydrogen evolution reaction (HER) was considered. The anodic reaction focused solely on the dissolution of Mg with the current coupled to the production of Mg^{2+} and OH^- species. The model assumed an infinitely diluted solution with constant diffusion coefficients.

This study explored only Case II from Moraes and Kelly's original work, which includes a sink term for $Mg(OH)_2$ precipitation and water hydrolysis equilibrium, K_w. The model was solved using **NPE**, **FST**, and **Lvk** over a simulation time of 7200 seconds. The mesh element size ranged from 7.3×10^{-6} m to 2.4×10^{-4} m, with a total of 26,998 elements.

Table i.1. Parameters utilized for the Moraes and Kelly model. All values obtained from the original publication. [1,2]

Parameter	***Description***	***Value***
i_0	Anodic and cathodic exchange current density	10^{-8} A/cm^2
$E_{0,a}$	Reverse potential for anodic reaction	-1.60 V vs.ref
$E_{0,c}$	Reverse potential for cathodic reaction	-0.834 V vs.ref
$\beta_{a/c}$	Anodic/Cathodic Tafel slope	-118mV
D_{Na^+}	Diffusion coefficient of Na^+	1.18×10^{-9} m^2/s
D_{Cl^-}	Diffusion coefficient of Cl^-	1.75×10^{-9} m^2/s
D_{H^+}	Diffusion coefficient of H^+	9.30×10^{-9} m^2/s
D_{OH^-}	Diffusion coefficient of OH^-	5.22×10^{-9} m^2/s
$D_{Mg^{2+}}$	Diffusion coefficient of Mg^{2+}	0.72×10^{-9} m^2/s
k	Reaction rate for $Mg(OH)_2$ precipitation	3.7 m^6/(s·mol^2)

k_{sp}	Apparent solubility product of $Mg(OH)_2$	4.12×10^{-12} m^3/dm^9
K_w	Water hydrolysis equilibrium	1.0×10^{-14}

Model 2: Galvanostatic Dissolution of Ag Wire in KNO_3

The model utilized here is the same as Fu and Chan mentioned in Chapter 6 of this dissertation. No changes from the model mentioned there are conducted. Hence, the reader is referred to the details in that section to read further on the input boundary conditions and the results

i4. Results

The results from the newly proposed subroutine model, **FST**, will be introduced. Comparative results among the **NPE**, **FST**, and **Lvk** models, based on Moraes and Kelly's galvanic couple model, will be demonstrated for various NaCl concentrations. In the final part, Fu and Chan's model will be employed to validate the **FST** model.

A case of galvanic couple- FST model

In the previous section, we demonstrated that, for a simple galvanic couple with homogeneous chemical reactions, the diffusion current plays a crucial role in the overall calculations and cannot be neglected. However, solving the **NPP** or **NPE** Equations simultaneously can be computationally expensive, time-consuming, and challenging to converge. In this section, we will compare the results obtained after 7200s using the **Lvk**, **NPE**, and **FST** methods for the simple galvanic couple from Moraes and Kelly using NaCl concentrations 1×10^{-4} M, 0.001M, 0.01M, 0.1M, and 1M. It is important to note that the **FST** method is a reduced-order approach that couples the solution of Laplace Equation and the Transport of Dilute Species while solving it into two distinct steps all while maintaining electroneutrality. This approach is designed to yield results comparable to those of the **NPE** method, but with reduced computational time, lower resource requirements, and improved ease of model convergence.

Table i.2. Comparison between the computational time and physical memory of different governing equations.

NaCl Concentration / M	**NPE**		**FST**		**Lvk**	
	Time / s	Memory / GB	Time / s	Memory / GB	Time / s	Memory / GB
1×10^{-4}	634	5.71	1847	3.55	207	3.49
0.001	1505	5.78	1312	3.57	309	3.50
0.01	10616	5.81	2667	3.61	2026	3.52
0.1	13696	5.87	2925	3.64	4354	3.51
1	13328	5.89	3341	3.62	5524	3.50

Table i2 compares the computational time and physical memory requirements for the tested NaCl concentrations across different governing equations. For a 1×10^{-4} M NaCl concentration, the **FST** method required more computational time than both the **NPE** and **Lvk** methods. However, as the concentration increased to 0.001 M and 0.01 M, the **FST** method surpassed the **NPE** method in speed, although it remained slower than the **Lvk** method. At higher concentrations of 0.1 M and 1 M NaCl, the **FST** method achieved convergence faster than both the **Lvk** and **NPE** methods.

It is important to note that the computational times for the **Lvk** method in this study differ from those reported in previous works by Moraes and Kelly. While the model dimensions and input parameters are identical, the model presented here includes additional geometrical features (*i.e.,* one-dimensional lines) which add to the computational expense but were needed to understand the intricacies on how the current and potential combined with mass transport equations are solved from the software. Regarding physical memory usage, the **FST** method demonstrated effective performance, ranking second among the three methods tested.

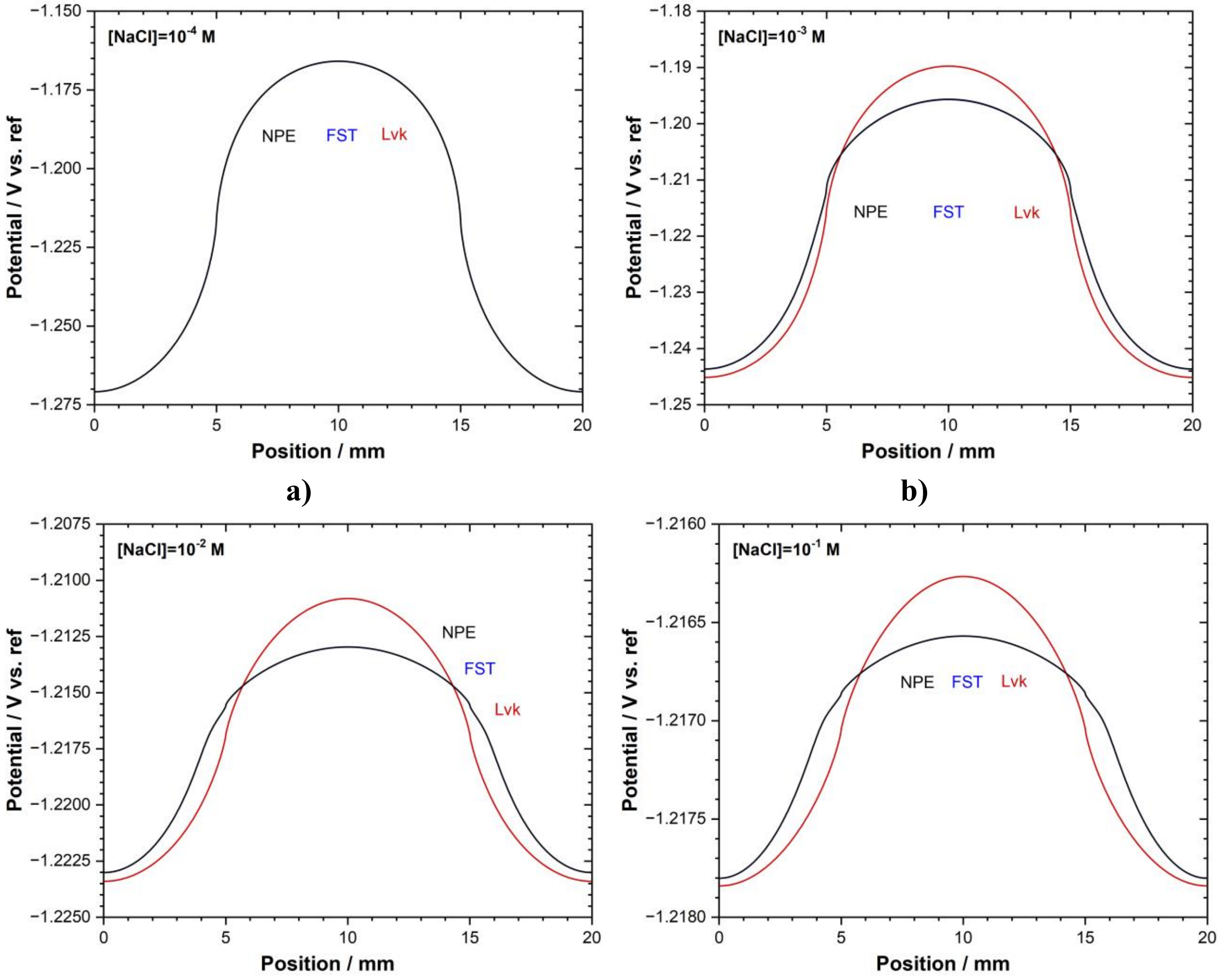

a)

b)

c)

d)

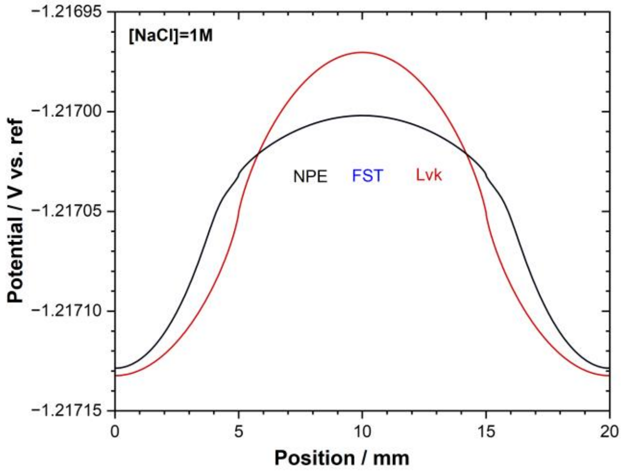

e)

Figure i.1. Potential distribution over the anode and cathode surface after 7200s obtained through using **NPE** (black), **FST** (blue), and **Lvk** (red) methods for NaCl electrolyte concentrations of **a)** 1×10^{-4} M, **b)** 0.001M, **c)** 0.01M, **d)** 0.1M, and **e)** 1M. Note that the curves from NPE and FST are indistinguishable as they are on top of one another.

Figures i2a through i2e display the potential distribution over the anode and cathode surfaces for NaCl concentrations ranging from 1×10^{-4} M to 1M after 7200 seconds, using the **NPE**, **FST**, and **Lvk** methods. The results clearly demonstrate that the solutions obtained with the **FST** method are in excellent agreement with those from the **NPE** method. The **FST** results, represented by the blue line, align perfectly with the **NPE** curve, shown as the black line. While the percent error in potential measurements is highly dependent on the reference potential, the maximum percent error observed for the **FST** method compared to the **NP** method is a mere 0.0038% for the 0.001M NaCl concentration. The potential distribution for the **Lvk** method will not be extensively discussed here, as has been thoroughly analyzed by Moraes and Kelly in previous studies. However, it is worth noting that the highest percent error for the **Lvk** method is 0.38%, occurring at the low NaCl concentration of 0.001M.

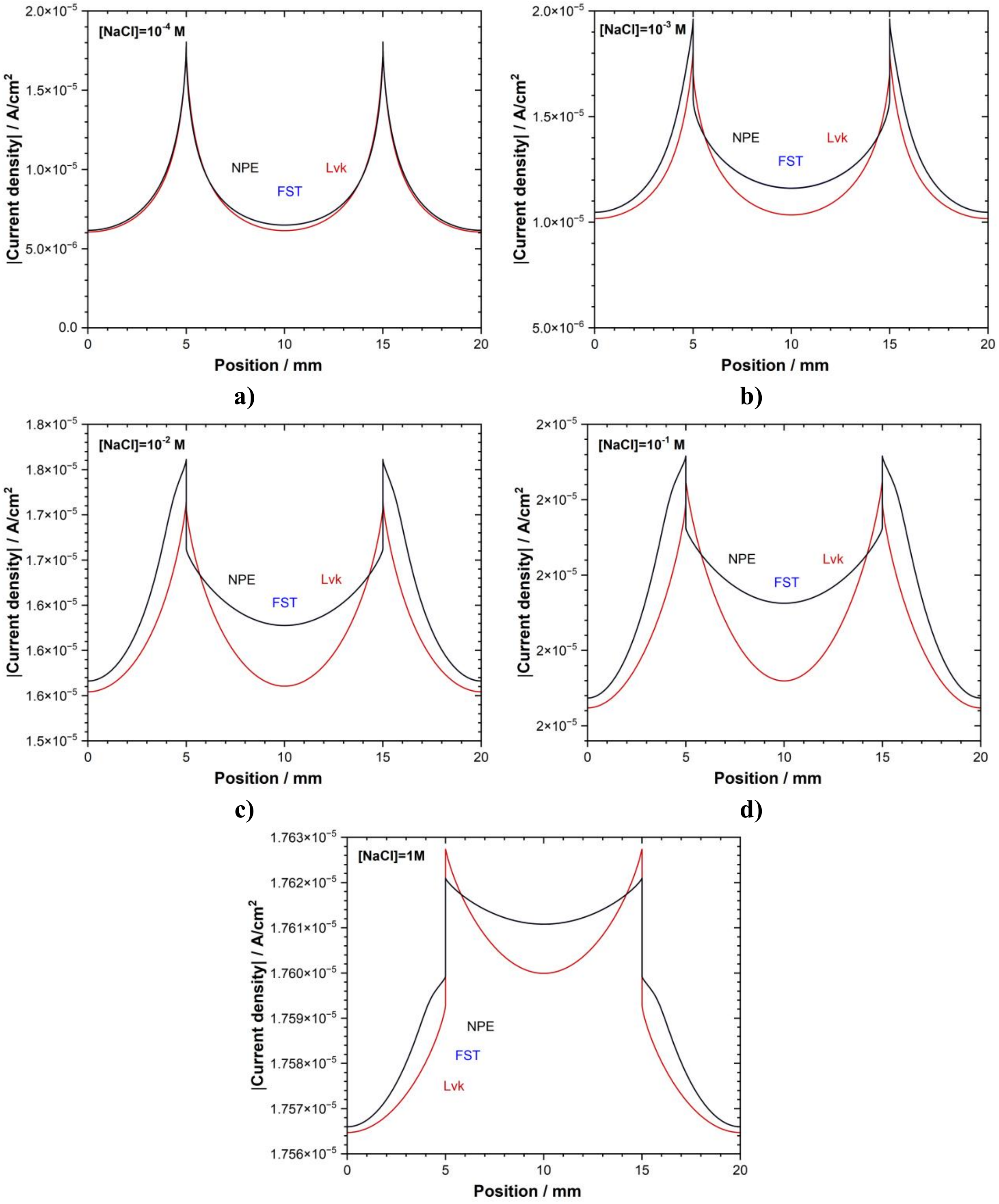

a)

b)

c)

d)

e)

Figure i.2. Absolute value of current density distribution over the anode and cathode surface after 7200s obtained through using **NPE** (black), **FST** (blue), and **Lvk** (red) methods for NaCl electrolyte concentrations of **a)** 1×10^{-4} M, **b)** 0.001M, **c)** 0.01M, **d)** 0.1M, and **e)** 1M. Note that the curves from NPE and FST are indistinguishable as they are on top of one another.

Figures i3a through i3e show the absolute value of the current distribution over the anode and cathode surfaces for NaCl concentrations ranging from 1×10^{-4} M to 1M after 7200 seconds, using the **NPE**, **FST**, and **Lvk** methods. Across all NaCl concentrations, the results from the **FST** method align perfectly with those from the **NPE** method. However, this level of agreement is not observed with the **Lvk** method, particularly at lower NaCl concentrations. The maximum percent error for the **FST** method is approximately 0.09%, while for the **Lvk** method, it is around 10.6% for a 0.001M NaCl electrolyte. In both methods, the highest percentage error occurs in the current density distribution over the cathode.

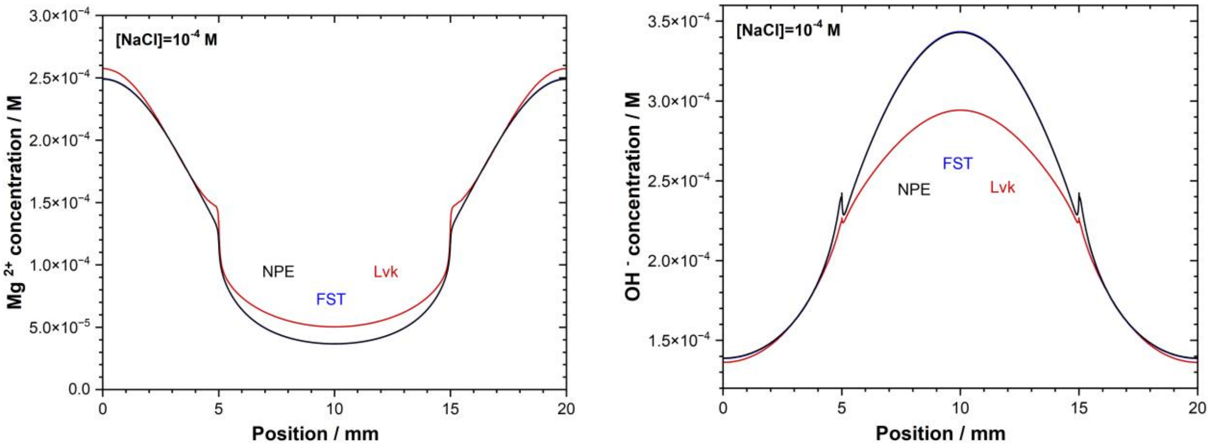

a)

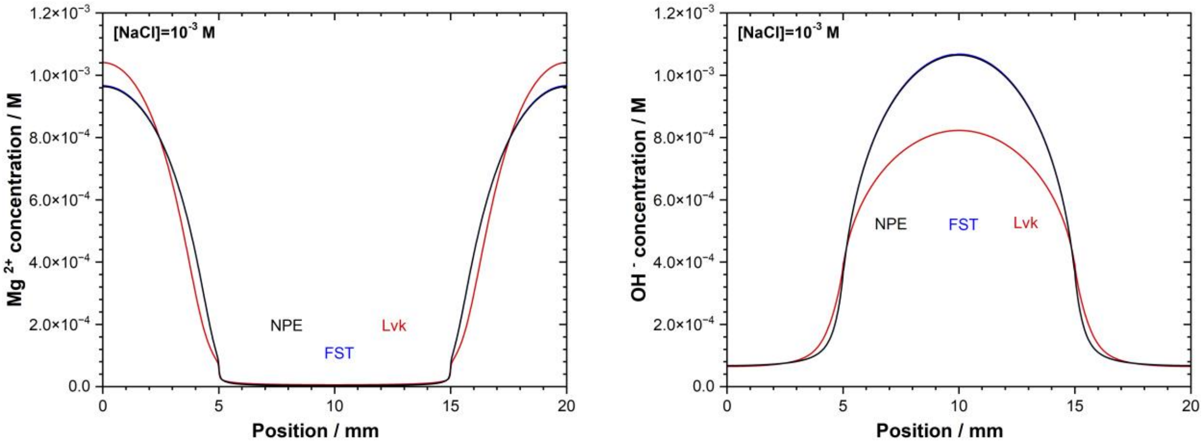

b)

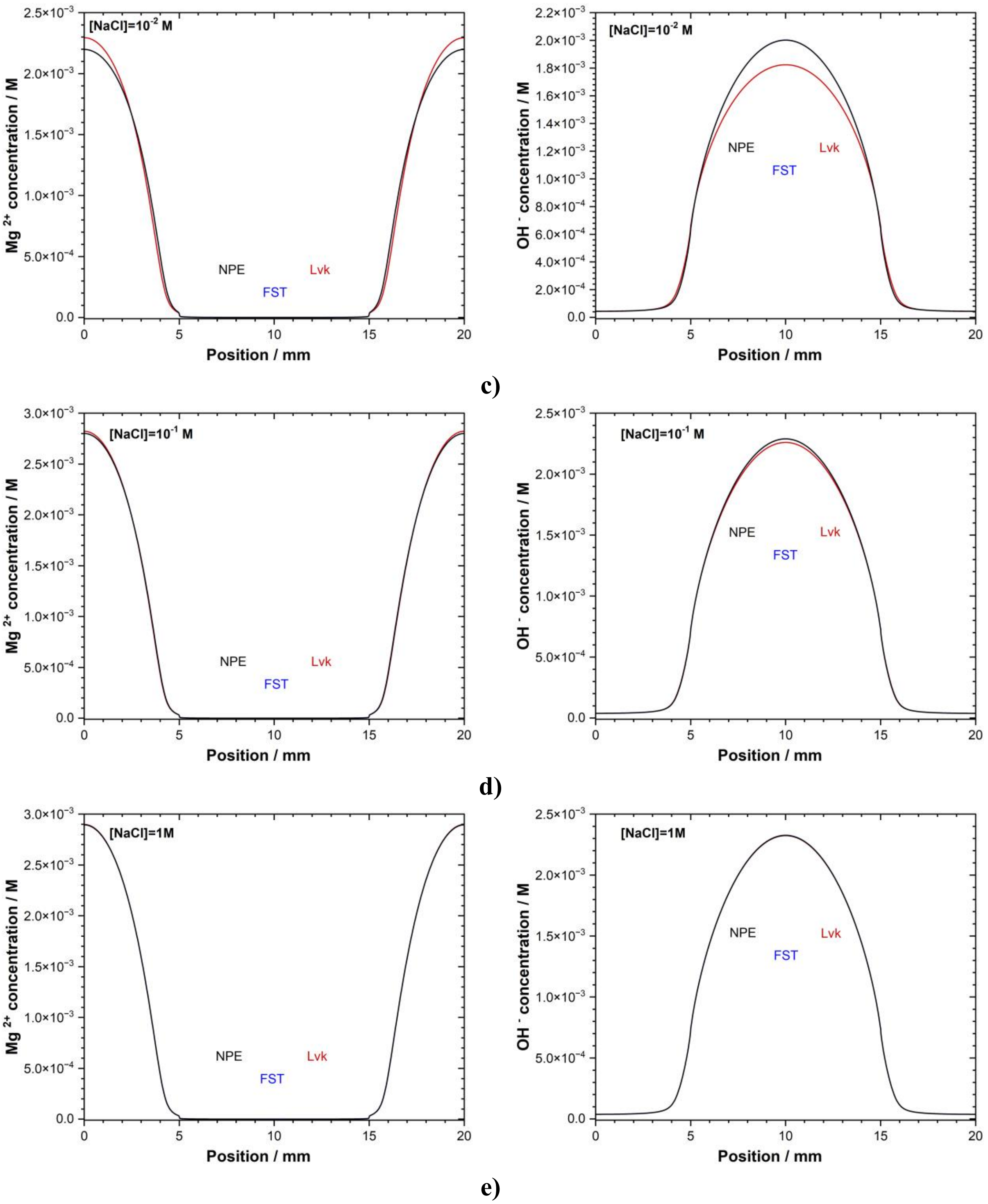

Figure i.3. Mg^{2+} concentration (1) and OH^- concentration (2) over the anode and cathode surface after 7200s obtained through using **NPE** (black), **FST** (blue), and **Lvk** (red) methods for NaCl electrolyte concentrations of **a)** 1×10^{-4} M, **b)** 0.001M, **c)** 0.01M, **d)** 0.1M, and **e)** 1M. Note that the curves from NPE and FST are indistinguishable as they are on top of one another.

Figures i4a through i4e depict the surface concentration distribution of Mg^{2+} (1) and OH^- (2) over the anode and cathode for NaCl concentrations ranging from 1×10^{-4} M to 1M after 7200 seconds, using the **NPE**, **FST**, and **Lvk** methods. Similar to the results for potential and absolute current density distribution, the highest percentage error is observed at the low NaCl concentration of 0.001M. Since Mg^{2+} are produced at the anode and OH^- at the cathode, with their accumulation occurring near their respective surfaces over time, it is appropriate to compare the percent errors of Mg^{2+} over the anode and OH^- over the cathode. For Mg^{2+}, the highest percent error over the anode surface is 0.8% for the **FST** method and 37.4% for the **Lvk** method. Conversely, the percent error for OH^- on the cathode surface is 0.31% for the **FST** method and 22.7% for the **Lvk** method.

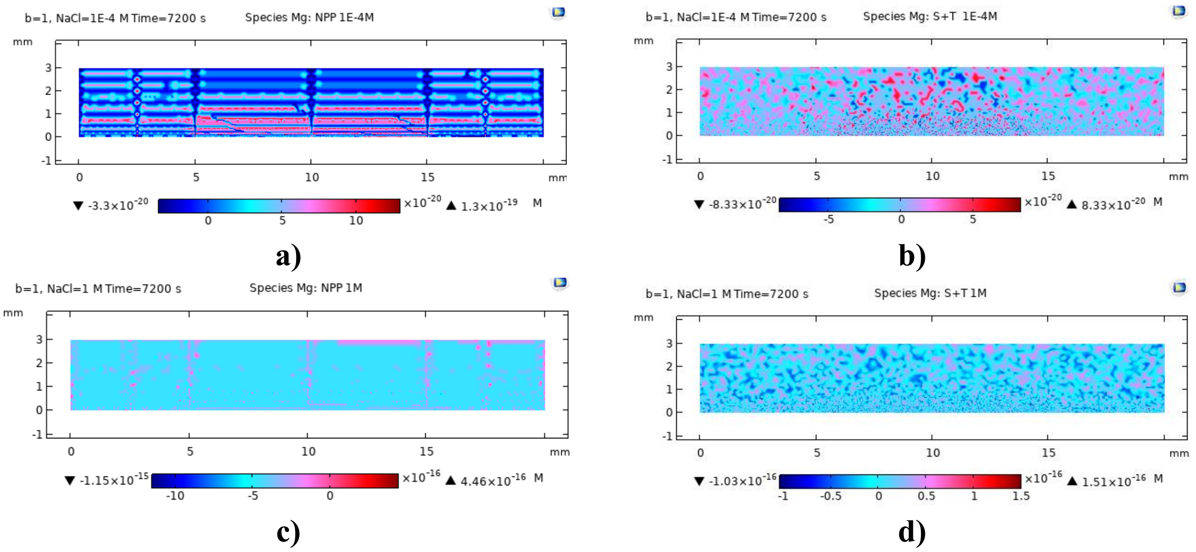

a) b) c) d)

Figure i.4. Charge density as a function of position in the electrolyte for concentrations of 1×10^{-4} M and 1M NaCl with **a)** and **c)** for **NPE** and **b)** and **d)** for **FST** after 7200s.

Figures i5a through i5d illustrate the charge density distribution within the 1×10^{-4} M and 1M NaCl electrolytes after 7200 seconds, as calculated using both the **NPE** and **FST** methods. These figures highlight the capability of the **FST** subroutine to accurately maintain electroneutrality across the entire electrolyte, a critical factor in ensuring the accuracy of the electrochemical model. The false-color plots effectively demonstrate that, even at these extreme NaCl concentrations, the **FST** method achieves charge density distributions that are nearly indistinguishable from those obtained using the **NPE** method. While Figures i5a and i5d focus on the extreme cases of 1×10^{-4} M and 1M NaCl, it is important to note that this consistency in charge density maintenance was observed across all tested NaCl concentrations, not just the extremes. This close alignment between the two methods underscores the robustness of the **FST** approach in handling variations in electrolyte concentration while maintaining the essential physical property of electroneutrality.

The results indicate that the **FST** method generally yields results that closely match those obtained with the **NPE** method while offering advantages in speed, computational efficiency, and ease of convergence. The newly developed subroutine demonstrates that the Nernst-Planck and Laplace Equations law do not need to be solved simultaneously. Instead, a step-based subroutine can be implemented where the potential distribution is first calculated and then used to solve the mass transport equations. The species flux from the mass transport solution can then be used to calculate the current and update the potential distribution in the next step. This iterative process continues until the desired time-dependent convergence is achieved.

i.5. Discussion

*The **FST** method is highly precise and accurate in predicting the same behavior and results as the **NPE** method.*

Figures 9 through 17 demonstrate the precision and accuracy of the **FST** method compared to the **NPE** method while highlighting its advantages compared to the **Lvk** one. Additionally, the results in Tables 3 and 4 highlight the advantages of the **FST** method in terms of computational time and resources compared to the **NPE** method. Note that the accuracy of the results is not limited to parameters such as potential, current, and concentration distribution, which are often the primary focus in FEM electrochemical systems. precision and accuracy of the **FST** model are due to its use of the same equations as the **NPE** method to solve for potential distribution and species flux, despite being done in two separate steps rather than the single step used by the **NPE**. An additional, often overlooked but important, benefit of the **FST** model is that it is easier to initiate and converge compared to models that solve current and transport equations simultaneously, as in the **NPE** method.

Limitations

As previously mentioned, the **FST** method offers a highly accurate, less computationally intensive, faster, and easier-to-converge approach for FEM electrochemical simulations. The **FST** method has demonstrated accuracy comparable to the **NPE** method across two models that include potential and current distribution, as well as the transport of chemical species with homogeneous reactions. However, there are two key limitations to the model:

1. ***Software compatibility:*** The model has only been tested using COMSOL Multiphysics Version 6.2. If other FEM software is to be utilized, it must include modules for current distribution and species transport, where necessary modifications to boundary condition equations can be made. Specifically, the user must be able to define the current in the secondary current distribution in terms of the migration and diffusion fluxes from the transport module. Additionally, in the transport module, the user must be able to redefine the concentration of the make-up ion in terms of other ions to maintain electroneutrality. These changes must be consistently applied across all equations involving the make-up ion concentration in the electrolyte and boundary conditions.

2. ***Limited customization in COMSOL Multiphysics 6.2:*** COMSOL Multiphysics Version 6.2 includes a predefined variable for ion concentration in the Transport of dilute species module. In this study, the authors encountered limitations in modifying the make-up ion, specifically the Na^+, in the boundary fluxes of the Transport of dilute species module, as certain boundary flux equations were not editable. This limitation may have contributed to the slight discrepancies observed when comparing the **FST** method to the **NPE** method.

i.6. References

1. Moraes, C. V. & Kelly, R. G. A comparison of FEM results from the use of different governing equations in a galvanic cell part I: In the presence of a supporting electrolyte. *Electrochim. Acta* **469**, 143146 (2023).
2. Moraes, C. V. & Kelly, R. G. A comparison of FEM results from the use of different governing equations in a galvanic cell part II: Impact of low supporting electrolyte concentration. *Electrochim. Acta* **468**, 143153 (2023).
3. Marshall, R. S. *et al.* Galvanic Corrosion between Coated Al Alloy Plate and Stainless Steel Fasteners, Part 2: Application of Finite Element Method and Machine Learning to Study Galvanic Current Distributions. *Corrosion* **79**, 157–173 (2023).
4. King, A. D., Lee, J. S. & Scully, J. R. Finite Element Analysis of the Galvanic Couple Current and Potential Distribution between Mg and 2024-T351 in a Mg Rich Primer Configuration. *J. Electrochem. Soc.* **163**, C342–C356 (2016).
5. Liu, C., Srinivasan, J. & Kelly, R. G. Editors' Choice—Electrolyte Film Thickness Effects on the Cathodic Current Availability in a Galvanic Couple. *J. Electrochem. Soc.* **164**, C845–C855 (2017).
6. Alkire, R., Bergh, T. & Sani, R. L. Predicting Electrode Shape Change with Use of Finite Element Methods. *J. Electrochem. Soc.* **125**, 1981–1988 (1978).
7. Fu, J. W. & Chan, S. K. Finite Element Method for Modeling Localized Corrosion Cells. *Corrosion* **40**, 540–544 (1984).